IMPROVING THE IMAGE AND QUANTITATIVE DATA OF MAGNETIC RESONANCE IMAGING THROUGH HARDWARE AND PHYSICS TECHNIQUES

by

Joshua D. Kaggie

A dissertation submitted to the faculty of
The University of Utah
in partial fulfillment of the requirements for the degree of

Doctor of Philosophy

in

Physics

Department of Physics and Astronomy

The University of Utah

August 2015

The University of Utah Graduate School

STATEMENT OF DISSERTATION APPROVAL

The following faculty members served as the supervisory committee chair and members for the dissertation of Joshua D. Kaggie.

Dates at right indicate the members' approval of the dissertation.

Brian T. Saam, Chair	October 21, 2014 Date Approved
Carleton DeTar, Member	October 21, 2014 Date Approved
J. Rock Hadley, Member	October 21, 2014 Date Approved
Glen R. Morrell, Member	October 21, 2014 Date Approved
Dennis L. Parker, Member	October 21, 2014 Date Approved

The dissertation has also been approved by Carleton DeTar

Chair of the Department/School/College of Physics and Astronomy

and by David B. Kieda, Dean of The Graduate School.

ABSTRACT

In Chapter 1, an introduction to basic principles or MRI is given, including the physical principles, basic pulse sequences, and basic hardware. Following the introduction, five different published and yet unpublished papers for improving the utility of MRI are shown.

Chapter 2 discusses a small rodent imaging system that was developed for a clinical 3 T MRI scanner. The system integrated specialized radiofrequency (RF) coils with an insertable gradient, enabling 100 μm isotropic resolution imaging of the guinea pig cochlea in vivo, doubling the body gradient strength, slew rate, and contrast-to-noise ratio, and resulting in twice the signal-to-noise (SNR) when compared to the smallest conforming birdcage.

Chapter 3 discusses a system using BOLD MRI to measure T_2* and invasive fiberoptic probes to measure renal oxygenation (pO_2). The significance of this experiment is that it demonstrated previously unknown physiological effects on pO_2, such as breath-holds that had an immediate (<1 sec) pO_2 decrease (~6 mmHg), and bladder pressure that had pO_2 increases (~6 mmHg).

Chapter 4 determined the correlation between indicators of renal health and renal fat content. The R^2 correlation between renal fat content and eGFR, serum cystatin C, urine protein, and BMI was less than 0.03, with a sample size of ~100 subjects, suggesting that renal fat content will not be a useful indicator of renal health.

Chapter 5 is a hardware and pulse sequence technique for acquiring multinuclear ^{1}H and ^{23}Na data within the same pulse sequence. Our system demonstrated a very simple, inexpensive solution to SMI and acquired both nuclei on two ^{23}Na channels using external modifications, and is the first demonstration of radially acquired SMI.

Chapter 6 discusses a composite sodium and proton breast array that demonstrated a 2-5x improvement in sodium SNR and similar proton SNR when compared to a large coil with a linear sodium and linear proton channel. This coil is unique in that sodium receive loops are typically built with at least twice the diameter so that they do not have similar SNR increases.

The final chapter summarizes the previous chapters.

May we always learn and discover more.

CONTENTS

LIST OF TABLES

LIST OF FIGURES

ACKNOWLEDGMENTS

I would like to thank Dennis Parker and Rock Hadley, for initially allowing me to volunteer in the RF coil lab. I doubt that I could have imagined how fascinating MRI is without that opportunity. I would like to thank them for the knowledge, training, funding, and expertise that they have passed on to me throughout the years. I am very grateful for having been able to work for and with them. Without Rock, I would never have developed knowledge of RF coils. Without Dennis, I never would have developed any knowledge of MRI and would never have achieved my PhD.

I would like to thank Neal Bangerter for allowing me to work with him in sodium imaging. The many late nights scanning with him and Glen were very fruitful. If he had not come to Utah, we would not have come up with the sodium breast coil that we all feel quite proud of.

I would like to thank Glen Morrell for allowing me to work with him. Glen's breast grant allowed me to scan for long periods during many off hours. Glen's mentoring helped me understand many of the more nuanced aspects of MRI.

I would like to thank Craig Goodrich for being a mentor and friend. Craig and I were able to share many discussions on life in general during those many weekends that we spent together scanning.

I would like to thank EK Jeong, for being able to develop the simultaneous MRI system and allowing me to work with his students, and for his exuberance for Python programming.

I would like to thank Vivian Lee for funding and for allowing me to work on so many interesting projects.

I would like to thank Brian Saam for being the Chair of my physics doctoral committee, and thank Carleton DeTar for his help on my committee as well.

I would like to thank David Kieda, who hired me years ago to do astrophysics simulations and hardware as an undergraduate. I wasn't sure then whether anyone actually ever enjoyed their job, but that was the start of a love of science and physics.

I also want to thank others in the physics department for their help along the way, Jackie Hadley, Heidi Frank, Jordan Gerton, Lynn Higgs, and Stephan LeBohec.

I would like to thank my parents. Their love, support, and the results of that are immeasurable.

I would like to acknowledge the following support: NIH grants R33 EB004803, 5K08 CA112449, R01 DC011497 and R01 EB002524, R21 MH096858, the Benning Foundation, the Ben B. and Iris M. Margolis Foundation, Utah Science Technology and Research initiative, BYU Fulton College of Engineering, the Clinical Merit Review Grant from the Veterans Administration Health Care System, and Siemens Health Care AG.

CHAPTER 1

INTRODUCTION

Magnetic resonance imaging (MRI) is a widely used diagnostic utility for the evaluation of human health. MRI is a sensitive health care diagnostic tool, and is often preferred where the diagnosis of disease is uncertain (1-4). There are an estimated 25000 MRI systems in use throughout the world (5). Similar to X-ray computed tomography (CT) and positron-emission tomography (PET), MRI is a noninvasive diagnostic technique. Unlike CT and PET, MRI does not have ionizing radiation. MRI can differentiate tissues through a multitude of physical properties, such as through spin density, relaxation parameter, and diffusion-weighted imaging. MRI has been applied to the diagnosis of disease in every part of the body, including the brain (6), heart (7), breast (8), and liver (9).

MRI is relatively new technology, when compared to X-ray imaging (10), and has undergone many improvements since its inception. The fundamentals of MRI were discovered by Isidor Rabi in 1937 in nuclear magnetic resonance (NMR) experiments (11). In 1952, the first one-dimensional MR images were reported in Hermann Carr's PhD thesis (12). In 1971, Raymond Damadian demonstrated that tumors and normal tissue can be distinguished in healthy humans through NMR techniques (13). In 1973 and 1974, Paul Lauterbur published the first MR images in a phantom (14) and in a live

rodent (14). And finally, the first human images (of a finger) occurred in 1976 (15) and first whole-body human images occurred in 1977 (16).

Since that time, MRI has significantly advanced (17) with improved hardware, pulse sequences, and reconstruction techniques, all resulting in better signal-to-noise ratio (SNR) and faster imaging times. The radiofrequency (RF) phased array is one common technique to improve SNR that can result in better image quality, faster scan times, and more reliable information in the image (18). Recent advances in multinuclear MRI techniques, including ultrashort TE imaging (19), nonproton phased arrays (20), and synchronous multinuclear imaging (21,22), show promise in obtaining better multinuclear information in clinically relevant scan times. Reconstruction techniques have also experienced changes since the earliest uses of the Fast Fourier Transform (FFT) (23), implemented more efficiently as the Discrete Fourier Transform (DFT) (24), to the more recent advances in CINE imaging to obtain images during separate cardiac cycles (25,26), as well as the use of the Nonlinear Fast Fourier Transform (NFFT) for reconstructing non-Cartesian sequences (27,28).

The ultimate goal of all of these hardware and sequence improvements is to result in better patient care, often by improving the signal-to-noise ratio (SNR) (29-31) or contrast-to-noise ratio (CNR) (31,32) of the MRI system. SNR is proportional to spin density (29-31), is directly related to image quality, and can impact CNR (31,32). By improving SNR, higher resolution images can be obtained or the scan times can be reduced (33,34) so that better quality information can be obtained from an imaging session.

1.1 Objectives and Significance

The work in this dissertation has the major objective of improving image and quantitative data for evaluating human health using MRI. The projects in this dissertation are varied, although many of the papers are focused on hardware improvements. The breadth of the papers requires a broad knowledge of MRI. This research uses the application of well-known physics and techniques to obtain higher quality images and quantitative information for the improvement in evaluating disease.

This introduction to this paper gives background on the topics covered in the remaining chapters. The introduction also contains images and experimental data that either did not fit within a chapter (paper) or was not as systematically done, but are still enlightening.

All of the images in this dissertation were created by the author.

Multiple papers are included in this dissertation as separate chapters, which is original research done by the author and the author's collaborators.

The first paper, attached as the second chapter, is the description of a system that describes a small rodent imaging system developed for a clinical 3 T MRI scanner. The system used a composite gradient system that achieved double the magnetic field gradient amplitudes, slew rates, and CNR when compared to the standard clinical system. The RF coils achieved twice the SNR when compared to the smallest birdcage conforming to the guinea pig shoulders. The composite gradient system required the development of specialized transmit and receive RF coils and electronics to image within the gradients. The coils were integrated with an animal monitoring system for animal safety during live imaging.

The second paper, attached as the third chapter, describes measurements of renal

oxygenation in a pig through both BOLD MRI and fiberoptic probes. The work was done to evaluate the usefulness of MRI BOLD T_2* measurements, which depend on renal oxygenation (pO_2). BOLD MRI is currently under investigation at many centers for its usefulness and accuracy in evaluating kidney disease. By obtaining real-time, in vivo, pO_2 data with invasive fiberoptic probes, better models of BOLD T_2* can be made to more accurately reflect renal pO_2 and the effects of disease. Our experiments demonstrated an r-value correlation of 0.6 between T_2* and pO_2. The significance of this work is that it demonstrated previously unknown physiological effects on pO_2, such as breath-holds that decreased pO_2 (~6 mmHg) immediately (<1 sec), and bladder pressure that resulted in pO_2 increases (~6 mmHg). These pO_2 differences are on the same order as the differences with the administration of furosemide, which, in conjunction with renal BOLD MRI, is being investigated as a diagnosis of chronic kidney disease (35-43).

The third paper, the fourth chapter, describes the use of T_1-weighted in- and out-of-phase MRI images to determine fat content (44) in evaluating kidney disease. Fat and water in the body resonate at slightly different frequencies, which can result in their signals coherently adding together or subtracting from each other. Lipids (fat) can be toxic and result in renal damage (45), and have been shown as an indicator of diabetes in a mouse model (46). This paper evaluates the correlation between renal fat content as determined through MRI indicators of renal health, including estimated glomerular filtration rate (eGFR), serum cystatin C, urine protein, and body-mass-index (BMI). This paper found nearly zero correlation between renal fat content and these indicators of renal health, suggesting that studies using renal fat content for evaluating renal health will not be useful.

The fourth paper, the fifth chapter, describes hardware and pulse sequence

techniques for acquiring images from both sodium and hydrogen nuclei in a single acquisition, without increasing hydrogen acquisition times. A standard clinical MRI images only hydrogen, due to the additional complexity and cost of acquiring data from other nuclear specie. Our system demonstrated a very simple, inexpensive solution to synchronous multinuclear imaging (SMI) and acquired both nuclei on two ^{23}Na channels using external modifications, instead of modifying internal scanner components (22). In addition, our implementation of SMI demonstrated flexibility in scan parameters that has not been previously shown, obtaining ^{23}Na-GRE images synchronously with ^{1}H-SE and ^{1}H-GRE images with flexibility in ^{1}H repetition times. Ours is also the first demonstration of radially acquired SMI for efficient sampling of ^{23}Na (47) before significant T_2* signal decay.

The fifth paper, attached as the sixth chapter, is a composite sodium and proton array that has achieved impressive sodium imaging results and standard proton results using a single coil. The array demonstrated a 2-5x improvement in sodium SNR when compared to a linear coil that covered a similar breast volume. This array required the development of both transmit and receive coils for both sodium and proton imaging for in vivo imaging of the human breast. The paper shows some unique techniques for tuning/detuning transmit coils by using a small forward-bias DC current with large RF waveform voltages, without the PIN diodes resulting in breakdown (48-50). In addition, this paper discusses the coupling that occurs when both sensitive proton and sodium coils are present.

Each chapter demonstrates physical methods to help improve the utility and accuracy of MRI. The remainder of Chapter 1 introduces the necessary background physics, techniques, and terminology that are used within the papers themselves.

1.2 Background: The Physics of MRI

1.2.1 Magnetic Spin

In order for a particle to be imaged with MRI, the particle must have a nonzero magnetic moment (51), which occurs with nonzero spins such as 1/2, 1, 3/2, etc. When an atomic nucleus has spin greater than 1/2, the nucleus will have a nonzero electric quadrupole moment (52). Protons, neutrons, and electrons all have spin 1/2. Clinical MRI occurs by imaging protons (53) with spin 1/2, also referred to as water or hydrogen (^{1}H) imaging.

An atomic nucleus has half-integer spin when the number of neutrons plus the number of protons in the nucleus is odd (54). Examples of spin 1/2 nuclei include ^{1}H, ^{13}C, ^{19}F, and ^{31}P. Examples of spin 3/2 particles include ^{23}Na and ^{31}Cl. If the number of neutrons and protons are both even, the nucleus will have zero spin, because the spins of the nucleons (neutrons and protons) will negate each other, such as occurs with ^{12}C and ^{16}O (54). If the number of neutrons is odd and the number of protons is odd, then the nucleus will have an integer spin, such as 0, 1, 2, etc. (54). Examples of spin 1 nuclei are deuterium (^{2}H) (55), ^{6}Li (56), and ^{14}N (57). There are some exotic nuclei that have uncommonly high spins, such as thulium (^{159}Tm) which has a spin of 61/2 (58).

Classically, spin describes the angular momentum or rotation of a particle around an axis. Although protons, neutrons, and electrons do not behave classically, they still follow similar mathematical principles of angular momentum and can be described with a total angular momentum vector, J (59). A spin 1/2 particle is often visualized as a spinning charged sphere that has magnetic moment, μ. Since angular momentum gives rise to the magnetic moment, the two are proportional to each other through the gyromagnetic ratio (59), γ, such that

$$\boldsymbol{\mu} = \gamma \mathbf{J}. \tag{1.1}$$

The total angular momentum, J, of a particle is equal to ħI (59), where I is the spin angular momentum operator and ħ is Planck's constant divided by 2π. I can only have integer or half-integer values. The gyromagnetic ratio, γ, describes the Larmor precession of a particle in a magnetic field (53,59). Classically, the gyromagnetic ratio for a charged particle in a magnetic field is equal to the particle's charge divided by twice its mass (60),

$$\gamma = \frac{q}{2m_p}. \tag{1.2}$$

The magnetic moment can be also written as,

$$\boldsymbol{\mu} = \gamma \hbar \mathbf{I}. \tag{1.3}$$

The magnetic moment is the basis of MRI, as it is the summation of numerous magnetic moments from many noninteracting nuclei, called magnetization, which creates a measurable magnetic field. Each of the individual magnetic moments can be summed to create a total magnetization vector for a given volume (51,53,59,61),

$$\mathbf{M} = \frac{\sum \boldsymbol{\mu}_i}{V}, \tag{1.4}$$

where V is volume.

1.2.2 Magnetization Statistics

The energy of a particle is described (59) with the Hamiltonian, $\hat{H}$, equal to

$$\hat{H} = -\boldsymbol{\mu} \cdot \mathbf{B}, \tag{1.5}$$

or, substituting the magnetic moment in from Equation (1.3),

$$\hat{H} = -\gamma\hbar\mathbf{I}\cdot\mathbf{B}. \tag{1.6}$$

The dominant source of energy in MRI is the z-component of the magnetic field, B_0, so the Hamiltonian further can be simplified to

$$\hat{H} = -\gamma\hbar I_z B_0. \tag{1.7}$$

The spin operator I_z is defined so that when it operates on the state $|m_z>$, the eigenvalue will be equal to m_z (59). Defined this way, the m_z eigenvalues can only take on values of m_z = -I, -I+1… I-1, I, which, for a spin 1/2 particle, results in $m_z = \pm 1/2$. When the Hamiltonian operates on the state, $|m_z>$, the eigenvalue or energy will be equal to

$$E = -\gamma\hbar B_0 m_z, \tag{1.8}$$

which is defined as the Zeeman energy (59). The Zeeman energy can be used to find the angular frequency of precession, ω, as the frequency is proportional to the change in Zeeman energy (59), $\omega = \Delta E/\hbar$, which can be rewritten as,

$$\omega = \gamma B_0. \tag{1.9}$$

Under normal circumstances, spins will be randomly aligned. In the presence of a strong magnetic field, the spins will be tend to align or antialign with the magnetic field after an equilibrium time, although in reality they will be in a superposition of both states (Figure 1). Boltzmann statistics describe the proportion of spins in the +1/2 and -1/2 states (59,62). For a spin 1/2 system, the fractional difference between particles oriented with and against the magnetic field is

$$\frac{N_{+1/2} - N_{-1/2}}{N_{Total}} = \frac{e^{\frac{+\gamma\hbar B_0}{2kT}} - e^{\frac{-\gamma\hbar B_0}{2kT}}}{e^{\frac{+\gamma\hbar B_0}{2kT}} + e^{\frac{-\gamma\hbar B_0}{2kT}}}, \tag{1.10}$$

where k is Boltzmann's constant and the other symbols have been previously defined. Using $\mu_{+1/2} = \gamma\hbar/2$ and $\mu = \mu_{+1/2} = -\mu_{-1/2} = \gamma\hbar/2$, this equation can also be written as

$$\frac{N_{+1/2} - N_{-1/2}}{N_{Total}} = \tanh\left(\frac{\mu B}{kT}\right). \tag{1.11}$$

When kT is much higher than μB, such as occurs at room temperature, this can be further simplified using a Taylor expansion to,

$$\frac{N_{+1/2} - N_{-1/2}}{N_{Total}} = \left(\frac{\mu B}{kT}\right). \tag{1.12}$$

At high temperatures, the total equilibrium magnetization is equal to,

$$\begin{aligned} M_z &= \mu_{+1/2}N_{+1/2} + \mu_{-1/2}N_{-1/2} \\ &= \mu N_{+1/2} - \mu N_{-1/2} \\ &= \frac{\gamma\hbar}{2}(N_{+1/2} - N_{-1/2}) \end{aligned}, \tag{1.13}$$

which results in the expression for net magnetization (53) of

$$M_z = \frac{\gamma^2\hbar^2 B_0 N_{Total}}{4kT}. \tag{1.14}$$

*1.2.3 Signal Relaxation: T_1, T_2, T_2**

There are three dominant decay rates or relaxation times when describing signal loss over time in MRI: T_1, T_2, and T_2*. These relaxation times are affected by interactions with nearby magnetic nuclei (63), chemical shift effects (64), quadrupole interactions with electric field gradients (65), and J-coupling modulation (66).

When the magnetization is not completely aligned with the magnetic field, it will approach thermal equilibrium with its surroundings (the "lattice") with a characteristic time, T_1, which is called the "spin-lattice relaxation time" (63). This time refers to the

process where spins give energy to the surrounding lattice and come to equilibrium. In other words, T_1 is the characteristic time before the magnetization aligns with the static magnetic field (59). In terms of spin populations, the spins will change populations at the rate $1/T_1$, such that

$$dn/dt = (1/T_1)(n_0 - n), \tag{1.15}$$

where n is the surplus population (n_+-n_-), and n_0 is the equilibrium population. Extended treatments of T_1 for spin 1/2 particles are in (59) and (63). The result in Bloembergen (63) is useful to help understand basic effects of different physical parameters on T_1, giving an estimate of T_1 for spin 1/2 particles to be $T_1' = 5kT/9\pi^2\gamma^4\hbar^2\eta N_0$, where η is the particle's "mobility" and N_0 is the number of molecules per cm^3.

The transverse magnetization, which is the portion of magnetization that results in the MRI signal, has an irreversible exponential decay towards its equilibrium value of zero with a characteristic time, T_2, known as the "spin-spin relaxation time" (53). T_2 signal decay is the result of individual nuclei precessing at different rates (59), resulting in a net signal decrease over time due to reduced phase coherence, also known as "spin dephasing". A very rough estimate of T_2 can be derived (59) by assuming that atoms will dephase at a rate equal to γH_{loc}, where H_{loc} is the local magnetic field of nearby nuclei. The local magnetic field will be approximately $H_{loc} \sim \mu / r^3$, where μ is the magnetic moment and r is the distance to the nearest atom. This gives an estimate of $T_2 = \frac{1}{\gamma H_{loc}} = \frac{r^3}{\gamma \hbar}$, and suggests that solids have much shorter T_2 values than gases.

Spin dephasing is induced by intravoxel field inhomogeneities that can be caused by both static and nonstatic fields (67). Transverse signal decay caused by static field

inhomogeneities is considered T_2* decay. These inhomogeneities are caused by macroscopic magnetic field imperfections, such as those caused by gradient fields, intertissue boundaries, magnetic blood cells, and ferrite particles (67). While a commonly repeated estimate of T_2* is $1/T_2^* = 1/T_2 + \gamma \Delta B_{inhom}$ (67), this result is inaccurate on macroscopic scales (68). T_2* decay can be very nonlinear in the presence of large magnetic field inhomogeneities, although this nonlinear decay can be estimated by considering the effect of macroscopic inhomogeneities on a subvoxel level (68).

1.2.4 The Bloch Equation

When a particle with a magnetic moment, μ, is in the presence of a magnetic field, it experiences a torque, τ, which is equal to the change of the magnetic moment with respect to time (59):

$$\tau = \frac{d\boldsymbol{\mu}}{dt} = \gamma \boldsymbol{\mu} \times \mathbf{B}. \tag{1.16}$$

Equations (1.16) and (1.4) can be combined to describe the effect of a magnetic field on magnetization,

$$\frac{d\mathbf{M}}{dt} = \gamma \mathbf{M} \times \mathbf{B}. \tag{1.17}$$

Under the effect of a large static magnetic field (and neglecting signal decay), Equation (1.17) results in a constantly rotating the transverse magnetic field, defined as $M_{xy} = M_x + iM_y$,

$$M_{xy}^{rot}(t) = e^{i\Omega t} M_{xy}(t) \tag{1.18}$$

where Ω is the rotation frequency and M_{xy}^{rot} is the rotating magnetic field in the reference

frame of the lab. For simplicity, many derivations and simulations neglect this rotation and consider everything from the rotating frame of the spins.

Equation (1.17) does not incorporate all physical effects on magnetization, in particular, T_1 and T_2 decay. When the magnetization equation incorporates these two relaxation times, it becomes the Bloch equation (69),

$$\frac{d\mathbf{M}}{dt} = \mathbf{M} \times \gamma \mathbf{B} + \frac{(M_z(t) - M_0)\hat{z}}{T_1} - \frac{M_x(t)\hat{x} + M_y(t)\hat{y}}{T_2} \tag{1.19}$$

where M_0 is the equilibrium magnetization.

The effects of T_1 and T_2 on magnetization is usually calculated in the rotational reference frame for simplicity, especially considering that it is generally straightforward to move between rotational and nonrotational frames. The solutions to the Bloch equations (53) can be calculated in the rotational frame by excluding the $\mathbf{M} \times \gamma \mathbf{B}$ portion of the equation and gives the results

$$M_{xy}(t) = M_{xy}(0)e^{-t/T2} \tag{1.20}$$

and

$$M_z = M_0 - (M_0 - M_z(0))\mathrm{e}^{-t/T_1}, \tag{1.21}$$

where M_0 is the equilibrium magnetization. The magnetization at time $t = 0$, i.e., $M_{xy}(0)$ and $M_z(0)$, is usually measured from the center of the first RF pulse that changes the magnetization so that it is no longer at equilibrium. To convert to the lab reference frame with constantly rotating fields, the transverse magnetization, M_{xy}, should be multiplied by $e^{i\omega t}$, resulting in

$$M_{xy}^{rot} = M_0 e^{-t/T2} e^{i\omega t}. \tag{1.22}$$

1.2.5 Magnetic Field and Susceptibility

In physics, the term "magnetic field" can describe either the **H** (59) or the **B** field. In MRI, "magnetic field" refers almost always to the **B** field (53), which includes susceptibility and magnetization effects. The relationship between **H** and **B** in a material (61) is

$$\mathbf{B} = \mu_0(\mathbf{H} + \mathbf{M}) = \mu_0(1 + \chi_v)\mathbf{H} = \mu\mathbf{H}, \tag{1.23}$$

where **M** is the magnetization, μ_0 is the magnetic permeability of air, χ_v is the magnetic susceptibility of the material, and μ is the magnetic permeability of the material.

The effects of magnetic susceptibility (and magnetic permeability) can be easily seen when pure iron is placed in an MRI (70). Regions near the iron will have an increased B field, due to the large magnetic susceptibility of iron, and will result in fast signal decay and distortion in the image (70). While the permeability ratio of water to air (0.999992) or copper to air (0.999994) seems relatively small compared to the ratio of iron to air (ratio = 5000+), these small differences can be seen on MR images (70). Susceptibility artifacts can be reduced by increasing the magnetic field gradients or decreasing the static magnetic field strength (70).

1.3 Background: Imaging Basics and Techniques

Magnetic resonance imaging is the process by which the spins of a system, such as the hydrogen atoms in a human or sample (both referred to as a phantom hereafter), are manipulated to create an image (53). The spins of the system are first polarized with a large magnetic field (53,59), with the polarization statistics described in Section 1.2. After the spins are polarized, a circularly polarized electromagnetic (EM) RF pulse

creates a rotating magnetic field perpendicular to the main magnetic field at (or near (71)) the resonant angular frequency, $\omega = \gamma B_0$ (53). This transmitted RF pulse will cause the spins to absorb energy and "tip" or "flip" them so that they have transverse magnetization (Figure 2). The axis that a spin is flipped or tipped about (Figure 2D) is largely determined by hardware, as a coil that is rotated by 90° (axially, around z) will cause the spins to be flipped about an axis that is similarly rotated. The transverse magnetization precesses around the dominant field and generates an RF signal that is then received by the MRI system to create an image (53). The RF signal will eventually reduce to zero after the spins return parallel to the main magnetic field (in the time T_1) or dephase and become incoherent (in the time T_2 or T_2*, depending on the sequence) (see Section 1.2.3).

In order to differentiate spin densities in different locations of the system, magnetic field gradients are applied that changes the frequency of the spin precession throughout the volume, which results in a change in the phase of magnetization from the perspective of a single receive frequency (Figure 3). With the continued application of gradients, the spins continue to accrue phase. The RF receiver receives the signal from all of the spins at a single frequency that will change in amplitude over time, based on the coherence of these spins. This amplitude, which varies dependent on spin coherence, forms the basis for reconstructing an image. (53)

To repeat and clarify, images in MRI are acquired by 1) polarizing the spins in a system with a static magnetic field so that they tend to align with the field, 2) tipping the spins to create transverse magnetization that generates RF signal, 3) applying magnetic field gradients to create magnetization phase changes based on physical position, 4) acquiring the resultant signal during or after gradient encoding, and 5) creating an image

based on the received signal and knowledge of the gradient waveforms.

1.3.1 k-Space

The Fourier transformation is the basis for MRI data acquisition and reconstruction (53). The Fourier transformation of an image is referred to as k-space, as shown in Figure 4, due to the frequent use of the variable k in the Fourier equation (53). Gradients are applied to the spin system so that spins in different positions within the system resonate at slightly different frequencies, so that they accrue varying phases dependent on position. These phases coherently or incoherently contribute to the overall signal. This signal is then sampled over time, allowing the creation of real-time Fourier data that can then be transformed into an image. The signal, *s(t)*, that is received by the MRI system (53) can be modeled by considering the effects of different magnetic field gradients on the system over time. These considerations result in the equation for signal,

$$s(t) = \int_x \int_y \int_z m(x,y,z) e^{2\pi i [k_x(t)x + k_y(t)y + k_z(t)z]} dx dy dz, \tag{1.24}$$

where $m(x,y,z)$ is the magnetization at the position (x,y,z) in the sample, and k_x, k_y, and k_z are defined as

$$\begin{aligned} k_x(t) &= \frac{\gamma}{2\pi} \int_0^t G_x(\tau) d\tau, \\ k_y(t) &= \frac{\gamma}{2\pi} \int_0^t G_y(\tau) d\tau, \\ k_z(t) &= \frac{\gamma}{2\pi} \int_0^t G_z(\tau) d\tau, \end{aligned} \tag{1.25}$$

and where $G_x = dB_z/dx$, $G_y = dG_z/dy$, and $G_z = dB_z/dz$.

The magnetization, $m(x,y,z)$, is the physical magnetization at the position (x,y,z), and incorporates effects such as spin density, T_1, T_2, and other signal effects based on the

particular pulse sequence. Direct knowledge of these decay rates is not necessary for reconstruction of an image, although the gradient waveforms and time of data acquisition must be known. To obtain the magnetization data, which is *the image data*, an inverse Fourier transform is performed on the obtained signal (after appropriate gridding of the signal into a k-space matrix), such that

$$m(x,y,z) = \int_{k_x}\int_{k_y}\int_{k_z} s(k_x,k_y,k_z)e^{2\pi i[k_x(t)x+k_y(t)y+k_z(t)z]}dk_x dk_y dk_z. \qquad (1.26)$$

The majority of pulse sequences that acquire data follow a Cartesian (rectangular coordinates) k-space acquisition trajectory (72). This allows for simple gradient waveforms and reconstruction that uses the Fast-Fourier Transform.

For clarity, Figure 5 shows a one-dimensional example of an image that consists of four delta functions, with the delta functions having twice the amplitude in the center of the image. The received signal is the summation of the magnitudes and phases from each point in the image (assuming a homogeneous receiver). Initially the phase of each magnetization is equal (Figure 5A). After the application of a gradient, the magnetizations at different positions in the image have unequal phases due to precessing at slightly different frequencies, which results in the signal having decreased magnitude and a phase offset (Figure 5B). Continued application of a gradient allows the acquisition of signal at four sufficient time-points so that the received signal can be Fourier transformed to obtain the initial magnitude image.

1.3.2 The Spoiled Gradient Echo Sequence

A pulse sequence is the sequence of RF pulses, gradients and data acquisition schemes that are used to create an image. By varying the RF pulses and gradient

patterns, different types of information can be obtained from a spin system (53). Images can be created that display the difference between tissues with different T_1 or T_2 values (53). These images are considered T_1- or T_2-weighted images (53). An image is considered a spin density image if T_1- or T_2-weighting effects are minimized, so that the image is near to the true spin density (53). An example sequence that can create T_1- or T_2-weighting is the spoiled gradient echo sequence (often referred to as SPGR, FLASH, or sometimes GRE (73)) (53).

Before a sequence begins, the spins are assumed to be in equilibrium, so that the magnetization, $\vec{M}$, is oriented parallel to the magnetic field with no transverse magnetization, such that $\vec{M} = M_0\hat{z}$. A basic pulse sequence will start by tipping the spins with a flip angle, α_1, so that the magnetization then becomes $\vec{M} = M_0 \sin(\alpha_1)\hat{x} + M_0 \cos(\alpha_1)\hat{z}$ (53). The transverse magnetization will then decay and the longitudinal magnetization will recover, so that the magnetization then becomes $\vec{M} = M_0 \sin(\alpha_1)e^{-t/T_2}\hat{x} + M_0(1-\cos(\alpha_1)e^{-t/T_1})\hat{z}$. Spoiling will often be used at this step, which refers to the process by which the transverse magnetization becomes zero by dephasing the transverse signal with large gradients or RF pulses (53). After spoiling, the magnetization then becomes $\vec{M} = M_0(1-\cos(\alpha_1)e^{-t/T_1})\hat{z}$. After time $t = TR$, the magnetization undergoes another RF pulse, α_2, so that the magnetization becomes

$$\begin{aligned}\vec{M} &= M_0(1-\cos(\alpha_1)e^{-TR/T_1})\sin(\alpha_2)\hat{x} \\ &+ M_0(1-\cos(\alpha_1)e^{-TR/T_1})\cos(\alpha_2)\hat{z}.\end{aligned} \tag{1.27}$$

After the RF pulse, T_2 magnetization signal decay occurs, which is measured at time TE and modeled with the additional term E_2, such that

$$\begin{aligned}\vec{M} &= M_0(1-\cos(\alpha_1)E_1)\sin(\alpha_2)E_2\hat{x} \\ &\quad + M_0(1-(1-\cos(\alpha_1)E_1)\cos(\alpha_2)E_1)\hat{z},\end{aligned} \tag{1.28}$$

with $E_1 = e^{-TR/T_1}$ and $E_2 = e^{-TE/T_2}$ to simplify visualization. The time where the signal is measured is referred to as TE (time-to-echo), and the time between RF pulses is referred to as TR (time-to-repetition).

While Equation (1.28) can be used to simulate complicated sequences, the spoiled GRE sequence has an analytical solution when using a constantly repeated flip angle, α, which matches the simulated steady state solution (Figure 6). The steady-state transverse magnetization of the spoiled GRE sequence (53) is

$$M_{xy} = \frac{M_0(1-E_1)\sin(\alpha)}{1-E_1\cos(\alpha)}\cdot E_2. \tag{1.29}$$

Since the transverse magnetization, M_{xy}, is directly proportional to the signal obtained in the sequence, it is often ideal to maximize this signal by minimizing the denominator of Equation (1.29), such that $1-E_1\cos(\alpha)=0$. The angle that maximizes the transverse magnetization for a given repetition time, TR, is called the Ernst angle and is when $E_1\cos(\alpha)=1$. The Ernst angle (74) is

$$\theta_E = \cos^{-1}(e^{-TR/T_1}). \tag{1.30}$$

1.3.3 Basic Pulse Sequences

Some commonly used MR imaging techniques and acronyms are gradient echo (GRE), spoiled gradient echo (commonly referred to as FLASH, SPGR, or sometimes GRE), spin echo (SE), inversion recovery (IR), short TI inversion recovery (STIR), and echo-planar imaging (EPI) (53). Each technique uses slightly different RF pulses,

gradients and image acquisition techniques to enable imaging with different tissue contrast or to enable measurement of other physical parameters (53).

Gradient echo (GRE) is perhaps the most basic and versatile (51) MRI sequence. A basic 2D GRE sequence is shown in Figure 7. A GRE sequence typically involves a simple transmit pulse (RF_a in Figure 7), a slice selection gradient ($G_{ss\text{-}1H}$ in Figure 7), a phase-encode gradient (G_{pe} in Figure 7), a readout gradient (G_{ro} in Figure 7), and spoiling (G_{sp} in Figure 7) (more accurately referred to as a FLASH or SPGR sequence) (73). The gradients are varied to acquire data at different k-space locations. The time between each RF pulse is the repetition time (TR), and the time between the RF pulses and the acquisition of the center point in a single k-space line (the center of each analog-to-digital conversion readout, ADC) is called the echo time (TE) in Cartesian imaging (53). Most GRE sequences acquire data with a Cartesian k-space trajectory, such that each point acquired in k-space lies on a rectangular grid with equal spacing between points. Data acquisition for a GRE sequence usually occurs nearly immediately after the transmit pulse to avoid T_2* signal decay.

Spin echo (SE) imaging uses a two RF pulses before data acquisition (51). Typically, these pulses will be a 90° RF pulse followed by a 180° pulse (53). The 180° pulse is called a refocusing pulse because it flips the spins upside-down and causes the static field inhomogeneities to be cancelled out, removing signal decay caused by those inhomogeneities (53). This refocusing enables SE to measure T_2 instead of T_2*. SE imaging can create T_1-weighted images by using a short TR and short TE, T_2-weighted images by using a long TE and long TE, and spin density images by using a long TR and short TE (51).

An inversion recovery (IR) sequence is a type of SE sequence (51), except that

that the 90° and 180° pulses are switched from standard SE imaging. The data are acquired nearly immediately after the 90° pulse. By varying time of inversion (referred to as TI), which is the time between the 90° and 180° pulses, the T_1 relaxation of the tissues can be calculated. A short TI inversion recovery (STIR) sequence (75) is an IR sequence, with the TI time chosen specifically so that fat has no signal when the 90° pulse occurs.

An echo-planar imaging strategy (EPI) (14) is a data acquisition strategy that can be applied to any of the above pulse techniques. EPI refers to acquiring multiple k-space lines between separate TRs (e.g., RF pulses). EPI can be either "single-shot", which refers to acquiring all of the k-space lines within a single TR, or "multishot", which uses multiple TRs to acquire a set number of k-space lines. The benefit of acquiring multiple k-space lines within a single TR is that the data acquisition time is significantly reduced, thereby reducing motion artifacts or allowing imaging of rapid physiologic processes (76). The drawback to EPI is that it has increased sensitivity to magnetic field inhomogeneities and susceptibility effects (77) when compared to other techniques. Increasing magnetic field gradients can reduce these effects (77). EPI is commonly used in diffusion, perfusion, and functional imaging (77).

1.3.4 Non-Cartesian Imaging: uTE, 3D PR and 3D Cones

Standard k-space acquisition occurs by acquiring data so that they fit onto a regular square or cubic Cartesian grid, with equally distributed k-space samples. Non-Cartesian imaging strategies have been implemented so that the center of k-space can be oversampled, which increases SNR of nuclei with short T_2* (Section 1.2.3) at the cost of blurring the image (47). By oversampling the center of k-space, substances that have

short T_2* can be imaged, where a normal sequence would result in complete loss of signal. These sequences often have very efficient pulses so that the TE is minimized, resulting in an ultrashort TE (uTE) sequence (47). Some applications for uTE sequences are cartilage (19), bone, and sodium imaging (47). uTE imaging also results in fewer motion artifacts than typical Cartesian imaging. Two non-Cartesian methods are the 3D radial (47,78) and the 3D cones (47,79) sampling schemes (Figure 8).

Because the k-space data are acquired on a non-Cartesian grid, the data cannot be reconstructed using the standard Cartesian Fast-Fourier Transform (FFT) routines (27,28). Different reconstruction schemes for non-Cartesian imaging include regridding algorithms (80,81), the nonlinear or nonequispaced FFT (NFFT) (82), the nonuniform FFT (NUFFT) (28), and the generalized FFT (GFFT) (83). The Cartesian discrete FFT (DFT) routine in most imaging software libraries uses very efficient implementations that take advantage of highly repeated operations (84). A DFT reconstruction on a regular grid takes on order $O(N^d \log N)$ calculations (85), where d is the number of dimensions and N is the matrix size flattened to a single dimension. A straightforward nonlinear reconstruction requires roughly $O(N^{2d})$ operations (85), suggesting that reconstruction requires more computational power than a Cartesian DFT. The regridding method is the simplest NFFT implementation (27,28), which consists of interpolating the k-space data onto a Cartesian grid and then doing a standard Cartesian DFT. Regridding may still run into memory and slow reconstruction problems (86), considering UTE sequences often oversample their data, resulting in much larger datasets than normal Cartesian imaging.

1.3.5 Fat and Water Imaging

The human body contains both water and fat (also referred to as adipose tissue (87)) that both give signal at nearly the same resonance frequency. Fat has multiple signal peaks that can show up in MRI that can have varying amplitudes in different tissues. The dominant fat peak occurs from methylene groups $(-CH_2)_n$ of triglyceride fatty acid chains that result in a spectral peak 3.6ppm (~444Hz at 3.0 T) lower than the main water frequency (88). Fat imaging often attempts to image only the dominant -3.6ppm peak, which is larger than the methyl, olenific, and carboxyl peaks by at least a factor of 6 (68,89).

Fat and water signals will coherently increase or decoherently decrease the signal when imaging at different echo times (90). Water imaging can occur by using a pulse sequence that removes the fat signal (75), typically by selectively exciting the fat signal and dephasing it before water imaging (91). Water and fat imaging can also occur by postprocessing magnitude and phase information obtained at multiple echo times with the IDEAL (92) or Dixon methods (90).

A very straightforward technique for obtaining fat (F) and water (W) images is the 2-point Dixon method (90) using two images at echo times that maximize and minimize the obtained signal,

$$\begin{aligned} Im_1 &= F + W \\ Im_2 &= F - W \end{aligned} \qquad (1.31)$$

Using simple algebra, the fat and water images can be obtained from images Im_1 and Im_2,

$$F = \frac{Im_1 + Im_2}{2}$$
$$W = \frac{Im_1 - Im_2}{2} \quad (1.32)$$

The 3-point Dixon method collects three different images in order to better estimate the fat and water images by correcting for nonoptimal echo times and B0 inhomogeneities (93). These images are two with the fat and water signals in-phase (coherently increasing) and one out-of-phase (coherently decreasing) (93). At 3 T, the TEs should be separated by a time of 1.05 ms. After these images have been obtained, the water, W, and fat, F, images can be calculated (as shown in Figure 9) using the following relations that correct for B_0 at 3 T:

$$W = (Im_1 - Im_2 e^{i2\pi(444 - \angle(Im_3/Im_1))(TE_2 - TE_1)}) / (1 - e^{i2\pi(TE_3 - TE_1)}) \quad (1.33)$$

$$F = Im_1 - (Im_1 - Im_2 e^{i2\pi(444 - B_0)(TE_2 - TE_1)}) / (1 - e^{i2\pi(TE_3 - TE_1)}). \quad (1.34)$$

1.3.6 Oxygenation Measurements with MRI

MRI that detects changes in blood oxygenation, often through T_2 or T_2* measurements using a GRE sequence, is referred to as Blood Oxygenation Level Dependent (BOLD) MRI (94). When the hemoglobin in blood does not carry any oxygen, it is called deoxyhemoglobin. The iron in deoxyhemoglobin has unpaired electrons, has a high spin state (S = 2), and is paramagnetic (95). In contrast, oxyhemoglobin has no unpaired electrons, is diamagnetic, and has zero magnetic moment. The increased susceptibility of deoxyhemoglobin (96), when compared to oxyhemoglobin, results in greater local magnetic field changes that reduce T_2 and T_2* decay rates (96).

BOLD MRI is the basis for functional MRI (fMRI) (97,98), which is a standard

MRI technique for measuring brain activity based on blood flow and volume. However, BOLD MRI is used for imaging other anatomy, such as for evaluating kidney disease by correlating oxygenation levels with physiological health (43).

1.3.7 B_0 Mapping

The main magnetic field in MRI is referred to as the B0 field. The B0 field is very homogeneous in the center of the MRI magnet. By maintaining a homogeneous field, the image has minimal distortion, spectroscopic measurements maintain accuracy, and signal (T2*) decay is reduced in the image (99). The B0 field inhomogeneity can be measured by measuring the phase change between images with two separate echo times and is calculated voxel-by-voxel (100). This inhomogeneity, which is the magnetic field offset from the main field, is calculated by measuring the difference between the phase of two complex images, such that

$$\Delta B_0 = \frac{\angle(\mathrm{Im}_2 / \mathrm{Im}_1)}{\gamma \Delta TE}. \tag{1.35}$$

When there are significant B_0 inhomogeneities, it is necessary to unwrap (101,102) the phase difference between Im_1 and Im_2. Otherwise ΔB_0 may be underestimated (Figure 10).

1.3.8 Flip Angle (B_1) and Homogeneity

In MRI, the transmit flip angle refers specifically to the angle that the magnetization is rotated away from the z axis. The transmit flip angle is also referred to as B_1 field, as it is the RF field perpendicular to the main magnetic B_0 field that causes the spins to flip. The signal in MRI is the direct result of "flipping" the spins. (53,59)

Within MRI, there are two types of B_1 fields referred to: B_1+ and B_1-. The B_1+ and the B_1- fields are defined as counter-rotating to each other (29). B_1+ is typically defined as the transmit field, and B_1- is the receive field (103). At field strengths below 3 T, the B_1+ and the B_1- fields are the same. However, at 3 T and higher, the wavelength of RF is comparable to that of the dimensions of human tissue, which results in differences in the B_1+ and B_1- fields (103). For the purposes of this manuscript, and, as referred to in many papers, "B_1" refers specifically to the B_1+ field.

For nearly all MRI applications, a homogeneous transmit flip angle is desired. By obtaining homogeneous flip angles, all the spins will be tipped by the same amount, simplifying interpretation of the image results reducing the need for flip angle correction (104). In addition, homogeneous flip angles ensure that an optimum flip angle can be obtained for maximum SNR throughout the entire image. As an example, spin echo images that do not have homogeneous fields experience severe signal loss (105). Homogeneity is also desired for patient safety to ensure that the patient does not experience any extreme flip angles that can cause tissue heating (106).

1.3.9 Flip Angle (B_1) Mapping

Flip angle mapping is used to measure transmit homogeneity. There are three dominant forms of flip angle mapping: the dual (double) angle method (107), the phase sensitive method (104,108), and the Bloch-Siegert method (71).

The dual angle is the simplest of all the methods (107), as it can use nearly any sequence that has a long TR. In its simplest form, two images are acquired with the GRE sequence, with the second flip angle double that of the first. The ratio of the image magnitudes can then be used to get the transmit flip angle (107), using the following

relation:

$$\alpha_{TX} = cos^{-1}\left(\frac{|\mathrm{Im}_{2\alpha}|}{2|\mathrm{Im}_{1\alpha}|}\right). \quad (1.36)$$

The phase sensitive method, developed by Glen Morrell at the University of Utah, relies on phase information instead of magnitude (104,108). The phase sensitive method is sensitive at very low SNRs, such as those that occur with sodium imaging (108). Similar to the dual angle method, two acquisitions are acquired and compared. The phase sensitive method involves a nonselective 180° pulse about the x-axis followed by a nonselective 90° pulse about the y-axis. Phase in the measurement accrues during the 180° pulse due to imperfections in the 180° pulse, giving the basis for this method (108). There are other effects that can result in phase accrual, such as B_0 inhomogeneity and chemical shifts. However most of these effects can be reduced by obtaining a second image with a negative flip angle of equal magnitude (108). After obtaining two images with opposite flip angles, ignoring B_0 inhomogeneity, the result is

$$\alpha_{TX} = \angle M_{xy}^{+} - \angle M_{xy}^{-} = 2\angle M_{xy}^{+}. \quad (1.37)$$

The above equations are also simplifications under the assumption that the TR is much longer than T_1 to remove T_1 dependencies on the signal (108). The long TR required for B_1 mapping results in clinically long scan times.

The Bloch-Siegert B_1 mapping is the most recent method developed for B_1 mapping and can be used to overcome the T_1 limitations on scan times (71). The Bloch-Siegert method involves applying an off-resonant RF pulse that does not excite the sample, but results in changes in precession frequencies throughout the image based on transmit inhomogeneities (71). Unfortunately, the Bloch-Siegert method requires very

high powered RF pulses to create the same sensitivity that the phase sensitive method has in low SNR scenarios within the same scan times (109).

1.3.10 Signal-to-Noise Ratio (SNR)

In MRI, the signal-to-noise ratio is defined as the ratio of the signal to the standard deviation of the noise (18,29,30).

The MRI signal is a result of the transverse magnetization precessing about the main magnetic field axis, creating a magnetic flux change over time (29). This flux change induces a current in nearby copper coils. The induced current oscillates at 42.596 MHz/T. By maximizing the transverse magnetization, the signal obtained can also be maximized. Since the equilibrium state is for the spins to align or antialign with the main magnetic field, the spins are "tipped" or "flipped" with an RF pulse before measurement in order to maximize the transverse magnetization. Since magnetization is directly proportional to the static magnetic field strength, the number of atoms, and inversely proportional to temperature, changes in these three properties directly changes SNR.

The dominant noise in MRI is caused by thermal fluctuations in the "sample" (the system or body being imaged) and electronics (29). The sample noise is caused by the random thermal fluctuations of the particular nuclei within the sample (29). The thermal fluctuations within the sample will add from the entire sensitive volume, so that RF coils that are larger (and more sensitive to a larger volume) will have increased noise (18). When the sample noise is minimal, the electronic noise will dominate. The electronic noise arises from Brownian motion of electrons in the conductor and its noise power, N, is described by (29)

$$N = 4kTR\Delta f, \tag{1.38}$$

where k is Boltzmann's constant, T is the temperature in Kelvins, R is the resistance of the sample or electronics, and Δf is the receiver bandwidth.

The noise between separate MRI scans is assumed to be statistically independent between scans. Noise independence allows the noise of separate but identical scans to be averaged and have a reduction in noise proportional to the square-root of the number of averages. When M scans are acquired, the signal will increase by M, while the standard deviation of the noise will increase by the square-root of M. When M scans are averaged, the total SNR will increase by the square-root of M while the total scan time increases by M. Increasing the voxel size has a similar effect to averaging, because when a voxel size is increased by a factor of M, the amount of information obtained by the voxel is increased by that same factor, and the SNR is increased by square-root of M. The receiver bandwidth will also affect SNR and bandwidth reduced by M will increase the SNR by square-root of M. (53)

One standard method of increasing SNR is by adding multiple receive coils to a system (18). Generally, a system with multiple receive coils will be more sensitive than a system with a single coil that covers the same area (18). There are practical limitations to the number of coils that can be added to a system, particularly since each coil adds complexity to the system and requires separate amplifier and receive channels (18).

1.4 Background: MRI Coils

1.4.1 The Main Magnet

The main magnetic field in MRI, which is also the strongest magnetic field in the

machine, is a homogeneous, static magnetic field typically created by six to ten superconducting coils (110-112). The homogeneous field is referred to as the longitudinal field, the B_Z magnetic field, or B_0 magnetic field. Over 90% of clinical MRIs occur at a field strength of 1.5 T, with 3 T being the second most common field strength (5). Human research occurs at field strengths below 0.1T up to 9.4T (5).

Early systems created the main magnetic field with a solenoid that had additional external windings to compensate for inhomogeneities (112,113). Multicoil magnets are presently more common due to their reduced bore size and copper requirements, when compared to solenoid magnets, which results in better patient comfort and decreased magnet cost (113).

The superconducting wires in MRI systems are often made of niobium titanium (NbTi) (110) embedded in copper and cooled by liquid helium (114). Early magnet designs insulated the helium by liquid nitrogen cooling, while newer designs use cryocoolers or refrigerators without liquid nitrogen (115). Magnesium diboride superconductors are being investigated due to their ability to superconduct at a higher temperature than NbTi (20 K versus 4 K), which may allow low field systems in regions where liquid helium is inaccessible or may allow more aggressive magnet designs (112).

Figure 11 shows a Biot-Savart simulation of a simple solenoidal coil, illustrating the central B_x, B_y, and B_z magnetic fields of a very simple magnet design. The B_z field has maximum strength and homogeneity at the center of the coil, where the B_x and B_y fields are negligible. The "fringe fields" of the magnet are near the solenoid openings and is where the B_x and B_y fields are strongest.

1.4.2 Magnetic Field Gradients

Magnetic field gradients are used to spatially vary the longitudinal (B_Z) field (53). By spatially varying the B_Z-field, different regions within the field can be distinguished by their resonance frequency. Three gradient systems are used to create a varying B_Z field in the x, y, and z directions. That is, the gradient in the x direction is $G_X = dB_Z/dx$, in the y direction is $G_Y = dB_Z/dy$, and in the z direction is $G_Z = dB_Z/dz$.

A simple magnetic field gradient can be made of two coils placed on opposite sides of the imaging region, with current going opposite in direction from each other (53). This configuration creates a spatially varying magnetic field and resembles (or is equivalent to) a Maxwell pair (53).

The gradients will switch between different strengths during an MRI scan, dependent on the requirements of the sequence (53). Gradient switching can induce currents in conductors, such as in RF shields or gradient windings resulting in image distortion (116) or in the human body resulting in nerve stimulation (117-119). Nerve stimulation due to gradient switching is at a maximum on the peripheries of the magnet where the magnetic fields due to the gradients the greatest rate of change (118). Gradient strengths and slew rates are regulated to reduce potential physiological effects, such as peripheral nerve stimulation (PNS) (118). Standard clinical maximum gradient strengths are roughly 40 mT/m with slew rates up to 200 T/m/s (118).

Smaller volume gradients can achieve higher maximum gradient strengths and slew rates, as the periphery of the gradients require lower overall magnetic field amplitude and result in less PNS (120,121). This effect was exploited in our composite gradient system, which consisted of the scanner's gradients linearly combined with an insertable gradient (120,121). The composite gradient system doubled our gradient strength to 80mT/m and slew rate to 400 T/m/s. The system could triple the strength but

due to safety concerns (for both patients and the system itself) was typically only used at double strength. Due to faster gradients and higher gradient fields, the readout bandwidth could be doubled, which improved diffusion weighted imaging, reduced susceptibility and motion artifacts, and reduced T_2* blurring (121).

Static discharge, mechanical stress and vibration, hardware failures, and leaks in the radio-frequency shield can cause unwanted k-space signal that reduces image quality (122). Figure 12 shows k-space spikes at random positions throughout the k-space image. In our experiments, these spikes were removed by implementation of a RF shield around the RF coils and by tightening the gradient cables.

1.4.3 The LC Circuit

Radiofrequency coils are used to flip the spins in MRI or receive the signals from the flipped spins (53,124). Radiofrequency coils are "tuned" to a specific frequency, which means that they resonate at that frequency. A tuned RF coil has minimum resistance at frequency, so that it can efficiently transmit to flip spins with minimum input power or so that it can efficiently receive RF from the flipped spins with minimum signal loss (124).

An RF coil is made by making a conductive loop, usually made out of copper, resonate at MRI frequencies. The inductance of the loop, L, is resonates with an inserted capacitance, C. The resonant circuit, also called a tank circuit, tuned circuit, or an LC circuit, will resonate at the angular frequency of (124)

$$\omega = 2\pi f = \frac{1}{\sqrt{LC}}, \tag{1.39}$$

where ω is angular frequency, f is ordinary frequency, C is capacitance, and L is

inductance. Given a frequency and inductance, the resonant capacitance will equal

$$C = \frac{1}{\omega^2 L}. \tag{1.40}$$

The LC circuit can either be made to have zero impedance at a given frequency when the inductor and capacitor are in series, or infinite impedance when the inductor and capacitor are in parallel (124). The circuit in Figure 13 is the basis for antennae, coils, as well as frequency filters such as trap circuits.

To achieve resonance in an LC circuit, an inductor should have an impedance of $Z_L = j\omega L$, and a capacitor should have an impedance of $Z_C = 1/j\omega C$, where j is the imaginary unit (124). When a capacitor and inductor are in series, the system has impedance

$$Z_T = Z_L + Z_C = j\omega L + 1/j\omega C = \frac{1-\omega^2 LC}{j\omega C}. \tag{1.41}$$

This impedance will be equal to zero when L and C are resonant. When a capacitor and inductor are parallel to each other, the system has the inverse impedance

$$Z_T = (Z_L^{-1} + Z_C^{-1})^{-1} = \frac{1}{j\omega L} + j\omega C = \frac{j\omega L}{1-\omega^2 LC}. \tag{1.42}$$

The total impedance of this system will be infinite when L and C are resonant, when the denominator of Equation (1.42) goes to zero.

A parallel, resonant capacitor and inductor, such as shown in Figure 13, are considered a trap circuit when inserted into a resonant coil, since it traps the resonant signal and disallows it from passing through the circuit (124). Traps are used to disable coils rom resonating (i.e., detune the coil) by creating high impedance in the coil circuit path.

Traps will often contain a diode so that when the diode is turned on (forward biased with a small positive DC current), the diode will be at a low resistance and allow the trap to resonate (124). The diodes will be in series with an inductor for standard receive coil detuning. The total impedance for this system can be calculated as

$$Z_T = ((Z_L + R)^{-1} + Z_C^{-1})^{-1} = \frac{R + j\omega L}{1 - \omega^2 LC + j\omega CR}, \tag{1.43}$$

where R is the diode resistance. When $(1-\omega^2 LC) = 0$, which is the resonant case, the equation becomes

$$Z_T = \frac{1}{j\omega C} + \frac{L}{CR}. \tag{1.44}$$

An ideal trap will have infinite impedance, which does not occur in practice. According to Equation (1.44), a trap will have maximum impedance when C and R are minimized, and L is maximized.

1.4.4 The Smith Chart

The Smith chart (Figure 14) is a tool that RF engineers use to analyze an RF circuit over a range of frequencies (125,126). The simplicity of the Smith chart is in its ability to measure and visualize complex impedances over many frequencies simultaneously, which allows a user to very quickly determine the resonant frequencies and the properties of a circuit. The Smith chart is based on measuring the reflection coefficient (125,126), also called the return loss when measured in dB, of a circuit by sending out an RF signal from one port of a Vector Network Analyzer (VNA), and then receiving signal from the same port. The return loss measurement is also called an S_{11} measurement when the measurement occurs on the first port of the network analyzer (and

S_{22} on the second port, etc.).

S_{11} is equal to the reflection coefficient, Γ, which is defined as the ratio of the reflected (received) RF wave to the incident (transmitted, forward) wave (125,126),

$$S_{11} = \Gamma = \frac{V_R}{V_F}, \tag{1.45}$$

where V_R and V_F are the reflected and forward voltages. The reflection coefficient can be translated into a normalized impedance with the following relation,

$$z = \frac{1+\Gamma}{1-\Gamma}, \tag{1.46}$$

where z is the complex, normalized impedance. To get the actual impedance, Z, the normalized impedance must be multiplied by the characteristic impedance Z_0. (A capital Z would indicate the non-normalized impedance.) Equation (1.46) can be rewritten to give S_{11} in terms of the load,

$$S_{11} = \Gamma = \frac{z-1}{z+1}. \tag{1.47}$$

When the normalized impedance of the load is matched (or equal) to the normalized impedance of the network analyzer, there will be zero reflection and all the power will be absorbed, giving $\Gamma = 0$. The reflection coefficient is positive for loads above Z_0, reaching +1 for infinite impedances, such as an open circuit. S_{11} is negative for loads below Z_0, and is equal to -1 for zero impedance, such as occurs with a short circuit.

Figure 14 shows a Smith chart with a characteristic impedance of 1Ω . Smith charts used in RF coils are typically normalized to have a characteristic impedance, Z_0, equal to 50Ω, which will be the impedance value at the center of the chart. The only straight line on the chart (the green line on Figure 14) shows the line of real impedance only (zero reactance). A series inductor or capacitor will cause the impedance to move

clockwise or counter-clockwise, respectively, along a circle of constant resistance (the blue circles in Figure 14). Increasing or decreasing the resistance of the circuit will cause impedance to move along the circles of constant reactance (the red lines in Figure 14).

Figure 15 shows a simulation and results of a coil using the Quite Universal Circuit Simulator (QUCS). The decibel plot of the magnitude of S_{11} is shown in Figure 15B and the Smith chart in Figure 15C. When referring to decibels for RF coils, the values are given in terms of power (125,126), which is related to S_{11} in Equation (1.45) through

$$\mathrm{dB}(S_{11}) = 20\log_{10}(S_{11}). \tag{1.48}$$

The dip ($|S_{11}| > 35$dB) at 123.23 MHz in Figure 15B shows that the coil absorbs nearly all transmitted energy, indicating that the coil is both tuned and matched. The 123 MHz point indicated on Figure 15C is at the 50Ω point and has zero reactance, indicating that the coil is tuned and matched. A typical well-tuned and matched RF coil will show a Smith chart similar to Figure 15C.

1.4.5 RF Coils

RF coils are made to transmit and receive magnetic fields perpendicular to the superconducting magnet (53,124). Most RF coils are copper loops that contain capacitors so that they are resonant (sensitive) at a specific frequency. In addition to being tuned to a specific frequency, coils are designed so they have a B_1-field that is either very sensitive to a particular geometry for receive coils or very homogeneous within a large region for transmit coils (53,124).

Faraday's Law (127,128) is enlightening to help determine the voltage that a coil

will obtain. Faraday's law states that the voltage induced in a loop will be equal to its change in magnetic flux over time:

$$|\mathrm{V}| = \left| \frac{d\Phi_B}{dt} \right| \tag{1.49}$$

Magnetic flux is defined as the surface integral through the area defined by the boundaries of the loop,

$$\Phi_B = \oint_A \mathbf{B} \cdot d\mathbf{A} . \tag{1.50}$$

In order to obtain the magnetic flux, the magnetic field can be modeled using Biot-Savart's Law (128) which relates magnetic fields to the currents that pass through them. Biot-Savart's Law states that magnetic field, B, due to current is equal to

$$\mathbf{B} = \frac{\mu_0}{4\pi} \oint_C \frac{I d\mathbf{l} \times \mathbf{r}}{|\mathbf{r}|^3}, \tag{1.51}$$

where *l* is the segment of wire that the current, *I*, passes through, and **r** is the vector between that wire segment and the point where the magnet field is calculated. A receive coil can be modeled as a transmit coil and vice versa, due to the Principle of Reciprocity (29,127,129). The Principle of Reciprocity (also called Lorentz reciprocity (129)) states that the relationship between an oscillating current and the resulting electromagnetic field is unchanged if the regions where the current is generated and the field is measured are interchanged.

When Biot-Savart's Law is analytically applied to a circular loop of radius *R*, the field at the center of that loop is (61)

$$B_z = \frac{\mu_0 I}{2R}, \tag{1.52}$$

where the z-axis is perpendicular to the plane of the loop. The field along the center axis

of the loop is (61)

$$B_z = \frac{\mu_0 R^2 I}{2\left(z^2 + R^2\right)^{3/2}}. \tag{1.53}$$

This result illustrates two points: when the radius of the coil increases, the magnitude of the magnetic field decreases proportional to the radius; the coil is most sensitive to magnetic fields near the coil itself and loses a lot of its field strength (~70%) at a depth equal to its radius. While a larger loop will result in a weaker magnetic field strength near the loop, it will have stronger fields distant from the loop and be more homogeneous than a smaller loop. SNR for a simple loop with body-noise dominance (discussed in Section 1.4.9) will have the SNR increase roughly proportional to $1/R^{5/2}$ (130,131). A rule of thumb for selecting coil size is that the coil radius should be comparable to the depth of the desired region to be imaged (18).

Deriving the complete analytical solution to the magnetic field perpendicular to a loop is beyond the scope of this work, but since the loop is a very commonly used geometry the analytical solution is given (132,133). The analytical solution for a magnetic field perpendicular to a loop (from the signal giving field of an RF coil) is

$$B_\perp = B_0 \frac{1}{\pi\sqrt{Q}}\left[E(k)\frac{1-\alpha^2-\beta^2}{Q-4\alpha} + K(k)\right], \tag{1.54}$$

where $\alpha = \frac{r}{a}, \beta = \frac{x}{a}, Q = ((1+\alpha)^2 + \beta^2), k = \sqrt{\frac{4\alpha}{Q}}$, B_0 is the magnetic field at the center of the coil ($B_0 = (\mu_o/2a)$), *K(k)* and *E(k)* are the complete elliptical integral functions of the first and second kind, a is the radius of the loop, *x* and *r* are the distances from the center of the loop, with *x* being the on-axis longitudinal distance and *r* being the transversal distance. This magnetic field is shown for a simple loop in Figure 16.

1.4.6 The Basic Receive Coil

The basic receive coil consists of inductive copper and capacitors to allow the coil to resonate, as discussed in Sections 1.4.3 and 1.4.5. For a very basic coil, there are five components, as shown in Figure 17: the tune capacitor (Ct), the match capacitor (Cm), and the match inductor (Lm), and two detuning circuits (the crossed diodes, Ld and Ct; and the single diode, Lm and Cm) (124).

Varying the tune and match capacitors and inductors will have slightly different effects on impedance. Figure 18 shows a QUCS simulation of a Smith chart for three different coils. A match capacitor that is too small will have a frequency circle that is too large (Figure 18A). A tune capacitor that is too small will have a resonance far away from the center of the Smith chart, but will have a circle of nearly the correct size (Figure 18B). A match inductor that is too small will have a slightly rotated circle (Figure 18C). It should be noted that Figure 18C will be a coil that is matched and works very well, but some experiments on varying the match inductor seem to indicate that preamplifier decoupling can be improved by rotating this circle slightly (although not by more than 0.5 dB in this situation).

Receive-only (Rx-only) coils also incorporate diodes that can activate to detune the coil during transmit (124). Detuning the coils during transmit prevents the coil from receiving the transmit RF energy, which is orders of magnitude larger than the RF energy received from the body and can cause the preamplifiers to burn out from high voltages. If the Rx-only coils are not detuned during transmit, they can also couple to the transmit coil and change the tune and match of the transmit (Tx) and/or Rx coils, resulting in less transmit and/or receive efficiency. The receive coils must also be detuned so that they do

not enhance or shield the transmit RF signal, which can result in reduced homogeneity by concentrating RF energy around the loops and potentially burn a patient (124).

The diodes activate during transmit and cause resonant circuits within the coil, for active detuning (creating a resonance with Cm and Lm) when a positive current is given (+100mA on our scanner), or for passive detuning if sufficient signal occurs (creating a resonance with Ld and Ct) that should only occur if the active detuning circuit fails (124). The receive signal is not sufficient to activate the diodes, so they do not affect the coil's resonance and present a high impedance during receive.

1.4.7 Mutual Inductance

Multiple coils will couple together through mutual inductance (18,61). Mutual inductance is the amount that a current through one coil creates a voltage in a second coil (61). For example, an RF transmit coil can affect the magnetic field, noise and resonance of RF receive coils (134), and different RF receive coils will affect other receive coils (18).

Mutual inductance can be derived using Maxwell's equations by relating the effect of magnetic flux created by one coil that is measured by a second coil. Mutual inductance is primarily a geometrical derivation (as long as permeability is constant), independent of the amount of current present in either coil. The formula for calculating mutual inductance directly (without directly involving Maxwell's equations) is called the Neumann formula (61). The Neumann formula for calculating mutual inductance between coil i and coil j is

$$M_{ij} = \frac{\mu_0}{4\pi} \oint_{C_i} \oint_{C_j} \frac{d\mathbf{s}_i \cdot d\mathbf{s}_j}{|R_{ij}|}, \tag{1.55}$$

where $d\mathbf{s}_i$, $d\mathbf{s}_j$, are infinitesimally small vectors that follow the length of coil i and coil j, and $\mathbf{R}_{ij}$ is the distance between those vectors. The same equation can be used to estimate self-inductance to a degree, but only by excluding singularities that occur.

1.4.8 Phased Arrays and Decoupling

When multiple coils are used simultaneously to receive signal from a volume at a single frequency, they are considered a phased array (18). One of the most significant improvements in MRI has been the development of the RF phased array to improve image quality (18), either through improved SNR with receive arrays (135) or improved homogeneity with transmit arrays. RF phased arrays have been applied extensively to MRI (136-139). RF phased arrays often improve the SNR in MRI (135) when compared to birdcage, Helmholtz, and saddle coils (140) by reducing the coil's sensitive volume to noise (18). Generally, multiple receive loops will be much more sensitive than a larger loop of a similar area (135,141). There is a limit to the useful size of smaller loops, due to increased complexity of the system and increased electronic noise (142). If coil electronic resistance could be zero, multiple small coils will have better SNR when compared to a larger coil of comparable area (18). However, the implementation of more coil elements to increase SNR increases the difficulty of implementing a phased array (18).

Phased arrays at 1.5 T and 3 T field strengths typically use a large, homogeneous transmit coil in conjunction with smaller receive loops, for optimal SNR (143). Phased arrays must be optimized for a particular body region, magnetic field strength, and nuclear frequency. Generally, a phased array with many small loops will outperform a larger loop that covers the same area (135,141). However, the complexity of the array

increases significantly with more phased array loops, often with decreasing benefits (18).

The coils must be decoupled from each other so that their interactions don't decrease their sensitivity. When the coils are not decoupled, they will share noise and change their sensitive frequency. There are two predominant methods to decouple receive coils from each other: preamplifier decoupling and overlap decoupling (18).

Preamplifier decoupling attempts to reduce interactions between the coils by reducing the amount of current that flows through the coils when in receive mode (18). By limiting the current that can flow through the coils, noise and signal coupling is significantly reduced through other receive coils. The preamplifier contains a resonant capacitor and inductor to enable low preamplifier impedance, which occurs by a quarter-wave transformation of the coil impedance through this resonant circuit to the high impedance of the first transistor in the preamplifier (18). Preamplifiers with lower input impedance have greater decoupling strength (18).

Overlap decoupling is used to reduce the mutual inductance between adjacent coils (18). Mutual inductive coupling between two coils is dependent on their geometry and position relative to each other (see Section 1.4.7). It is theoretically possible to eliminate mutual inductance between two circular loops (or at least, significantly reduce) by placing the loops either very far apart or overlapping them by ~25% of their diameters (18). By overlapping adjacent coils to minimize their mutual inductance, the coils interact significantly less, share less noise, and maintain their Q-ratio (discussed in the next section).

1.4.9 Q-ratio

The quality-factor, Q, of a coil is the ratio of the peak magnetic energy stored

within the coil over the average energy dissipated (142). Q-ratio measurements are useful in determining the resistances of the coil. The Q of a coil can be described in terms of energy,

$$Q = \frac{2\pi \cdot \text{max instantaneous energy stored in circuit}}{\text{energy dissipated per cycle}}, \tag{1.56}$$

or, in terms of the reactance and resistance of the resonant coil,

$$Q = \frac{\omega L}{r}. \tag{1.57}$$

When a coil is loaded by being placed next to a sample, (such as a body or phantom,) the Q of the coil will change due to its interaction with the sample (142). An unloaded coil will have a resistance, r_{coil}, due only to the coil itself, while a loaded coil will have contain the resistance of the coil and of the sample:

$$Q_{\text{unloaded}} = \frac{\omega L}{r_{\text{coil}}} \tag{1.58}$$

$$Q_{\text{loaded}} = \frac{\omega L}{r_{\text{coil}} + r_{\text{sample}}}. \tag{1.59}$$

The lower case "r" is used here to symbolize resistance because it describes the internal resistance of the coil/sample and its usage is common in other coil papers (142).

A high unloaded Q value is desired, since that suggests that the electronic components of the coil contribute very little to the coil's noise (142). A high Q also indicates a low rate of energy loss relative to the stored energy. A low loaded Q value is desired, since that suggests that the coil is strongly interacting with the sample. The ratio of the unloaded to loaded Q values is regarded as the sensitivity of a coil, where a higher Q-ratio suggests higher coil sensitivity:

$$\text{Q-ratio} = \frac{Q_U}{Q_L} = \frac{r_{coil} + r_{sample}}{r_{coil}}. \quad (1.60)$$

The Q of the coil is measured with two decoupled magnetic probes, also called pickup probes, near the coil (124). RF power is transmitted through one of the magnetic probes. RF power near the resonant frequency of the coil will be absorbed temporarily by the coil. The subsequent power transmitted from the resonant coil will be detected by the second magnetic probe. This measurement will occur between a span of frequencies. Q can be determined experimentally by measuring the frequency with peak power transfer, f_p, and determining the bandwidth from the peak, Δf (the difference between the frequencies where 50% of the energy has been lost) (124):

$$Q = \frac{f_p}{\Delta f}. \quad (1.61)$$

Coil resistance and sample resistance change as a function of frequency, as shown through experimental evidence in Table 1, which shows measured loaded and unloaded Q values at different frequencies, with the capacitor values measured before placement in the coil. The most noticeable effects are that low frequency coils have small sample and coil resistance. Sample resistance changes dramatically as frequency increases. This measurement is important because it informs us that a lower frequency coil is more sensitive to changes in coil resistance, such as might occur when diodes are inserted serially into the coil. The measurement also informs us that Q-ratio increases as a function of frequency, given a similar diameter coil. A higher Q-ratio at higher frequencies suggests that higher frequency RF will be more sensitive to a sample than low frequency RF.

1.4.10 Noise Figure (NF)

Every component that is used for signal detection contributes noise to that signal (144). Noise figure (NF) is the measurement of how much noise a measurement and detection system adds (144). NF is the difference in decibels between the noise output of an actual receiver to that of an ideal, noiseless receiver. There is a direct correlation between NF and signal to noise ratio - a 3 dB decrease in NF will result in a 3 dB increase in SNR. NF's are especially important for first stage amplifiers (preamplifiers), since the noise from one device will be added and amplified in the following device. A NF equal to zero means that the detection system adds no noise. A large amount of noise results in a high NF. The NF for an MRI preamplifier is typically between 0.3 and 0.5 dB.

Noise factor (F) is defined as the loss of SNR from a measurement device (144), $F = SNR_{in} / SNR_{out}$. Noise figure is the noise factor in decibels,

$$NF = 10\log_{10}(SNR_{in} / SNR_{out}). \tag{1.62}$$

The variable, $SNR_{in} = S_{in} / N_{in}$, is related to the SNRout through the amplification (by gain factor G) of both the signal and noise, and through the addition of amplified noise from the device-under-test (DUT), which is whatever component is being measured and is often the preamplifier. Thus, $SNR_{out} = GS_{in} / G(N_{in} + N_{DUT})$. These SNR equations let us express NF in terms of noise only by using Equation (1.62),

$$NF = 10\log_{10}\left(\frac{1/N_{in}}{1/N_{in} + 1/N_{DUT}}\right). \tag{1.63}$$

The noise can be expressed in terms of a temperature with Johnson noise (144), $N = 4kT\Delta f$, which further simplifies the NF to

$$NF = 10\log_{10}\left(\frac{T_{in} + T_{DUT}}{T_{in}}\right). \tag{1.64}$$

NF is measured in our lab using a noise meter (Rhode and Schwarz Network Analyzer with the FS-K30 option, shown in Figure 19) and noise source (Noise Com NC346A, shown in Figure 20). The NF meter generates a 28 VDC signal that reverse biases the avalanche diodes in the noise source beyond diode breakdown and generates white noise. The noise from the noise source then enters the preamplifier. NF is calculated by measuring the difference between the noise source on and noise source off.

1.4.11 The MRI Preamplifier

Preamplifiers (preamps) are used for amplifying the RF signal as immediately as possible prior to sending the RF down long cable lengths that can result in signal loss (18). The preamplifiers used in MRI are charge-sensitive semiconductor detectors (145). MRI preamplifiers are typically powered by +5 or +10 V through the port that goes to the scanner. Protection circuitry, such as in the TR switch for transmit coils and detuning circuits in receive coils, prevents potentially high RF (>30 dBm typical, where 0 dBm = 1 milliWatt and 30 dBm = 1 W; Power (dBm) = $10\log_{10}$(Power (mW)) on the preamp input that can cause semiconductor breakdown and cause the preamp to not work properly (146).

When selecting a preamplifier, the NF (see Section 1.4.10), gain, and input impedance of the preamplifier are major considerations (18). The NF of MRI

preamplifiers are typically <0.5 dB and the gain is usually >25 dB (18). Low-impedance preamplifiers are used in RF receive arrays as the low-impedance preamplifiers result in better decoupling between other array loops (18). Preamplifiers with 50Ω impedance are desirable for birdcage transmit coils to maintain coil sensitivity between transmit with the scanner transmit port at 50 Ω and receive with the preamplifier.

A schematic of a proton preamplifier (preamp) is shown in Figure 21 as experimentally mapped by removing and measuring individual components:

- The first inductor and capacitor of the preamplifier resonate with the match circuit in the coil, so that the coil appears to have infinite impedance to other coils, thereby reducing coupling to other coils (18).
- Following the LC circuit are crossed diodes that activate when excessive signal reaches the preamp, in an attempt to protect the amplifier circuits. The preamps are still not completely protected, as very excessive signals can cause the crossed diodes to permanently short. The opposite side of the preamp can also result in the preamp breaking, such as if excessive current is induced on the cable between the scanner and preamp, which may happen during pulse intensive sequences (e.g., SSFP, DTI) if that cable does not have traps on it.
- A field-effect transistor (FET) is used as the first-stage amplifier (18). Pseudomorphic high-electron-mobility transistors (pHEMT) are used as the FET device (147), which have better noise properties at microwave frequencies when compared to typical transistors (148). The pHEMT also has a very high resistance that is quarterwave transformed by the initial LC circuit on the board into a very low impedance (18,147).

- A bipolar junction transistor (BJT) follows the pHEMT for second-stage amplification. The BJT is used in common base mode, which allows it to have high voltage gain, low input impedance, and high output impedance (149). The base of the BJT separates the input and output, increasing the impedance between them and reducing oscillations that can contribute to noise.

1.4.12 Specific Absorption Rate (SAR)

When a coil is transmitting, some of the RF energy will be deposited in the sample. Specific absorption rate (SAR) is the rate that a body absorbs RF energy (150). SAR is reported using the maximum level from the body or volume-of-interest (VOI). SAR is calculated as (150)

$$\mathrm{SAR} = \int_{\mathrm{sample}} \frac{\sigma(\mathbf{r})|E(\mathbf{r})|^2}{\rho(\mathbf{r})} d\mathbf{r}, \tag{1.65}$$

where σ is the body electrical conductivity, ρ is the body density, and E is the root-mean-square electric field. According to Equation (1.65), a smaller coil will have a small volume that deposits much less energy into the sample than a large coil.

1.4.13 Transmit Coils

In order to take full advantage of the phased array, a large homogeneous transmit coil is necessary (124). A large, homogeneous transmit RF coil allows signal to be acquired deep into a sample and reduces the requirement to correct for inhomogeneous flip angles. Often a large transmit coil is used to maximize field homogeneity in conjunction with smaller receive loops to increase the overall sensitivity of the system (18).

The scanner is equipped with a permanent proton coil, referred to as the body coil, that can be used for transmit-only or for both transmit/receive. While the body coil is ideal for most situations, due to its large homogeneous volume, other transmit coils are occasionally needed. When compared to the body coil, a local transmit coil will have increased SNR (Section 1.4.5) and reduced patient heating (i.e., SAR, Section 1.4.12) due to its reduced size and more localized fields. This reduction in SAR allows a local transmit coil to be used in more SAR intensive sequences when the body coil cannot. Local transmit coils are also required when the transmit fields from the body coil are shielded, preventing transmit RF penetration. In addition, nonproton experiments require specialized transmit hardware because the scanner is not equipped with nonproton coils.

Transmit coils are designed to maximize the homogenous transmit field (124). While a circular loop can be used to transmit, a more efficient and homogeneous design at field strengths at and below 3 T is the birdcage coil (124). Above 3 T, the high frequencies result in low capacitor values that make tuning difficult, and the high frequencies result in less homogeneous fields, so coils besides birdcages are used, including the TEM volume resonator (151,152) and transmit arrays (153).

If a transmit coil remains tuned during receive, the transmit coil can couple to the receive loops and make them less sensitive, resulting in a lower overall SNR. Transmit coils require circuitry to detune them, such as those described in Section 1.4.15.

Larger transmit coils require electronic parts that can tolerate hundreds of volts (154). A coil that is only a few centimeters in diameter will require only a few volts of RF energy to tip the spins 180°. A coil that is more than two feet in diameter can require hundreds of volts to tip the spins 180°.

1.4.14 Birdcage Coils

A birdcage coil, so named because it looks like a birdcage, is a common transmit coil. Birdcage coils consist of circular copper end rings attached to copper rungs (legs) that are arranged cylindrically. A shielded, end-cap birdcage coil is shown in Figure 22.

There are three types of birdcage coils – low pass, high pass, and band pass (155). Low pass birdcage coils have capacitors on each rung; high pass birdcage coils have capacitors on each end ring segment; band-pass birdcages consist of both high and low pass birdcages. A high pass birdcage requires larger capacitor values than a low pass birdcage to create a homogeneous field at the same frequency (155).

The birdcage coil has a current variation around its circumference, where the current is related to the sine of the angle of the rung (155). Because of this sinusoidal relation, the birdcage can be driven in quadrature at two different ports that are 90° apart to become more efficient than a flat loop – both in transmit RF fields and receive RF fields (130,156). A quadrature birdcage creates a circularly polarized RF wave perpendicular to its rungs and is very homogeneous throughout its central region.

A birdcage with N rungs will have N/2 resonant frequencies, wavenumbers or modes (130,155,157,158). Only the first mode generates a homogeneous field in the center of the birdcage, which is the lowest frequency of a low-pass birdcage and highest frequency for a high-pass birdcage. The resonant frequencies of a low-pass birdcage (shown in Figure 23), with zero resistance and zero rung inductance, are

$$\omega = \frac{2}{\sqrt{2LC}} \sin \frac{\pi M}{N}, \tag{1.66}$$

where N is the number of rungs and M is the mode. More complex analytical models are in (155,157-159). High-pass birdcages also have zeroth modes, called the corotating and

anticorotating modes, which are resonant modes that do not pass through the rungs but are resonant modes in the end rings themselves (157). These are usually much smaller peaks when detected with a magnetic probe at around a 10% higher frequency than the homogeneous 1st mode.

A birdcage can be tuned by placing a large circular magnetic probe (142) in the center of the birdcage, oriented parallel to a high-pass birdcage loop or perpendicular to a low-pass birdcage loop that will be tuned. A straightforward method to tune a birdcage is to put similar lumped element capacitors on each rung / end ring segment, and then to replace the capacitors with adjustable ones to remove the variation of starting with adjustable capacitors of unknown sizes.

An end cap is often used to improve the SNR and size of the homogeneous region of the birdcage by acting as a current mirror (160). The end cap pictured in Figure 22C has copper strips separated by ~1mm gaps, with 15000 pF capacitors placed across them. The gaps reduce eddy currents (128) that can cause field distortion (116), which is caused from switching gradients inducing currents. The capacitors allow the system to be low impedance to RF, so that the end cap results in induced RF currents and acts similar to a solid copper end cap. The capacitors and gaps present high impedance to the gradient magnetic fields, so that eddy currents are not induced on the shield and yet still allow the gradient fields to pass through.

Generally, smaller coils do not have significant frequency shifts when placed inside the bore of the magnet, while larger coils, like birdcages, will have shifts due to their position and orientation, which affect their tune and match. The RF shield around the birdcage allows the coil to be placed anywhere in the MRI without significant frequency shifts. An RF shield can also allow a birdcage to be placed near to other

electronic components, such as the insertable gradient in Figure 24, without any significant changes in tune / match.

Without any shield, the birdcage resonance frequency changed by 7 MHz when placed into the insertable gradient of Figure 24, but with a shield the resonance changed by less than 0.5 MHz. Similar to the construction of the end-cap, the birdcage shield (Figure 22B) had copper strips with ~1mm gaps, with 15000 pF capacitors connecting the strips from adjacent gaps, to create a low RF impedance at 123 MHz and high gradient field impedance for frequencies below 200 kHz. The number of capacitors and capacitor locations were empirically determined by placing capacitors at first far apart, measuring the frequency shift with the coil inside and outside the insertable gradient, and then adding capacitors half-way between the nearest capacitors where there were the greatest frequency shifts. This process was repeated until the capacitors no longer had any effect on the frequency shift. Adding capacitors near the end-cap had a much greater effect than adding them in the center of the shield or near the front of the coil; adding capacitors near the open-end of the coil shield had a much greater effect than adding capacitors towards the center. The shield was more effective when connected to the end-cap, reducing the shift from 1.5 MHz to < 0.5 MHz.

The effectiveness of the shield was also tested with SNR measurements using a GRE sequence. The SNR when the shielded birdcage was completely inside, halfway inside, and completely outside of the insertable gradient shown in Figure 24. The SNR results in Figure 25 show less than a 10% SNR change with the different configurations, demonstrating that the birdcage could be useful in different scenarios.

Asymmetries in the shield and end cap affected the balance (the homogeneity) of the birdcage. The unshielded birdcage was symmetric, but the shield created asymmetric

resonances that could be seen with different probe orientations, with frequencies varying up to 3 MHz. Future iterations of shielded birdcage coils were implemented with easily removable shields, such as the one pictured in Figure 26, so that shielding effects during bench-measurements could be more closely observed when the shield was placed over the birdcage.

1.4.15 Forward-Biased Diodes

An important feature of a PIN diode is its ability to control large RF signals while using much smaller levels of DC current (161). The behavior of waves passing through DC biased diodes at RF frequencies (> 3 kHz) is different from the behavior at AC frequencies where signals can be clipped, which is when the negative half of the wave is set to zero. When a PIN diode is forward biased, holes from the P-region and electrons from the N-region enter the I-region, reducing the resistance of the I-region (161). This movement of holes is not an immediate effect. If a diode is forward-biased with a current, I_F, it results in a stored charge, $Q = I_F\tau$, which puts the diode in an activated, low resistance state. The diode's resistance under forward bias is inversely proportional to the stored charge, Q. When the diode forward bias is removed, the negative and positive charges in the diode will eventually recombine, with a recombination time of τ, also called the carrier lifetime.

When a PIN diode is forward biased, the maximum RF current the diode can control depends on the amount of stored charge, Q, supplied by the DC forward bias relative to the charge variations produced by the RF signal (161). For a half cycle of a wave, the charge, q, introduced to the diode is

$$q = \int_0^{T/2} I dt = \int_0^{T/2} A \sin(\omega t) dt = I_{RF} / \pi f . \quad (1.67)$$

In order for the diode to remain on, the stored charge, Q, must be greater than the introduced charge, q (161). The charge ratio can also be rewritten as

$$I_{DC} \tau > I_{RF} / \pi f . \quad (1.68)$$

A PIN diode forward-biased with 100 mA will remain activated if a 100 MHz wave passes through it, up to many kilowatts of power, with little to no distortion of the wave (48,50,162). This effect is shown in Figure 27.

The effect of diode insertion on SNR was tested on a single square coil that had a diode (MACOM MA4P7464F-1072T) inserted serially into it after an initial SNR experiment (Figure 28). The insertion of the diode resulted in similar SNR values, despite the high RF voltage (~132 V) and current (= 132 V / 50 Ω = 2.6 A) being much greater than the DC bias voltage (+10 V) and current (+100 mA) that the scanner supplies.

Despite previous experiments (48) and predictions of PIN diode behavior under forward-biased conditions, our lab conducted experiments using a high voltage setup to confirm that diodes behaved as predicted. Experimental verification was desired before this technique was used in transmit coils because the calculated voltage toleration levels seemed unreasonably high (greater than hundreds of volts), considering the relatively low reverse breakdown voltages of diodes (dependent on the diode, these can range anywhere from -60V to -500V or greater). Second, verification that the PIN diodes did not distort high-voltage waves in forward-biased conditions was desired.

Nonmagnetic PIN diodes (Macom MA4P7464F-1072T, Macom, Lowell, MA, USA) were used for high-voltage experiments. The diodes can handle 50 dBm (100 W)

continuous wave incident RF power, and have a reverse bias breakdown voltage of -400 VDC. RF waveforms at 30 MHz were generated with a Wavetek Sweep Generator at varying powers between -40 and 10 dBm, which were then amplified by 55 dB using an E&I RF Power Amplifier. The amplified RF waveforms then passed through the test circuits, which varied between a simple copper wire, unbiased diode, forward-biased diodes, unbiased crossed diodes (also known as reverse-diode pairs), and forward-biased crossed diodes. After each test circuit, the waveform then passed through a high power resistor that acted as a voltage divider to reduce the ~500 V RF waveforms to ~1 V before measurement with a Tektronix oscilloscope. The results of this experiment are in Table 2, which shows a reduction in circuit heating and stability when a forward-bias current is used with high RF power.

Many authors have demonstrated success in the use of serial forward diodes for tuning transmit coils when forward-biased (with > 20 mA) and detuning them when unbiased (163-167). Diodes with low reverse breakdown voltages and low forward-biasing currents provide adequate tuning (and decoupling), even with large RF voltages. For comparison, the Siemens body RF coil uses -440 V when tuned (during transmit or receive) and 5000 mA when detuned, which is significantly more than 20 – 200 mA for tuning/detuning using this method. (These values are listed in the Siemens help manual accessible on the scanner.) The serial forward-biased diode method is simple and straightforward, doesn't distort RF waveforms, can tolerate very high voltages, can use inexpensive diodes, provides broadband decoupling, and has proven itself as an excellent method for decoupling coils. This method is demonstrated and used in two chapters of this manuscript.

1.4.16 Detuning Transmit Coils

When coils are tuned to a specific frequency, they will strongly interact (couple) with other coils tuned to the same frequency. If a receive coil is tuned during transmit such that the receive coil is sensitive to the transmit RF, then the coil can suffer from diode breakdown permanently detuning the coil, the preamplifiers could be destroyed so that they no longer properly amplify, and the transmit field homogeneity could be significantly altered, potentially even resulting in overheating. Alternately, if a transmit coil is tuned during receive, then the transmit coil could alter the receive coil's field profile and reduce the coil's SNR. Coils must be decoupled from other nearby coils to maintain their sensitivity and magnetic field profiles. Transmit coils must not become detuned from the large RF voltages that it uses during transmit, while still detuning during receive.

The most generic method to detune transmit or receive coils is to place an active RF trap using a capacitor on the coil, which consists of a diode and inductor parallel to the capacitor. When the diode is activated ("on") with a forward current, the diode becomes a low resistance device. At low resistance, the inductor and capacitor will resonate with each other, creating a high resistance at their resonant frequency. When the diode is reverse biased or unbiased ("off"), the diode is a high resistance device. The diode's high resistance will be parallel to the capacitor, so that neither the capacitor nor coil will be affected by diode and inductor. This method has been used with great success in both transmit and receive coils for years. The biggest limitation of this decoupling method is that it can be expensive to implement and can limit the number of transmit channels available. Each channel requires a large negative voltage source to prevent the diodes from activating during transmit.

The method employed in the transmit coils in this dissertation is serial diodes that tune/detune the transmit coils when appropriate with small DC bias (+100 mA). A forward-biased diode can tolerate kilowatts of RF energy, and remain at low resistance, as discussed in Section 1.4.15.

An unbiased or negatively biased diode has a maximum negative voltage limit where the diode will break down. Although a forward-biased diode is very effective at keeping an RF coil tuned during transmit, a significant weakness is that there may be times when the diode is not appropriately biased, which can cause the diode to burn out. A diode may not be appropriately biased due to mechanical failure, improper programming, or operator error. To alleviate this concern, a second diode can provide protection against high RF voltages by placing the second diode antiparallel to the first. Unfortunately, an antiparallel diode can cause a secondary problem: our scanner supplies both a forward and a negative voltage to tune/detune our coils. The negative voltage will activate the antiparallel diode so that one of the diodes on the circuit will always be active. A single diode in the DC bias path can be used to remove the negative portion of the DC bias, thus preventing the antiparallel diode from activating.

Serial diodes can also be used in receive coil decoupling, but the diodes will introduce resistance to the coil that can reduce the coil's efficiency. The diode will have a low resistance when compared to a coil at high frequency and a higher resistance with a coil at low frequency.

1.4.17 Coaxial Cables

Coaxial cables are used to connect coils to the preamplifiers, the preamplifiers to the scanner, for impedance transformation, and for hybrid splitters. This section is

included because of the effect of coaxial cables on RF coils.

Coaxial cables are designed for RF transmission, so that they have a specific resistance, inductance, and capacitance per unit length (168). Care must be used in selecting the cable, because many cables of the same type (e.g. RG-58) can be magnetic, which can cause artifacts during imaging. Our lab uses either RG-316 or RG-58 cable, which both have a characteristic impedance of 50 Ω. RG-316 is more common in our lab due to its smaller diameter.

The prevalence of 50 Ω cables has defined much of the current MRI RF technology: RF coils are matched to 50 Ω impedance in order to reduce signal losses between the coils and cables; the receive coil preamplifiers used in our lab have the lowest noise figure when the coils are matched to 50 Ω (18).

The velocity factor (169) for RG-316 is 0.695, which means that the full wavelength of the 123 MHz proton signal within the cable is 1.69 m, and the quarter-wavelength is 42 cm.

A coil will have its resonance changed if an arbitrary length of cable is added to it. A quarter-wavelength cable that is shorted (e.g., when one end has a wire connection between the central conductor and shield) will have infinite impedance at the opposite end of the cable and not affect the circuit (154); a half-wavelength cable with a shorted end will look similar to a shorted connection at the resonant circuit.

Quarter-wave transformers can provide matching between two separate impedances (154), with a quarter-wavelength of cable, through the following relation:

$$\frac{Z_1}{Z_0} = \frac{Z_0}{Z_2}, \tag{1.69}$$

where Z_0 is the quarter-wave transformer between an impedance of Z_1 and Z_2.

1.5 Nonproton MRI

Common nuclei studied for clinical purposes with MRI or magnetic resonance spectroscopy (MRS) are shown in Table 3. The most common atomic nucleus used in MRI is hydrogen (^{1}H) (53), which consists of a single proton, has spin 1/2, and has a natural abundance of 99.99% (170). Sodium (^{23}Na), a spin 3/2 atomic nucleus (171), is attractive for clinical MRI applications because it is the second most abundant atomic nucleus, by count, in the human body with nonzero spin, and it has a strong correlation with cellular metabolism and physiology (172). Phosphorous (^{31}P) is important in the ATP-ADP cycle and in phospholipid metabolism (173). Flourine (^{19}F), which has spin 1/2, resonates near proton frequency (γ_{19F} = 40.1 MHz/T), and while it has negligible endogenous concentrations, ^{19}F may have clinical usefulness when perfluorination is used, which is the process by which ^{1}H nuclei are replaced with ^{19}F nuclei in C-H bonds (174).

Every stable nonproton nucleus has a lower gyromagnetic ratio than proton, which has the minimum mass of any nuclei (a single proton), and the gyromagnetic ratio is inversely proportional to mass (60). The low gyromagnetic ratio reduces the SNR further from a very simple consideration that SNR $\propto M_0 \propto \gamma^2$ (see Equation (1.14)). Further consideration of the received electromotive force (EMF) from any RF coil is proportional to frequency (29), so that signal from EMF $\propto \omega$ and noise from EMF $\propto \omega^{-1/2}$, resulting in an overall SNR dependency of SNR $\propto \omega^{1/2}$. Since $\omega \propto \gamma$ (see Section 1.2.2), SNR is proportional to $\gamma^{1/2}$ from EMF considerations alone. These two considerations result in an overall SNR dependency on gyromagnetic ratio of $\gamma^{5/2}$.

Quadrupolar nuclei have much lower decay rates than proton due to their

increased interactions with electric fields (65), such as sodium that has T_1 decay rates near 30 ms (175), and can have biexponential relaxation rates in solids, which are predicted in (65).

Lower in vivo concentrations, reduced gyromagnetic ratio, and reduced decay rates in quadrupolar nuclei all reduce the available SNR in nonproton imaging. The reduced SNR of nonproton MRI is perhaps the largest hurdle to nonproton imaging, making it currently unfeasible for clinical imaging due to the increased scan time requirements to obtain higher, but still poor, SNR.

1.5.1 Electric Quadrupolar Hamiltonian

Every nucleus that has spin > 1/2, such as sodium (spin = 3/2), has a nonuniform distribution of charge within its nucleus that interacts with nearby electric fields. The electric quadrupolar Hamiltonian, H_Q, can be defined simply (190) as

$$H_Q = -\frac{1}{6} eQ\nabla\mathbf{E}, \tag{1.70}$$

where eQ is the magnitude of charge deformation and $\nabla\mathbf{E}$ is the electric field gradient. The magnitude of charge deformation, eQ, is defined as

$$eQ = \int_{Vol} \rho r^2 (3\cos^2\theta - 1) dV, \tag{1.71}$$

where e is the charge of a proton, ρ is charge density, r is the distance from the center of the nucleus, and θ is the angle to the charge density element. The elements of the electric field gradient, $\nabla\mathbf{E}$, are defined as

$$\nabla E_{ij} = -\frac{\partial^2 V}{\partial x_i \partial x_j} = -V_{ij}, \tag{1.72}$$

where V is the electrostatic potential and x_i indicates the x, y, or z direction. A more

useful definition of the electric quadrupolar Hamiltonian that considers the above is (190)

$$H_Q = \frac{e^2 qQ}{4I(2I-1)}\left[3\mathbf{I}_z^2 - I(I+1) + \frac{\eta}{2}(\mathbf{I}_+^2 + \mathbf{I}_-^2)\right], \tag{1.73}$$

where η is considered the asymmetry parameter, $\eta = \frac{V_{xx} - V_{yy}}{V_{zz}}$.

1.5.2 Sodium Imaging

Sodium (^{23}Na) imaging is more challenging than proton imaging due to its much lower in vivo concentration, short decay times, lower gyromagnetic ratio, lack of hardware, and biexponential decay (177). In vivo sodium concentrations are between 10 and 150mM, where hydrogen concentrations are near 50M. The long T_2* sodium relaxation time, between 10-50 ms depending on the tissue, is much shorter than the T_2* relaxation times of hydrogen that can be around 250ms. The lower gyromagnetic ratio of sodium, being a quarter of hydrogen's, results in $4^{5/2}$ = 32 times lower SNR (see Section 1.5). Sodium imaging requires specialized hardware, due to its infrequent use in both clinical and research settings, as there are still relatively few centers studying its clinical effectiveness.

Despite these challenges, sodium has a large enough concentration in certain tissues and diseases that make it an interesting and favorable candidate for imaging. In addition, the frequency of sodium (32 MHz at 3 T) when compared to proton (123 MHz at 3 T) allows it to be imaged simultaneously with proton, which can improve its viability and usefulness. Sodium imaging has been studied for the evaluation of tumors (178,179), cartilage (180-183), kidneys (184,185), stroke (186), and multiple sclerosis (187).

Sodium, like all spin 3/2 nuclei, has a biexponential relaxation that arises from

quadrupolar splitting between the four nuclear states (+3/2, +1/2, -1/2, -3/2) (188,189). Spectroscopy studies show three spectral lines for sodium: a large central line due to the transitions between +1/2 and -1/2, two smaller lines due to transitions between the +3/2 and +1/2 states, and the -3/2 and -1/2 states.

Sodium in complex environments, such as the intracellular space of tissue, exhibits a larger biexponential effect (Figure 29), while less complex environments, such as purely aqueous solutions and extracellular space, do not demonstrate biexponential decay. The biexponential decay is largely a result of the intracellular and macromolecule electrostatic field gradients interacting with the quadrupolar sodium (63,188).

The values of the short and long components of sodium T_2^* are related to physiological changes in sodium concentration, both in the intracellular and extracellular space. This phenomenon is noted in the changes of different types of brain edemas that cause the expansion of either the extracellular or intracellular space, dependent on the type of edema (188). Besides sodium T_2^* changes, sodium concentration can also point to physiological changes, since intracellular sodium increases three to four times in malignant cells (188). Figure 30 shows sodium and proton images of a mouse that has cancer, obtained on a 3 T clinical scanner.

1.5.3 Sodium and Proton Loop Coupling

Unlike separate loops of the same frequency, sodium and proton loops have very different frequencies at 3 T (32.596 MHz and 123.23 MHz on our scanner, respectively). A tuned sodium loop will have 14 times the capacitance of a similarly sized proton loop as a result of the changed frequency (see Section 1.4.3). The much higher capacitance of a sodium loop results in a circuit that appears very similar to a solid conducting copper

loop to the proton loop, resulting in shielding of the proton signal (191).

Measurements shown in Figure 33, of an overlapping 70cm proton and sodium loop, were done to evaluate the effects of frequency shift, Q-value change, and shielding. Measurements were taken at varying center-to-center loop distances. The frequency shift was measured from the return loss (S_{11}) of a magnetic probe. The Q-values were measured by maintaining the same distance between the coils, phantom, and magnetic probe. The insertion loss (S_{21}) was measured with the magnetic probe placed above the sodium loop, which was above the proton loop, when measuring at proton frequency, to more accurately show the effects of shielding; the proton and sodium loop positions were interchanged when measuring at sodium frequency. The S_{21} change (Figure 33C) suggests that the sodium loop shields the proton loop significantly. A similar experiment (but not shown), repeated with a solid conducting wire, showed similar but less dramatic changes in frequency, Q, and S_{21}.

The capacitors and Q-values of the 70 mm diameter proton and sodium loops were measured, and the resistances were calculated according to Equation (1.58). The measured / calculated values were used in a QUCS circuit simulation (Figure 32). The simulation varied the coupling coefficient, k, which is proportional to mutual inductance, by 0.1 from 0 to one.

Figure 33 shows results of the simulation. The hydrogen coil is dramatically affected by the sodium coil, tripling its frequency with very maximum mutual inductance. The sodium coil, on the other hand, is barely affected by the proton coil, although there are minor effects.

A sodium and proton coil can be decoupled from each other by similar methods to decoupling two proton coils: they can be separated or overlapped to minimize their

mutual inductance, which is the same overlap required from decoupling two proton coils. A technique used in this dissertation is to intersect the sodium coil with proton coils, so that the mutual inductance is merely reduced. This intersection considers that the volume-of-interest is typically the same for both coils and that they do not interact as strongly as two coils of the same frequency.

Many techniques exist to create dual-tuned sodium / proton coils, including multiple end rings (192) (Figure 34A,B); two separate coils (155,193,194) (Figure 34C); butterfly coils (195,196) (Figure 34D); decoupling traps that resonate at hydrogen's frequency on the sodium coil and resonate at sodium's frequency on the hydrogen coil (197-201) (Figure 34E); transformer-coupling (202); band filters (203); alternating birdcage rungs (204) or rings (205); shield inserts (206); and diodes (207) (Figure 34F).

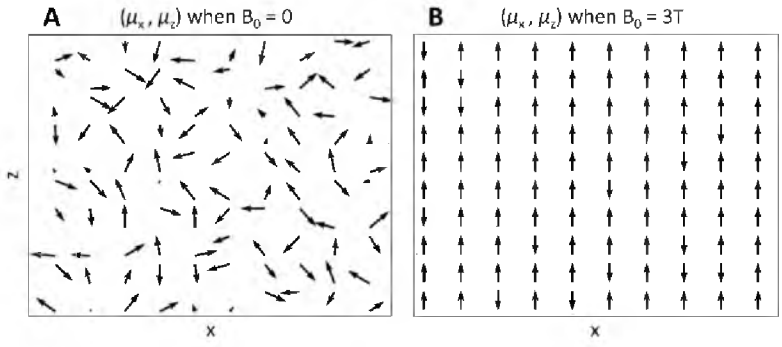

Figure 1. Magnetic moments with and without a magnetic field. Images depicting the magnetic moments, μ_Z and μ_X, in two directions of individual spins at different x and z locations. (A) When there is zero magnetic field, the spins will have a randomly-oriented magnetic moment. (B) At strong magnetic fields, such as at 3 T, individual spins will tend to align or antialign with the magnetic field. This image is useful for illustrative purposes only, as the spins will be in a superposition of different states and this does not incorporate temperature dependencies.

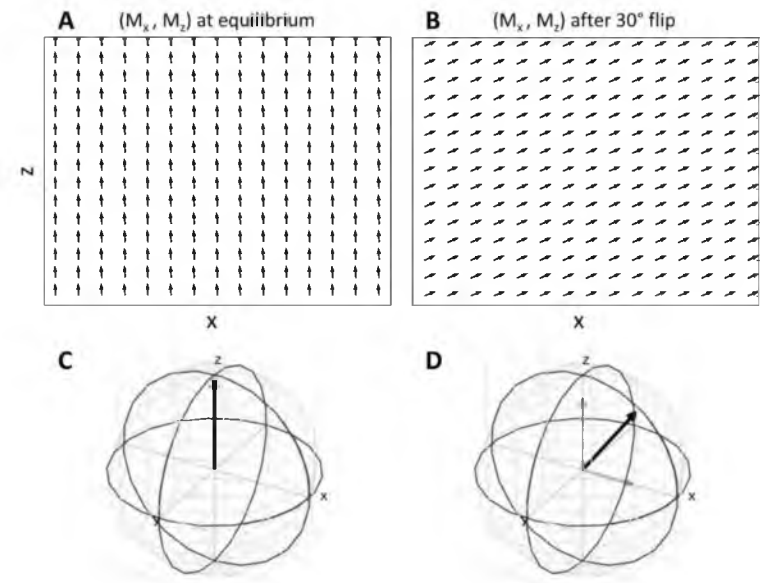

Figure 2. Magnetization before and after a flip angle. Two-dimensional magnetization vectors at different positions in an image at (A) equilibrium in a static magnetic field and (B) after the spins are flipped about the y-axis by 30°. An individual spin at (C) equilibrium and (D) after the spin is flipped about the y-axis by 30°. The horizontal arrow in (D) indicates the magnitude of the transverse magnetization (M_{XY}, which equals M_X at this point in time), which is the signal giving portion of the magnetization. The vertical arrow in (D) indicates the longitudinal magnetization (M_Z), which does not yield any signal.

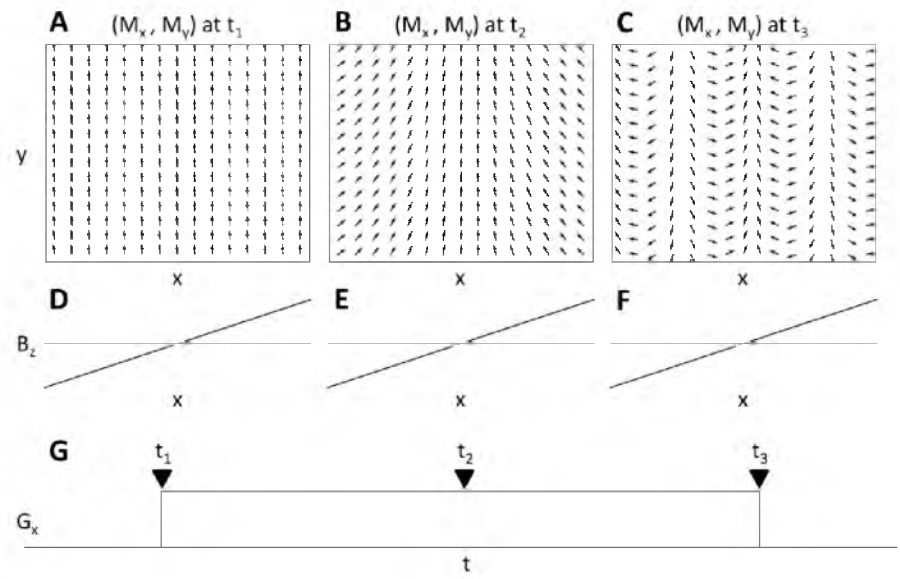

Figure 3. Magnetization phase changes due to a magnetic gradient. (A-C) Magnetization vectors that demonstrate phase changes at different positions and times when a (D-F) static magnetic field gradient has been applied across the image. (G) The pulse sequence diagram shows a constant gradient ($G_X = dB_Z/dx$) at times t_1, t_2, and t_3.

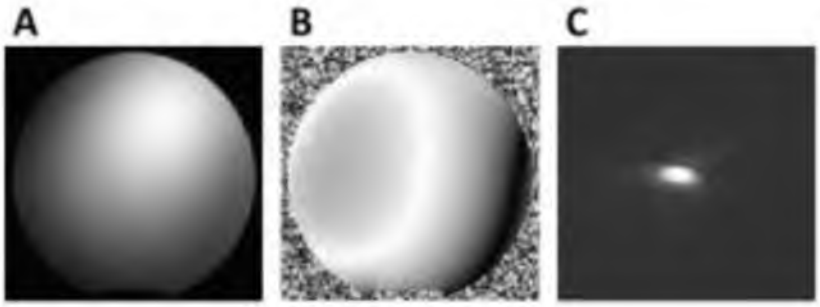

Figure 4. Image space and k-space. (A) Magnitude and (B) phase image of a spherical phantom and the magnitude image of the corresponding (C) k-space / 2D Fourier transform.

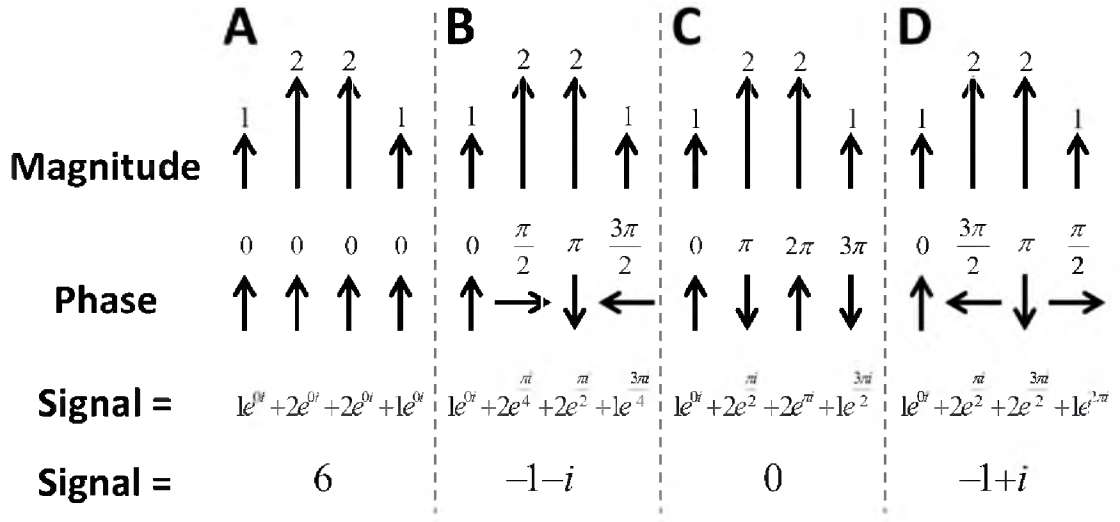

Figure 5. A one-dimensional Fourier transform. This figure shows a one-dimensional example of acquiring data of an image that consists of four delta functions (equal to 1, 2, 2, 1, respectively). (A) Initially, the phase throughout the image is equal (and zero). The received signal is the summation of the magnitudes/phases from each point, which in this case = 6. (B) With the application of a magnetic gradient field, the spins precess at slightly different frequencies so that after some time period, the summed signal from each point in this example will be equal to -1-*i*. (C-D) With further application of magnetic gradient fields, the phases will eventually be equal to 0, and -1+*i*. The inverse Fourier transform of (6, -1-*i*, 0, -1+*i*) is equal to the initial magnitude data, (1, 2, 2, 1).

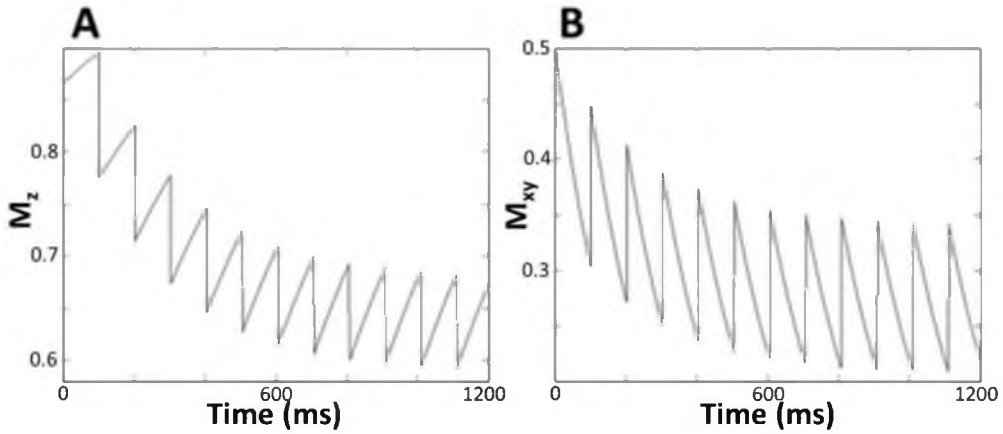

Figure 6. Magnetization decay after flip angles. (A) Longitudinal and (B) transversal magnetization of a GRE sequence with complete initial polarization, simulated with scan parameters of TR = 100 ms, T_1 = 400 ms, T_2 = 200 ms, flip angle = 30°. Flipping the spins / magnetization increases the signal, after which the signal decays until the next flip angle. Steady-state is reached after about the eighth repetition.

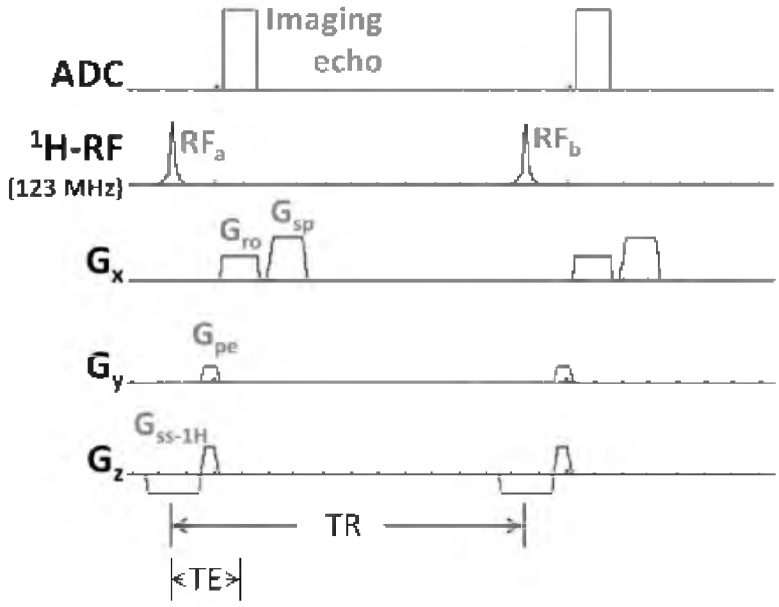

Figure 7. A 2D GRE sequence. A 2D GRE pulse sequence for the first two repetitions, showing the gradient strengths (G_x, G_y, G_z), data acquisition (ADC), and RF pulses (^{1}H-RF). A 2D GRE will have a slice select gradient (G_{ss-1H}) that occurs during the RF pulse, exciting only spins within the slice. A phase encode gradient (G_{pe}) changes the y-position in k-space by homogeneously varying the phase of all the spins in the slice. Following the G_{pe}, a readout gradient occurs (G_{ro}) that reads a single line of k-space for x-positions. A spoiler gradient (G_{sp}) then makes all of the spins dephase so that they do not contribute to the signal in the next repetition. The repetition time (TR) between two RF pulses and echo time (TE) between the RF pulse and readout are indicated on the figure.

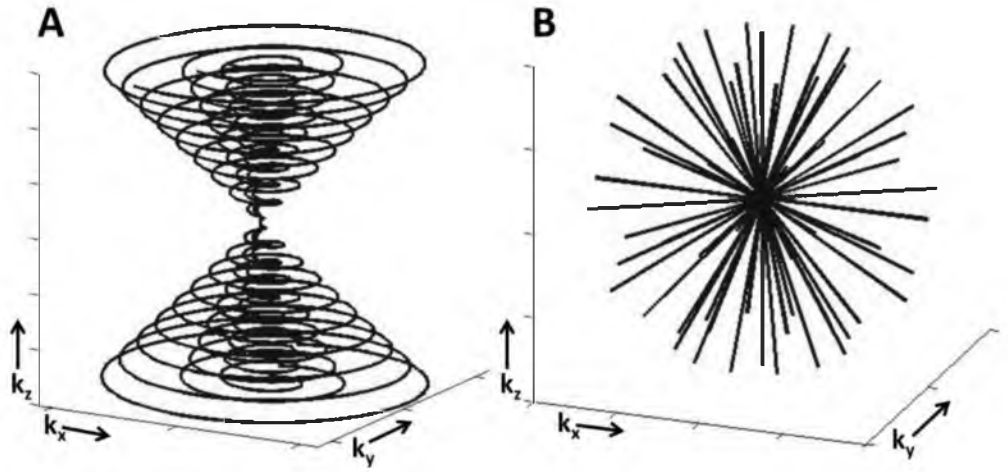

Figure 8. The 3D cones and radial acquisition trajectories. (A) 3D cones and (B) radial acquisition trajectories. The full k-space trajectories include more (A) cones or (B) spokes. These are two non-Cartesian trajectories that enable short T_2* imaging.

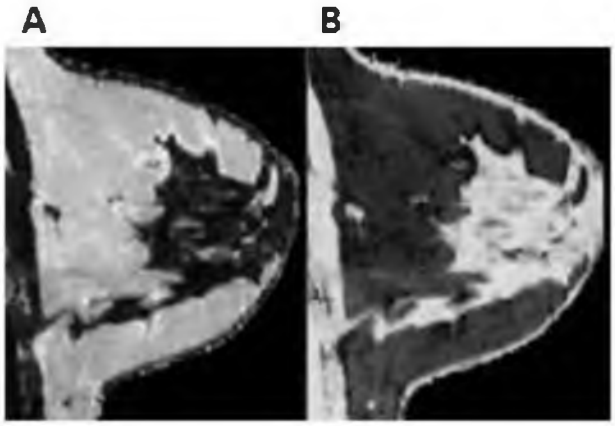

Figure 9. Breast images after a 3-point Dixon. (A) Fat / adipose tissue and (B) water images of a normal human breast. These images were created from three GRE scans at different TEs and reconstructed using the 3-point Dixon method.

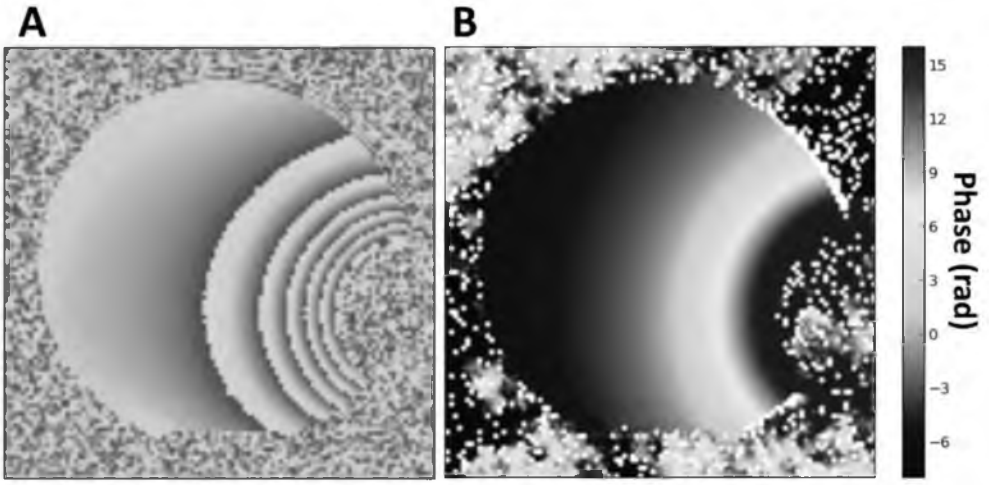

Figure 10. Phase images before and after phase unwrapping. (A) Wrapped and (B) unwrapped phase difference maps between two echo times of a homogeneous, cylindrical phantom with a paperclip positioned on one side. (A) A wrapped map is limited to a 2π range. (B) An unwrapped phase difference map is directly proportional to ΔB_0.

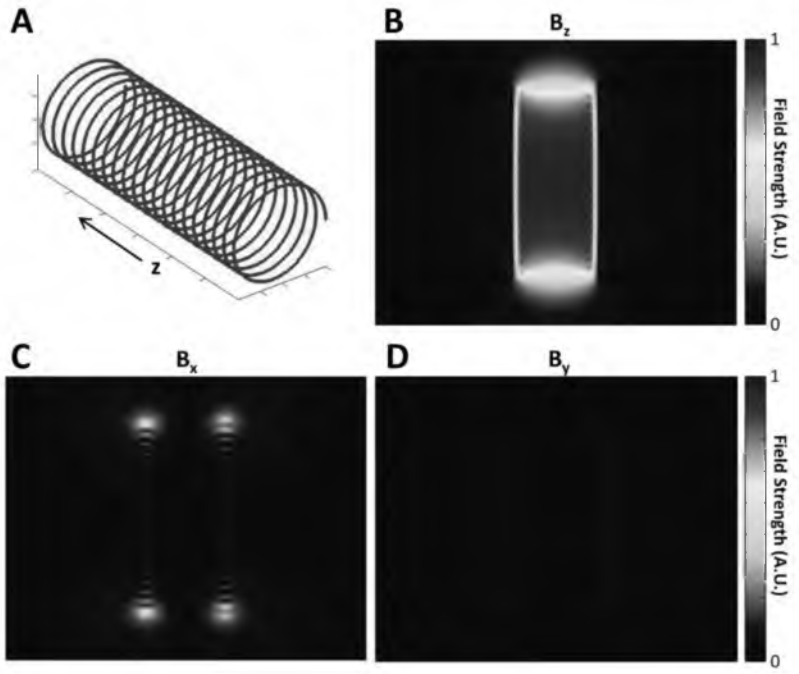

Figure 11. Solenoid magnetic field simulations. (A) Picture of a solenoid used for magnetic field Biot-Savart Law simulation. The static B_0 field in MRI is created by superconducting coils based off of the solenoid design. The static (B) B_z, (C) B_x, and (D) B_y fields through the central coronal slice of the solenoid calculated through a Biot-Savart Law simulation. The color corresponds to the strength of each magnetic field component in space. The B_x field near the edge of the solenoid is larger than in the center because it does not have the same field cancellation from other loops.

Figure 12. Demonstration of k-space spikes. The bright points on the edges of this k-space image could be the result of gradient cables that are not sufficiently tightened (123) resulting of electric arcing that is detected by the RF receive coils. In our experiments, tightening the gradient cables and implementing RF shielding was effective in removing the k-space spikes.

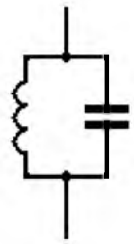

Figure 13. The standard LC circuit. This circuit is the basic component to a resonant coil and to high impedance traps. This circuit has infinite impedance when the inductor and capacitor resonate.

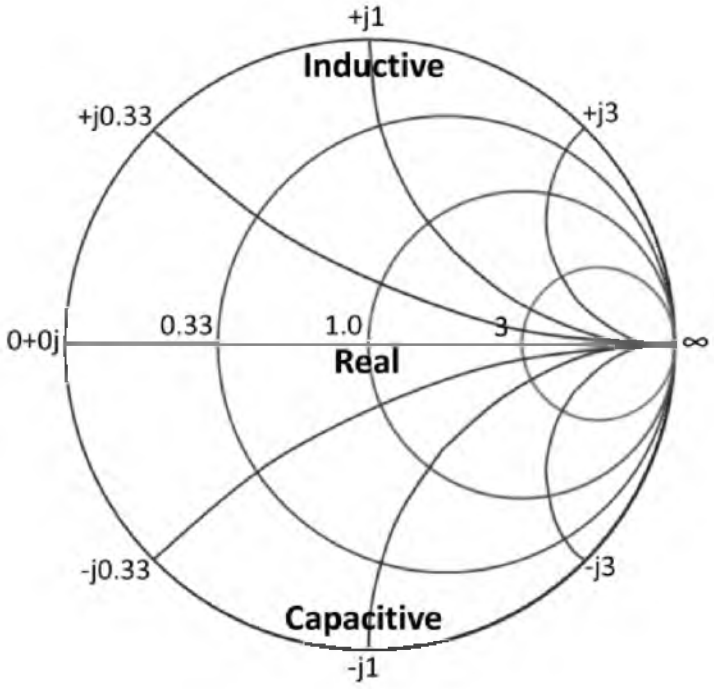

Figure 14. The Smith chart normalized to 1 Ω as the characteristic impedance. Smith charts used in RF coils are typically normalized to 50 Ω, which will be the impedance value at the center of the chart. The horizontal line indicates the real impedance line (also known as the resistance line), where there are no reactive components. The circles indicate constant real impedance. The non-circle but curved lines indicate constant imaginary impedance (also known as reactance). If a point lies above the real line, it is inductive, whereas below the real line it is capacitive. (125,126)

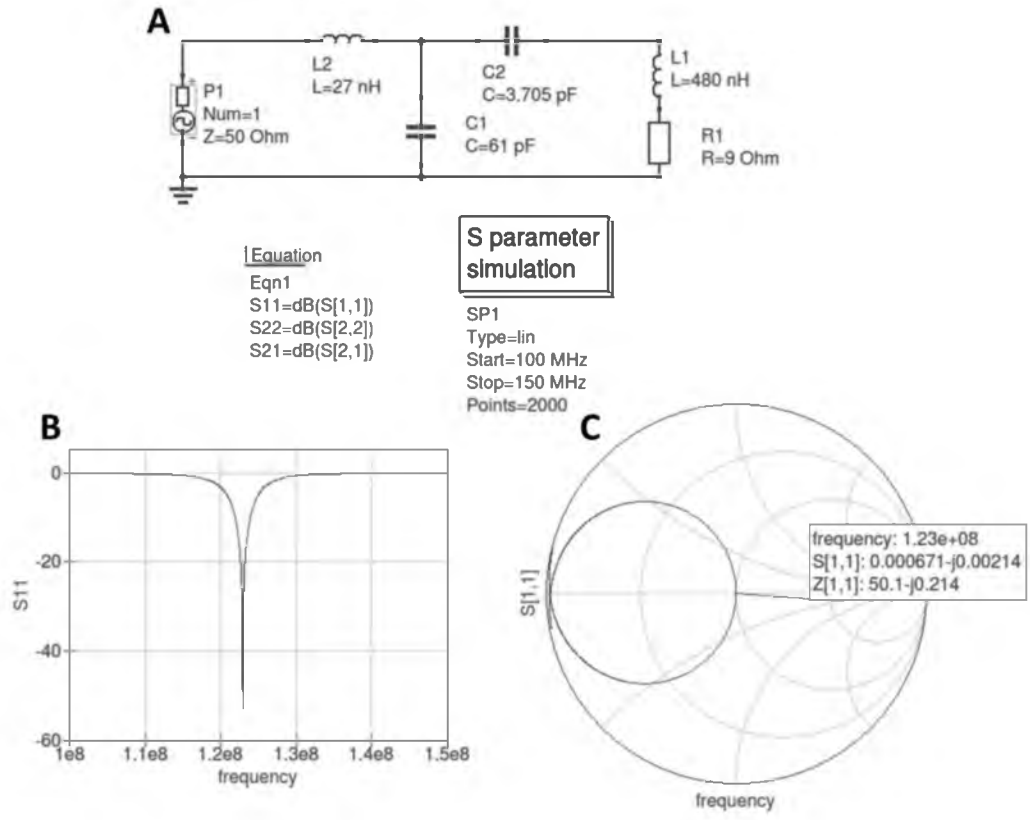

Figure 15. A Quite Universal Circuit Simulator (QUCS) simulation of a coil. (A) Schematic of the QUCS circuit. (B) A plot showing the reflective power at different frequencies. At 123 MHz, the magnitude of reflective power is >40 dB, showing that the resonator absorbs nearly all of the incident power. (C) A Smith chart showing that at 123 MHz the coil is both tuned and matched to 50 Ω.

Figure 16. The magnetic field of a loop. The magnitude of the magnetic field perpendicular to the loop (outlined in black), created from the analytical solution of the magnetic field of a loop.

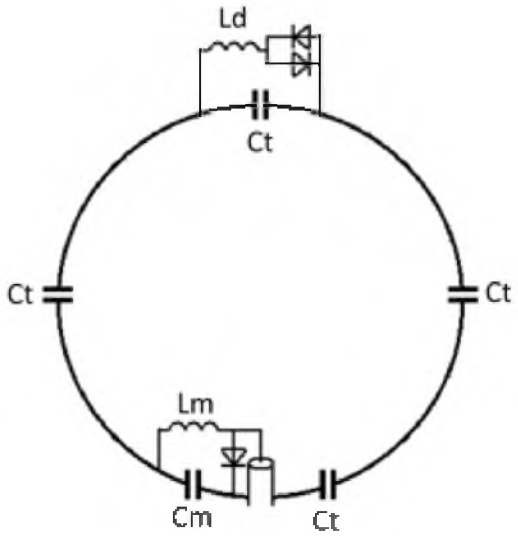

Figure 17. The basic receive coil. The center of a coaxial cable connects to a match inductor (Lm), which then is connected to a match capacitor (Cm) and tune capacitors (Ct). The diode connected to Lm and Cm is activated during transmit with a forward-bias current, causing Lm and Cm to resonate and detune the coil. The diodes connected to Ld and Ct activate only if the sufficient signal occurs, causing Ld and Ct to resonate and detuning the coil. The diodes have a high impedance during receive so they do not affect the coil significantly.

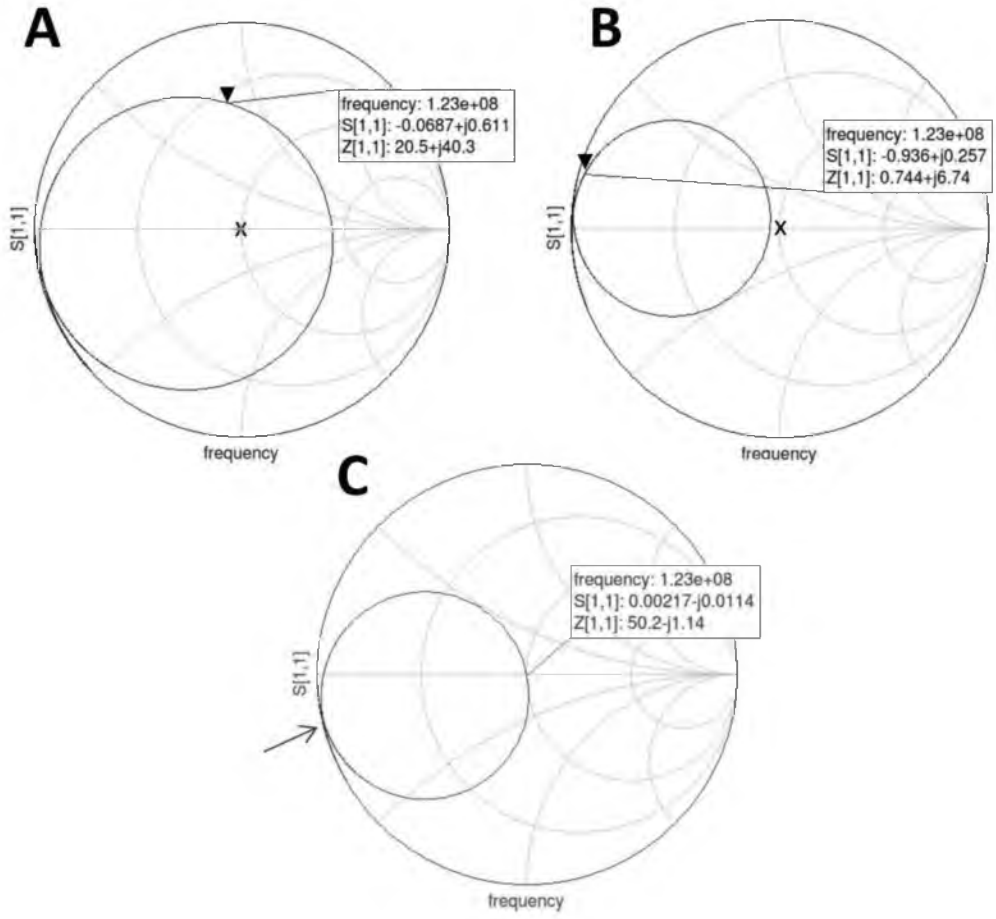

Figure 18. Unmatched, untuned, and tuned Smith charts. Three different Smith charts show coils that: (A) need more match capacitance, which will shrink the circle of impedance frequencies; (B) need more tune capacitance, which will rotate the frequency around the circle and very slightly increase the circle's area; and, (C) require no changes, as it is a tuned and matched coil. However, in (C) a slightly larger match inductor is ideal, because it will rotate the frequency circle slightly so that the intersection of the high and low frequencies' impedance (marked by the red arrow) is at zero real and imaginary impedance, which experimental evidence suggests will slightly improve preamplifier decoupling.

Figure 19. A Rhode and Schwarz Network Analyzer with noise figure meter option.

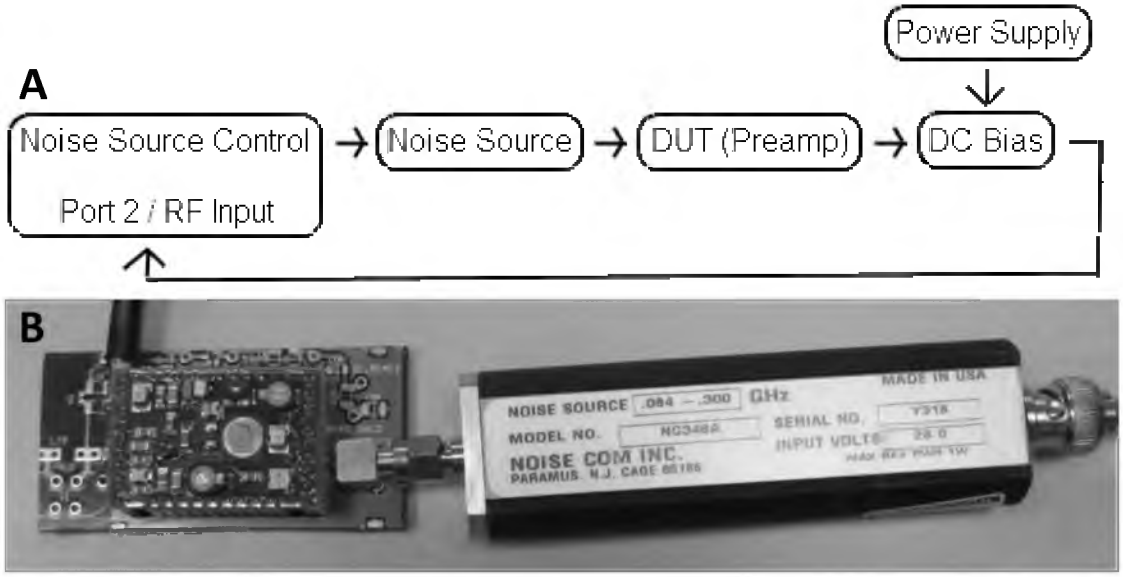

Figure 20. A noise source and preamplifier. (A) Schematic showing the flow of hardware connections to obtain a noise figure measurement. (B) Noise figure meter connected to a preamplifier.

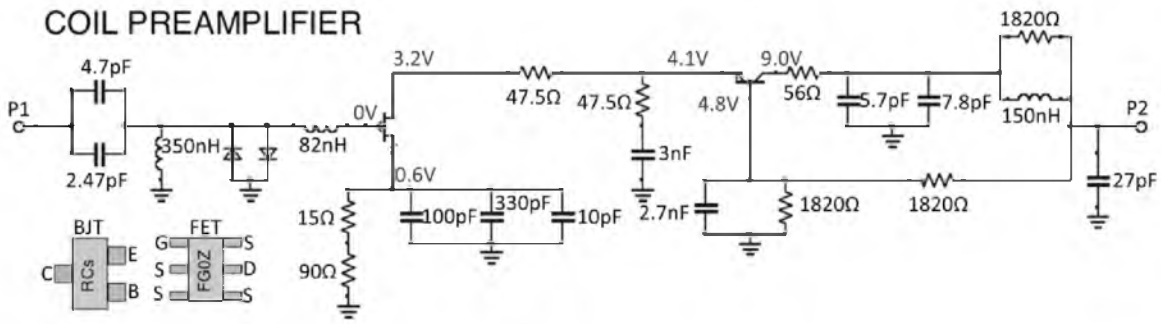

Figure 21. A coil preamplifier circuit schematic. The preamplifier circuit for the proton preamps used in this dissertation. P1 (the first connection on the left) is port 1 where the coil connects. The voltages listed in red were measured on a working preamp.

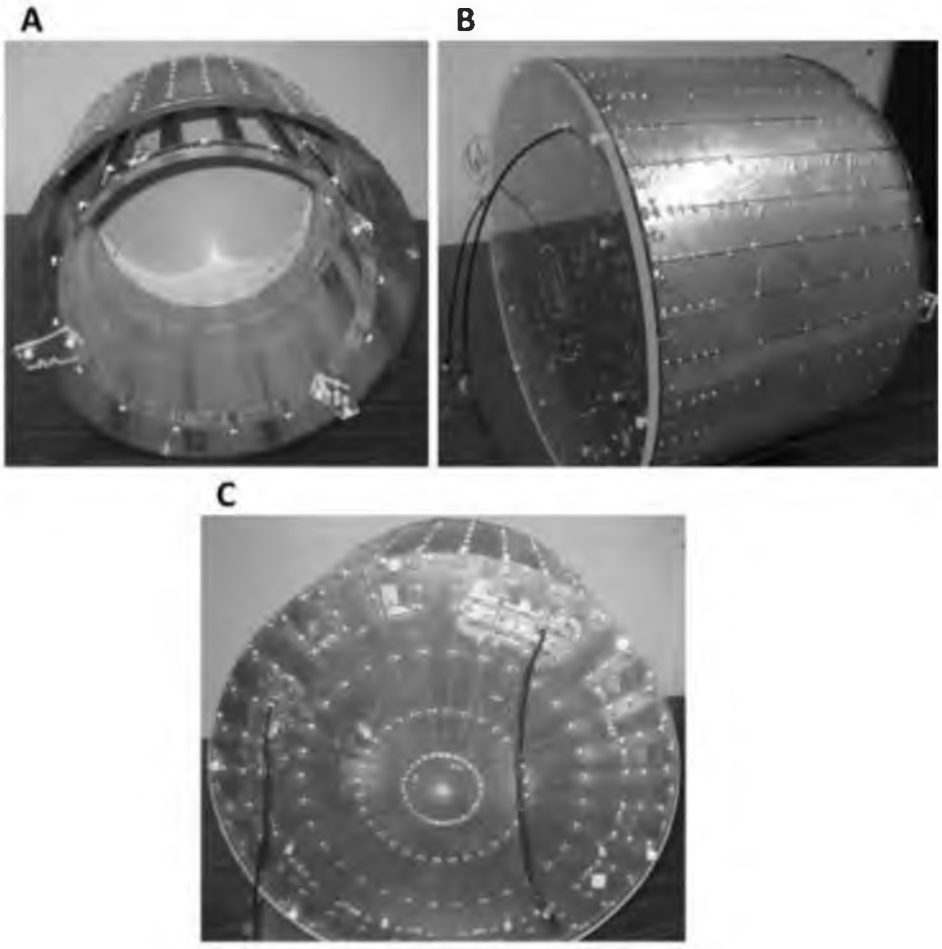

Figure 22. A shielded birdcage coil with endcap. (A) The front, (B) shield, and (C) endcap of a high-pass birdcage coil. The shield and endcap have copper strips that are separated by ~1mm gaps, with capacitors placed across them, to reduce eddy currents from the gradients yet still allow magnetic gradient field penetration and RF shielding.

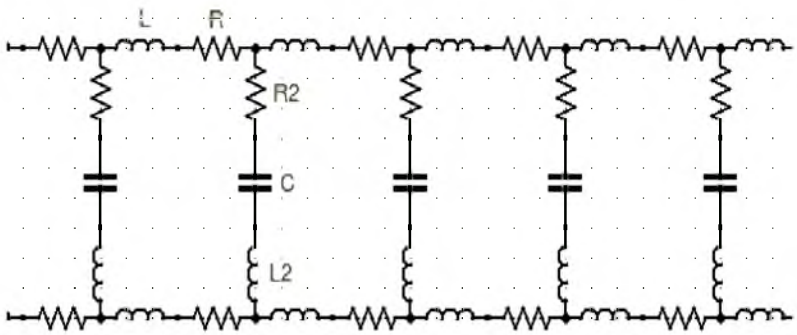

Figure 23. Circuit schematic of a birdcage coil. Circuit schematic of a low pass birdcage coil, which has capacitors on the birdcage legs/rungs.

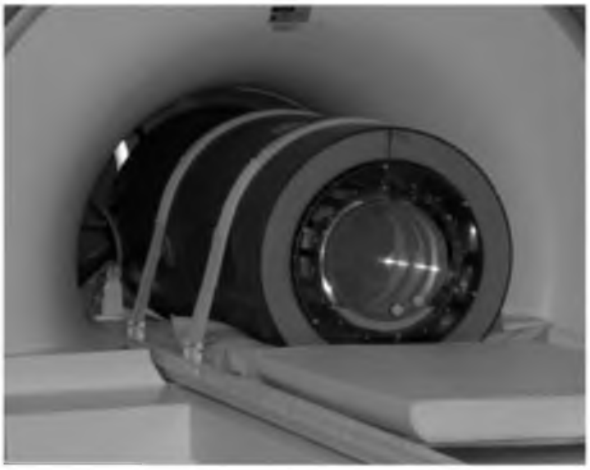

Figure 24. A birdcage coil inside an insertable gradient. Shielded birdcage coil inside of an insertable gradient, pictured inside of the clinical magnet.

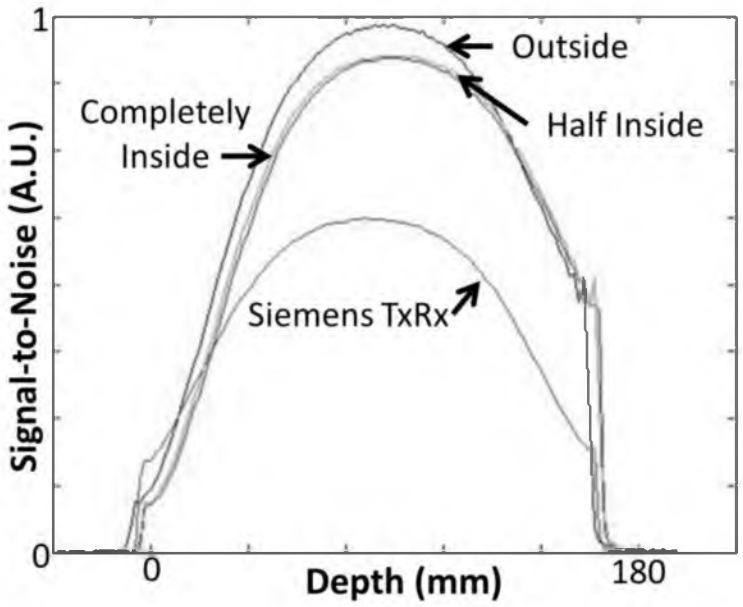

Figure 25. SNR comparisons of a shielded birdcage coil. Different SNR comparisons of the birdcage of Figure 22 when: completely inside the insertable gradient of Figure 24; half inside the insertable gradient; and, completely external to the insertable gradient. The birdcage was compared to a Siemens TxRx birdcage coil.

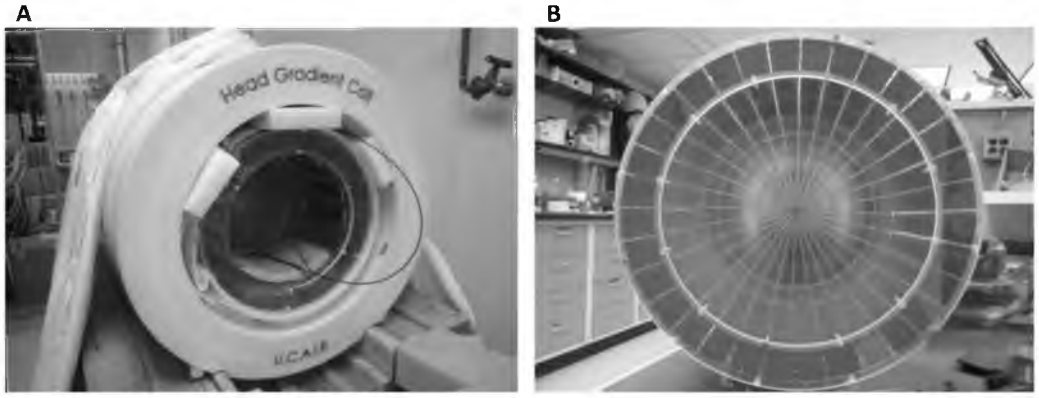

Figure 26. A large birdcage coil and insertable gradient. An (A) insertable gradient system with a shielded birdcage RF coil inside. (B) A shielded birdcage coil with end cap. This insertable gradient and birdcage had larger inner diameters than the system pictured in Figure 24.

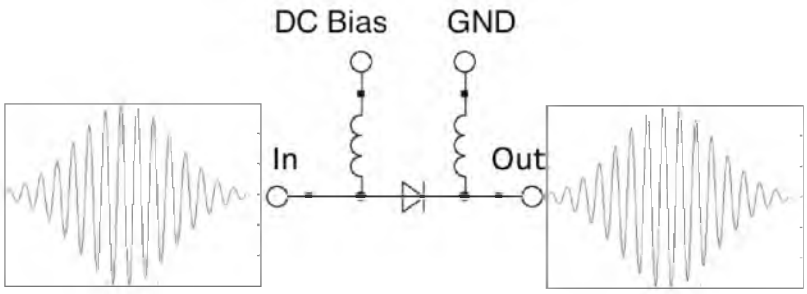

Figure 27. The effects of a PIN diode. An RF wave that passes through a PIN diode that is biased with a low positive DC current will have little to no distortion.

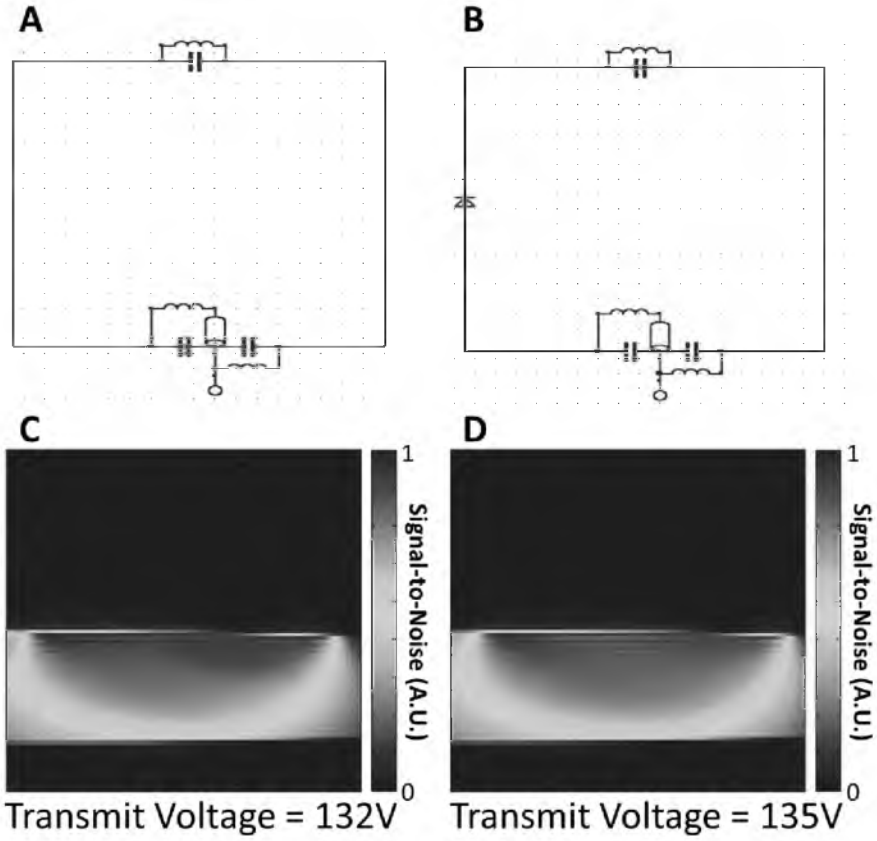

Figure 28. SNR experiments using a serial PIN diode. An experiment showing the SNR obtained with two different coils, (A,C) one without a diode and (B,D) one with a diode inserted serially, resulted in similar (C-D) SNR maps. The voltage necessary for a 90° flip angle was slightly higher with the diode.

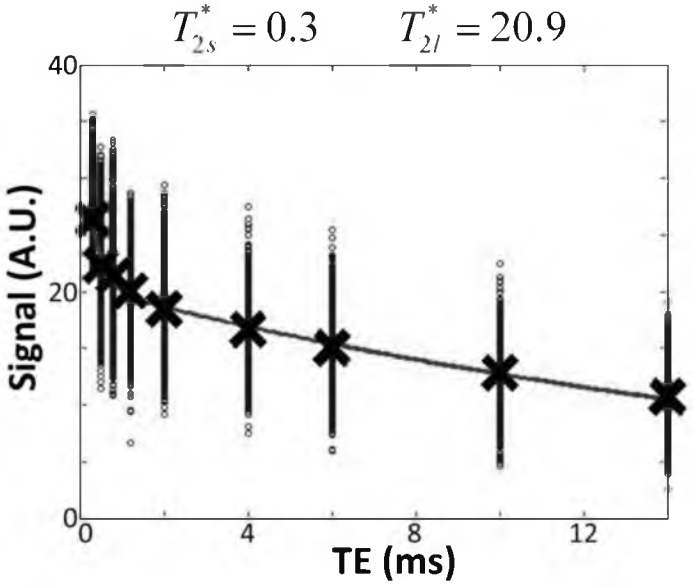

Figure 29. Biexponential sodium decay. Biexponential T_2* decay curve for sodium, obtained from the signal-yielding region of a breast. The individual voxel signals are in circles, the average of the signals are shown with a big X, and the fit is shown with a line.

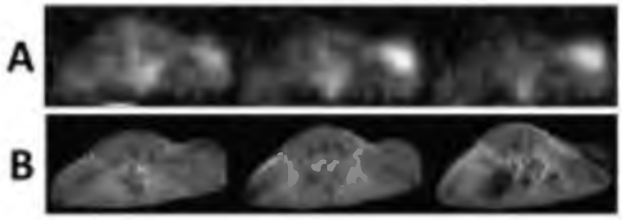

Figure 30. Sodium and proton images of a mouse. (A) Sodium and (B) proton image of a mouse, obtained on the 3 T MRI scanner. The bright areas on the sodium image indicate the tumor in the rodent.

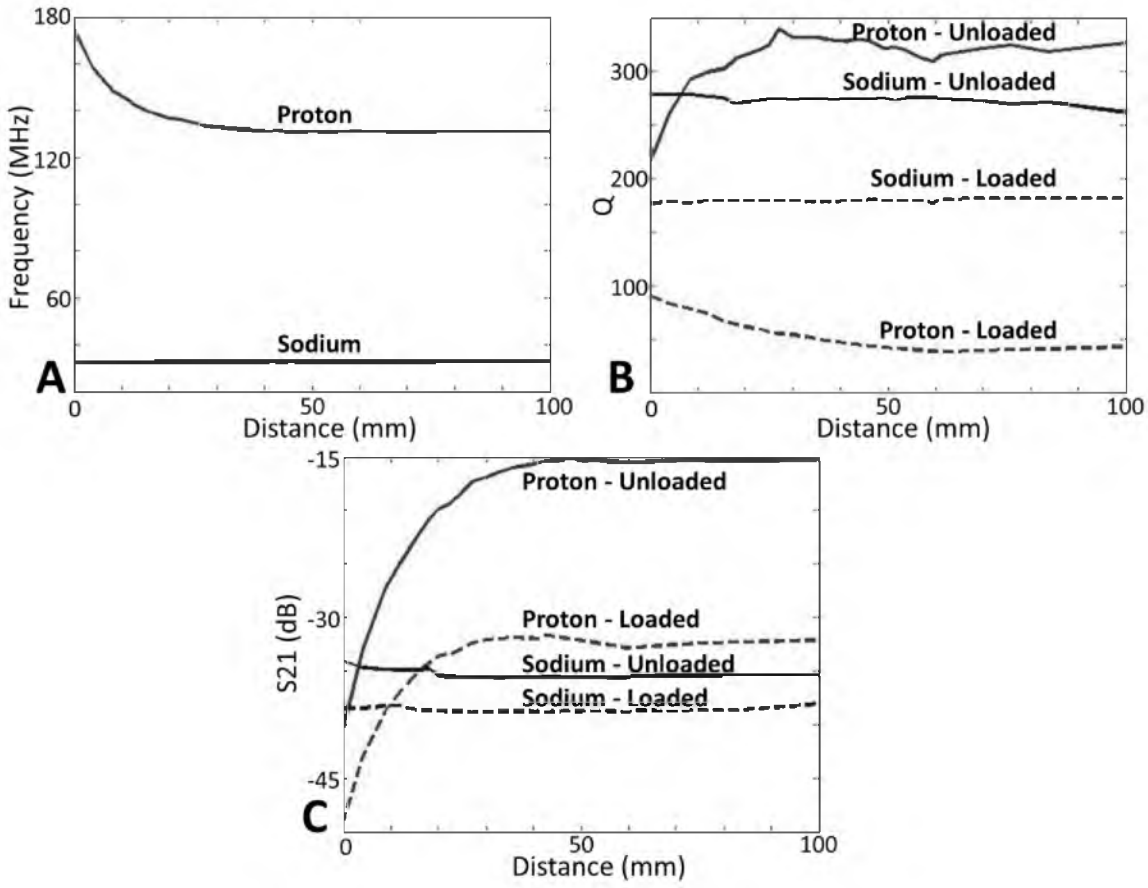

Figure 31. The changes in coil properties in dual-nuclear conditions. Measurements (A) frequency shift, (B) Q-values, and (C) S21 shielding for different in-plane center-to-center coil distances for a 65 mm diameter proton (red, dashed) and sodium (blue, solid) loop that overlap each other. The proton loop is strongly affected by the presence of the sodium loop, while the sodium loop has minor, if any changes, due to the presence of the proton loop.

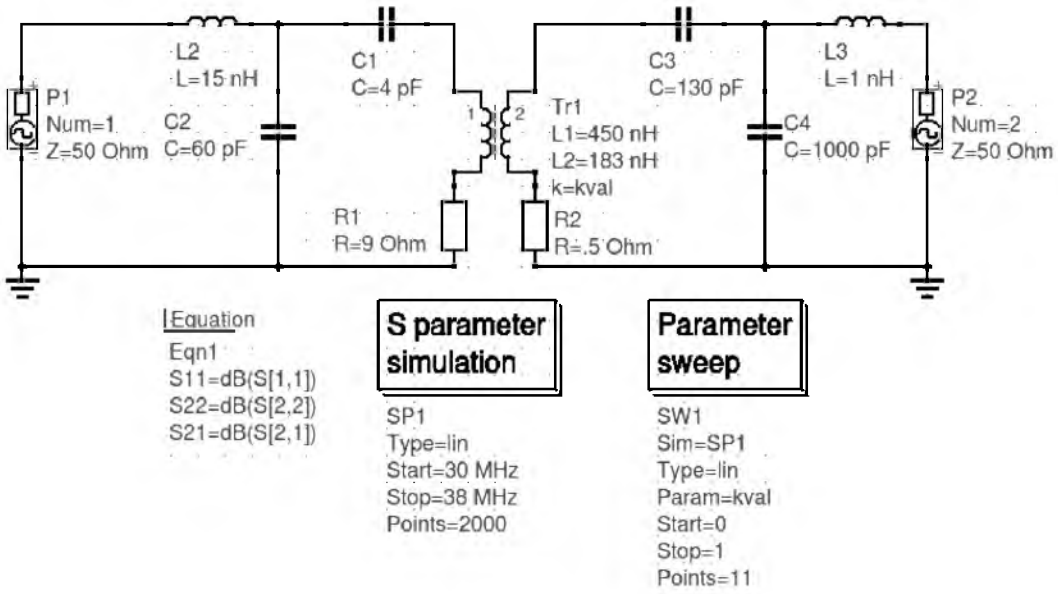

Figure 32. QUCS circuit simulation of two coupled loops. QUCS circuit simulation of a sodium (right loop) and proton (left loop) coil. The resistances and inductances were calculated from the measured resonant frequency, capacitance and Q values of 65 mm diameter loops.

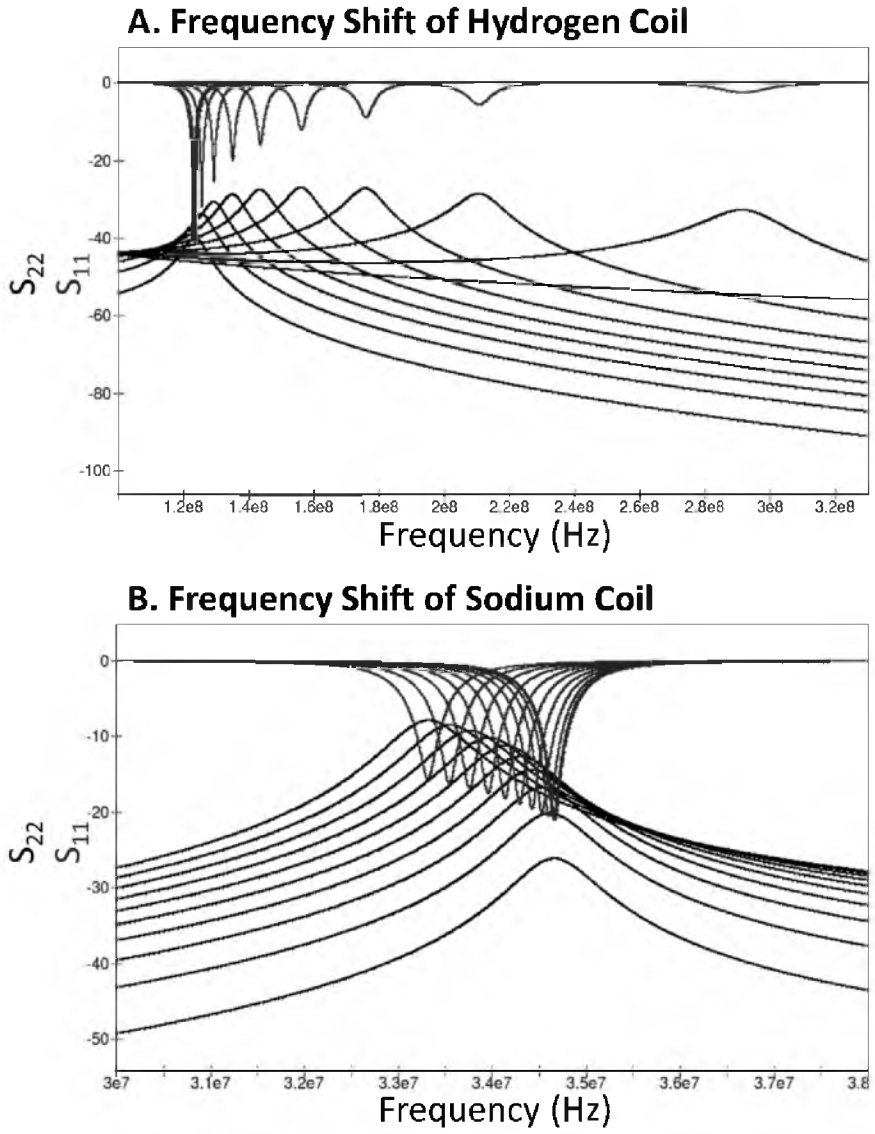

Figure 33. QUCS circuit simulation results of two coupled dual-nuclear loops. The results of a QUCS circuit simulation of a coupled sodium and proton coil, using measured capacitance, inductance, and resistance, and with the coupling coefficient, k, varied between 0 and 1 by 0.1. The (A) hydrogen coil frequency drastically increases with increasing coupling to the sodium coil, while the (B) sodium loop has a minor frequency shift downwards. The (B) sodium coil is still affected by the (A) hydrogen coil, although the effect is minor in comparison to the effect on the proton coil.

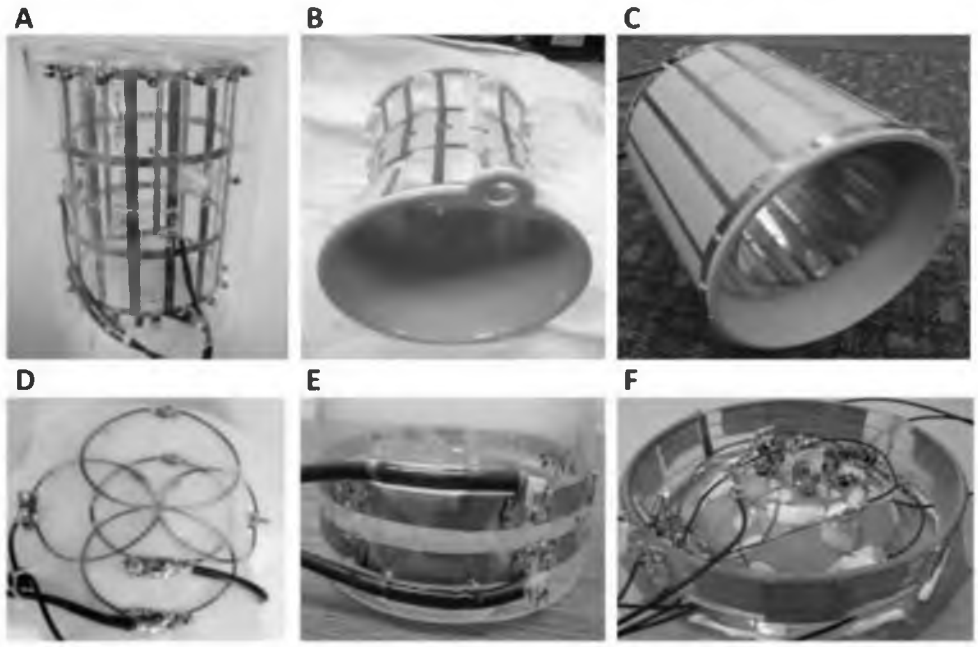

Figure 34. Dual-tuned sodium proton coils. (A,B) The central birdcage is tuned to sodium and the entire structure is tuned to proton. (C) The central birdcage is tuned to sodium, and the external birdcage is tuned to proton. (D) The central loop and one butterfly coil are tuned to sodium, and a proton butterfly intersects the sodium coils. (E) Decoupling traps are used so that the proton and sodium loop coupling is reduced. (F) A composite sodium / proton array that interleaves sodium and proton coils and uses diodes for additional decoupling.

Table 1. Capacitance values required to tune a 7.5cm diameter coil at different frequencies. The unloaded and loaded Q-values were measured, and the inductances, coil resistances, and sample resistances were calculated.

f (MHz)	C (pF)	L (nH)	ωL	Q_u	Q_l	Ratio	R_{coil}	R_{sample}
27.85	188.9	172.9	30.3	150	101	1.49	0.21	0.10
43.77	76.4	173.1	47.6	200	130	1.54	0.24	0.13
82.8	20.2	182.9	95	180	69	2.61	0.53	0.85
118.3	9.4	192.5	143	170	38	4.57	0.84	2.92

Table 2. Results of inputting a 30 MHz RF voltage (~500 V) for 20 minutes into various circuits with and without DC bias. An unbiased diode became permanently shorted and excessively hot (enough to burn a finger) after only a minute. By forward-biasing a diode or crossed-diode pair, the temperature that the circuit increased was nearly the same as that of a copper wire.

Circuit	DC (mA)	Temperature Increase (ΔC)	Performance After Test
Copper Wire	N/A	1-2	Normal
Diode	0	>20	Permanently Shorted
Diode	100	1-2	Normal
Crossed Diode	0	10	Normal
Crossed Diode	100	1-2	Normal

Table 3. Common nuclear species and their gyromagnetic ratio, natural abundance, abundance within the human body by mass, and spin. The abundance in the body is only of that particular isotope. (176)

Nucleus	$\gamma/2\pi$ (MHz/T)	Natural Abundance (%)	Abundance in Body by Mass (%)	Spin
^{1}H	42.576	99.9885	9.5	1/2
^{3}He	32.434	0.000137	-	1/2
^{7}Li	16.546	92.41	-	3/2
^{13}C	10.705	1.07	0.198	1/2
^{15}N	-4.316	0.368	0.012	1/2
^{17}O	5.772	0.038	0.025	5/2
^{19}F	40.052	100	-	1/2
^{23}Na	11.262	100	0.2	3/2
^{27}Al	11.103	100	-	5/2
^{31}P	17.235	100	1.0	1/2
^{35}Cl	4.176	75.77	0.0015	3/2
^{39}K	1.989	93.258	0.373	3/2
^{57}Fe	1.382	2.2	-	1/2
^{63}Cu	11.319	69.17	-	3/2
^{67}Zn	2.669	4.1	-	5/2
^{129}Xe	11.777	26.4	-	1/2

CHAPTER 2

HIGH RESOLUTION IN VIVO GUINEA PIG COCHLEA IMAGING ON A 3 T CLINICAL MAGNET WITH INSERTABLE GRADIENT AND RF COIL TECHNOLOGY

This chapter has identical content to a submitted paper titled, *"High Resolution In Vivo Guinea Pig Cochlea Imaging on a 3 T Clinical Magnet with Insertable Gradient and RF Coil Technology,"* authored by Joshua D. Kaggie, K. Craig Goodrich, Seong-Eun Kim, Michael J. Beck, Dennis L. Parker, Robb Merrill, Travis A. Abele, Richard Wiggins, Gretchen M. Oakley, and J. Rock Hadley. The paper was accepted in the journal Concepts in Magnetic Resonance B in February 2015. (Reprinted with permission.)

2.1 Abstract

2.1.1 Purpose

The purpose of this work was to develop and evaluate a system consisting of an insertable gradient, RF coils, and animal positioning hardware to enable imaging of the internal structure of the cochlea and other inner ear structures of a guinea pig model at 3 T.

2.1.2 Methods

Transmit and receive RF coils, and an animal positioning system, were developed and integrated with an insertable gradient and animal monitoring system for improved guinea pig cochlea imaging when compared to a standard clinical 3 T MRI system. A resolution phantom with 120 μm line separations was used to assess the contrast improvements with the insertable gradient. A homogeneous phantom was used to assess the SNR and homogeneity of the RF coils. FLASH imaging was used to observe the temporal passage of gadolinium contrast through the guinea pig cochlea.

2.1.3 Results

The insertable gradient enabled increased resolution imaging with nearly twice the contrast-to-noise ratio. The small animal array had better SNR for imaging the guinea pig cochlea (about 14 mm deep) than the commercial Siemens wrist coil (2.2x) and the small birdcage coil (1.6x). The positioning device kept the animal secure and stationary. Injected gadolinium contrast allowed visualization of the internal cochlear structures with FLASH image acquisition, which achieved 100μm isotropic resolution images in 33 minutes.

2.1.4 Conclusion

The specialized RF coils and animal holding equipment designed to operate within the composite gradient enabled higher resolution images than could be obtained from the available RF coils operating in the conventional gradients on the clinical MRI system.

2.2 Introduction

The development of high resolution MRI techniques for small animal models can be used to assess shared pathologies between humans and guinea pigs. As an example of a similar anatomical system, both human and guinea pig cochlea have three tiny fluid filled chambers. The basilar membrane and Reissner's membrane, which separate the three chambers, are indicators of the health of the inner ear (208,209). By obtaining higher resolution MR images of the cochlear chambers, better assessment of these inner ear structures can be obtained, allowing for more focused treatment of hearing loss and more accurate diagnosis of inner diseases such as vestibular schwannoma, cochlear malformation, labyrinthine ossificans, and possibly endolymphatic hydrops (208,209).

Both ex vivo and in vivo MRI studies of the cochlea have achieved high spatial and temporal resolution. In excised human (210) and animal (211,212) inner ear cadaveric samples, voxel resolutions of 32x43x49 μm, 25x25x250 μm, 58x58x300 μm have been achieved at 9.4 T, 7 T, and 4.7 T, respectively. The highest reported resolution for in vivo human cochlear imaging is nearly 300 μm isotropic at 3 T (213). In vivo 2D images of a guinea pig have been obtained at 4.7 T, using a 200mT/m gradient system and semicircular coil, at 117x117x500 μm resolution (214). The highest resolution reported for imaging the inner ear of a live animal is 78μm isotropic images of a mouse at 4.7T using the RARE sequence, 2 averages, with a 300mT/m gradient, 80μs rise time, and a linear 38mm diameter birdcage coil in 34 minutes (215). The limitations in spatial and temporal resolution occur because of limits in magnetic field strength, magnetic gradient strength, and RF coil sensitivities.

Gadolinium enhancement has been a primary tool for improving inner ear imaging both in cadaveric samples (210,216) and in vivo human studies (209,217). The

cadaveric studies have achieved direct visualization of the vestibular (Reissner's) membrane, the thin partition separating the perilymph containing scala vestibule, and endolymph containing scala media (210,216). Other internal structures of the cochlea, including the basilar membrane (which divides the scala tympani from the scala media and vestibuli) and modiolus, have been resolved in vivo on clinical 3 T MR scanners (209,217).

Typical clinical gradient systems have gradient strengths of 40 mT/m and slew rates up to 200 T/m/s, while dedicated state-of-the-art small rodent systems can have gradient strengths up to 1000 mT/m and slew rates up to 5000 T/m/s (218). Most clinical MRI scanners have self-imposed gradient performance limits conforming to the U.S. Food and Drug Administration (219) and the International Electrotechnical Commission guidelines (220), to avoid peripheral nerve stimulation during a human MRI study. Gradient field strengths and slew rates can be increased without inducing additional peripheral nerve stimulation when the gradient's imaging volume is decreased (121,221). Better gradient performance enables higher resolution imaging by reducing the readout duration, which can reduce susceptibility artifacts, reduce T_2* blurring, and enable shorter echo planar imaging scan times. In collaboration with industry, our institution has developed a novel MRI composite gradient system that simultaneously uses both the whole body and a local insertable gradient (120,121). This system increases gradient amplitude, slew rate, and achievable spatial resolution while maintaining acceptable SNR and a clinically relevant scan time on a clinical MRI scanner (120,121).

Several different types of radiofrequency (RF) coils are possible for small animal imaging. Despite the lower field strengths and limited gradient performance of clinical scanners, small animal MRI coils and setups for clinical systems have been widely

investigated (218,222,223). Surface coils are simple to implement and have been used in many small animal studies (223), but the nonuniform sensitivity can result in signal nonuniformities, especially when the coil is used for both transmit (Tx) and receive (Rx). Volume coils can achieve greater signal uniformity than surface coils. A solenoid coil can achieve the highest signal uniformity, but is most sensitive with its axis aligned perpendicular to the main B_0 magnetic field. Use of solenoid coils requires a scanner bore with a diameter large enough to accommodate the length of the rodent, which significantly limits the use of solenoid coils in small bore systems. Other common homogeneous coil configurations are the birdcage (140), Helmholtz (140), and saddle coils (140), which allow the coil and the rodent to be aligned with the field of the magnet. Birdcage coils are more homogeneous and efficient than Helmholtz and saddle coils (140). However, the animal geometry may require that birdcage and other volume coils be much larger in diameter than the image volume of interest. For example, the optimal coil position and diameter that accommodates the head and allows for imaging the inner ear of a rodent can be compromised by the coil diameter required to accommodate the shoulders and body of the rodent. In vivo visualization of the small features of the cochlea requires high spatial resolution and long imaging times, which can be reduced when the coil is designed specifically for cochlear imaging. For some rodent imaging applications, a small phased array will often have higher SNR within the radius of the loops (147) than a small volume coil that surrounds the same imaging volume, as demonstrated in 3 T mouse imaging (224). Commercial receive arrays exist for full-body rat and mouse MRI (218), while commercial volume coils are typical for larger rodents, such as large rats or guinea pigs.

The purpose of this work was to develop a system for high resolution imaging of

a live guinea pig cochlea on a 3 T clinical scanner, by developing and integrating RF coils for the composite gradient system, integrated with an animal support system for animal positioning, monitoring and anesthesia. The SNR and homogeneity of the RF coils were evaluated with a homogeneous phantom, and the gradient system was evaluated with a resolution phantom. This work also demonstrates novel techniques for improving the robustness of the coils and circuits used for transmit and receive. The high isotropic spatial resolution (100 μm) achieved of the live guinea pig cochlea demonstrates that this system can be used, in conjunction with gadolinium contrast injection, to study the chambers of the cochlea.

2.3 Methods

To achieve high resolution on a live rodent, components of our standard clinical MRI system were augmented with an insertable gradient system (120), a local volume transmit-only RF coil, a dedicated rodent receive RF coil array, and an animal positioning device (see Figure 35 and Figure 36A). System quality was assessed using imaging studies on phantoms and a live guinea pig.

2.3.1 Gradient System

The gradient coils used in this work consisted of either the standard whole body gradients of the scanner or the standard whole body gradients combined simultaneously with a small insertable gradient for composite gradient mode imaging (120). The body gradient system was controlled using the standard Siemens host computer, gradient control lines, and gradient amplifiers. The insertable gradient was controlled by a separate computer, control lines, and an additional set of gradient amplifiers. Each

gradient system was set at 40 mT/m field strength with a slew rate of 200 T/m/s. Pulse sequences were modified to control each individual gradient waveform independently on the two separate gradient systems. The sequences for each gradient system were set to have identical gradient waveforms and timing, with the insertable gradient waveform amplitude controlled by modifications to the gradient sensitivity tables. Composite mode imaging doubled the maximum gradient strength and slew rate over that of the body gradients used alone, thereby reducing the echo time, echo spacing, and repetition time while maintaining high spatial resolution (121). The composite gradient system had a total gradient field strength of 80 mT/m with a slew rate of 400 T/m/s.

The inner diameter of the insertable gradient was 15.2cm, and the outer diameter was 32.4 cm. The imaging region was 17 cm in length, along the magnet bore. The insertable gradient strength was limited to 40 mT/m field strength, as the gradient was not vacuum potted and consisted of 14 gauge wire, making it sensitive to large currents and mechanical damage. While the insertable gradient could have been used without the body gradients, the imaging results would have been similar to using the body gradients alone (121). The insertable gradient did not have any shimming capabilities and relied on the clinical scanner's shim gradients. B_0-field shimming was performed with the insertable gradient in place, so that experiments with the body gradients alone and in composite mode had the same shim parameters.

2.3.2 RF Shielding

RF shielding was placed along the inner diameter (150 mm) of the insertable gradient set to remove RF coupling between the insertable gradient and RF coils (Figure 36B). The RF shielding also removed signal from water in the insertable gradient

cooling system, so that a smaller field-of-view (FOV) could be used without the cooling liquids aliasing into the images.

The RF shield consisted of 260 mm long, rectangular copper strips oriented along the longitudinal direction of the bore. The copper strips were 31 mm wide with a 1 mm gap between adjacent strips. A similar set of copper strips was placed on the opposite side of the kapton substrate, and offset from the first set by half the copper strip width. The capacitance measured between the copper strips inside and outside of the shield was 740pF, which provided low impedance at the RF frequency of 123 MHz and high impedance at the gradient frequencies of ~20 kHz. The change in isolation, with and without the shield in place, was 20 dB, measured between a tuned, centered, 27mm diameter surface coil and a similarly sized test probe (29) placed on the opposite side of the shield. The isolation change (20 dB) was similar to that of a solid copper cylinder of the same length and diameter. The gaps in the shield were used to reduce induced gradient eddy currents, which could result in gradient field distortions.

2.3.3 RF Coils for SNR Comparisons

This work compared three RF coils to ensure that the system developed used the best available coil for high SNR visualization of the rodent inner ear. The three coils used for this comparison were: 1) a commercially available ***Siemens Tx/Rx wrist coil*** (Figure 37A) (Alpha III Tx/Rx Wrist Coil, USA Instruments Inc, Aurora, Ohio, USA), 2) a ***small Tx/Rx birdcage*** coil (Figure 37B), and 3) a custom ***4-channel Rx phased array (4chPA)*** and corresponding ***local Tx-only birdcage*** coil. The wrist coil was selected for a baseline commercial coil comparison. The SNR tests were done without the animal monitoring equipment or insertable gradient, as the wrist coil would not fit inside the

insertable gradient bore. The small birdcage was selected for this comparison because it was more sensitive than the Siemens wrist coil and still large enough to provide homogeneous sensitivity around the cochlea. The custom 4-channel Rx phased array and local Tx-only coil were designed to be sensitive specifically to the cochlear region of the rodent.

2.3.3.1 Small Tx/Rx Birdcage

An 8-rung small diameter birdcage Tx/Rx coil was constructed for SNR comparisons with the 4chPA. The rings and rungs had a width of 10mm and 5mm, respectively. The birdcage was 75 mm long and had a diameter of 64mm, with an acrylic cylinder wall thickness of 3 mm. The diameter was chosen so that it could accommodate the entire rodent head and shoulder region with maximal filling factor. A smaller ~40 mm diameter birdcage could have been implemented to fit over the guinea pig head, but it would not have fit over the guinea pig shoulders, excluding the inner ear anatomy from the sensitive central region of the coil. In such a coil, the inner ear images would be acquired near the end ring of the birdcage, resulting in image inhomogeneity, lower SNR, and increased RF power requirements to obtain 90° flip angle near the end ring and thus higher specific absorption rate at the center of the birdcage.

2.3.3.2 4-Channel Array (4chPA)

2.3.3.2.1 4-Channel Rx Phased Array

The 4-channel receive-only phased array coil was designed and constructed so that it could fit close to the guinea pig's head, directly over the inner ear of both sides of the head, to maximize SNR for inner ear imaging. The four loops were 27 mm in

diameter and were mounted on a 160 mL plastic syringe with a 41 mm outer diameter. A portion of the plunger end of the syringe was cut away and the coils were mounted on the top half of the cylinder allowing the coils to be placed over the ears of rodents of different head sizes, as shown in Figure 38. The conical end of the syringe was used to connect the anesthesia tubing to the coil housing for delivery of anesthetic. Because the small diameter of the overlapping loops reduced the space available for capacitors and because fewer capacitors also increased the Q-unloaded to Q-loaded ratio(137), a single match and tune capacitor (Figure 39) were used for each loop. The loops had an unloaded Q-factor of 270 and loaded Q-factor of 85.

For each receive channel, the matching circuit of the coil loop was attached to a 24 cm coaxial cable. The cable was connected to an RF trap to reduce common-mode currents, followed by a Pi-network phase-shifter to obtain a 180-degree phase shift between the coil and preamplifier to achieve preamplifier decoupling (Figure 39). The receiver preamplifiers were positioned so that they entered into the insertable gradient bore with the coils, to minimize the coaxial cable distance between the coils and preamplifiers to reduce unnecessary signal loss.

To ensure the safety of the rodents and electronics, active and passive detuning was used and combined into a single circuit by placing a crossed diode pair (MA4P7464F-1072T, Macom, Lowell, MA, USA) in series with an inductor that was resonant with the tune capacitor when forward biased (Figure 39). The crossed diodes operated similar to a single diode, while enabling secondary passive protection of the diode electronics in the event of high RF occurring with improper DC biasing, such as could occur with mechanical failures(20).

Each loop was connected to an independent DC bias line. The scanner provided

100 mA / 10 VDC forward bias or -30 VDC reverse bias that controlled the diodes in the RF coils and circuits. The forward bias current enabled the diodes to remain at a low impedance for very high RF powers (48). To avoid biasing the crossed diodes with the negative DC bias, a single diode was added into the bias line so that only positive DC current could be supplied to the loops (Db in Figure 39 and Figure 40B).

2.3.3.2.2 Local Transmit-Only Birdcage

To obtain homogeneous transmit flip angles inside the insertable gradient and for use with the 4chPA, an 8-rung, low-pass, transmit-only RF birdcage was developed. The body RF coil was unusable for imaging inside the insertable gradient due to the gradient RF shield and increased RF power requirements necessary to penetrate the gradients, so a local transmit-only birdcage coil was used. The rungs and rings were 10 mm and 6 mm wide, respectively. The birdcage was 102 mm in diameter and 98 mm long and centered over the 4chPA to maximize homogeneity.

The Tx-only birdcage incorporated crossed diodes as a tuning/detuning mechanism during Tx/Rx operation, respectively, to decouple the Tx-only birdcage from the receive array coils. The crossed diodes were placed in each end ring segment of one end ring of the birdcage (Figure 40A). The diodes were forward biased to tune the Tx-only birdcage, and unbiased when the coil was detuned. When forward biased, the diodes presented a low DC resistance, thereby tuning the coil. When unbiased, the diodes on the birdcage end ring detuned the coil and resulted in high decoupling to the receive array during receive (>43 dB), allowing the birdcage to have very close proximity to the receive array (separated by ~35 mm) without deteriorating the receive array SNR. RF chokes ensured that the DC current had a complete path between the DC source and

ground. Both end rings of the birdcage had 15000 pF capacitors placed across a gap in the copper trace (Cb in Figure 40A), to reduce gradient-induced eddy currents on the end rings and to ensure that the DC current passed through all of the diodes.

The diodes allowed the Tx-only birdcage to be used in Tx-only, Rx-only, or Tx/Rx modes, depending on when the coil was DC biased. All of the SNR and imaging studies in this work used the coil in Tx-only mode, while one of the B_1 studies used the coil in Tx/Rx mode.

2.3.3.2.3 TR Switch

The TR switch incorporated a hybrid splitter (1J0280-3, Anaren, Inc., East Syracuse, NY, USA), circuitry to ensure 50 Ω connections to all hybrid ports during both transmit and receive with the birdcage, and an additional DC bias to actively tune the transmit coil (Figure 40B). The hybrid splitter had good isolation (20/27 dB Minimum/Typical) between the input and output ports when all the ports had 50 Ω connections. Two DC biases (DC1 and DC2 in Figure 40B) were forward biased only during transmit, activating the TR switch diodes that ensured the Tx signal went to the coil and not the preamplifier. A third DC bias (DC3 in Figure 40B) was used to provide positive current (+100 mA) to tune the local Tx-only birdcage to allow it to function as a Tx-only, Rx-only, or Tx/Rx coil.

2.3.3.2.4 Animal Positioning, Safety and Monitoring

An acrylic support structure was built so that the animal, coils, and monitoring equipment could be positioned outside the gradient system. The acrylic support consisted of a semicircular, half cylinder cradle that was attached to two circular end pieces (Figure

41). The cradle positioned the animal in a prone position at the center of the gradient magnetic fields and contained the animal within the setup if accidentally wakened. One end piece had a passage for the anesthetic and heating tubes, the coil, and the safety and monitoring cables to pass through (Figure 41). The other end piece had a 25 mm diameter hole so that the vaporized anesthetic and heated air had proper flow, while not being large enough for rats and guinea pigs to escape.

Isoflurane (Fluriso, Vet One, USA) was used for anesthesia for animal comfort and to reduce animal movement. The isoflurane was administered using a vaporizer (Matrx VIP 3000 Iso, Veterinary Anesthesia Systems, Inc., UT, USA). The animal was under full anesthesia before positioning occurred.

An MR-compatible monitoring and gating system (ERT Module 1030, SA Instruments, Inc., NY, USA) was used to monitor the animal's breathing, pulse rates, and temperature. The monitoring system contained a heater and fan module to keep the animal at 37 C. Since the monitoring cables passed near to the transmit RF coil in order to reach the extremities of the guinea pig, the cables were shielded and an RF cable trap was implemented to reduce common mode currents.

2.3.4 Studies

2.3.4.1 Phantom Imaging

A homogeneous, 36 mm diameter, cylindrical phantom with concentrations of 12 mM $CuSO_4$ and 150 mM NaCl was used for noise correlation, SNR and B_1 mapping tests. A resolution phantom with similar geometry was created with interleaved paper and plastic to test gradient performance.

Noise correlation measurements were done using a standard gradient echo (GRE)

sequence with the transmit voltage set to 0 V, setting the TE and TR to a minimum, and receiving with the 4chPA (18).

To test the effect of the 4chPA receive loops on transmit homogeneity, transmit flip angle (B_1) maps were obtained using the Tx-only birdcage for transmit and using the 1) Tx-only birdcage for receive and 2) the 4-channel array for receive. B_1 maps were obtained using the dual angle method (225) using a GRE sequence, with scan parameters: TR = 2500 ms, TE = 4.15 ms, FOV = 83x64x30 mm, voxel size = 0.64x0.64x3 mm, flip angle = 45°/90°, averages = 1, total scan time = 8.2 min. Acceptable homogeneity was deemed sufficient if there was less than 5° variation (211).

SNR maps of the 4chPA, Siemens wrist coil, and small birdcage were obtained using a GRE sequence, with the following scan parameters: TR = 2500 ms, TE = 4.15 ms, FOV = 83x64x30 mm, voxel size = 0.64x0.64x3 mm, flip angle = 90°, averages = 1, total scan time = 4.1 min. The SNR comparison studies were performed without the insert gradient. The 4chPA setup consisted of the acrylic supports, RF coils and RF shield. The SNR maps were obtained by normalizing the magnitude images by the standard deviation of the noise, and combining them through root-sum-of-squares.

To determine the benefit of composite gradient performance a resolution phantom was created using wet paper layered between plastic. Using paper soaked in water overcame surface tension that would have prevented water alone from entering between the plastic layers. The paper was initially measured at having a thickness of 80 μm when dry, but thickened to 120 μm after being soaked in water. Three thicknesses of plastic were interleaved with the wet paper, with the plastic layers measuring 120 μm, 80 μm, and 140 μm in three sections of the phantom. The interleaved plastic/paper was placed into a 36 mm diameter cylindrical phantom with 12 mM $CuSO_4$ and 150 mM NaCl.

Resolution phantom studies were performed using the 4chPA and a 3D fast low angle shot (FLASH) sequence with both the 1) body gradients only (40 mT/m), and 2) composite gradient mode (80 mT/m). The scan parameters were different between the two setups, as the scanner limited the scan parameters when using the body gradients only. The voxel size was matched exactly to determine the improvement in image contrast. In both setups, the TE was minimized and bandwidth was maximized, as this shorter TE and faster readout were the primary advantages of the composite gradient system, and an equal TE and readout would result in similar images (121). The imaging time was matched as closely as possible, although this study was a test of resolution and contrast, which relied on gradient performance and not SNR performance. The scan parameters for: 1) body gradient alone were TR = 20 ms, TE = 4.37 ms, FOV = 50x50x13.2 mm, voxel size = 150 μm isotropic, flip angle = 20°, averages = 3, pixel bandwidth = 128 Hz/pixel, total scan time = 21.3 min; and for 2) composite gradients were TR = 20 ms, TE = 2.22 ms, FOV = 40x40x13.2 mm, voxel size = 150 μm isotropic, flip angle = 20°, averages = 4, pixel bandwidth = 369 Hz/pixel, total acquisition time = 19.2 min. The resolution phantom images were interpolated to 75 μm isotropic voxel size to more clearly observe the separation between plastic/paper. Contrast-to-noise ratio (CNR) was calculated by subtracting the peak SNR from each strip of wet paper from the lowest SNR of the adjacent plastic strip on the image (31).

2.3.4.2 *Live Guinea Pig Imaging*

A live guinea pig experiment was performed to test and illustrate gradient performance and contrast/SNR improvements of the system. The study occurred with Institutional Animal Care and Use Committee approval. For this experiment, a male

308g guinea pig was scanned in vivo to observe the separation between the scala media and scala vestibule. 3D FLASH MR images with the composite gradient were obtained at 100μm isotropic voxel size with the following scan parameters: TR/TE = 20/3.1 ms, flip angle = 50°, averages = 5, pixel bandwidth = 241 Hz/pixel, total scan time = 32.9 min. In order to obtain enough SNR to observe the cochlear membranes with FLASH, gadolinium enhancement was used. Imaging occurred at a relatively high flip angle (50°) to improve signal from the inner ear, as the high concentration of gadolinium in the inner ear would have resulted in a low cochlear T_1. The flip angle used in this study was chosen empirically to maximize the signal, although further optimization is possible. Images were acquired 7.5 hours after gadolinium injection.

2.3.4.2.1 Gadolinium Enhancement

One ear of the rodent was injected with a gadolinium contrast agent (Multihance, Bracco Diagnostics, Inc., Monroe Township, NJ, USA) through the tympanic membrane. A 24 gauge flexible catheter tip (Insyte Autoguard Shielded IV Catheter, BD Medical, Sandy, Utah) was inserted into the external auditory canal and advanced through the tympanic membrane into the middle ear. Placement of the catheter tip within the middle ear was confirmed by tactile feedback (rupture of tympanic membrane or contact of hard bony medial wall of the middle ear). The second ear was not injected to obtain comparison images without gadolinium. The gadolinium was used to improve the SNR of T_1-weighted sequences by shortening the T_1 of surrounding tissue. The gadolinium was diluted with saline by a factor of four and approximately 0.4 mL was injected into the rodent ear.

2.4 Results

2.4.1 Coil Measurements (4chPA)

The change in loaded receive loop sensitivity ($|S_{21}|$) between tuned and detuned states was greater than 45 dB, when measured with two small decoupled magnetic probes. Loaded preamplifier detuning was 19.5 dB. The loaded isolation ($|S_{21}|$) between adjacent receive loops was greater than 14.7 dB. The isolation between the tuned birdcage and detuned receive loops was greater than 31 dB, and the isolation between the detuned birdcage and tuned receive loops was greater than 43 dB. The maximum and average off diagonal noise correlation coefficient was 0.27 and 0.17, respectively (Table 4).

2.4.2 Phantom Imaging

The flip angle of the Tx-only birdcage for the 4chPA without the receive array was 40±5°, showing reasonable homogeneity (Figure 42A). With the receive array inside the Tx-only birdcage, the flip angle was 41±4° throughout the signal giving region of the central slice (Figure 42B), and near the cochlea the flip angle was 44±1° (which was calculated within the outlined circle of Figure 42B). The flip angle was slightly less than the prescribed flip angle (45°) during B_1 mapping, due to the difficulty of determining an exact flip angle over a small imaging/coil volume during prescan calibration.

The SNR of the 4chPA (Figure 42C) had roughly 1.6 times the SNR of the small birdcage (Figure 42E) near the cochlear region (14 mm deep, marked with an "x" on Figure 42F), and 4 times greater near the surface coils (Figure 42F). The SNR performance of the 4chPA was superior to that of the other RF coils tested in this work so it was used for the animal studies.

The resolution phantom images are much more clear when using the composite gradient (Figure 43B) when compared to the body gradients alone (Figure 43A). The CNR between the water peak signals and the plastic minimums is on average double when using the composite gradient system (Figure 43C).

2.4.3 Live Guinea Pig Imaging

Images obtained using 3D FLASH at 100 μm isotropic resolution (Figure 44 & Figure 45) show a clear separation between the scala vestibuli and scala tympani. These chambers are primary indicators of the health of the inner ear. The FLASH images (Figure 44A) are hyperintense (bright) near the right middle ear cavity where gadolinium was injected (Figure 44B-D), and have reduced signal and contrast in the left cochlea that had no enhancement (Figure 44E-G).

Three orthogonal reconstructed magnified views (Figure 44B-D) of the right cochlea show magnified views, demonstrating the high resolution images obtained with gadolinium enhancement. An enlarged image (Figure 45) shows marked anatomical features, including the (1) modiolus, (2) scala vestibuli, (3) basilar membrane separating the inner ear chambers, and (4) scala tympani.

The coils were slightly rotated on the rodent during imaging, so that there is a slight asymmetry in the axial image (Figure 44A). Despite this rotation, the SNR near the cochlea appears unaffected.

2.5 Discussion

The goal of this work was to develop and evaluate a system consisting of an insertable gradient, RF coils and animal positioning hardware to enable imaging of the

internal structure of the cochlea and other inner ear structures of a guinea pig model at 3 T. The composite gradient enabled increased resolution imaging with roughly twice the CNR. The small animal array had better SNR for imaging the guinea pig cochlea (about 14mm deep) than the Siemens wrist coil (2.2x) and the small birdcage coil (1.6x). The primary advantage of the 4chPA over a volume coil was its ability to fit snugly over the rodent ears so that the coils were close to the imaging region to maintain high SNR. The 4chPA and composite gradient system were used in conjunction with the anesthesia and monitoring system, and allowed for easy, yet robust and repeatable, positioning of the RF coils, animal monitoring cables, and other equipment for optimal image quality and animal safety. Injected gadolinium contrast allowed visualization of the internal cochlear structures with FLASH image acquisition. The improved setup achieved in vivo 100 μm isotropic resolution images in 33 minutes for FLASH imaging, at 7.5 hours after gadolinium contrast injection.

Intravenous injection was considered in place of intratympanic injection. However, other unpublished results of the authors suggested that both the signal and contrast of the cochlear chambers are lower with intravenous injection. A study by Yamazaki (226) came to the same conclusion, after intravenous and intratympanic injections were done on subjects with Meniere's disease.

Many small animal imaging systems have much higher gradient performance than could be obtained with our composite gradient system; however, this system relied on the same gradient performance that can be obtained with our 3 T human system. Commercially available insertable gradients can provide the same gradient performance as the composite gradient for human imaging.

This work used FLASH imaging to demonstrate the hardware capabilities of the

system, although other sequences are also common for cochlear imaging, such as constructive interference in the steady-state (CISS) (208,209,213), fluid attenuated inversion recovery (FLAIR) (208,209), and turbo spin echo sequences with variable flip angles (VFE-FSE (213)). The advantage of a sequence with strong T_1-weighting, such as FLASH used in this work and FLAIR (208,209), is that it can be used to study gadolinium concentrations that change between cochlear chambers at different times between injection and imaging (212); the disadvantage is that gadolinium injection is very invasive (213). CISS can obtain high SNR images without gadolinium injection, but suffers from banding artifacts (213) that complicate image interpretation, so is used primarily for obtaining anatomical reference images (208,209). VFE-FSE has been used to obtain cochlear images without gadolinium injection, although it requires a homogeneous B_1 field and a long scan time that can limit high resolution images.

2.6 Conclusions

Improved imaging of the guinea pig inner ear on a clinical MRI system was achieved using composite imaging gradients, specially designed transmit and receive RF coils that operated within the composite gradients, in conjunction with an animal holder designed to operate in the reduced volume of the composite gradient system. 3D FLASH 100 μm isotropic resolution images of the cochlea were obtained with visualization of the inner ear anatomy in 33 minutes. The composite gradients doubled the CNR ratio when compared with the system body gradients. The composite gradients also allowed for higher resolution imaging than the system body gradients alone would allow. The 4-channel RF phased array obtained SNR that was double that of a small birdcage coil that was designed to fit over the animal shoulders. Simple and effective RF decoupling

techniques were demonstrated in the RF coils. Dynamic gadolinium enhancement improved the contrast of the separate cochlear chambers in FLASH imaging with many of the chambers visible 7.5 hours after injection. This combination of imaging and animal hardware was essential in obtaining the high-resolution images of a live guinea pig cochlea on the 3 T clinical scanner.

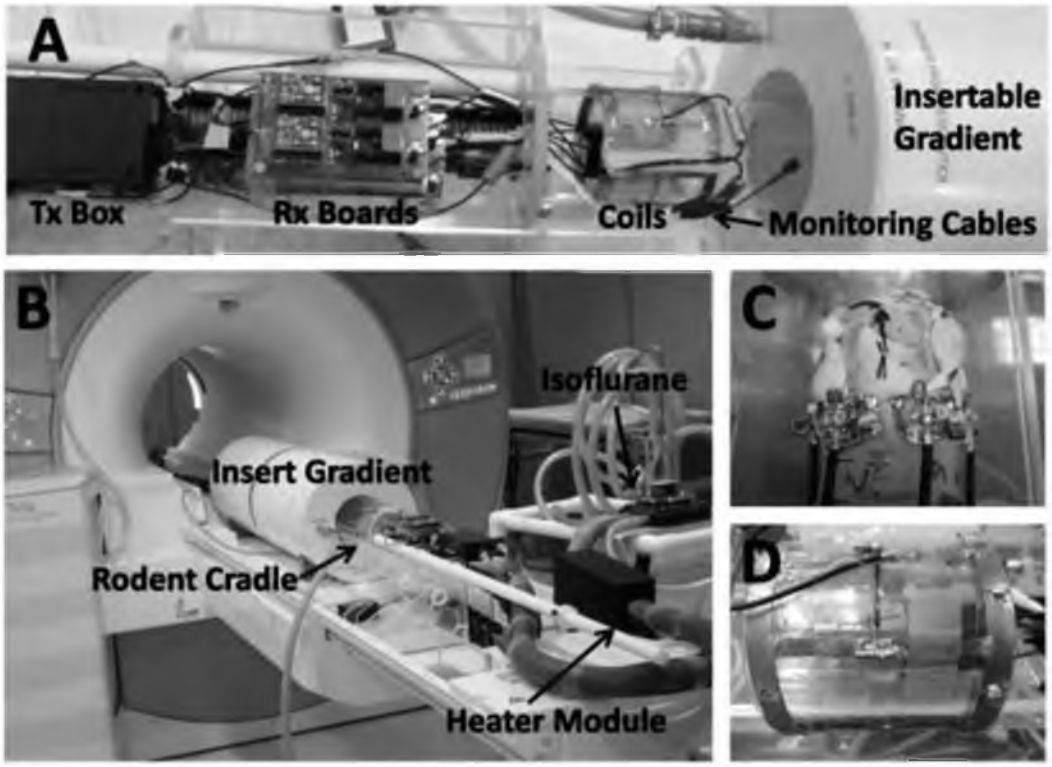

Figure 35. Small animal setup. (A) Top-down view of the insertable gradient and RF circuitry. (B) Picture of the entire setup. (C) RF receive coils with clay padded around them to hold them in position. (D) RF transmit coil.

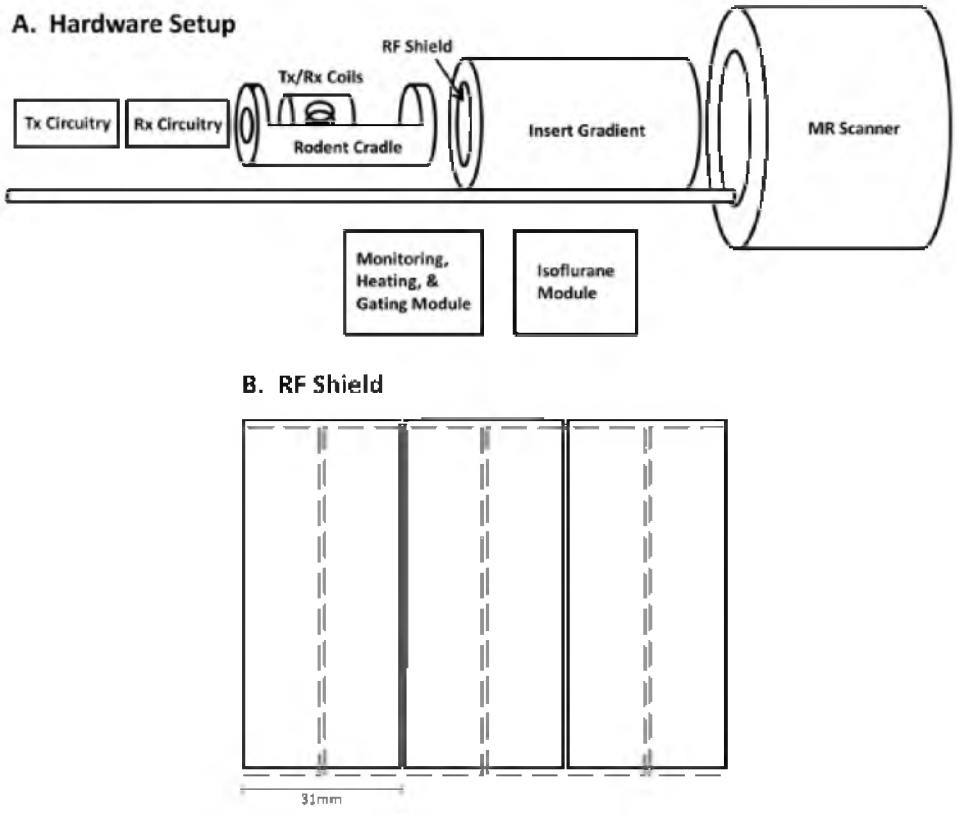

Figure 36. Illustration of the small animal setup. (A) Schematic showing the scanner, insertable gradient, RF coils, and monitoring equipment, prior to insertion into the scanner. (B) Schematic of the RF shield that lined the inner diameter of the insertable gradient.

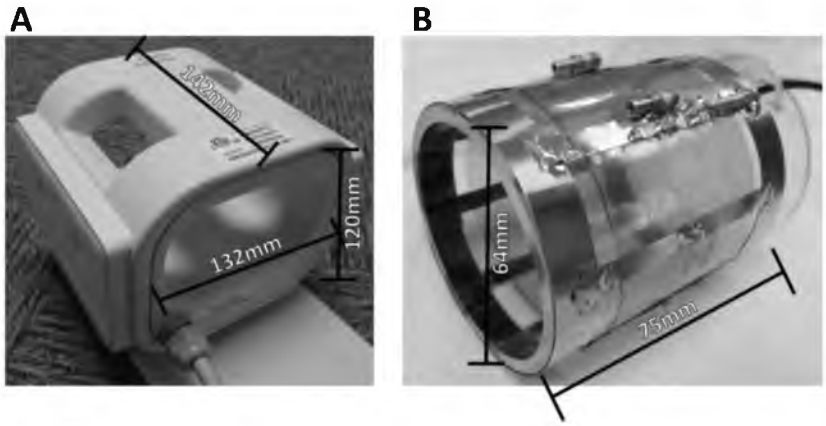

Figure 37. Two coils that were used for small animal imaging. (A) Siemens commercial wrist Tx/Rx coil and a (B) small Tx/Rx birdcage coil used for SNR comparisons with the phased array. The wrist coil (A) was 132 mm wide, 120 mm tall, and 142 mm wide. The small birdcage (B) had 8-rungs, was 75 mm long, and had a diameter of 64 mm. A smaller Tx/Rx birdcage would have excluded the inner ear anatomy from the sensitive central region of the coil.

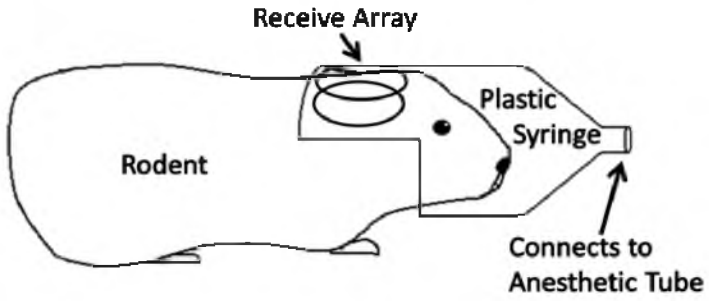

Figure 38. Schematic of the rodent with the receive array placed over its ears. The needle end of the syringe was connected to a tube delivering anesthetic to the rodent.

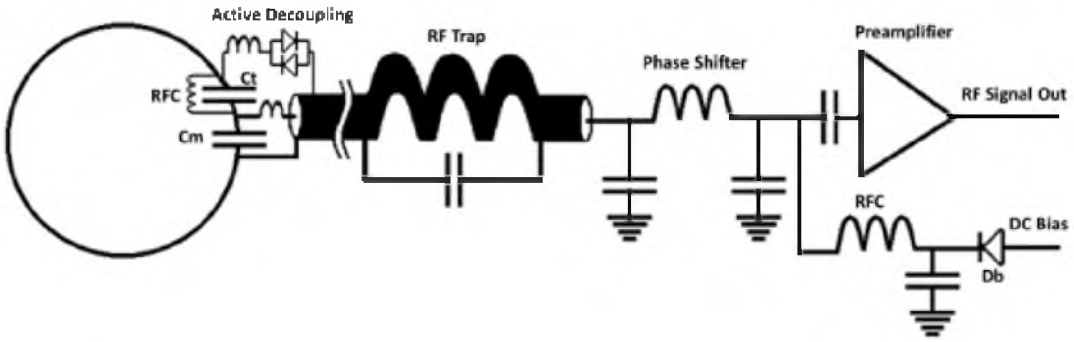

Figure 39. A single receive coil schematic. Schematic for a single receive coil in the 4-channel phased array, showing the location of the capacitors, decoupling circuitry, and necessary components between the coil and the preamplifier.

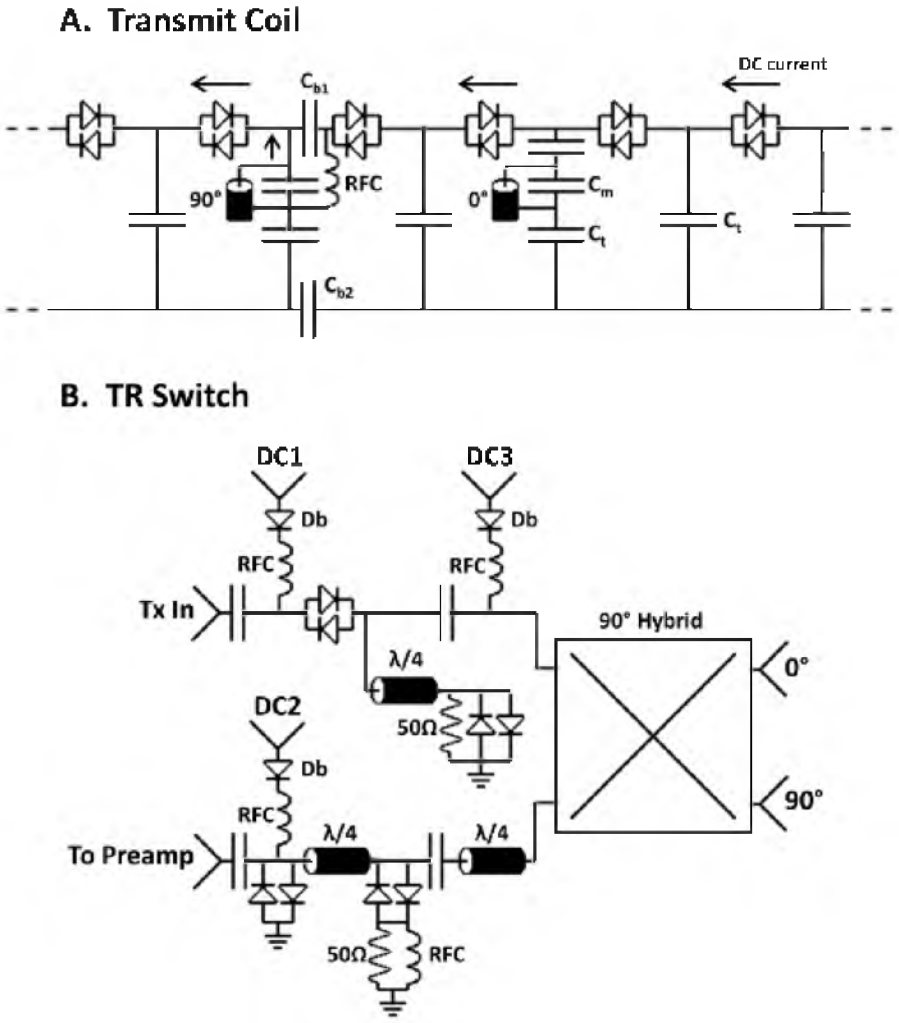

Figure 40. Transmit coil circuits. (A) Schematic of the RF transmit coil and the decoupling method employed. The reverse diode pairs are forward biased to tune the transmit coil, and unbiased to detune it. A DC blocking capacitors (CB_1) and RF choke (RFC) ensure that DC current passes through all of the reverse diode pairs to ground. A second DC blocking capacitor (Cb2) reduces eddy currents in the end ring. (B) Schematic of the TR switch used for the transmit coil. DC1 and DC2 are forward biased during transmit. The circuitry enables a 50 Ω connection to the hybrid ports during both Tx/Rx. The quarter-wave length circuits at the isolation port of the hybrid add additional protection to the preamplifier if too much power is received on that port. The diodes connected to DC bias line (Db) remove the negative DC bias provided by the scanner and are protected from high RF power by the RF chokes.

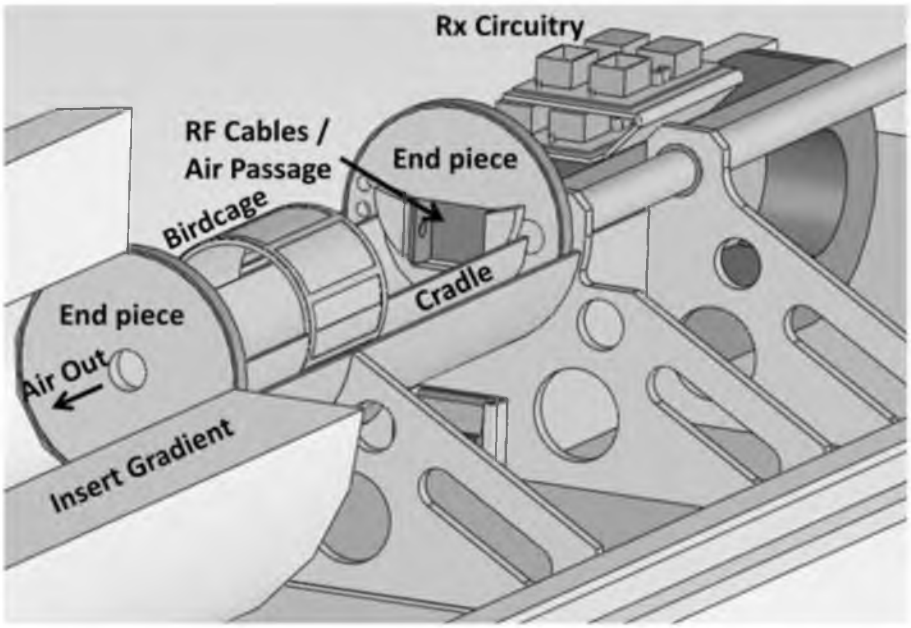

Figure 41. Acrylic structure model. Model of the acrylic structure used for positioning of the rodent and hardware.

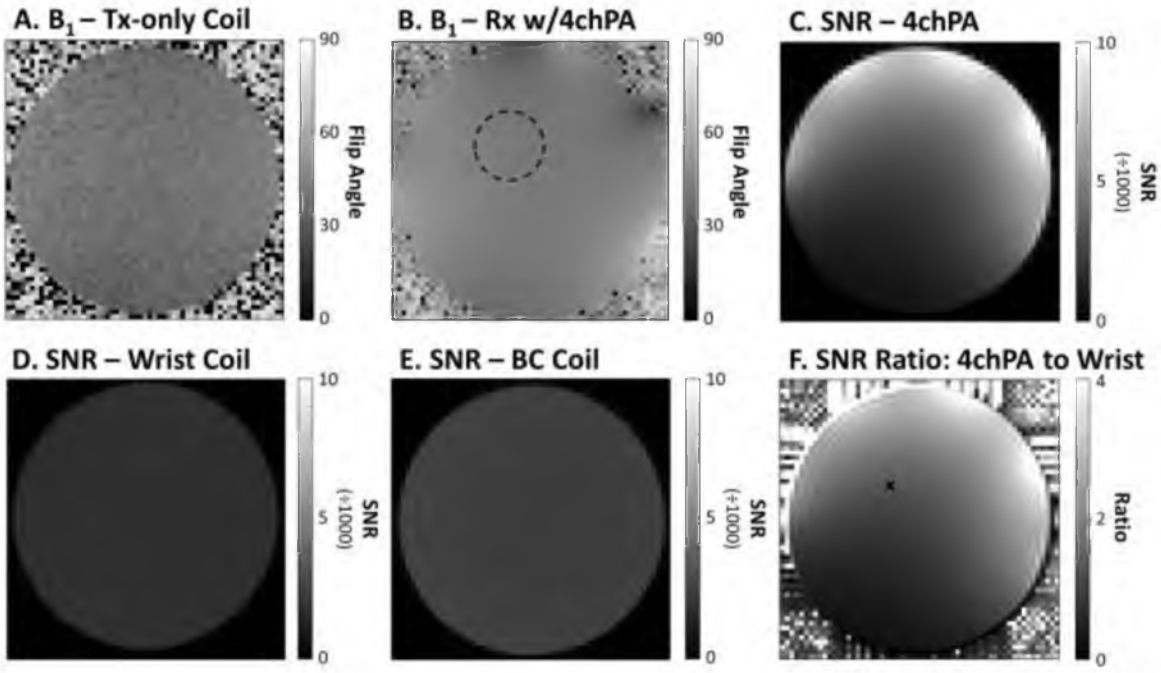

Figure 42. SNR and B_1 maps of rodent coils. (A) Transmit B_1 map of the Tx-only birdcage for the 4chPA when used for both Tx and Rx, with the RF phased array not in the Tx-only coil. (B) Transmit B_1 map of the Tx-only birdcage for the 4chPA when the RF phased array is used for Rx and located inside the birdcage. Within the outlined circle, the flip angle was 44±1°. SNR maps of the (C) RF phased array, (D) Siemens wrist coil, and (E) small birdcage. (F) SNR Ratio between the phased array and small Tx/Rx birdcage. An "x" marks the location where the cochlea is expected, about 14mm deep.

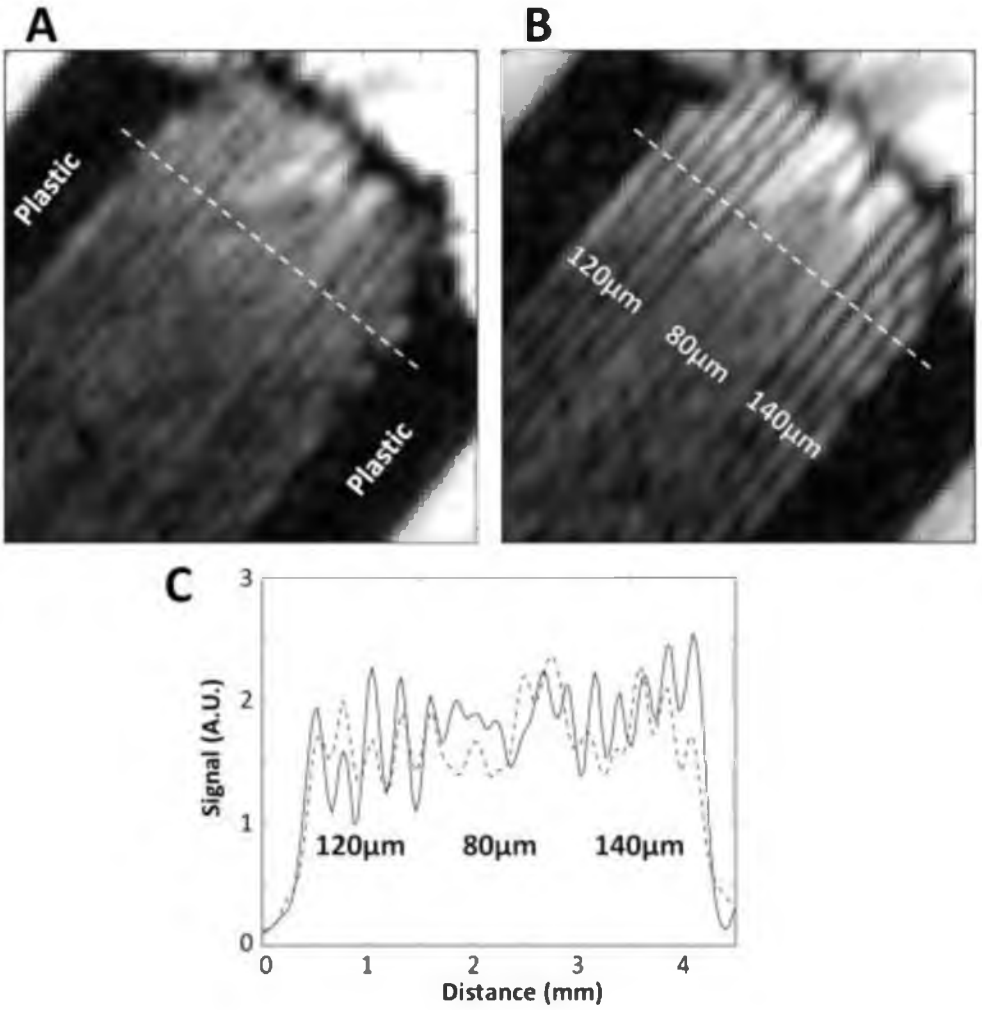

Figure 43. Resolution comparisons. Images of a resolution phantom obtained with the (A) body gradients only and with the (B) insertable gradient. The resolution phantom had 120 μm thick sheets of wet paper interleaved with plastic sheets of 120 μm, 80 μm, and 140 μm thicknesses. (C) Plot through the phantom of signal obtained using the body gradient (dashed) and composite gradient (solid) systems. The dashed white line in (A) and (B) indicates the region where the (C) signal was plotted. The widths of the interleaved plastic sheets are indicated on the figures (120 μm, 80 μm, and 140 μm).

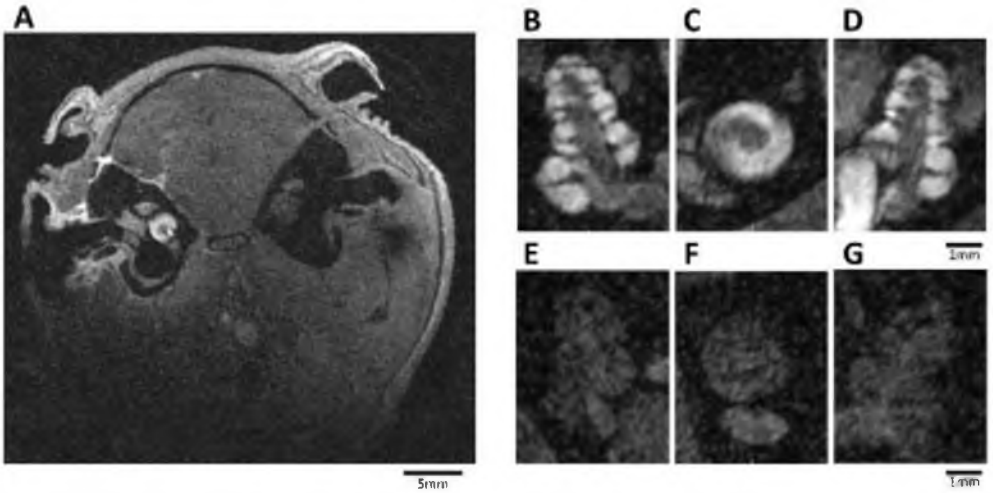

Figure 44. Images of the rodent cochlea. Axial plane image (A) of the entire guinea pig head. Note that only the right middle ear cavity had gadolinium injected. B-D: Three orthogonal reconstructed magnified views of the right cochlea. E-G: The left middle ear cavity was not injected and remains unenhanced with poor CNR.

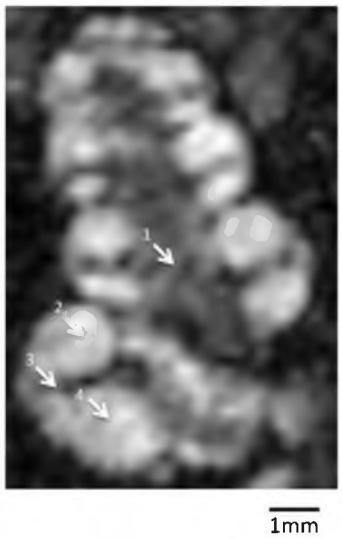

Figure 45. Enlarged image of a cochlea. Enlarged cross sectional image from a live guinea pig through the right cochlea 7.5 hours after gadolinium injection. The arrows mark the (1) modiolus, (2) scala vestibuli, (3) basilar membrane, and (4) scala tympani.

Table 4. Noise correlation matrix of the RF receiver coils.

Coil	1	2	3	4
1	1.00	0.15	0.12	0.29
2	0.16	1.00	0.17	0.15
3	0.12	0.17	1.00	0.12
4	0.30	0.15	0.12	1.00

CHAPTER 3

AN APPARATUS FOR IN VIVO OXYGEN PROBE MEASUREMENTS DURING RENAL BOLD MRI

This chapter is based on an unsubmitted technical note titled, *"An Apparatus for In Vivo Oxygen Probe Measurements During Renal BOLD MRI,"* authored by Joshua D. Kaggie, Vivian S. Lee, and Glen R. Morrell. The technical note will soon be submitted to an appropriate journal.

3.1 Abstract

3.1.1 Purpose

The goal of renal BOLD MRI is to evaluate renal tissue oxygen tension (pO_2) based on T_2* maps. Many factors affect T_2* besides renal tissue pO_2 and must be accounted for in pO_2/T_2* signal models. Simultaneous renal BOLD MRI and measurement of renal pO_2 with invasive probes is a powerful tool to investigate the relationship of renal pO_2 to BOLD T_2* maps. We present a new technique for simultaneous renal BOLD MRI and invasive pO_2 measurement in pig kidneys.

3.1.2 Methods

Fiberoptic probes were inserted into pig kidneys through a plastic sheath, which was placed percutaneously over a needle with real-time ultrasound guidance. Renal BOLD MRI was performed while continuous oxygen measurements were obtained from the probes using a custom real-time data logging system. Intravenous furosemide was administered to cause alterations in renal pO_2. Changes in T_2* maps from renal BOLD scans were correlated with changes in oxygen probe measurements.

3.1.3 Results

The fiberoptic system was visible on MRI images, which allowed determination and optional adjustment of probe location. Changes in medullary oxygenation measured by probe mirrored changes in T_2* measured by renal BOLD MRI. Continuous real-time oxygen probe measurement also revealed second-by-second variations in medullary pO_2 caused by bladder filling and short periods of apnea, which have previously unconsidered implications for estimation of renal pO_2 from renal BOLD MRI data.

3.1.4 Conclusion

A system for real-time measurement of renal pO_2 during renal BOLD MRI has been developed for in situ evaluation of pig kidneys, which correlated with T_2* and elucidated previously unknown causes of renal pO_2 changes.

3.2 Introduction

Chronic kidney disease (CKD) affects more than 20 million people in the United States, and more than 10% of the world's population (227,228). Renal parenchymal

hypoxia is thought to play a central role in the progression of CKD (229). Oxygen tension (pO_2) varies within the normal human kidney by roughly 30 mmHg between the cortices and medulla (230). Medullary pO_2 can decrease due to indicators of CKD, such as diabetes (231) and low hematocrit (232), but can increase due to urinary obstruction (35); cortical pO_2 may decrease due to diabetes (231), low hematocrit (232), and urinary obstruction (35). Despite the importance of renal hypoxia in the progression of CKD and the potential for therapeutic intervention for CKD treatment, no satisfactory noninvasive method exists for evaluating renal hypoxia.

Renal BOLD MRI has been proposed as a means of investigating renal hypoxia (35-43). Renal hypoxia is expected to cause higher deoxyhemoglobin concentration, which would be reflected in decreased T_2* values (94) on renal BOLD T_2* maps. Many factors besides deoxyhemoglobin contribute to T_2*, including inhomogeneities caused by contrast agents, iron deposits and air-tissue interfaces (such as frequently occur in the intestines). Whether BOLD MRI, with or without diuretic challenge, reflects the severity of CKD remains an open question (233,234). In order to estimate hypoxia from T_2* data, all factors affecting T_2* must be modeled and accounted for (235). Invasive measurements of kidney pO_2 are essential to develop and calibrate these models.

Initial porcine studies have been performed to calibrate BOLD MRI with in situ oxygen measurements using Clark-type electrode probes (35,36). Clark electrodes (236), unfortunately, disturb the local environment by constantly depleting oxygen in the sample, result in increased susceptibility artifacts due to their metallic nature, require calibration with an oxygen-free medium, and require constant stirring for accurate measurements. In addition, kidney exposure and nonsimultaneous measurements could result in differences between the measured pO_2 and associated MRI BOLD experiments.

In Warner's study (36), pO_2 measurements were performed a week after the MRI BOLD study, which could result in significant physiological differences. In Pedersen's study (35), pO_2 measurements from an exposed kidney were interleaved with BOLD MRI measurements opposite to the exposed kidney, to avoid artifacts introduced from the probe. However, despite these challenges, these studies (35,36) demonstrated a correlation between pO_2 and T_2* that is very encouraging.

Only very recently has the combined use of an invasive, nonmetallic, fiberoptic oxygen probe used in concert with noninvasive MRI for renal evaluation been demonstrated and evaluated with MR-PHYSIOL (237). The experiments with MR-PHYSIOL (237) compared hypoxia and hyperoxia in rats by using varied oxygen content in the inhaled gas mixture. During the experiment, T_2 maps and T_2* maps were acquired 5 minutes apart and the pO_2 data were logged continuously (at 1Hz). The results of those studies showed good correlation between renal pO_2 and T_2 (and T2*) in the cortex, and some correlation in the medulla. Further investigation with MR-PHYSIOL using 21 different rats showed that the relationship between T_2* qualitatively mirrored pO_2 during hypoxia, hyperoxia, and aortic occlusion, but the quantitative correlations were weak (238).

This work demonstrates the techniques and early results of invasive pO_2 measurements at our institution and their correlation to BOLD MRI using a porcine model. To our knowledge, ours is the first report of simultaneous invasive oxygenation measurements and renal BOLD MRI in pig kidneys in situ. This work has been performed with T_2* measurements with temporal resolution (~1 minute) faster than has been achieved previously (35,36,237,238) to help correlate renal pO_2 and T_2* measurements. The continuous logging of pO_2 data has also resulted in unique,

previously unobserved, physiological effects on renal pO_2. We share our technical methods that have achieved excellent agreement in tissue oxygenation, under varying physiologic conditions, between BOLD MRI and the invasive reference probe.

3.3 Methods

3.3.1 Oxygen Probe Measurement System

A 7 cm 8.0 Fr. paracentesis catheter (Cook Medical, Blomington, IN) was placed percutaneously into a porcine kidney under ultrasound guidance (Figure 46A,B). The catheter needle was advanced to the desired location of the probe tip, and then both needle and catheter were withdrawn 5 mm, which was the length that the fiberoptic tip extended beyond the catheter. The needle was then removed from the catheter while a small quantity of saline was infused to prevent the formation of air bubbles in the catheter and reduce susceptibility effects of air within the catheter. A bare tipped fiberoptic pO_2 probe (Oxylite, Oxford Optronix, Oxford, UK) was inserted through the catheter. The probe and catheter were attached to each other by a Luer lock fitting, which ensured that the probe tip extended exactly 5 mm beyond the end of the catheter.

The catheter and probe were then immobilized by a small custom clamp placed on the exposed portion of the paracentesis catheter sewn onto the skin of the pig (Figure 46C). The clamp was developed to reduce the movement of the probes when moving the pig from the surgery table to the scanner table, or the movements that resulted from the pig breathing. The clamp was created from PLA plastic using 3D computer-aided design (SolidWorks, Dassault Systèmes SolidWorks Corp, Massachusetts, USA) and rapid prototyping with a 3D printer (CubeX Duo, Cubify, 3DSystems Inc., Rock Hill, SC, USA). The clamp was padded with thin polyurethane foam (86225K51, McMaster-Carr,

Santa Fe Springs, CA, USA) so that the probe could be securely clamped without being damaged. Another custom 3D printed part covered the system so that MRI coils could be placed over the kidney without disturbing the oxygen probe or clamp (Figure 46D).

The oxygen probe was then connected through a long fiberoptic cable to an oxygen measurement system (OxyLite Pro, Oxford Optronix Ltd., Oxford, UK) outside the scanner that interpreted the probe measurements, provided real time information, with outputs for a data acquisition device to permanently record data. The oxygen measurement system had a serial connector that output a voltage proportional to the oxygen sensor levels. The voltage was then collected by the additional data acquisition device, which consisted of an Arduino (Arduino Uno, Adafruit, New York, New York) that connected through a USB to a computer. The computer used a custom Python program developed to acquire and permanently save the real-time data for later analysis.

The method for placement of oxygen probes into the pig kidney was developed and refined in a series of experiments on five pigs that were used for unrelated invasive cardiac MRI studies. These pigs were sacrificed after unrelated cardiac studies; we used them before sacrifice to refine our method of probe placement and securement. All experiments were performed with the approval of the local Institutional Animal Care and Use Committee. The pigs were under general anesthesia for the entire experiments. Renal BOLD data from these initial five pigs were not valid, as the pigs had received a large load of gadolinium contrast in the earlier unrelated experiments, which severely affected T_2* relaxation. However, after the probe placement technique had been refined with these five experiments, a sixth experiment was performed on a pig that had not undergone previous contrast injection. Probe pO_2 data and renal BOLD T_2* data presented in this manuscript are from this sixth pig, from a probe which was observed to

be in the renal medulla.

3.3.2 MRI Study

After placement of the oxygen probe, the pig was moved into the scanner. Renal BOLD images were acquired with the following scan parameters: TR = 80 ms, TEs = 5,10,15,20,25,30 ms, flip angle = 25°, matrix = 256x256x1, voxel size = 0.78x0.78x8 mm, FOV = 200x200x8 mm, averages = 1, with a total scan time of 20 seconds. Initial BOLD images were obtained to confirm that the probe was in the proper position and to evaluate the robustness of the oxygen measurements. After a sufficient baseline was acquired, 20 mg of furosemide (Hospira Inc., Lake Forest, IL, USA) was injected intravenously. BOLD images were taken roughly twice per minute after furosemide injection. During each 20 second BOLD image acquisition, the respirator was stopped so that kidney motion was minimized.

The r-value correlation coefficient and p-value against the null hypothesis were calculated to evaluate the correlation between the oxygen probe measurements and T_2* measurements. The oxygen probe correlations were calculated using a pO_2 measurements averaged for 20 seconds, as the time resolution of the T_2* measurements (20 seconds) was much lower than that of the oxygen probe that recorded pO_2 once per second. A region-of-interest (ROI) within the kidney surrounding the oxygen probe tip was defined on the renal BOLD images for analysis, as indicated by the white dotted outline in Figure 47A.

3.4 Results

A BOLD first-echo source image and T_2* image are shown in Figure 47. The simultaneous pO_2 and T_2* measurements are shown in Figure 48. Correlation calculations between the pO_2 and T_2* measurements for all 8 measurements gave an r-value and p-value of 0.59 and 0.12, respectively.

While the correlation between pO_2 and T_2* is interesting, the results of the continuous pO_2 probe measurements, shown in Figure 49, are more notable. Oxygen tension was initially steady, prior to the furosemide study (Figure 49A). An immediate decrease (<1 second) in pO_2 was observed whenever the animal underwent apnea, which lasted for 20 seconds in our BOLD studies, although other slightly longer measurements and incomplete studies are shown in the continuous data. (Apneic periods are marked with dark gray horizontal lines at the bottom of the graphs in Figure 49.) After furosemide injection, the renal medulla experienced a decrease in oxygen levels due to an apneic period, but the baseline oxygen level consistently increased (Figure 49B). After 15 minutes, the oxygen levels returned to normal. The pO_2 difference from furosemide injection was similar to the pO_2 change before and after the animal bladder was drained (~6 mmHg) (Figure 49B,C). When gadolinium was injected, pO_2 sharply and significantly increased for a short period of time (Figure 49D). Touching or moving the animal also resulted in slight changes in pO_2.

Oxygen saturation of venous blood in the pig's ear measured with a pulse oximeter did not show any change in saturation over these short periods of apnea.

A picture of the sectioned kidney confirmed that the fiberoptic probe was inserted into the medulla (Figure 50).

3.5 Discussion

While many studies have tried to determine the usefulness of BOLD imaging in CKD, these results indicate that there may be many confounding factors to using T_2* measurements to estimate oxygen levels to assist indication of CKD. Similar to the other invasive renal studies (35,36,237,238), our results show a correlation between T_2* and pO_2. Unlike other invasive porcine studies (35,36), our probes were minimally invasive and were able to acquire data truly simultaneously from the same kidney that the probe was inserted into. We showed a correlation between pO_2 and T_2* similar to rodent measurements with MR-PHYSIOL (237), although our data were acquired with a porcine model with higher temporal resolution.

Continuous monitoring of probe data during a period of almost three hours revealed many second-by-second changes in medullary pO_2 due to unexpected factors. For instance, the effects of apnea and bladder urine volume on pO_2 have not been previously demonstrated. There was a drop of about 2.5 mmHg in medullary pO_2 when respiration was suspended for a 20 second renal BOLD MRI scan. This drop occurred immediately (<1 second) after apnea, and pO_2 returned to normal roughly 8 seconds after respiration resumed. Since the time course of the observed change in medullary pO_2 is too rapid to reflect actual changes in blood pO_2, we hypothesize that an autonomic nervous system mediated phenomenon may decrease medullary pO_2 transiently during breath-holding. Similarly surprising is the significant effect of bladder filling and emptying on renal medullary pO_2. Removal of a few hundred mL of urine from the pig bladder caused a decrease in medullary pO_2 of around 6 mmHg, which is similar to the magnitude of change caused by administration of furosemide. Further studies are required to assess a more accurate correlation and to determine all of the confounding

factors on T_2* / pO_2 correlations.

Another notable point is that the return to baseline pO_2 occurs about 15 minutes after injection of furosemide, which suggests that T_2* measurements after furosemide should occur consistently at the same time after furosemide is administered.

The T_2* maps are poor partly due to the lower SNR caused by extra distance between the receive coils and the kidneys, as the coils were distanced further from the pig body than typical to accommodate the probes. B_0 inhomogeneities caused by air in the gut also decreased the quality of the T_2* maps. The authors believe that porcine studies may result in more consistent results than rodent studies, as pigs have kidneys much nearer to function and size to humans, and the increased size of the porcine kidney will result in better B0 homogeneity and reduced renal damage from probe insertion.

3.6 Conclusions

We have presented a method of simultaneous measurement of renal oxygenation with invasive probes and renal BOLD MRI in pig kidneys. Previous studies on pig kidneys required dissection of the kidney for probe placement and did not allow true simultaneous pO_2 measurement and BOLD MRI. Our method is minimally invasive, with percutaneous placement of probes through catheters into the kidney, and with true simultaneous acquisition of MRI data. This method can be a powerful tool to investigate the relationship of renal T_2* with oxygenation levels to provide essential data to calibrate pO_2 estimation models based on T_2*. The similarity of pig kidneys to human kidneys in terms of size and anatomic structure suggests that these data may be useful for non-invasive modeling of human kidney oxygenation based on renal BOLD. Our experiments also reveal potential confounding factors in BOLD MRI which have not

been previously described, including immediate changes in medullary pO_2 with breath-holding, and strong dependence of medullary pO_2 on bladder urine volume. The combination of MR techniques and invasive measurements (35,36,237,238) appears very promising in improving the interpretation of BOLD MRI for evaluating disease.

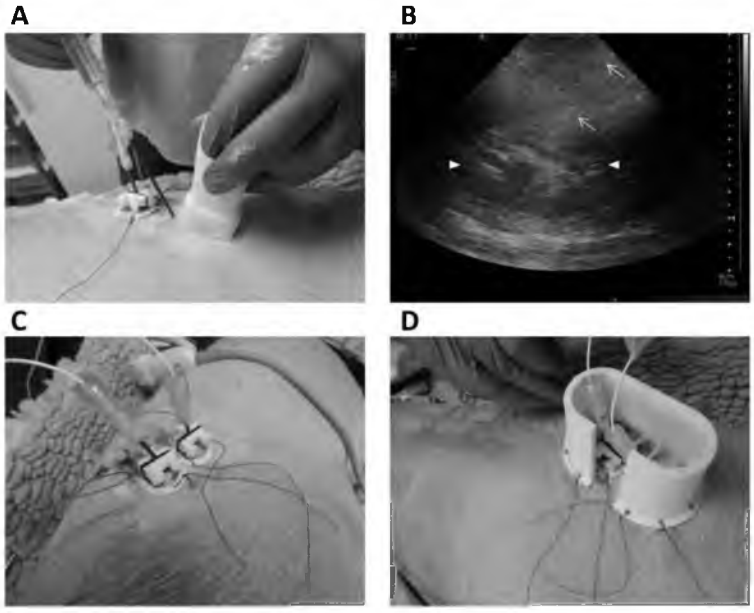

Figure 46. Images showing the insertion probes into a kidney. (A) The insertion of the metallic needle and plastic sheath is shown, with guidance from an ultrasound probe. (B) A typical ultrasound image showing the kidney (between the horizontal triangles) and the probe (indicated with arrows). (C) Two fiberoptic probes shown in position in the pig kidney. The plastic sheaths were clamped down by 3D printed parts that were sewn onto the pig. (D) A 3D printed cover protected the probes and their position, so that coils could be placed near the kidneys, just above the probes.

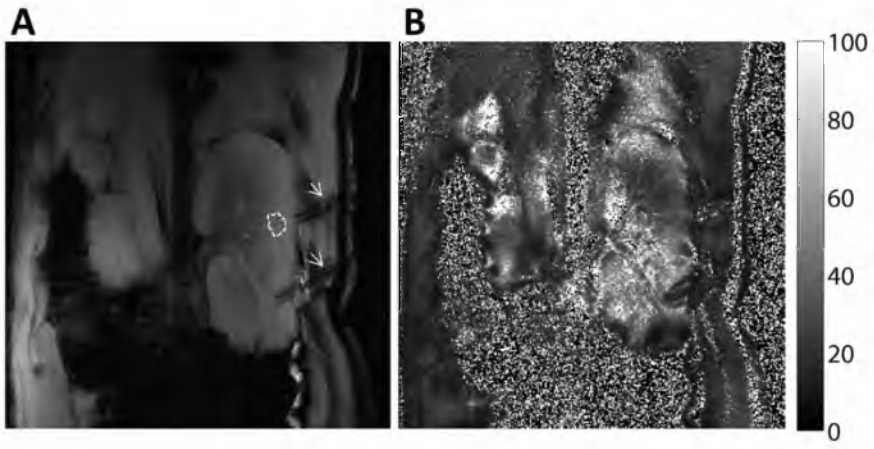

Figure 47. MRI-derived images showing the probe location. The plastic sheaths (marked with arrows) that the oxygen sensor probes passed through are shown on the (A) VIBE images and the (B) first TE of the renal BOLD images. (C) A T_2* map of the same region.

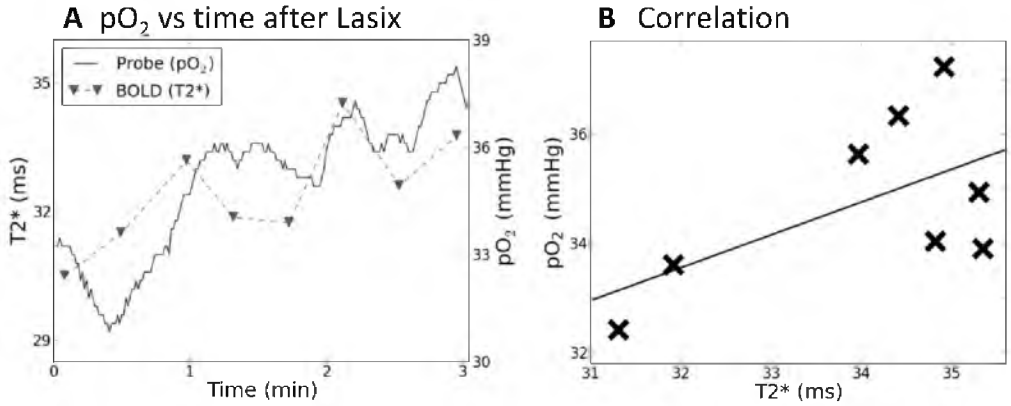

Figure 48. Changes in T2* and pO_2 with furosemide. (A) T_2* and pO_2 measurements against time. The downward triangles indicate the measured T_2* values. The solid line indicates the measured pO_2 values with the probe. (B) pO_2 versus T_2*. The solid line shows the linear fit.

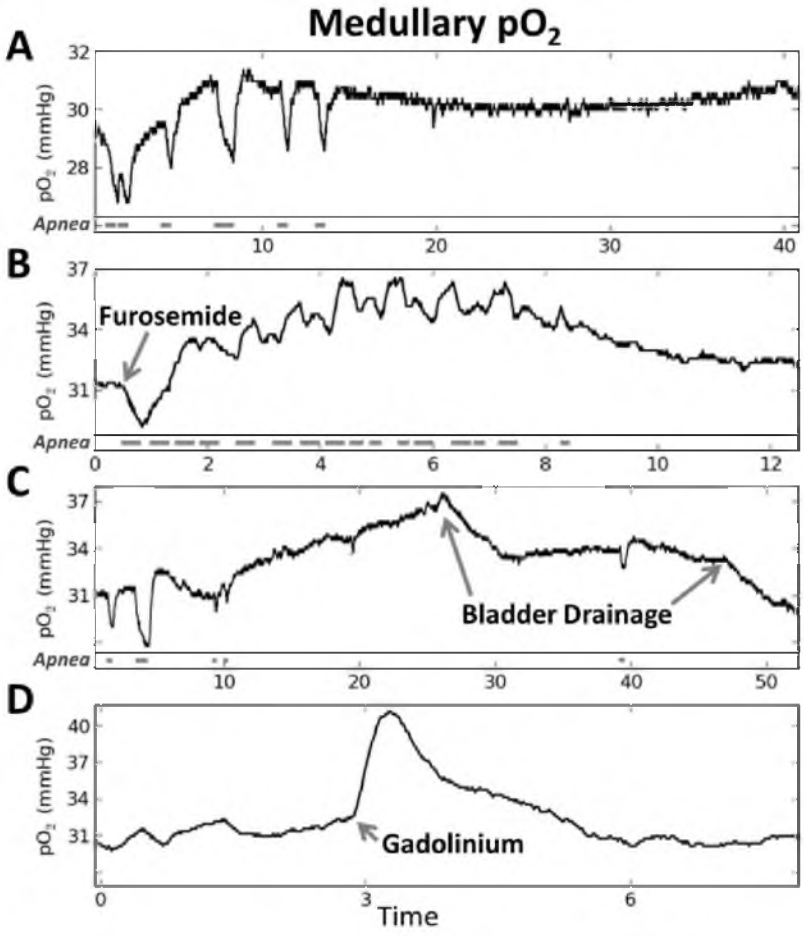

Figure 49. Excerpts from continuous pO_2 measurements throughout this study. The gray horizontal bars at the bottom of the graphs indicate periods where apnea occurred. (A) Time course during breath-hold BOLD measurements and during free-breathing. Medullary pO_2 was constant here when apnea did not occur. (B) pO_2 increase after intravenous administration of furosemide. The image shows many pO_2decreases due to apnea for BOLD MRI and other acquisitions. (C) Bladder pressure increased pO_2 levels, while bladder drainage decreased pO_2. (D) The injection of gadolinium resulted in a sharp increase and decrease in pO_2.

Figure 50. The sectioned kidney. A picture of the sectioned kidney confirmed that the fiberoptic probe was inserted into the medulla (marked with the arrow).

CHAPTER 4

RELATIVE SIGNAL LOSS FROM FAT USING IN- AND OUT-OF-PHASE IMAGES FOR INDICATING RENAL HEALTH

This chapter is based on an unsubmitted paper titled, *"Relative Signal Loss from Fat Using In- and Out-of-phase Images for Indicating Renal Health,"* authored by Joshua D. Kaggie, Vivian S. Lee, and Glen R. Morrell. The paper will soon be submitted to an appropriate journal.

4.1 Abstract

4.1.1 Purpose

The presence of renal lipid deposits has been associated with kidney disease. However there have been differences in animal and laboratory models. Lipotoxicity may result in CKD either directly from within the kidneys or indirectly from effects external to the kidney, such as systemic inflammation, oxidative stress, hormonal changes, and vascular injury. A recent diabetic mouse model used MRI with spectrally selective excitation to show an increase in cortical fat in diabetic kidneys compared to normal controls. This work attempts to determine the correlation between renal fat content and indicators of kidney disease and general health, such as eGFR, urine protein, serum

cystatin C, and BMI.

4.1.2 Methods

In-phase and out-of-phase axial T_1-weighted images were obtained through the kidneys of 200 subjects, and regions-of-interest were drawn around the kidney, liver, cortices, and medulla. The R^2 correlation coefficient was calculated for the renal fat content versus eGFR, urine protein, serum cystatin C, and BMI.

4.1.3 Results and Conclusion

The R^2 correlation coefficients showed no correlation between the renal fat content and indicators of renal and general health, across a range of etiologies.

4.2 Introduction

Diabetes has been linked to an increased risk in end-stage renal disease (ESRD) (239). The presence of renal lipid deposits has been associated with diabetic kidney disease (240) and fatty acids have demonstrated to contribute to the progression of chronic kidney disease (CKD) (241-243). While lipotoxicity has been demonstrated to result in renal damage, differences in animal and laboratory models have varied (45). Lipotoxicity may result in CKD either directly from within the kidneys or indirectly from effects external to the kidney, such as systemic inflammation, oxidative stress, hormonal changes, and vascular injury (45). A recent diabetic mouse model used MRI with spectrally selective excitation to show an increase in cortical fat in diabetic kidneys compared to normal controls (46). The applicability of these models in humans remains to be established (45).

This study raises the possibility that quantification of renal fat might be useful to assess CKD severity in humans. This study was done using retrospective data from 200 human subjects with varying degrees of renal failure ranging from normal renal function to dialysis dependence.

In- and out-of-phase T_1-weighted images were used to determine renal fat content using a 2-point Dixon method (244). While other methods exist for determining fat content, such as IDEAL (92) or 3-point Dixon methods (90), as well as chemical shift-selective imaging (46), these T_1-weighted images are obtained clinically at our institution, which enabled a large sample size through retrospective analysis.

The correlation between fat content measured with the in-phase/out-of-phase images and estimated glomerular filtration rate (**eGFR**) or the body mass index (**BMI**) was investigated.

4.3 Methods

In-phase and out-of-phase axial T_1-weighted images were obtained through the kidneys of 97 subjects (ages 18 to 81, roughly half on dialysis) in a retrospective study approved by the institutional review board. These images are routinely collected at our center as part of abdominal health evaluations. Data were collected from both 1.5 T and 3.0 T scanners. Because the study was retrospective, similar scan parameters were not possible across the entire patient population. Typical scan parameters at 1.5 T were: TR = 130 ms, TE_1 = 2.17 ms, TE_2 = 4.48 ms, flip angle = 70°, matrix size = 512x416, FOV = 380x310 mm, slice thickness = 6mm; and at 3.0 T were: TR = 163 ms, TE_1 = 3.5 ms, TE_2 = 7.0 ms, flip angle = 70°, matrix size = 240x320, FOV = 380x310 mm, and slice thickness = 5 mm.

A central kidney slice was chosen and multiple regions-of-interest (ROI's) were drawn on that slice 1) around the entire kidney, 2) around potential cortical regions, 3) around potential medullary regions, and 4) in the liver. When differentiation of the cortical and medullary regions was not clear in subjects, such as those patients with severe renal disease (245), small regions were selected near the kidney capsule for likely cortical regions. Multiple likely cortical and medullary regions were selected within each kidney to increase the number of voxels used in the statistics.

The relative signal loss from fat (**FAT**) is defined as the magnitude signal from the in-phase image minus the out-of-phase image, over the in-phase image:

$$\left(\left[\text{In}-\text{Phase}\right] - \left[\text{Out}-\text{of}-\text{phase}\right]\right)/\left[\text{In}-\text{phase}\right]. \tag{1.74}$$

A sample out-of-phase image and FAT image is shown in Figure 51. FAT was compared with eGFR, BMI, serum cystatin C, and urine protein to observe any statistical correlations. Serum cystatin C was collected on ~50 subjects and urine protein was collected on most subjects. BMI was calculated using the relation:

$$\text{BMI} = \frac{\text{weight (kg)}}{\text{height}^2(\text{m}^2)}. \tag{1.75}$$

eGFR was calculated using the following relation:

$$\begin{aligned}\text{eGFR (mL/min/1.73 m}^2) = 175\ (\text{Scr})^{-1.154}(\text{Age})^{-0.203}\times \\ (0.742 \text{ if female})\times(1.212 \text{ if African American})\end{aligned}, \tag{1.76}$$

where Scr is the serum creatinine.

FAT was plotted against the eGFR and BMI for the four ROI's, and the R^2 correlation was calculated. The R^2 correlation was calculated for all subjects, for healthy subjects, and for diabetic subjects.

4.4 Results

The plots of FAT versus eGFR (Figure 52), serum cystatin C (Figure 53), urine protein (Figure 54), and BMI (Figure 55) are shown, with trend-lines that show a fit for all subjects. The diabetic subjects are shown with downward pointing triangles, and the nondiabetic subjects with upward triangles.

The R^2 correlation coefficient was < 0.08 for all subjects, both diabetic and nondiabetic, indicating no correlation between FAT and eGFR, serum cystatin C, urine protein, and BMI.

4.5 Discussion

Renal fat estimated with in- and out-of-phase images do not correlate with eGFR, serum cystatin C, urine protein, or BMI in this retrospective study. There appear to be no changes in renal fat content with worsening renal disease. The results of our current study suggest that such differences would be slight, if they exist.

While better methods for fat quantification exist, including multipoint Dixon or IDEAL methods (246), the use of in- and out-of-phase images enabled acquisition of data from a large patient population, due to the routine collection of these images by health-care providers at our center. Despite not using Dixon or IDEAL methods, renal fat content differences should have been evident in a population this large. Additionally, no statistical difference was observed when using the entire population, diabetic population, or nondiabetic population.

The results of this study do not disprove the diabetic mouse model (46), as a more controlled environment and population may have more observable differences. However, this work suggests that the assessment of cortical fat will not indicate general renal

dysfunction.

4.6 Conclusions

This work has demonstrated that there is no correlation between fat content in the kidneys, as estimated by in-phase and out-of-phase images, with renal dysfunction across a range of etiologies. This work compared renal fat with eGFR, serum cystatin C, urine protein, and BMI, and found no correlation.

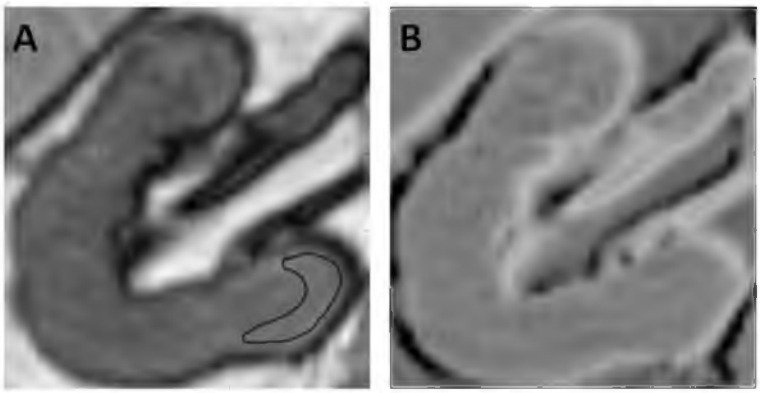

Figure 51. MRI-derived images of a kidney. (A) Kidney image from an out-of-phase axial slice. A sample cortical ROI is outlined. When the cortex was not distinguishable from medulla, an ROI was chosen near the kidney wall to obtain likely cortical regions. (B) Relative signal loss from fat on the out-of-phase images (defined as FAT).

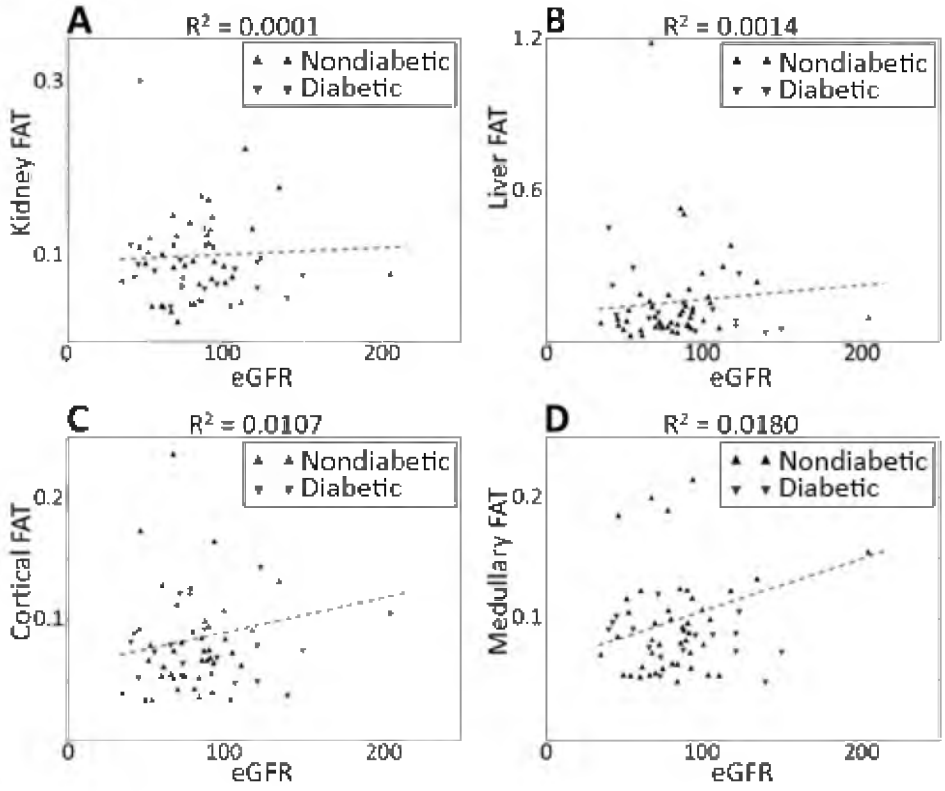

Figure 52. FAT versus eGFR. FAT versus eGFR for (a) whole kidney, (b) whole liver, (c) cortical and (d) medullary regions. The nondiabetic patients and diabetic patients are indicated with up-triangles (black) and down-triangles (red), respectively. A trend-line and R^2 correlation coefficient is shown for all subjects.

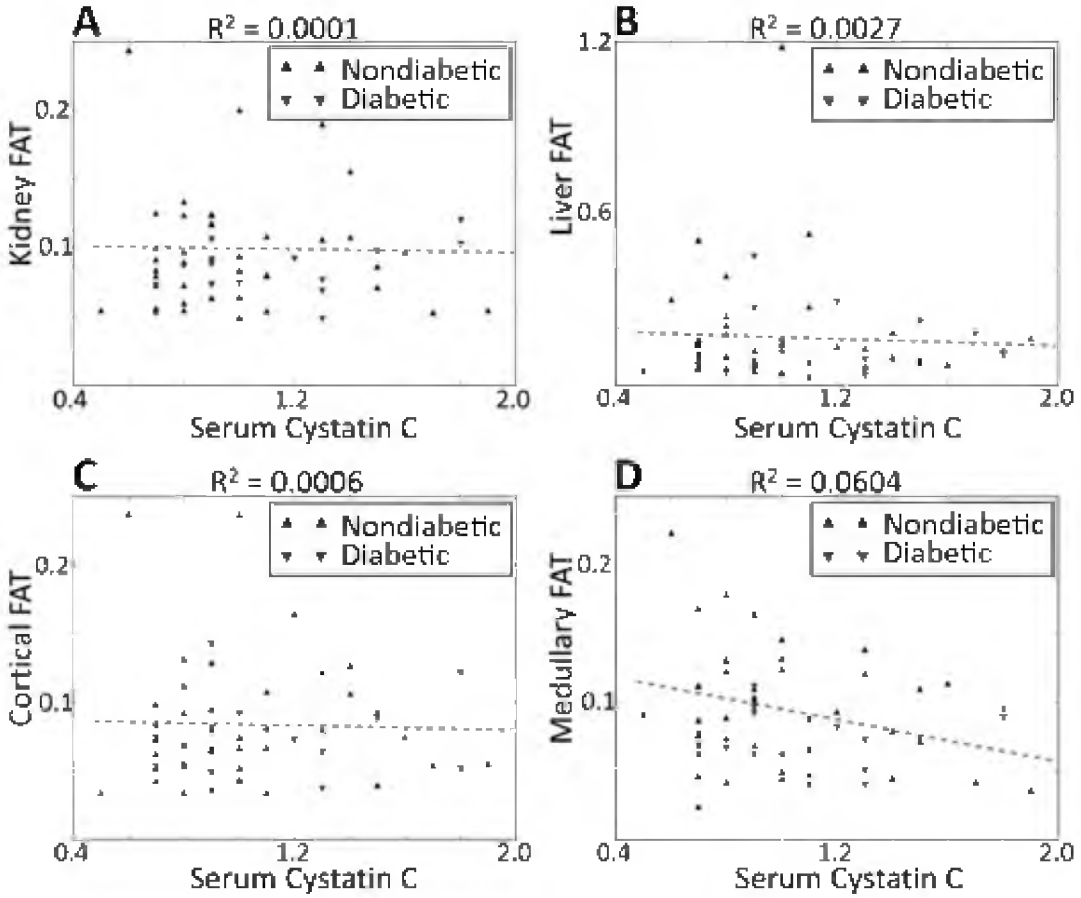

Figure 53. FAT versus serum cystatin C. FAT versus serum cystatin C for (a) whole kidney, (b) whole liver, (c) cortical and (d) medullary regions.

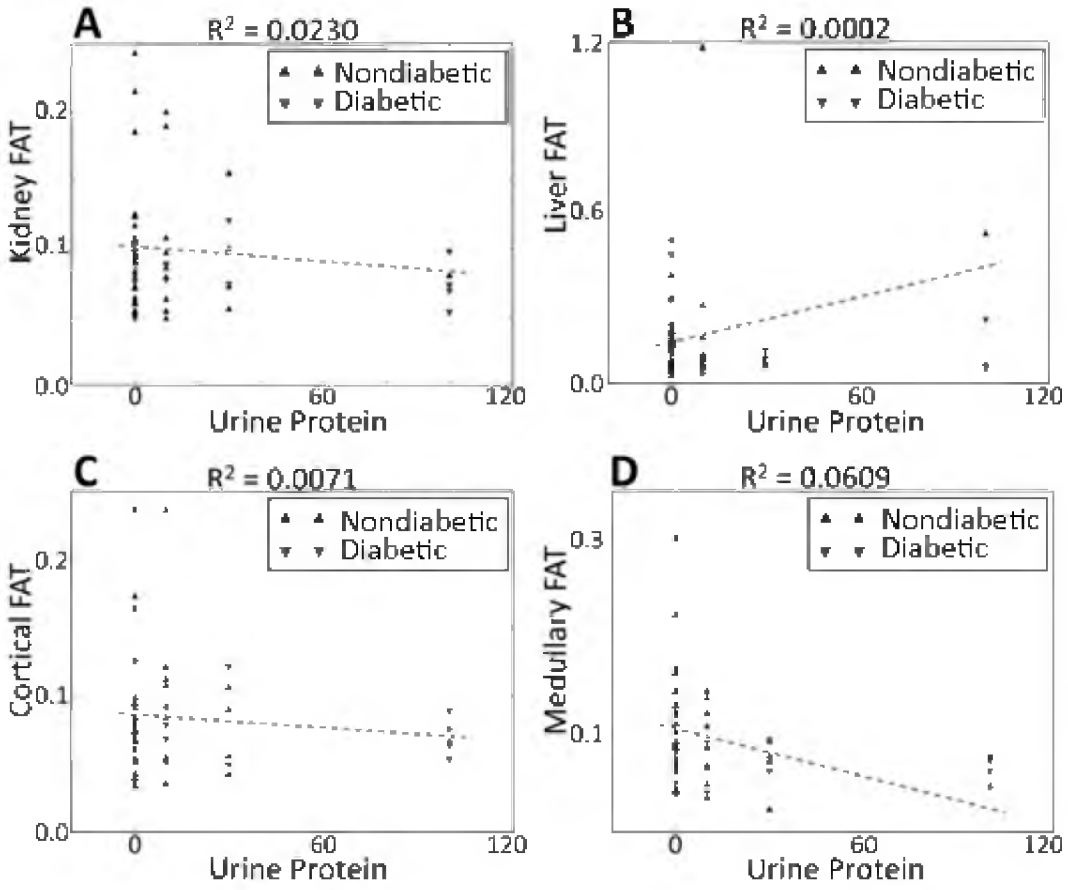

Figure 54. FAT versus urine protein. FAT versus urine protein for (a) whole kidney, (b) whole liver, (c) cortical and (d) medullary regions.

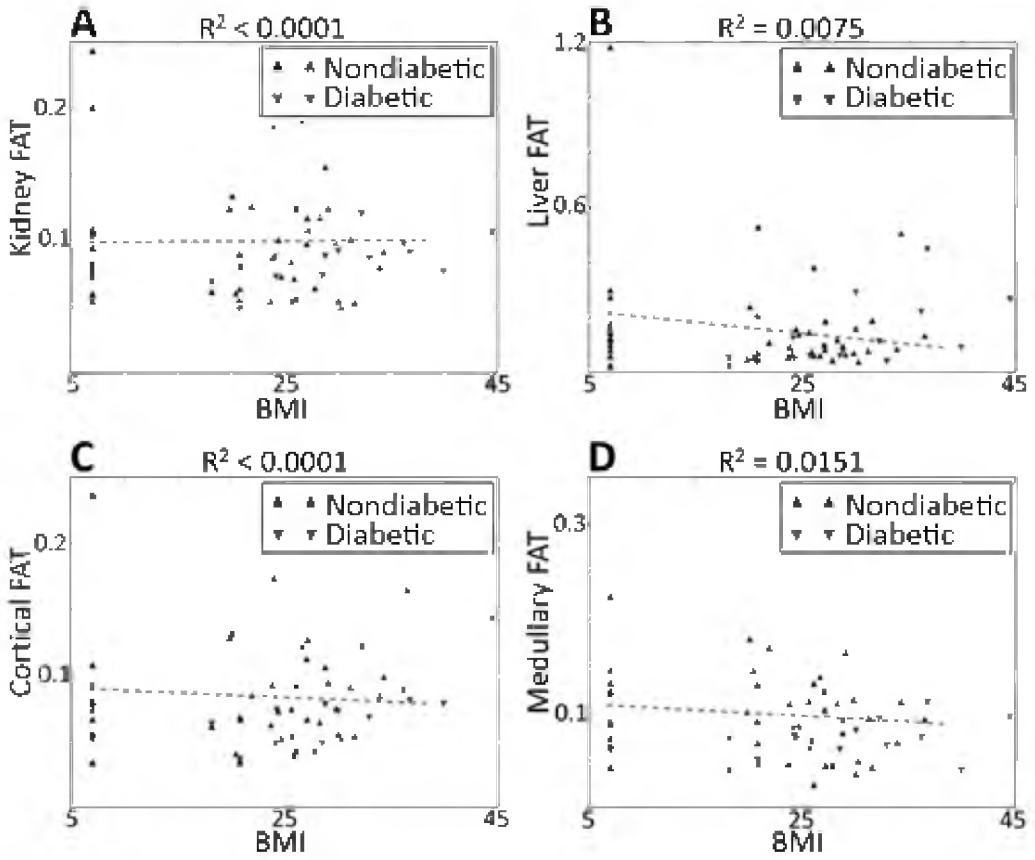

Figure 55. FAT versus BMI. FAT versus BMI for (a) whole kidney, (b) whole liver, (c) cortical and (d) medullary regions.

CHAPTER 5

SYNCHRONOUS ^{1}H AND ^{23}Na DUAL-NUCLEAR MRI ON A CLINICAL MRI SYSTEM, EQUIPPED WITH A TIME-SHARED SECOND TRANSMIT CHANNEL

This chapter is based on the paper titled, *"Synchronous ^{1}H and ^{23}Na dual-nuclear MRI on a clinical MRI system, equipped with a time-shared second transmit channel,"* authored by Joshua D. Kaggie, Nabraj Sapkota, Kyle Jeong, Xianfeng Shi, Glen Morrell, Neal K. Bangerter, and Eun-Kee Jeong. This paper had been submitted and rejected from a journal. A revision will soon be sent to a new journal.

5.1 Abstract

5.1.1 Purpose

To synchronously acquire proton (^{1}H) and sodium (^{23}Na) image data at 3 T within the same sequence, for accurate co-registration of ^{23}Na and ^{1}H images within significantly reduced scan times, without internal modification of the clinical hardware.

5.1.2 Methods

A dual-tuned $^{1}H/^{23}Na$ breast coil was used to acquire both phantom and in vivo data. Proton GRE and SE MR images were separately acquired, synchronously with ^{23}Na

GRE images. To overcome scanner limitations: the $^{1}H/^{23}Na$ transmit pulses were interleaved; additional hardware was added to the scanner to down-convert the ^{1}H signal, so that both the ^{23}Na and ^{1}H signal were acquired at ^{23}Na frequency through the scanner; the sequence allowed multiple ^{23}Na acquisitions to occur between ^{1}H acquisitions; and the ^{1}H signal used phase stabilization to reduce external hardware phase effects.

5.1.3 Results

The synchronous $^{1}H/^{23}Na$ setup obtained images in half the time that it would have taken to sequentially acquire the same ^{1}H and ^{23}Na images with the given setup and parameters.

5.1.4 Conclusions

Dual-nuclear hardware and sequence modifications were used to acquire synchronous $^{1}H/^{23}Na$ image data. This work demonstrates a viable technique to acquire dual-nuclear image data without increases in scan time, and without modifying the scanner's internal hardware.

5.2 Introduction

While standard proton (^{1}H) MRI is currently the gold standard for diagnosing and characterizing many diseases, there are still many diseases which cannot be diagnosed and characterized by ^{1}H-MRI. Sodium (^{23}Na) MRI is being pursued as a complement to clinical ^{1}H-MRI. Sodium MRI is less sensitive than ^{1}H-MRI, due to the relatively low in vivo ^{23}Na concentrations, rapid biexponential signal decay, and a low gyromagnetic ratio. Despite these challenges, ^{23}Na-MRI has the potential to help improve the characterization

and assessment of tumor viability (178,247), cartilage health (182,183,248,249), renal failure (185,250), tissue damage following stroke (186), and multiple sclerosis (187).

A significant barrier to ^{23}Na-MRI in clinical settings is the increased time requirements for obtaining both ^{23}Na and ^{1}H data, since ^{23}Na and ^{1}H images are typically acquired sequentially in separate MRI sequences (251). Data acquisition schemes that synchronously image multiple nuclei (as recently demonstrated in (22)) could potentially provide additional multinuclear image data to complement ^{1}H image data without a significant scan time penalty compared to ^{1}H imaging alone. During nonproton MR spectroscopy, a ^{1}H-RF transmit is used in conjunction with a nonproton pulse for ^{1}H decoupling (252), nuclear Overhauser enhancement (253), ^{31}P-^{1}H cross-polarization (254), and polarization transfer (255-257). However, only recently have the first synchronous MR images been reported on clinical systems, obtaining synchronous ^{1}H data using ^{23}Na (251) and ^{19}F (22) imaging and ^{31}P (258) spectroscopy. Synchronous ^{1}H/^{23}Na imaging has the potential to preserve the information from standard ^{1}H-MRIs, while obtaining additional ^{23}Na information from the same sequence without increasing scan time, improving the feasibility of ^{23}Na-MRI.

Dual-nuclear MRI acquisitions can be performed in a variety of ways. Excitation can be either interleaved or sequential, as can gradient field encoding and acquisition. For the purposes of this paper, we use the term "simultaneous" when dual-nuclear excitation, reading, or encoding is truly performed at exactly the same time. We use the term "interleaved" when any of these steps occur in rapid succession. And, broadly speaking, we term any dual-nuclear technique "synchronous" that is capable of exciting and acquiring signals from both nuclei in a single pulse sequence, whether in a simultaneous, tightly interleaved, or an overlapped fashion.

Most clinical and human research scanners lack sufficient hardware for synchronous multinuclear imaging. Even though many sites have multinuclear capabilities and dual resonant $^{1}H/^{23}Na$ coils (259-264), synchronous $^{1}H/^{23}Na$ images have only been reported by Keupp (251) of a human knee in vivo, due to the increased hardware difficulties in obtaining synchronous images. Keupp's solution (265) requires modification of internal scanner components, such as modifying the input feeds into the RF amplifier.

In this manuscript, we present a new solution for synchronous dual-nuclear imaging. Our solution does not involve acquiring or transmitting both the $^{1}H/^{23}Na$ signals simultaneously, avoiding some of the significant scanner modifications required for other solutions. Unlike a typical preclinical small bore MRI system equipped with a second independent radiofrequency (RF) channel, for which two separate RF systems (Tx/Rx) can independently operate within an appropriate pulse sequence, our human research scanner is capable of irradiating or receiving only one frequency at a time. The human research scanner can, however, switch between broadband and baseband transmission within 100 μs; unfortunately, the scanner limits reception to only one frequency within a given sequence. The ability to transmit at two frequencies within a sequence allows us to acquire synchronous data, by manipulating both ^{23}Na and ^{1}H spin systems within the same pulse sequence. In order to take advantage of the scanner's ability to rapidly switch between broadband and baseband transmission, the receive techniques must incorporate external hardware to acquire data from the second nucleus.

While the imaging schemes demonstrated in this paper are not truly simultaneous (the ^{1}H transmit pulse occurs just prior to the ^{23}Na transmit), the results are nearly the same as if they were simultaneous. This paper also demonstrates another synchronous

imaging scheme that acquires ^{1}H image data after a set number of ^{23}Na repetition times, so that the ^{1}H and ^{23}Na repetition times are different yet data from both nuclei are simultaneously acquired at certain TRs. While each synchronous imaging scheme will constrain the choice of imaging parameters, there can be significant benefits from obtaining information from a second nucleus within a single sequence.

In this work, we present a novel method for synchronous acquisition of ^{23}Na and ^{1}H images which avoids the extensive modifications to the scanner required of previous solutions. Our solution exploits the capability of our scanner to rapidly switch between normal and broadband excitation. Several synchronous acquisition variations are presented for dual-nuclear $^{1}H/^{23}Na$ imaging, and proof-of-concept demonstrations provided in phantoms and in the human breast.

5.3 Methods

The objective of this study was to demonstrate hardware and sequence techniques to acquire synchronous ^{23}Na and ^{1}H breast images. External hardware capability, as shown in Figure 56 and Figure 57, was developed and added to a clinical MRI system with multinuclear MR option to sample both ^{23}Na and ^{1}H MR signals within the same acquisition. A dual-nuclei MRI pulse sequence (Figure 58) was developed to manipulate both spin systems within the same pulse sequence. Sodium was selected as the main measurement nucleus and ^{1}H as the second transmit nucleus.

All experiments were performed on a 3 T clinical MRI scanner equipped with multinuclear option (Tim-Trio, Siemens Medical Solution, Erlangen, Germany). The multinuclear option equips the scanner with a narrowband ^{1}H RF amplifier, a broadband RF amplifier, and a switch box that can switch between the ^{1}H and the broadband RF

amplifiers. The broadband RF amplifier is used for nonproton RF transmission and the main baseband ^{1}H RF amplifier is used for proton RF transmission. The baseband and broadband signals are combined into a single transmit channel that is supplied to the RF coil. IDEA (Siemens Medical Solution, Erlangen, Germany), a development environment for pulse sequence and image reconstruction software, was used for pulse-sequence programming.

5.3.1 Dual-Resonant $^{1}H/^{23}Na$ Coil

A custom-made $^{1}H/^{23}N$ coil was used consisting of a single ^{23}Na loop concentric with a single ^{1}H loop (264) (Figure 57). The mutual inductance between the ^{1}H and ^{23}Na loops is reduced through a single passive resonant trap in each coil (Figure 57B). Both the ^{1}H and ^{23}Na loops are single-turn coils built using 10 mm wide copper tape placed on a 65 mm tall 133 mm diameter acrylic tube. The ^{23}Na loop was positioned so that it would surround the center of the breast with a 10 mm gap between the ^{1}H and ^{23}Na loops.

The coil assembly was placed over a hemispherical fiberglass former. During experiments, the coil was placed in a support structure (264,266) such that the subject could lie prone, head first on the scanner table, to reduce respiratory and other motion artifacts. The support structure consists of an acrylic ramp, a flat carbon fiber board that holds the coil, and a head rest. The entire setup is padded for subject comfort during scanning.

5.3.2 Transmit/receive (TR) Switching

Transmit switching for both ^{1}H and ^{23}Na channels was done using a dual-resonant TR switch (Stark Contrast, Erlangen, Germany) that uses passive traps to separate the ^{1}H

and ^{23}Na transmit frequencies. The TR switch contained two connectors for transmit/receive on both ^{1}H and ^{23}Na channels for standard nonsynchronous single-frequency operation.

Because the dual-resonant TR switch is still intended for use without losing current imaging functionality, an additional ^{1}H TR switch was placed between the ^{1}H output of the dual-resonant TR switch (Figure 56A) and coil. The ^{1}H TR switch was added to direct the ^{1}H NMR signal onto the ^{23}Na receive channel, down-convert and receive the ^{1}H signal at the carrier frequency of 32.6 MHz (the same frequency as ^{23}Na) through the scanner, without modifying the current hardware. The ^{1}H TR switch incorporated standard TR switch circuitry, such as a serial PIN diode, quarter-wave cables that were connected by PIN diodes to ground for preamplifier protection, and an RF preamplifier (Figure 56B). The host MRI system provides DC biasing that is controlled with coil-control files, to switch the ^{1}H PIN diodes. During ^{1}H transmit, a forward-bias current (+100 mA) shorts the PIN diodes in the ^{1}H TR switch (Figure 56B) so that the ^{1}H RF transmit can easily pass through, but is negatively biased during receive (- 30V) to ensure that the receive signal is directed to the ^{1}H preamplifier (Figure 56B). The inductance of the RF chokes (L in Figure 56B) used to pass DC bias is 15 μH; the capacitor values (C in Figure 56B) to block the DC bias are 15 nF.

During ^{1}H reception, the ^{1}H signal is (i) amplified by a 24 dB preamplifier (Advanced Receiver Research, Burlington, CT, USA), (ii) converted to 32.6 MHz using an RF mixer (ZAD-1, Mini-Circuit Inc., Brooklyn, NY) by mixing a 90.6 MHz sine wave from a precision frequency synthesizer (SG382, Stanford Research Systems, Sunnyvale, CA), which is synchronized using a 10 MHz clock signal from the host MRI system, and, (iii) filtered using a low-pass filter to pass the 32.6 MHz signal only (Figure 56a). The

frequency of the synthesizer is determined by subtracting the ^{23}Na frequency from the ^{1}H frequency, which is explained in the Appendix. The resultant ^{1}H signal at the carrier frequency of 32.6 MHz is then (iv) attenuated and (v) fed into one of the ^{32}Na receive channels (258).

5.3.3 Pulse Sequence

Synchronous imaging of ^{23}Na occurred with a standard gradient-echo (GRE) for ^{23}Na, and a GRE or spin echo sequence (SE) for ^{1}H, with both ^{1}H and ^{23}Na transmit and receive occurring in the same sequence (Figure 58). RF and gradient pulses for ^{1}H imaging were added prior to the ^{23}Na excitation RF pulse, so that the pulse sequence for ^{23}Na imaging is not altered at all. The zeroth moment of the gradient pulses for ^{23}Na slice-selection is compensated in the refocusing gradient of the ^{1}H slice-selection. Sampling for both ^{1}H and ^{23}Na at the carrier frequency of 32.6 MHz occurred simultaneously on two ^{23}Na channels, regardless of whether a ^{1}H pulse recently occurred.

Figure 58A shows the pulse sequence for the ^{1}H SE and ^{23}Na GRE imaging. Because a longer repetition time is desired for the ^{1}H SE acquisition than that of the ^{23}Na GRE acquisition, multiple ^{23}Na acquisitions occur between the ^{1}H acquisitions, while the ^{1}H longitudinal magnetization is relaxing toward thermal equilibrium. In this example, the repetition time for ^{1}H MRI is an integer multiple of the ^{23}Na-TR. Between two adjacent acquisitions of ^{1}H imaging data, measurement of ^{1}H FIDs with very low-angle ($\sim 5^{o}$) is repeated to acquire a ^{1}H phase reference echo. This reference echo is used to correct phase errors, as detailed below. Note that the ^{23}Na phase reference echo is not useful for phase error correction because of its low SNR. The dual-nuclear imaging of ^{1}H/^{23}Na GRE requires disabling the 180^{o} RF pulse, slice-selection and crusher gradients.

Although the external synthesizer was synchronized with the host MRI system using a 10 MHz reference signal, the single stage mixing introduced a systematic and incremental phase-error into the ^{1}H channel data (Figure 59A). This systematic phase-error was straightforward to correct using the ^{1}H phase reference echoes, which are simultaneously acquired for each ^{23}Na FID.

Gradient spoiling occurred after each ^{1}H or ^{23}Na signal and phase stabilization acquisition. Gradient spoiling between ^{23}Na acquisitions did not affect ^{1}H image data; the ^{1}H image data were acquired immediately after ^{1}H transmit, prior to any gradient spoiling in that TR, and ^{1}H acquisition did not occur until the next ^{1}H-TR.

5.3.4 Postprocessing Using Phase Reference Echoes

The $^{1}H/^{23}Na$ image data were transferred to and processed on an offline computer. For each ^{1}H imaging echo, the systematic phase error, θ, was estimated at the peak of the ^{1}H phase reference echo, and subtracted from the ^{1}H imaging echo by multiplying by $e^{-i\theta}$ (267,268). Note that the phase of the ^{23}Na signal is not affected by this systematic phase in the ^{1}H data.

5.3.5 MRI Experiments

Using the additional hardware shown in Figure 56 and the synchronous $^{1}H/^{23}Na$ MRI pulse sequence, ^{1}H and ^{23}Na MRI images were acquired of a cylindrical phantom. The phantom contained three cylindrical tubes with different concentrations of $MnCl_2$ and NaCl (0.4 mM $MnCl_2$ and 300 mM NaCl, 0.2 mM $MnCl_2$ and 150 mM NaCl, 0.1 mM $MnCl_2$ and 75 mM NaCl). The liquid surrounding the tubes contained 0.2 mM $MnCl_2$ and

no NaCl.

For synchronous phantom imaging using a 3D ^{1}H-GRE and ^{23}Na-GRE, the imaging parameters were: ^{1}H/^{23}Na-TR = 50/50 ms, ^{1}H/^{23}Na-TE = 7.27/2.25 ms, ^{1}H/^{23}Na-flip angle = 25°/70°, ^{1}H/^{23}Na field-of-view (FOV) = 118/448 mm, ^{1}H/^{23}Na-voxel size = 0.9/3.5 mm^{3} isotropic, ^{1}H/^{23}Na averages = 5/5, acquisition matrix = 256x128x40 with 6/8 asymmetric sampling along phase-/slice-encoding directions and 5/8 asymmetric sampling along the readout direction, bandwidth (BW) = 500 Hz/pixel, and a total scan time = ~ 21 min. This experiment is equivalent to acquiring separate ^{23}Na-GRE images and ^{1}H-GRE images that would have taken ~ 21 minutes each.

Human imaging of a normal, healthy human female volunteer was conducted after informed consent and with approval of the local institutional review board (IRB). Images were acquired in the sagittal plane with the read-out along the AP direction to reduce motion artifacts.

Two in vivo experiments were performed: (1) a synchronous ^{1}H-GRE and ^{23}Na-GRE with an equal ^{1}H-TR and ^{23}Na-TR; and (2) a synchronous ^{1}H-SE and ^{23}Na-GRE with an unequal ^{1}H-TR and ^{23}Na-TR. For 3D ^{1}H-GRE/^{23}Na-GRE synchronous imaging, the scan parameters were: ^{1}H/^{23}Na-TR = 50/50 ms, ^{1}H/^{23}Na-TE = 7.8/2.0 ms, ^{1}H/^{23}Na-flip angle = 18°/63°, ^{1}H/^{23}Na FOV = 118/448 mm^{3}, ^{1}H/^{23}Na-voxel size = 0.9/3.5 mm^{3} isotropic, ^{1}H/^{23}Na averages = 6/6, ^{1}H/^{23}Na-matrix size = 256x128x64 with 6/8 asymmetric sampling along phase-/slice-encoding directions and 5/8 asymmetric sampling along the readout direction, bandwidth (BW) = 500 Hz/pixel, and a total scan time = ~ 23 min. 3D ^{1}H-SE/^{23}Na-GRE synchronous imaging was performed using similar acquisition parameters to those for 3D ^{1}H-GRE/^{23}Na-GRE, except for ^{1}H-TR/TE = 250 /12.4 ms, ^{1}H-flip angle = 90°, ^{1}H averages = 1, and with a ^{1}H-phase reference pulse

of 5°, and a total scan time = ~ 19 min.

5.4 Results

5.4.1 Phantom Studies

Figure 59a indicates the phase at the peak of the first 90 ^{1}H phase reference echoes. The magnitude and phase images of the center slice are shown without (Figure 59B,C) and with (Figure 59D,E) correcting systematic phase-error, respectively. Gibb's ringing artifact is visible along both vertical and horizontal directions due to phase-encoding with a low (128) resolution.

The $^{1}H/^{23}Na$ dual-nuclear MRI obtained ^{1}H-GRE images synchronously with ^{23}Na-GRE images (Figure 60) of three orthogonal planes. The acquisition of ^{23}Na data is not interrupted by synchronous ^{1}H imaging. The ^{1}H images show T_1 contrast among different $MnCl_2$ concentrations.

The full FOV is shown in the ^{1}H images in all planes in Figure 6. Because the ^{1}H and ^{23}Na signals are acquired using the same gradients for readout and phase-encoding, the ^{1}H image data have a 3.8 times higher resolution and smaller FOV due to the ratio of the ^{1}H and ^{23}Na gyromagnetic ratios ($=\gamma_{1H}/\gamma_{23Na}$).

5.4.2 In Vivo Human Breast Study

Figure 61 shows the result of a synchronous $^{1}H/^{23}Na$ of the breast of a healthy volunteer. Both GRE and SE sequences were performed for acquisition of conventional ^{1}H images. Synchronous ^{23}Na-GRE imaging was performed throughout the duration of both of these ^{1}H sequences.

Imaging was also demonstrated using a ^{1}H-TR equal to the ^{23}Na-TR during ^{1}H-

GRE, and unequal during ^{1}H-SE.

The images are quite noisy compared to the phantom study, as a noncentric Cartesian trajectory was used for ^{23}Na image acquisition for simplicity. To improve the quality of the in vivo ^{23}Na acquisition, a centric trajectory such as 3DPR (78), 3D TPI (269), or 3D cones (79) should be implemented with the technique. However, the inclusion of such a trajectory in this preliminary proof-of-concept work would have introduced unnecessary complexity in the initial experimental design. Despite the inhomogeneities in the ^{1}H-SE image and the poor SNR of the ^{23}Na-GRE images, synchronous ^{1}H and ^{23}Na imaging has been shown here, demonstrating the ability to remove sequential ^{1}H and ^{23}Na imaging.

5.5 Discussion

We have demonstrated synchronous acquisition of both ^{1}H and ^{23}Na nuclei on a clinical scanner, in what normally would require twice the scan time for the same sequential acquisitions. The most important advantages of using synchronous ^{1}H/^{23}Na-MRI are the substantial reduction of acquisition time for acquiring image data from both nuclear species and improving the direct correlation between the ^{23}Na and ^{1}H data. As one of the major limitations of in vivo ^{23}Na-MRI is its long acquisition time, mainly due to low in vivo ^{23}Na concentrations, synchronous ^{1}H/^{23}Na MRI may greatly improve the practical applications of ^{23}Na-MRI. Synchronous ^{1}H/^{23}Na MRI may potentially improve the diagnosis of breast cancer, cartilage evaluation, and other diseases, by obtaining additional information to standard ^{1}H imaging, without requiring additional scan time.

Although synchronous dual-nuclear MRI/MRS can be achieved using an MRI or NMR system equipped with multiple physical transmit/receive channels and/or with

internal hardware modification with an appropriate pulse sequence, as reported by Keupp (265), dual-nuclear MRI was performed by adding external conversion hardware, without modifying any internal hardware of the clinical MRI system. The modifications for synchronous acquisition demonstrated in this paper are relatively minor, requiring only additional standard RF receive hardware, a mixer, a frequency synthesizer, and a multinuclear sequence.

During the lengthy scans that often occur for ^{23}Na imaging, the subject may move, reducing the quality of ^{23}Na data. By using synchronous ^{1}H/^{23}Na-MRI, the ^{1}H phase reference FID could be used to correct the phase error in ^{23}Na FIDs that may be induced by eddy-currents and small motion, which is not easily done using ^{23}Na data alone due to ^{23}Na's low intrinsic SNR. ^{1}H/^{23}Na-FID data with severe corruption by the subject's motion can be identified using the ^{1}H-FID and excluded from processing. By using this ^{1}H phase reference echo in real-time self-gated ^{23}Na-MRI, the phase and magnitude of the phase reference echo peak would be calculated. The phase and magnitude would then be compared to those of the reference echoes to determine if the ^{23}Na and ^{1}H imaging echoes are corrupted by the subject's motion, which then would be rejected and reacquired (270). This method requires accurate estimation of the systematic phase increment.

Although the current work has demonstrated some flexibility in imaging parameters, some parameters must be identical using this setup, such as receiver bandwidth and FOV, because both NMR signals are simultaneously sampled within the same acquisition window. The FOVs can be completely independent by applying additional gradients prior to ^{23}Na excitation, which adds or subtracts the phase-encoding gradient appropriate for the ^{1}H-FOV. The restriction in other imaging parameters may be

completely removed by interleaving the acquisitions between two nuclei with a minor cost in time efficiency.

As a result of simultaneous $^{1}H/^{23}Na$ acquisition, the ^{23}Na-FOV is 3.8 times the ^{1}H-FOV, and the ^{1}H resolution is 3.8 times the ^{23}Na resolution. This result can be very practical and useful for many sequences, as ^{1}H imaging occurs at a typically higher resolution than ^{23}Na imaging because the ^{23}Na-SNR is much lower than the ^{1}H-SNR. Enlarging the ^{23}Na-FOV is equivalent to signal averaging, which is typically performed in ^{23}Na imaging. In other words, increasing the FOV of the ^{23}Na image by a factor of four is equivalent to performing four signal averages over the original FOV, from the standpoint of SNR. The constraint on the ratio of ^{23}Na to ^{1}H FOV and resolution thus fits very naturally into the typical parameters for both ^{23}Na and ^{1}H imaging.

This study demonstrates proof-of-concept synchronous imaging, as several refinements are possible to improve the ^{23}Na image quality. The ^{23}Na images were obtained with a conventional GRE Cartesian k-space acquisition. Because of the very short T_2* relaxation time of sodium, Cartesian k-space acquisition results in much lower signal than other acquisition schemes, such as 3DPR (78), 3D TPI (269), or 3D cones (79). The SNR of the ^{23}Na images can also be improved by the use of a ^{23}Na phased array coil, as demonstrated in (264). In our current implementation, we use only two of the receive channels of our scanner. One channel receives the ^{23}Na signal directly, while the second receives the ^{1}H signal mixed down to the ^{23}Na frequency. Additional ^{23}Na receive channels in the existing scanner hardware can be used to accommodate a phased array ^{23}Na receive coil. Additional mixers could also be used to down-convert multiple ^{1}H channels to ^{23}Na frequency, so that synchronous imaging could occur on a composite $^{1}H/^{23}Na$ array for better SNR of both nuclei (264).

The current mixing scheme for ^{1}H-data in the receive data causes a consistent, *not random,* phase error along the increasing FID numbers. This systematic incremental phase-error was small as the synthesizer frequency is accurately set to match the down-converted ^{1}H signal to the carrier frequency. The systematic phase-error caused by down-conversion was straightforward to estimate and correct using the ^{1}H phase reference signal during the postprocessing.

An RF mixer is not a power device, which generally adds noise. However, the SNR of the measured NMR signal may be degraded during the mixing process, because the synthesizer signal for demodulation may carry extra noise into the local-oscillator port. This noise may be completely or partially reduced by transmitting the synthesizer signal via the optical cable, for instance using an RF-over-fiber link.

Synchronous dual-nucleus MRI can be used to study the NMR characteristics of other nuclei, such as ^{31}P chemical shift imaging, ^{13}C MR spectroscopy and ^{19}F MRI. For instance, ^{19}F MRI is being considered as an alternative method to study drug delivery using a fluorinated compound with a large number of ^{19}F atoms with a single chemical environment (271,272).

5.6 Conclusions

Synchronous ^{23}Na and ^{1}H image acquisition is very attractive due to the significant decreases in scan time when compared to sequential ^{23}Na and ^{1}H imaging. In addition, synchronous MRI is attractive for improving the correlation between ^{23}Na and ^{1}H data. This work demonstrates a viable technique to acquire dual-nuclear image data without increases in scan time, and without modifying the scanner's internal hardware.

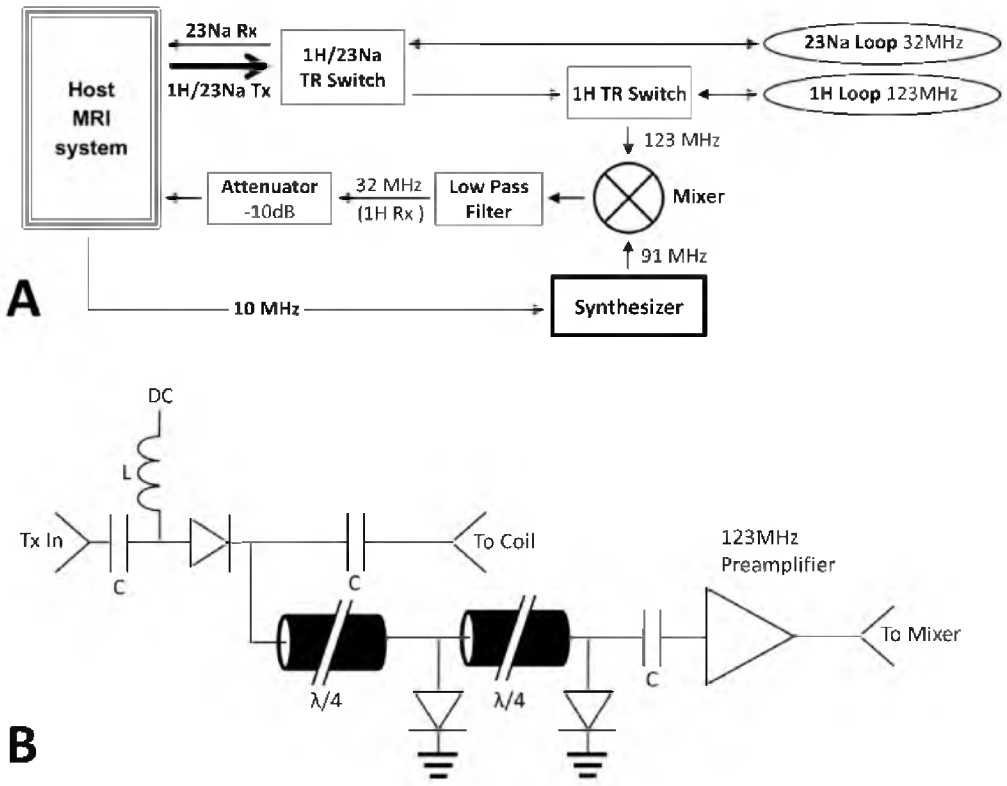

Figure 56. Electronics used to acquire synchronous ^{23}Na/^{1}H images. (A) Transmit/receive hardware for both ^{1}H and ^{23}Na. Arrows indicate transmit / receive pathways. The host system provided both ^{1}H and ^{23}Na transmit pulses through a single channel, which passed through a commercial ^{1}H/^{23}Na TR switch. The ^{23}Na loop connected directly to the ^{1}H/^{23}Na TR switch; the ^{1}H channel of the TR switch connected to a separate ^{1}H TR switch before connecting to the coil. The second ^{1}H TR switch was necessary to redirect the ^{1}H RF for mixing and down-conversion to 32MHz for simultaneous ^{1}H/^{23}Na reception. An attenuator is necessary due to the significant signal difference between ^{23}Na and ^{1}H. (B) TR switch schematic for ^{1}H. The ^{1}H signal is amplified at 123MHz before down-conversion to 32MHz.

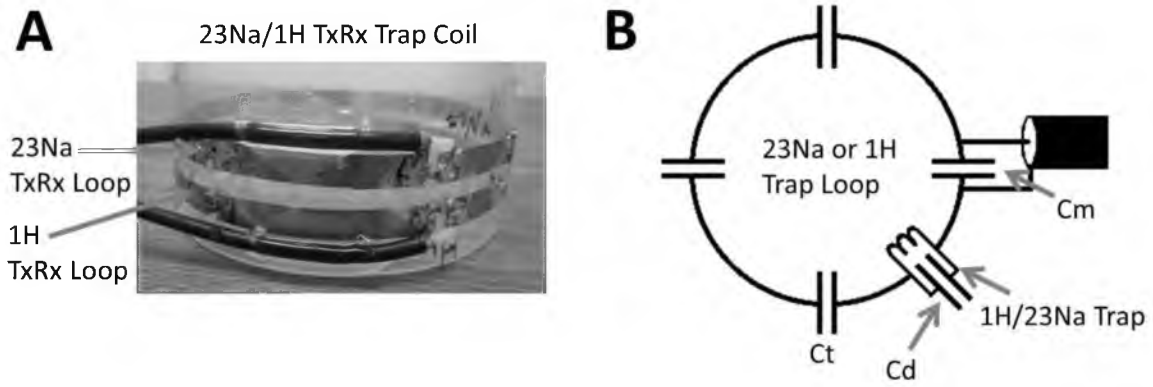

Figure 57. Dual-resonant coil. (A) Picture of the dual-resonant sodium/proton coil. (B) Circuit diagram of either sodium or proton loop on the coil.

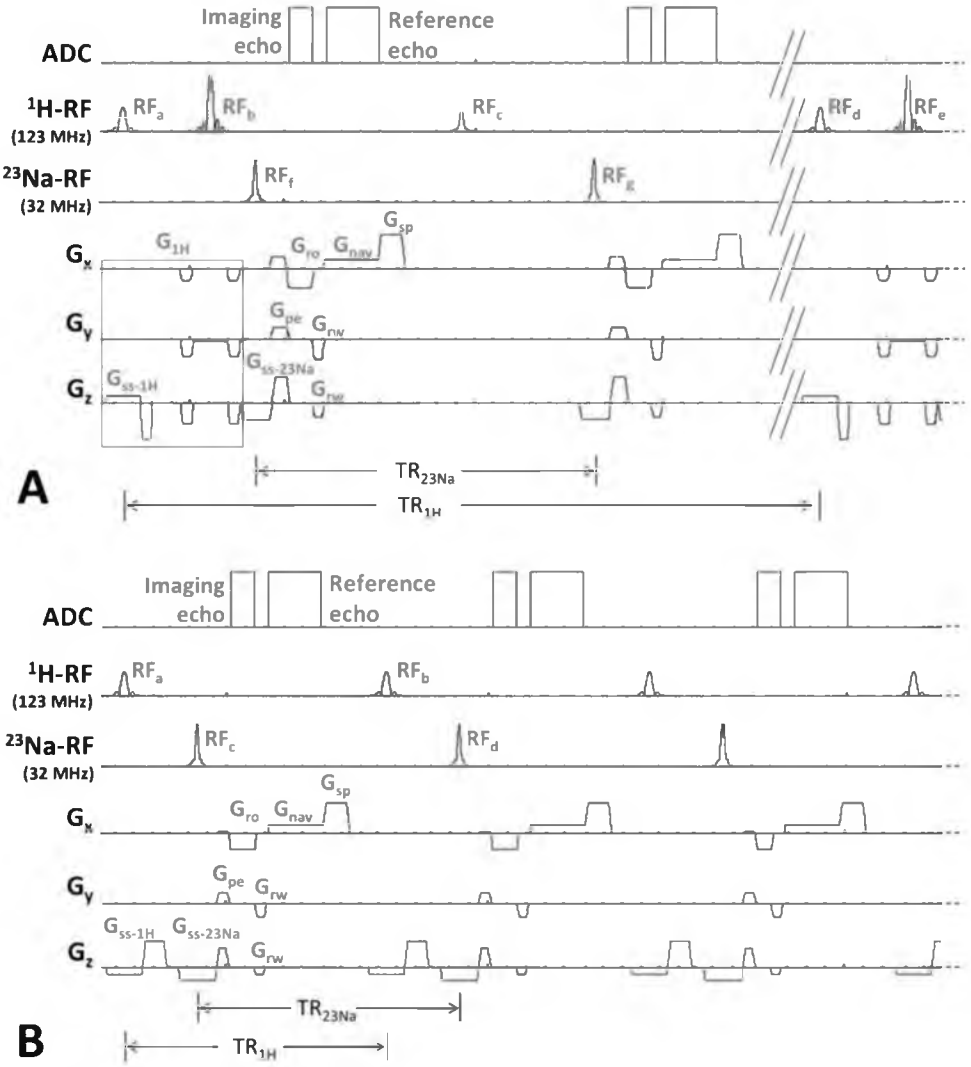

Figure 58. Pulse sequence for synchronous GRE or SE imaging. Pulse sequence diagram for synchronous imaging of ^{23}Na-GRE and (A) ^{1}H-SE or (B) ^{1}H-GRE MRI. RF and gradient pulses for ^{1}H imaging are applied prior to the ^{23}Na excitation RF pulse. All phase-encoding gradients are rewound just before the acquisition of the phase reference echo. In (A), multiple ^{23}Na acquisitions occur between the ^{1}H acquisitions during ^{1}H-SE, while the ^{1}H signal is relaxing. For ^{1}H-SE, RF_a is a 90° pulse and RF_b is a 180° pulse. The ^{1}H gradients before the ^{23}Na pulse do not affect the ^{23}Na signal (with sufficient spoiling), so that the ^{1}H slice and phase encodes can be independent from ^{23}Na slice and phase encodes.

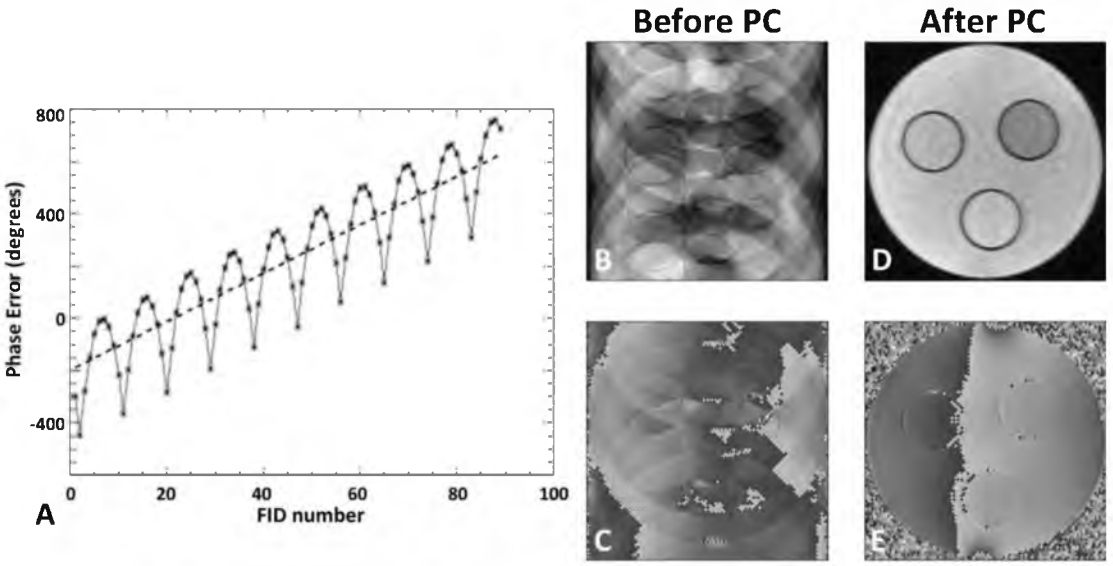

Figure 59. Phase correction required for synchronous MRI. (A) The phase of the peak voxel is plotted for each phase reference readout. The synthesizer introduces a linear increase to the phase, and the difference between the scanner's frequency for sodium detection and the carrier frequency introduces a phase error equal to the absolute value of a sinusoid. (B) Magnitude and (C) phase proton image before phase correction. The systematic phase increase introduced by mixing causes an artifact similar to ghosting. (D) Magnitude and () phase proton image after phase correction.

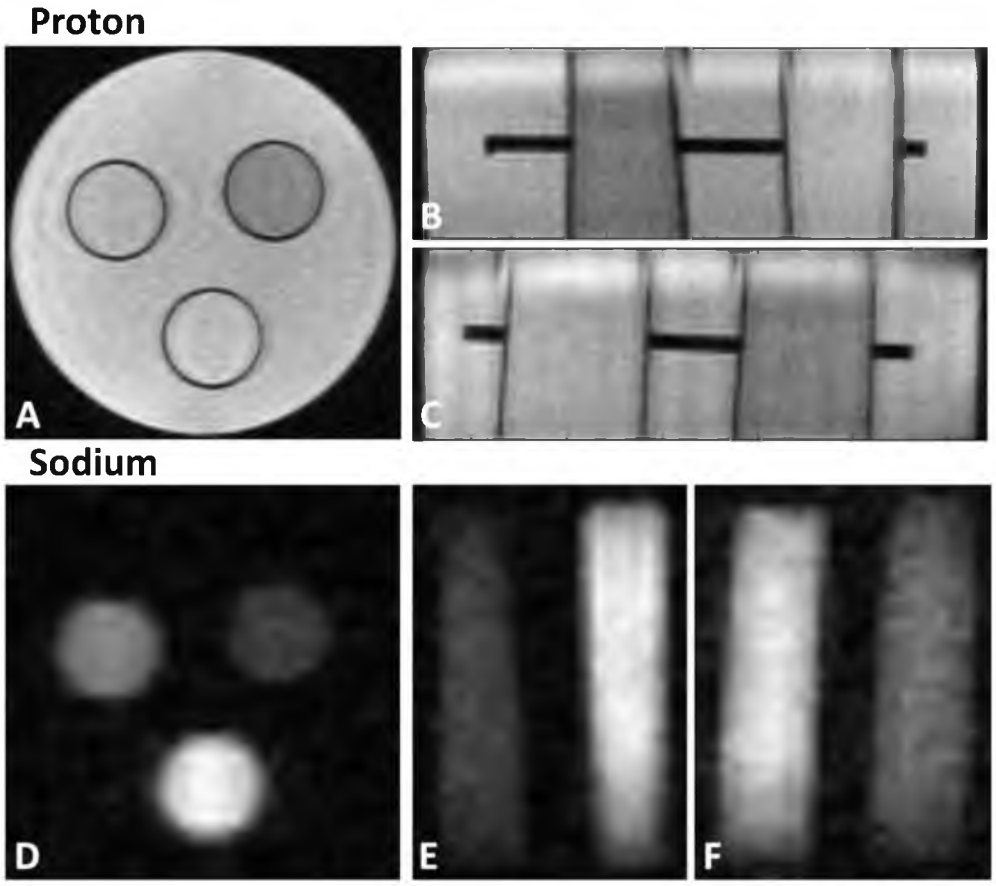

Figure 60. Phantom results of synchronous MRI. (A-C) Proton and (D-E) sodium images acquired during a single 20-minute 3D GRE acquisition. Three orthogonal slices are shown for both proton and sodium images.

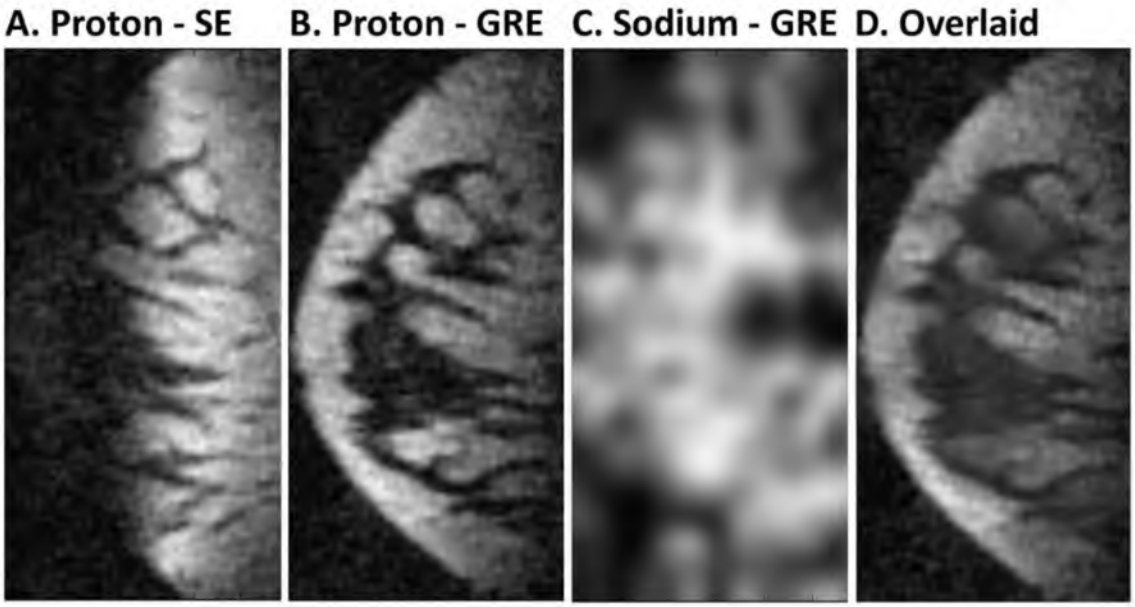

Figure 61. In vivo results of synchronous MRI. Synchronous (A) ^{1}H-SE, (B) ^{1}H-GRE, and (C) ^{23}Na-GRE images. The ^{1}H-SE and ^{1}H-GRE images were each acquired in 20 minutes, while the ^{23}Na-GRE image was acquired by averaging the ^{23}Na data acquired during the entire 40 minutes of ^{1}H imaging (for a total scan time of 40 minutes). D: The ^{23}Na-GRE image overlaid onto the ^{1}H-GRE image.

CHAPTER 6

A 3 T SODIUM AND PROTON COMPOSITE ARRAY BREAST COIL

This chapter has identical content to a published paper titled, *"A 3 T Sodium and Proton Composite Array Breast Coil,"* authored by Joshua D. Kaggie, J. Rock Hadley, James Badal, John R. Campbell, Daniel J. Park, Dennis L. Parker, Glen Morrell, Rexford D. Newbould, Ali F. Wood, and Neal K. Bangerter. The paper was first published online at the journal of Magnetic Resonance in Medicine (MRM) in September 2013. (Reprinted with permission).

6.1 Abstract

6.1.1 Purpose

The objective of this study was to determine whether a sodium phased array would improve sodium breast MRI at 3 T. The secondary objective was to create acceptable proton images with the sodium phased array in place.

6.1.2 Methods

A novel composite array for combined proton/sodium 3 T breast MRI is compared to a coil with a single proton and sodium channel. The composite array

consists of a 7-channel sodium receive array, a larger sodium transmit coil, and a 4-channel proton transceive array. The new composite array design utilizes smaller sodium receive loops than typically used in sodium imaging, uses novel decoupling methods between the receive loops and transmit loops, and uses a novel multichannel proton transceive coil. The proton transceive coil reduces coupling between proton and sodium elements by intersecting the constituent loops to reduce their mutual inductance. The coil used for comparison consists of a concentric sodium and proton loop with passive decoupling traps.

6.1.3 Results

The composite array coil demonstrates a 2-5x improvement in SNR for sodium imaging and similar SNR for proton imaging when compared to a simple single-loop dual resonant design.

6.1.4 Conclusion

The improved SNR of the composite array gives breast sodium images of unprecedented quality in reasonable scan times.

6.2 Introduction

Cancer is responsible for a quarter of all deaths in the United States (273). Breast cancer is projected to cause 458,000 deaths worldwide with 1,383,000 new cases worldwide in 2012 (274). Breast cancer is also estimated to include 29% of all new cancer cases in women in the United States during 2012, resulting in 14% of cancer related deaths (273). Early detection and improved treatment have increased breast

cancer survival rates in the United States over the past two decades (273). While proton (^{1}H) magnetic resonance imaging (MRI) is used for cancer detection due to its improved sensitivity when compared to mammography and ultrasound, ^{1}H-MRI suffers from intermediate specificity which can result in false positive studies leading to unnecessary interventions (275). Because sodium (^{23}Na) concentration is known to increase in malignant lesions when compared to surrounding healthy tissues (247,276), ^{23}Na-MRI may be able to improve specificity, potentially improving evaluation and assessment of breast lesions (277).

Sodium MRI shows promise in characterizing and assessing tumor viability (178,247), cartilage health (182,183,248,249), renal failure (185,250), tissue damage following stroke (186), and multiple sclerosis (187). However, in comparison with conventional ^{1}H-MRI, ^{23}Na-MRI is challenging due to relatively low ^{23}Na concentrations in biological tissues, rapid biexponential signal decay, and a low gyromagnetic ratio. Despite these challenges, recent improvements in coil and gradient hardware, the availability of whole-body scanners with high polarizing field strengths, and the development of more efficient pulse sequences have spurred renewed interest in ^{23}Na-MRI (178). These advances have enabled the acquisition of higher quality in vivo ^{23}Na-MRI images than previously possible, often within clinically reasonable scan times (47,269,278). While ^{23}Na-MRI has become more promising, there is still a need for improved image quality and signal-to-noise ratio (SNR) to make quantitative ^{23}Na-MRI feasible for many of the clinical applications under consideration.

Phased array coils can be used to improve the SNR of ^{23}Na-MRI. This is achieved through simultaneous data acquisition from multiple surface coils which have inherently increased signal sensitivity and limited noise volume by being placed in close

proximity to the object or anatomy of interest (18). Specifically designed coil arrays also allow reductions in image acquisition time through the application of parallel imaging techniques (72,279,280). Phased array coil concepts have been extensively applied to ^{1}H-MRI coil design (136-139), routinely providing improved SNR and accelerated image acquisition (18) compared to that provided by volume coils (135) or other large coils of similar area (141). However, phased arrays have not been widely used in nonproton imaging, and typically require sophisticated custom hardware for implementation on commercial scanners. Despite these challenges, sites with the capability to support multichannel nonproton receivers are becoming increasingly common. The first reported nonproton phased array was built for phosphorous imaging in 1992 (281) almost a decade before the first reported ^{23}Na array at 1.5 T in 2000 (282). In the past few years, there has been a substantial increase in the number of ^{23}Na coil arrays developed for 3 T (259-261,283,284), 4T (262), and 7T (263,285,286). Some of these array configurations are dual resonant, with the ability to image ^{1}H and ^{23}Na without repositioning the subject (259-263).

This paper presents a new dual resonant breast coil design consisting of a 7-channel ^{23}Na receive array, a larger ^{23}Na transmit coil, and a 4-channel ^{1}H transceive array. The new composite array design utilizes smaller ^{23}Na receive loops than those typically used in ^{23}Na imaging. Novel methods are also employed to decouple the receive loops from the transmit loops. A novel multichannel ^{1}H transceive coil is superimposed on the ^{23}Na receive array, and decoupling between ^{1}H and ^{23}Na elements is achieved by intersecting the constituent loops to reduce the mutual inductance between the ^{1}H and ^{23}Na arrays. The performance of the new array design (both SNR and homogeneity) is compared to that of a coil used in prior studies consisting of a single

^{23}Na loop concentric with a single ^{1}H loop (287,288), both with decoupling trap circuits (289-291). Comparisons were performed both in a phantom and in vivo. The new design achieves excellent ^{23}Na-SNR over the sensitive volume while also providing good image quality for conventional ^{1}H imaging.

6.3 Methods

The objective of this study was to determine whether a ^{23}Na phased array would be useful in improving ^{23}Na-MRI at 3 T. The secondary objective was to create acceptable ^{1}H images with the ^{23}Na phased array in place.

The new dual-resonant ^{23}Na/^{1}H composite array design is first described, including the ^{23}Na receive array loops and circuitry, the ^{23}Na transmit coil, the ^{1}H transceive array elements, the associated transmit and transmit/receive (TR) switches, and the decoupling techniques employed. Subsequently, the trap coil consisting of a ^{23}Na loop concentric with a ^{1}H loop is used for comparison. Finally, the phantom and in vivo studies are detailed for assessment of coil performance. All experiments were done on a Siemens TIM Trio 3 T MRI scanner (Siemens Healthcare AG, Erlangen, Germany).

6.3.1 ^{23}Na/^{1}H Dual Resonant Composite Array

The composite array design consists of a hemispherical fiberglass former with seven ^{23}Na receive loops, four ^{1}H transceive loops, and a single circular ^{23}Na transmit loop that surrounds the perimeter of the coil (Figure 62A). A patient friendly support structure is used to position the coil and subject (Figure 62B) (266).

6.3.1.1 ^{23}Na Receive Array

Prior to construction of the ^{23}Na receive array, multiple 65mm diameter loops were tested with different gauge copper wires and capacitor positions. Wire thicker than 14 AWG was not considered feasible for a receive array with small loops, due to the difficulty of using very thick wire for coil construction. The quality factors (Q) (142) of these loops were measured using two stationary decoupled magnetic field probes when the coil was unloaded and loaded (Table 5). The highest Q-ratios were measured using 14 AWG and 16 AWG wire with two capacitors per loop (Table 5). Because these values were similar, the receive array was constructed using 16 AWG wire for its increased ease of use when overlapping the coils on the hemispherical former.

Seven 16 AWG circular ^{23}Na receive loops were positioned on a hemispherical fiberglass former (Figure 62A). Six of the loops are 65 mm in diameter, and surround a single 75 mm diameter loop placed at the top of the hemisphere (Figure 63A). Each loop was positioned for appropriate overlap decoupling. A loaded isolation (S21) of -18 dB was achieved between adjacent coils without preamplifier decoupling. The preamplifiers (Stark Contrast, Erlangen, Germany) had a gain of ~35 dB and noise figure less than 0.5 dB. The change in any receive coil sensitivity (S21) while loaded, measured with two decoupled magnetic probes with and without preamplifiers, was 15 dB. Each loop incorporates a matching and a tuning capacitor (Series 1111P_P501X, Passive Plus, Huntington Station, NY; GYA36000, Sprague-Goodman, Westbury, NY), with combined active/passive ^{23}Na decoupling circuitry positioned at the tuning capacitor location (Figure 63B). The capacitor values are ~180 pF and ~1000 pF for tune and match respectively. The change in loop sensitivity (S_{21}) between resonant and detuned states is greater than 45 dB when loaded, when using two decoupled magnetic probes. The

maximum and average off diagonal noise correlation coefficient was 0.49 and 0.29, respectively.

Combined active/passive decoupling is achieved by placing a crossed diode pair (MA4P7464F-1072T, Macom, Lowell, MA, USA) in series with an inductor that is resonant with the tune capacitor when forward-biased (Figure 63B). Active and passive decoupling were combined to simplify the coils by using only one decoupling circuit, while maintaining the ability to detune the coil with DC biasing and detune the coil if high power RF is used with improper current biasing. The loops remain resonant during receive when the diodes are not biased. Each loop is connected to an independent DC bias line that provides the 100 mA / 10 VDC or -30 VDC bias current. To avoid biasing the crossed diodes with the negative DC bias, a single diode was added into the bias line so that only positive DC current can be supplied to the loops (Figure 64A). By eliminating the negative DC voltage at the loop, the crossed diodes are not activated during receive.

Passive ^{1}H traps are not used in the ^{23}Na receive loops because they would increase coil resistance, reducing sensitivity. Unfortunately, the match/tune capacitor values are too large to implement active ^{1}H decoupling across those capacitors so no active ^{1}H decoupling is implemented in the ^{23}Na loops. Larger coils or decreased wire thickness could be used to decrease the capacitor values (Table 5); however, this would likely result in reduced ^{23}Na receive sensitivity and the capacitor values would still be too large to implement effective active ^{1}H-decoupling.

Each receive loop is attached to a 60 cm coaxial cable (< 1/10 of the NMR signal wavelength for ^{23}Na at 3 T in the coaxial cable). The long coaxial cable allows the receive circuitry to be placed in a convenient location for patient positioning and comfort.

A ^{23}Na trap on the coaxial cable shield is used to reduce common mode currents in the long cables, and a phase shifter circuit is used to obtain a 180-degree phase shift between the coil and preamplifier to achieve preamplifier decoupling (18).

6.3.1.2 ^{23}Na Transmit Coil

The ^{23}Na transmit coil consists of five co-axial copper loops equally spaced on a 57 mm tall, 178 mm diameter acrylic tube (Figure 63C,D). The loops are connected at their capacitors, making the transmit coil behave like a single-turn solenoid (Figure 63C,D). The capacitors are distributed along the height of the coil to help evenly distribute the current on the cylinder of the coil. The coil has four tuning capacitor junctions. The transmit coil was tuned inside a large copper shield that simulated the radiofrequency (RF) shield in the bore of the scanner. The capacitor values are ~500 pF and ~660 pF for tune and match capacitances, respectively.

Decoupling is achieved by breaking the RF current path with serial diodes in two positions. At each of these two positions, four diodes are placed in parallel, equally spaced along the acrylic tube to distribute current along the height of the coil. The coil is designed so that it is resonant when forward-biased with +100 mA and detuned when unbiased. When forward-biased, the coil remains tuned and the diodes remain on even when high RF transmit power is used (up to many kilowatts) (48-50). As shown in Figure 63D, a fifth diode was placed antiparallel to the original four diodes to protect them from large reverse bias voltages that can occur during transmit resulting in permanent diode breakdown if not properly forward-biased. Loaded isolation between the detuned transmit coil and resonant receive coils was measured to be -39 dB. Loaded isolation between the tuned transmit coil and detuned receive coils was -42 dB.

6.3.1.3 ^{1}H Transceive Array

The inherent drawback of many ^{1}H and ^{23}Na coil configurations is that the ^{23}Na loops have high capacitor values when compared to the ^{1}H loops, creating low impedance loops at the ^{1}H frequency. The low impedance ^{23}Na loops have a shielding effect at the ^{1}H frequency, resulting in ^{1}H flux blockage (191), which is similar to the effect of a solid conducting copper loop. When a ^{23}Na and ^{1}H loop overlap, the ^{1}H loop will be affected by the presence of the ^{23}Na loop to a much greater degree than the ^{23}Na loop will be affected by the presence of the ^{1}H loop. When frequency shift, Q-ratio, and SNR are measured for two overlapping in-plane 65mm diameter ^{1}H and ^{23}Na loops, the ^{23}Na loop will have only minor changes (<1%) when a ^{1}H loop is present, regardless of the center-to-center coil distance. In comparison, the ^{1}H loop Q-ratio decreases with increasing overlap, and ^{1}H frequency greatly increases when the center-to-center distance is less than one radius. The shielding effects of the ^{23}Na loops on the ^{1}H RF can be reduced substantially by intersecting the ^{23}Na loops with the ^{1}H elements (191).

The composite array design employs four local ^{1}H loops arranged as a ladder network (292), with a minimum loaded isolation between any two loops of the coil measured at -9.5 dB. The ^{1}H loops are positioned over the ^{23}Na receive array such that the wire elements of the ^{1}H loops bisect the ^{23}Na loops (Figure 62A & Figure 63A). The ^{1}H loops are mounted 1cm away from the fiberglass former to reduce coupling with the ^{23}Na loops, to fit over ^{23}Na loop circuits, and to improve ^{1}H homogeneity. The tune and match capacitors were adjustable (Series 1111P_P501X, Passive Plus, Huntington Station, NY in conjunction with Series NMA_HV, Voltronics Corp, Salisbury, MD) so that the coil could be tuned/matched without any additional circuitry such as a match inductor (18). The capacitors on the shared rungs were used to minimize coupling

between adjacent loops. The capacitor values are ~30 pF, ~14 pF and ~160 pF for the tune, decoupling and match capacitances, respectively.

The ^{1}H transceive loops contain a crossed diode pair that is forward-biased during ^{1}H transceive but unbiased during ^{23}Na transmission and reception (Figure 63E). The crossed diode pair allows easy tuning/detuning of the ^{1}H loops for further decoupling between the ^{1}H and ^{23}Na loops. The minimum isolation between any ^{23}Na receive loop and ^{1}H loop when the coil was loaded was: -20d B at the ^{23}Na resonant frequency (32 MHz) when the ^{1}H loops were tuned, -37 dB when the ^{1}H loops were detuned; -41 dB at the ^{1}H resonant frequency (123 MHz) when the ^{1}H loops were tuned, and -75 dB when the ^{1}H loops were detuned. The isolation between ^{23}Na and ^{1}H loops was unchanged regardless of whether the ^{23}Na loops were tuned.

The ^{1}H loops each use quarterwave cables that, when combined with the quarterwave cable in the TR switches described below, form a half-wave phase shift between the loops and preamplifiers for optimum preamplifier decoupling.

6.3.1.4 Dual Resonant TR Switching

The scanner provides a single transmit port for both the ^{1}H and ^{23}Na RF transmit signal. The transmit RF is passively filtered with the use of ^{1}H and ^{23}Na traps (Figure 64B) before going into the ^{23}Na transmit switch or ^{1}H power splitter (Figure 64C). The filter attenuates the ^{1}H signal by -39dB on the ^{23}Na output, and the ^{23}Na signal by -47 dB on the ^{1}H output.

After the filter, the ^{23}Na transmit signal passes through a large capacitor before arriving at the cylindrical ^{23}Na transmit coil. A DC bias line inserted between the large capacitor and transmit coil allows the transmit coil to be biased during ^{23}Na transmit with

+100 mA and unbiased during ^{23}Na receive.

The ^{1}H transmit signal is split across four different ports by using 90° hybrid couplers (1J0280-3, Anaren, East Syracuse, NY, USA) to initially divide the signal evenly in half, followed by two more hybrid couplers to divide the signal evenly between four ports (Figure 64C). The isolation port of each coupler is terminated with 50 Ω. Between the initial coupler and one of the secondary couplers, an extra cable length is added to create a 45° phase shift. The four outputs of the power splitter each have equal magnitude but different phase shifts of 0°, 45°, 90°, and 135°. Each output is then connected to a ^{1}H TR switch.

The ^{1}H TR switches are different from standard TR switches, in that they incorporate a reverse diode where only a standard forward diode would typically be used, offering improved protection against incorrect DC biasing (Figure 64D). The TR switches are supplied with a forward current during transmit (DC1 in Figure 64D) to activate the preamplifier protection circuitry, which consists of a quarterwave cable and a diode that is shorted during transmit. A second DC line (DC2 in Figure 64D) was added between the TR switch and the loops, so that the ^{1}H loops can be turned on during ^{1}H transceive. Large DC blocking capacitors are used to ensure that the DC bias that controls the TR switch is independent from the DC bias that controls the loops.

6.3.1.5 ^{23}Na/^{1}H Dual Resonant Trap Coil

Multiple sodium breast MR studies to date have employed ^{23}Na/^{1}H dual resonant trap coils (287,288). To gauge the performance of the composite array design, the composite array is compared to a coil with a single ^{1}H loop concentric with a single ^{23}Na loop that is similar to coils used previously in dual resonant ^{23}Na/^{1}H breast MRI (Figure

65). Both the ^{1}H and ^{23}Na loops are single-turn coils built using 10mm wide copper tape placed on a 65mm tall 133mm diameter acrylic tube. The ^{23}Na loop was positioned so that it would surround the center of the breast with a 10mm gap between the ^{1}H and ^{23}Na loops. The mutual inductance between the ^{1}H and ^{23}Na loops is reduced through a single passive resonant trap in each coil (Figure 65B) (289-291). The traps were tuned prior to insertion into the coil. The ^{23}Na loop has four tuning capacitor junctions with ~390 pF per junction and a match capacitance of ~600 pF. The ^{1}H loop has three tuning capacitor junctions with ~17 pF per junction and a match capacitance of ~42 pF. The ^{1}H trap on the ^{23}Na loop has a 41 pF capacitor and the ^{23}Na trap on the ^{1}H loop has a ~780 pF capacitor. Loaded isolation measured between the ^{1}H and ^{23}Na loops was -30.5 dB at ^{1}H frequency and -14.5 dB at ^{23}Na frequency. The low isolation at ^{23}Na frequency and larger isolation at ^{1}H frequency does not completely indicate the effect of each coil on each other, since the presence of the ^{23}Na coil affects the ^{1}H-SNR far more than the ^{1}H coil affects the ^{23}Na-SNR (191). Switching for both ^{1}H and ^{23}Na channels was done using a dual-resonant TR switch (Stark Contrast, Erlangen, Germany).

The trap coil was compared to a similar dual-tuned coil without traps and to single-tuned coils without traps to consider the effects of $^{1}H/^{23}Na$ coil coupling at 3 T. The ^{23}Na loop on the trap coil received 80% of the SNR of the single-tuned ^{23}Na coil. The SNR performance of the ^{23}Na loop on the dual-tuned coil that contained no traps had no detectable difference from that of the single-tuned ^{23}Na coil. The ^{1}H loop on the trap coil had similar SNR when compared to the single-tuned ^{1}H coil and received 1 to 4 times the SNR of the dual-tuned coil without traps. The primary advantage of the traps is to improve ^{1}H-SNR by reducing ^{23}Na shielding effects, despite the decreased ^{23}Na-SNR caused by the nonzero impedance of the trap (290). When comparing a single resonant

^{1}H loop to a ^{1}H loop on a dual-tuned coil without traps, the dual-tuned coil will have similar ^{1}H-SNR near the ^{1}H loop but will exhibit significant reductions in SNR on the opposite side of the ^{23}Na loop (often losing as much as 75% of the SNR).

Comparisons to the composite array were done with the trap coil design due to the trap coil's use in published ^{23}Na breast studies (276,287,288). The trap coil is placed over a hemispherical fiberglass former similar to the one used with the composite array. During experiments, the coil was placed in a support structure (Figure 62B) (266) such that the subject could lie prone, head first on the scanner table, to reduce respiratory and other motion artifacts. The support structure consists of an acrylic ramp, a flat carbon fiber board that holds the coil, and a head rest. The entire setup is padded for subject comfort during scanning.

6.3.2 Phantom Studies

A fast-gradient spoiled sequence using the 3D cones k-space trajectory was used to image ^{23}Na in a 10cm diameter spherical NaCl/$CuSO_4$ phantom (278). The 3D cones sequence consists of spirals that follow a cone-like trajectory, using cones of many different shapes and sizes to fill k-space for a given resolution and field-of-view (FOV). The 3D cones sequence is used to minimize image blurring and signal loss caused by the short T_2* of ^{23}Na as the trajectory achieves more efficient k-space coverage than radial acquisition trajectories and samples the signal before significant T_2* decay. (79)

Phantom studies were conducted with the composite array fully assembled. A spherical phantom with concentrations of 12 mM $CuSO_4$ and 150 mM NaCl were used. The 3D cones scan parameters were: TR/TE = 50/0.27 ms, flip angle = 70°, voxel size = 2.5x2.5x2.5 mm, FOV = 22.5 cm, cones = 143, shots = 1378, readout time = 9.0 ms,

averages = 75, with a total scan time of ~1.5 hours. A long scan time was chosen to produce images of very high SNR for the phantom study. A 2D GRE sequence was used to image ^{1}H with the following scan parameters: TR = 1000 ms, TE = 3.28 ms, flip angle = 45°, voxel size = 1.0x1.0x3.0 mm, FOV = 250x125x3 mm, averages = 4, total scan time of ~8.5 minutes. All scans were acquired in both the sagittal and axial planes and repeated with both the composite array and trap coil. The final SNR values of the composite array were calculated using the root sum-of-squares from images of the individual coil elements normalized by their noise (18). For statistical analysis of the phantom studies, the FOV was segmented into three regions: [1] a hemispherical region expected to contain the breast tissue of interest (referred to as the volume of interest, or VOI), [2] a region of background noise with no signal-yielding tissue, and [3] a signal-yielding region outside the VOI. Signal homogeneity and SNR were evaluated across the VOI.

While resolution is determined by the point-spread-function of a sequence and not determined by a coil, a resolution phantom was scanned to demonstrate the strength of this setup. The resolution phantom was 3D printed with varying line thicknesses between 1.25 mm and 3.0 mm (Figure 67A,B). The 3D print was inserted into a hemispherical mold that was filled with water, 12 mM $CuSO_4$ and 150 mM NaCl. Coronal ^{23}Na images were obtained with 3D cones using the following scan parameters: TR/TE = 40/0.27 ms, flip angle = 70°, voxel size = 1.25x1.25x4 mm, FOV = 22.4 cm, cones = 80, shots = 1078, readout time = 8.2 ms, averages = 20, with a total scan time of ~20 minutes. A 3D GRE sequence was used to obtain coronal ^{1}H images with the following scan parameters: TR = 15 ms, TE = 5.75 ms, flip angle = 25°, voxel size = 0.23x0.23x0.7 mm, FOV = 180x123x73 mm, averages = 1, total scan time of ~14

minutes.

Transmit flip angle (B_1) maps of the ^{1}H transceive loops were obtained using the dual angle method (225) using a GRE sequence repeated in both the sagittal and axial planes, with scan parameters: TR = 1000 ms, TE = 3.28 ms, FOV = 250x125x3 mm, voxel size = 1.0x1.0x3.0 mm, flip angle = 45°/90°, averages = 4, total scan time = 17 minutes.

B_1 maps of the ^{23}Na transmit coil were obtained using the phase sensitive method (104,108). Sodium B_1 mapping scan parameters were: TR = 100 ms, TE = 15 ms, FOV = 386x145x108 mm, resolution = 128x48x36, voxel size = 3.0 mm isotropic, averages = 30, readout bandwidth = 166 Hz/pixel, EPI factor = 3, total scan time = 58 minutes. The high number of averages used for the ^{23}Na phantom experiment was used to achieve high SNR for the comparisons.

6.4 Human Imaging Studies

Human imaging studies were conducted after informed consent and with approval of the local institutional review board (IRB). A fast-gradient spoiled sequence using the 3D cones k-space trajectory was used for ^{23}Na imaging in the breast of a normal volunteer (278), with the following scan parameters: TR/TE = 40/0.27 ms, flip angle = 70°, voxel size = 1.25x1.25x4 mm, FOV = 22.4 cm, cones = 80, shots = 1078, readout time = 8.2 ms, averages = 20, with a total scan time of ~20 minutes. A standard ^{1}H GRE acquisition was performed to compare ^{1}H-SNR. The GRE scan parameters were: TR = 11 ms, TE = 4.7 ms, flip angle = 15°, voxel size = 0.90x0.90x1.2 mm, FOV = 172x172x88 mm, 1 average, with a total scan time of ~3 minutes. To generate water and fat images using 3-point Dixon, the same ^{1}H GRE acquisition was performed at TE =

5.75 ms and TE = 6.8 ms. All scans were repeated with both the composite array and trap coil. Images were acquired in the sagittal plane. The volunteer was moved when switching coils but not between ^{23}Na and ^{1}H scans. The final images were combined using root sum-of-squares of the individual coil element magnitude images with normalized noise floors (18). The FOV was large enough so that the noise floors could be calculated using slices that contained no signal.

6.5 Results

6.5.1 Phantom Results

6.5.1.1 ^{23}Na-SNR Performance

Within the VOI of the phantom, the composite array had a mean ^{23}Na-SNR of 123±43 and the trap coil had a mean ^{23}Na-SNR of 29±8. An image comparing the central sagittal slice shows an improvement in ^{23}Na-SNR by a factor of five near the expected location of the nipple, and a factor of three or more across most of the remaining breast volume (Figure 66). A histogram created from the voxels within the VOI (Figure 66D) shows that while the spread of ^{23}Na-SNR values is much larger using the composite array, the dramatic improvements in ^{23}Na-SNR are also clearly evident.

The 1.25 mm thick lines are distinguishable on the ^{23}Na images using the resolution phantom (Figure 67C).

6.5.1.2 ^{23}Na Homogeneity

Flip angle maps for ^{23}Na excitation using the ^{23}Na transmit and receive loops are shown in Figure 69. Reasonable homogeneity is observed across the VOI, although some variation is observed, particularly in the center of the coil near the nipple and toward the

edges of the breast.

6.5.1.3 ^{1}H-SNR Performance

The composite array had a mean ^{1}H-SNR of 725±494 and the trap coil had a mean ^{1}H-SNR of 530±224. The ^{1}H-SNR in the composite array relative to the trap coil improved by roughly a factor of two near the ^{1}H loops, although it decreased by 20% near the center of the breast phantom (Figure 70A-C).

6.5.1.4 ^{1}H Homogeneity

The composite array had a mean ^{1}H flip angle of 48±19° and the trap coil had a mean ^{1}H flip angle of 44±12° in the signal-yielding region in the central sagittal slice. The composite array obtains adequate homogeneity in the VOI for GRE images. There is some transmit B_1 focusing near the center of the ^{23}Na loops and transmit B_1 shielding where the ^{23}Na loops overlap (Figure 70E).

6.5.2 Human Imaging Studies

6.5.2.1 ^{23}Na-SNR Performance

Sodium SNR improvements similar to those seen in the phantom study were observed in vivo in a normal human volunteer using the composite array (Figure 71A,C). The fibroglandular tissue in the central sagittal slices of the composite array had a mean ^{23}Na-SNR of 30±18 and the trap coil had a mean ^{23}Na-SNR of 8±3. Improved ^{23}Na-SNR is evident with noticeably improved depiction of small anatomic features within the breast (Figure 72A). The composite array obtains excellent ^{23}Na-SNR over the entire VOI (Figure 72A).

6.5.2.2 ^{1}H-SNR Performance

Both the trap coil and the composite array obtain good ^{1}H images (Figure 71B,D). The signal-yielding region of the breast in the central sagittal slices had a mean ^{1}H-SNR of 32±10 using the composite array and a mean ^{1}Ha-SNR of 24±7 using the trap coil. The in vivo ^{1}H-SNR in the composite array was double that of the trap coil on the edges of the breast and similar throughout most of the breast.

6.6 Discussion

The composite array obtains a 2-5x increase in ^{23}Na-SNR, which is a substantial improvement over anything that has been obtained in the past by single channel coils used in many ^{23}Na breast studies (247,276,287,288). A 2-5x increase in ^{23}Na-SNR translates to a 4-25x decrease in scan time for a given resolution, which can make a dramatic impact on the use of ^{23}Na-MRI, improving the clinical feasibility of breast ^{23}Na-MRI. The in vivo sodium breast images show a level of detail and structure not previously achieved, demonstrating imaging at a 1.25x1.25x4 mm nominal voxel size at 3 T in a scan time of only 20 minutes.

The high ^{23}Na-SNR images of the breast were obtained by using a receive array of small receive loops that are well decoupled from a large, homogeneous transmit coil during both transmit and receive. Although the Q-ratios of the ^{23}Na composite array receive loops (Q-ratio = 1.5) would typically be considered low (293), the loops were still very effective in improving ^{23}Na-SNR.

Superimposing and intersecting the ^{1}H loops with ^{23}Na loops in this array design preserves the high SNR of the ^{23}Na receive array while achieving acceptable ^{1}H image quality. While the composite array has some ^{1}H transmit inhomogeneities due to the

presence of the ^{23}Na receive array, the sensitive volume is reasonably homogeneous (Figure 70E). Although not presented in the paper, when the scanner's body coil or a smaller 135mm circular coil was used to image ^{1}H with the ^{23}Na receive array in place, the ^{1}H images contained signal focusing and signal voids worse than those shown on the ^{1}H-B_1 maps of the composite array. A larger ^{1}H transmit array will not be more homogeneous, since most of the inhomogeneity arises from the shielding effects of the ^{23}Na loops. A ^{1}H ladder coil with more elements should also be investigated as this should improve ^{1}H-SNR due to the smaller ^{1}H elements. The quality of the ^{1}H images produced by our current coil design may not be sufficient to replace a conventional ^{1}H coil for routine breast MRI, but the ^{1}H-SNR is currently sufficient for registration between ^{23}Na and ^{1}H images. A single coil capable of both ^{23}Na and ^{1}H examination with no sacrifice in ^{1}H image quality compared to commercially available ^{1}H coils is the ultimate goal of this work, and this will guide future refinements to the current coil prototype.

The coil has similar safety concerns and benefits when compared to other transceive coils used at 3 T, such as transceive birdcage coils that have high RF voltages relatively close to the subject. Following similar design principles for birdcage coils, the electronics are well insulated and are positioned at a reasonable distance from the subject. The increased flip angles for ^{1}H near the ^{23}Na loops suggests that only low flip angle ^{1}H sequences should be used to avoid heating the subject. Future versions of the coil will address the increased RF deposition near the ^{23}Na loops by either including ^{1}H traps on the ^{23}Na loops, or by using more ^{1}H transceiver segments to reduce the RF focusing caused by the ^{23}Na loops. The use of a transceiver array will result in less RF deposition into the body overall, due the relatively small size of the transceiver array when

compared to the scanner's body coil.

Further improvements to ^{23}Na-MRI using the composite array are still possible. Some improvements include shorter cables between the receive loops and preamplifiers, resulting in reduced cable interactions with the ^{1}H signal; improving preamplifier decoupling; and fiberglass formers that conform better to different breast sizes and shapes. It is uncertain whether the decrease in the transmit ^{23}Na-B_1 near the nipple results from the decoupling circuits (Figure 69). If from the decoupling circuits, placing the decoupling circuits at any other location where less ^{23}Na-SNR is obtained may not be desirable. Better ^{23}Na image quality could likely be obtained using a more optimal multi-coil image reconstruction with noise decorrelation (18,286).

Future work will explore whether higher ^{23}Na resolution can improve detection and evaluation of breast cancer in vivo (277). The improvements in ^{23}Na-SNR will allow better ^{23}Na T_1 and T_2* measurements for the evaluation of lesions, although quantitation of sodium concentrations is still desirable. The experiments in this study did not demonstrate the accuracy with which quantitative measurements of ^{23}Na concentration could be obtained. The low Q-ratios of the ^{23}Na loops suggest that the loops are relatively insensitive to changes in loading (293), so that field profiles obtained with a phantom may potentially be used for accurate quantitation. If necessary, a ^{23}Na transmit flip angle map could be acquired within a few minutes for transmit field correction (108). Receive field profiles could potentially be corrected using sensitivity encoding (SENSE) reconstruction techniques that use the central regions of k-space to estimate coil sensitivities (286,294,295).

The described breast coil is unilateral. However, implementation of a bilateral ^{23}Na receive array for simultaneous imaging of both breasts would be relatively

straightforward. Due to the small diameters of the ^{23}Na loops, the separation between the left and right coil receive elements is expected to be sufficient to avoid any significant loss in performance of a bilateral design vs. the demonstrated unilateral design. Bilateral sodium breast imaging is feasible without additional loss in scan time due to the large number of averages typically performed in ^{23}Na imaging. Increasing the FOV has the same SNR advantage as signal averaging, so in any scenario in which signal averaging is needed, the FOV can be increased without a scan time penalty. For instance, doubling the imaging FOV and reducing the number of averages by a factor of two does not change scan time, resolution, or SNR efficiency.

6.7 Conclusions

This work has demonstrated a 2-5x increase in ^{23}Na-SNR using a novel composite array coil design compared to a single-loop trap coil design, significantly improving breast ^{23}Na-MRI image quality at 3 T. The coil demonstrates an array superposition technique that can improve decoupling between ^{1}H and ^{23}Na array coils, so that excellent ^{23}Na and good ^{1}H images can be obtained without repositioning the subject. The improved SNR of the ^{23}Na composite array gives breast ^{23}Na images of unprecedented quality in reasonable scan times. High quality ^{23}Na images of the breast may improve the specificity of breast MRI for the detection and characterization of breast cancer.

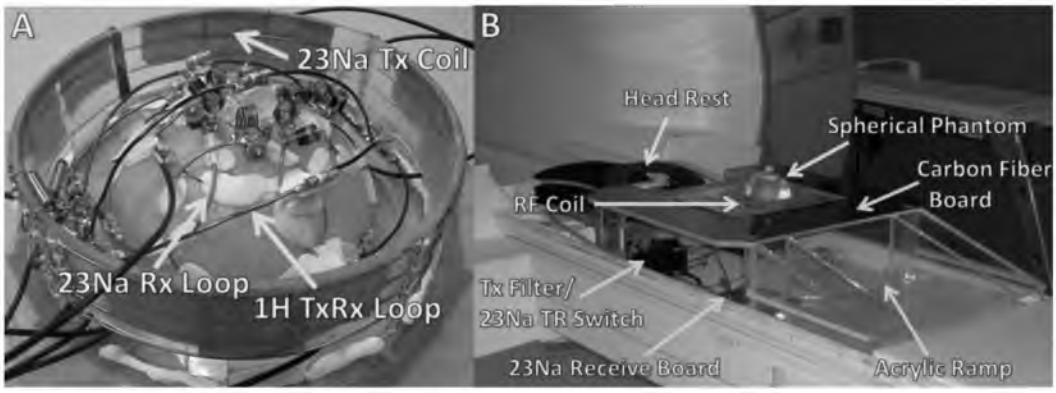

Figure 62. Composite $^{1}H/^{23}Na$ breast array. (A) $^{23}Na/^{1}H$ dual resonant multichannel composite array. (B) Complete (unpadded) patient setup on the scanner table, with a 10 cm spherical phantom placed in the hemispherical fiberglass former. An acrylic ramp and board supports the patient in the prone position. The RF Tx/Rx circuitry is between the scanner table and the patient support device.

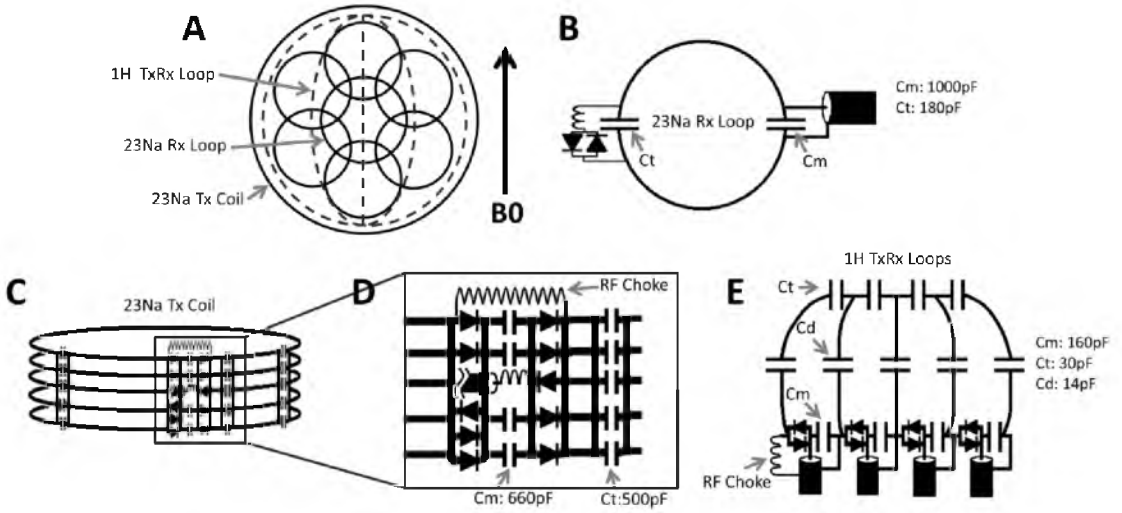

Figure 63. Illustrations of composite array coil. (A) Top view schematic of the composite array coil layout. The proton coil layout is shown in red / dashed. The sodium loops are shown in black / solid. (B) Circuit diagram of the ^{23}Na receive loops. (C) Schematic of the single channel ^{23}Na transmit coil. (D) Enlarged view of the decoupling circuitry for the transmit coil. (E) Warped schematic of the ^{1}H transceive loops. The capacitors for matching, tuning, and decoupling adjacent loops are marked on one loop as Cm, Ct, and Cd, respectively.

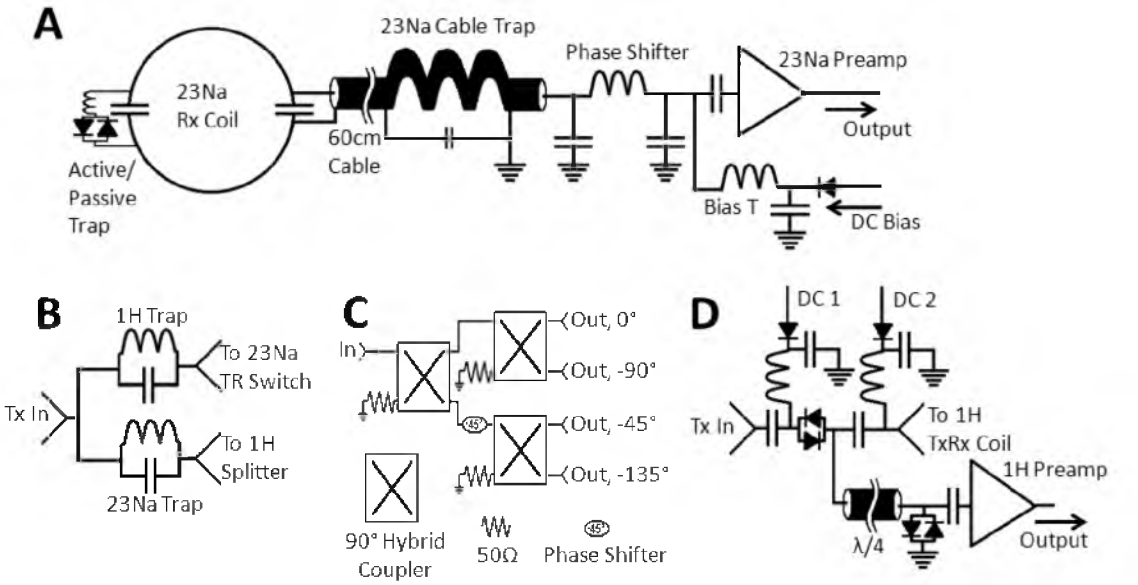

Figure 64. Circuit diagram of transmit/receive electronics. (A) Circuit diagram of the ^{23}Na receive loops and hardware. The active/passive trap was forward-biased during ^{23}Na transmit, detuning the receive loops. The phase shifter completed a half-wave phase shift between the coil and preamp for preamp decoupling of the loop during the receive portion of the pulse sequence. (B) Traps were used to filter the ^{1}H and ^{23}Na Tx RF signal. (C) The ^{1}H 4-way power splitter used three 90° hybrid couplers and a coaxial cable phase shifter to split the transmit power evenly between each element of the ^{1}H transceive array, with each element transmitting at a different phase. (D) The TR switches for the ^{1}H TxRx loops had DC1 forward-biased during transmit, while DC2 was forward-biased during ^{1}H transmit and receive.

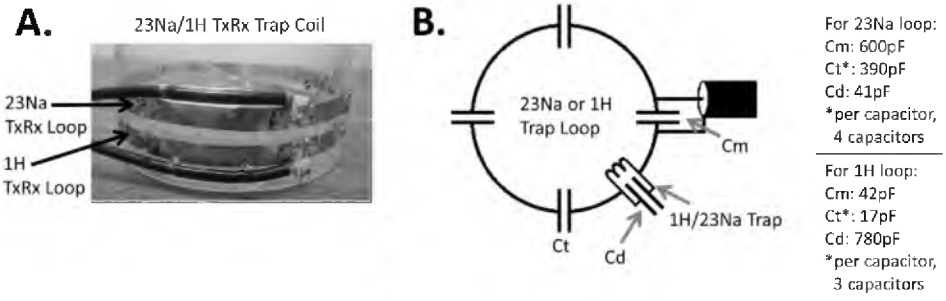

Figure 65. A ^{1}H/^{23}Na trap coil. (A) Picture of the single ^{23}Na and single ^{1}H loop trap coil. (B) Circuit diagram of either ^{23}Na or ^{1}H loop on the trap coil.

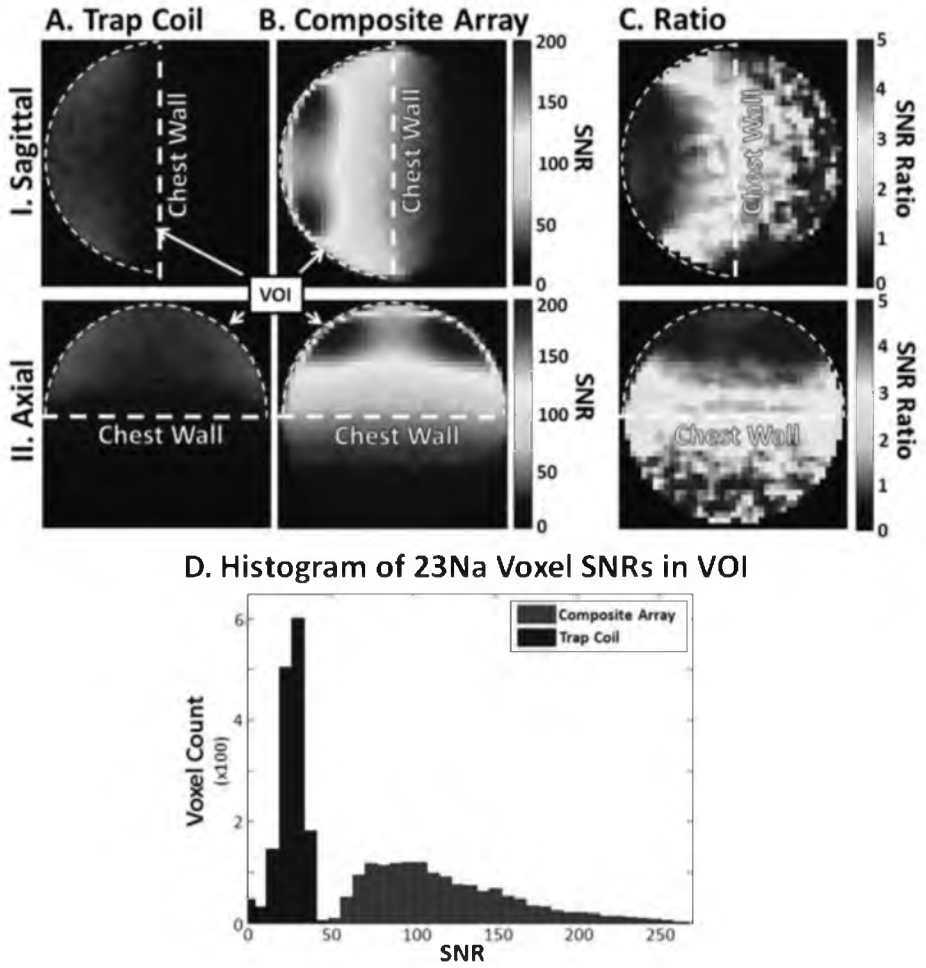

Figure 66. Phantom SNR plots of the sodium channels. Phantom sodium SNR maps of the central (I) sagittal and (II) axial slices using the (A) composite array and (B) trap coil. (C) Ratio of the composite array to trap coil SNRs. (D) Histogram of sodium voxel SNRs obtained from the VOI within the phantom comparing the trap coil (blue) and composite array (red).

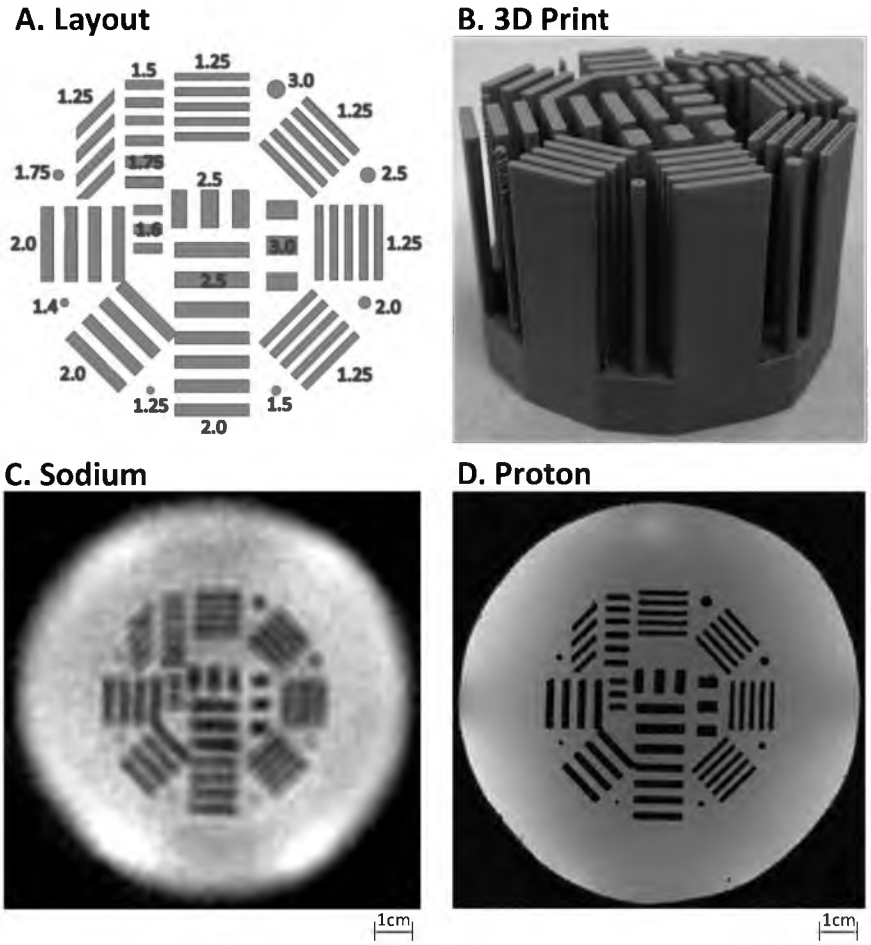

Figure 67. Resolution imaging results. (A) Layout of the lines and gaps in the resolution phantom, with sizes indicated on the schematic. (B) Photograph of the 3D print that was inserted into the phantom solution. (C) Sodium image obtained with the composite array in ~20 minutes. The 1.25 mm lines of the phantom are distinguishable on the sodium image. (D) Proton image obtained with the composite array.

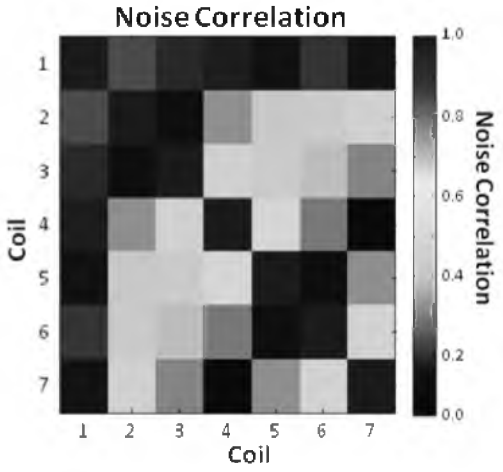

Figure 68. Noise correlation matrix of the sodium receive array.

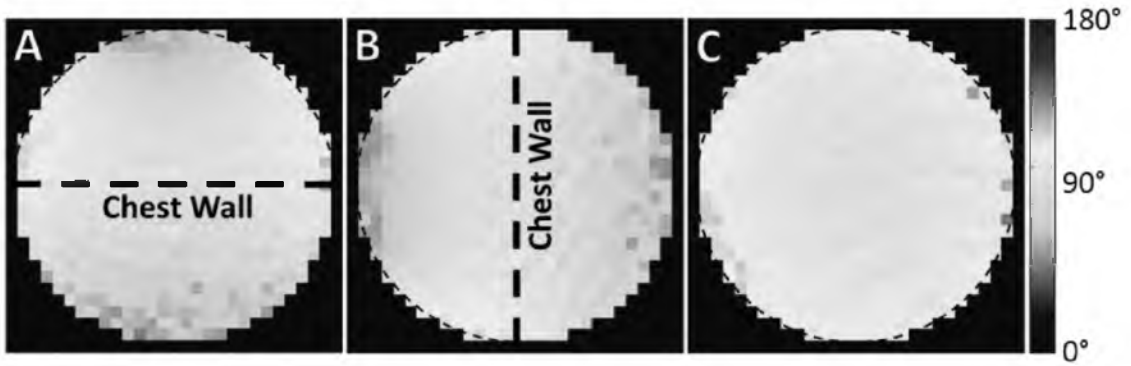

Figure 69. B_1 plots of the sodium transmit coil. (A) Axial, (B) sagittal, and (C) coronal sodium transmit flip angle maps of the central slices from the composite array.

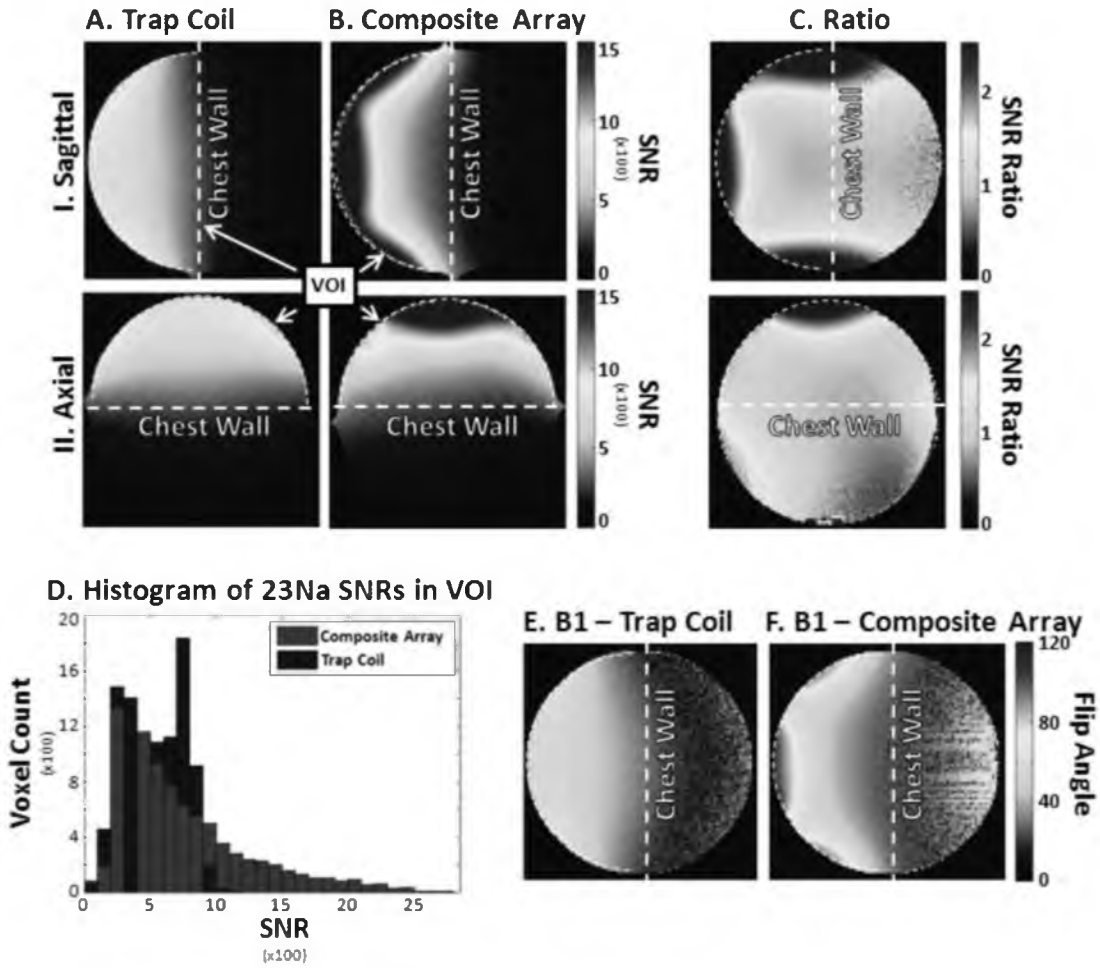

Figure 70. SNR and B_1 plots of the proton channels. Proton SNR maps of the central sagittal slice using the (A) trap coil and (B) composite array. (C) Ratio of the composite array to trap coil SNRs. (D) Histogram of proton voxel SNRs obtained from the phantom comparing the trap coil (blue) and composite array (red). Flip angle maps of the (E) trap coil and (F) composite array.

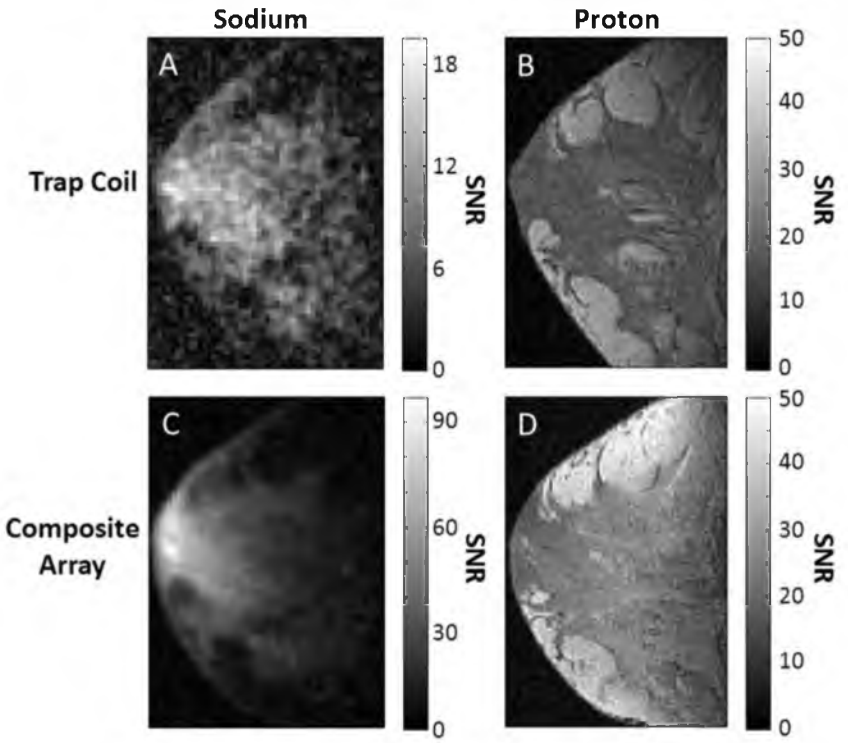

Figure 71. In vivo sodium and proton SNR comparison. In vivo (A,C) sodium and (B,D) proton breast images of a normal volunteer obtained using the (A,B) trap coil and (C,D) composite array.

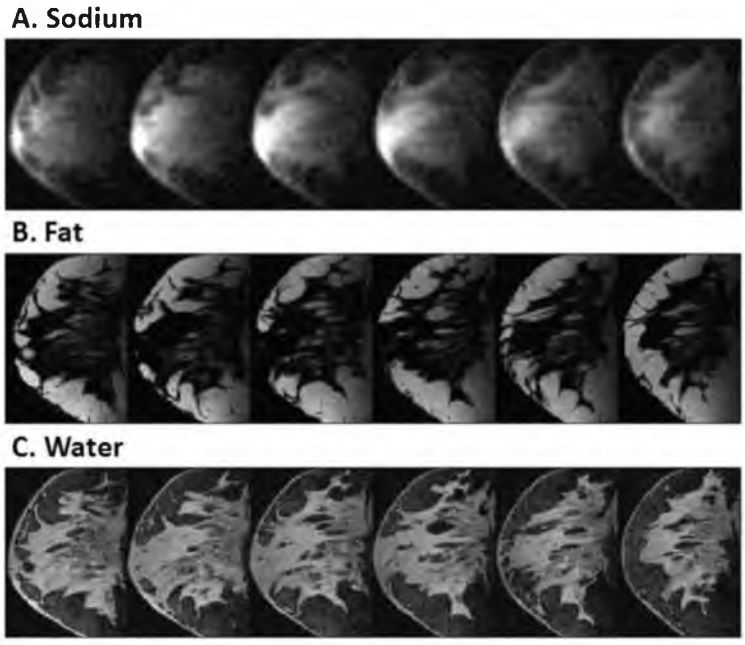

Figure 72. In vivo images from the composite array. Multiple slices of in vivo (A) sodium, (B) water, and (C) fat breast images of a normal volunteer obtained using the composite array. The (B) water and (C) fat images were obtained using 3-point Dixon.

Table 5. Capacitor values and Q-factors for 65 mm diameter resonant loops at 32.60 MHz. Q-unloaded, Q-loaded, and Q-ratio were measured using two stationary magnetic probes and are displayed for 65 mm diameter coils with different wire thicknesses and capacitor segments. The coils were all tuned to 32.60 MHz.

Thickness (AWG)	# Capacitor segments	Capacitance per segment (pF)	$Q_{unloaded}$	Q_{loaded}	Q_{ratio}
20 (thin)	3	391	222	161	1.38
20	2	268	213	160	1.33
16	3	465	263	179	1.47
16	2	295	282	187	1.51

CHAPTER 7

CONCLUSIONS

7.1 Summary

The introduction to this dissertation provided historical background to MRI. The introduction then discussed basic imaging techniques, including the basic principles for imaging with a GRE sequence and using that sequence for B_0 field mapping and for flip angle mapping. The introduction also gave a background to the electromagnetic and electronic analysis that can be used in the creation of RF coils for transmission and reception of the MRI signal. The background discussed basic coils used for MRI. The introduction discussed experiments and simulations of sodium and proton coils that are used together.

A small animal RF coil array was developed, with unique transmit coil detuning techniques, in conjunction with an insertable gradient, that achieved 100μm cochlea images from a live rodent. The insertable gradient, when combined with the body gradients, resulted in double the body gradient strength, slew rate, and contrast-to-noise ratio. The transmit-only and receive phased array coils, integrated with the composite gradients enabled further image improvements, and had twice the signal-to-noise (SNR) when compared to the smallest conforming birdcage.

BOLD MRI T_2* measurements were compared with an invasive oxygen probe for

an initial evaluation of the accuracy of renal BOLD MRI. Hardware was developed for the acquisition of 1 Hz renal oxygenation data inside of an MRI scanner. Invasive oxygen probes were surgically inserted into a live pig kidney. The probes were protected by hardware developed in lab. Oxygen probe measurements were acquired simultaneously with both BOLD MRI and the invasive oxygen probes. This system demonstrated an r-value correlation of 0.6 between T_2* and pO_2. The significance of this experiment is that it demonstrated previously unknown physiological effects on pO_2, such as breath-holds that had an immediate (<1 sec) pO_2 decrease (~6 mmHg), and bladder pressure that had pO_2 increases (~6 mmHg). These pO_2 differences are on the same order as the differences with the administration of furosemide, which, in conjunction with renal BOLD MRI, is being investigated as a diagnosis of chronic kidney disease. Better investigative tools of renal pO_2 will enable better models of renal T_2*, and will ultimately improve the utility of renal BOLD MRI.

A retrospective statistical analysis of renal fat content, as determined through in- and out-of-phase imaging with MRI, was compared against eGFR, BMI, serum cystatin C, and urine protein, to determine whether renal fat content is an indicator of renal health. The results of the study gave nearly zero correlation ($R^2 < 0.03$) between renal fat and these other indicators with a sample size of ~ 100 people, which is an opposite result obtained from a diabetic mouse model. This study suggests that renal fat content will not be a useful indicator of renal health.

A system was developed, including hardware and pulse sequences, that enabled the simultaneous acquisition of sodium and proton images. This system required the development of dual-tuned RF coils, TR switches that incorporated frequency mixing, pulse sequences that incorporated both sequential proton and sodium transmit pulses, and

reconstruction techniques that corrected an introduced phase error. While there are other systems that can do synchronous multinuclear imaging (SMI), they are prohibitively expensive and require internal modification of the MRI system. Our system demonstrated a very simple, inexpensive solution to SMI and acquired both nuclei on two ^{23}Na channels using external modifications. In addition, our implementation of SMI demonstrated flexibility in scan parameters that has not been previously shown, obtaining ^{23}Na-GRE images synchronously with ^{1}H-SE and ^{1}H-GRE images with flexibility in ^{1}H repetition times. Ours is also the first demonstration of radially acquired SMI for efficient sampling of ^{23}Na before significant T_2* signal decay.

A composite sodium and proton array was developed and unique decoupling techniques were introduced. The composite array demonstrated a 2-5x improvement in sodium SNR and similar proton SNR when compared to a large coil with a linear sodium and linear proton channel. This coil is unique in that sodium receive loops are typically built with at least twice the diameter so that they do not have similar SNR increases. The sodium array enabled unprecedented breast sodium images, while still obtaining good proton images.

7.2 Future and Current Work

The small animal system was used as an initial evaluation of obtaining animal cochlea images. The use of small animal systems allows for the evaluation of imaging techniques on relatively inexpensive rodents, when compared with human imaging. The ultimate goal of this work is to extend similar techniques to obtain high quality human cochlea images. Human cochlea images could be obtained with other sequences, although the use of the GRE sequence in this work allowed for the visualization of

gadolinium that transits within the guinea pig cochlea. Current work at UCAIR is focused on improving human cochlea imaging. Future work could include using GRE imaging of gadolinium and acquiring the time-transit of the gadolinium as it disperses through various cochlear chambers.

The BOLD MRI T_2* measurements correlated with the invasive oxygenation measurements. Future work needs to be done to further determine all the causes to changes in renal oxygenation. Higher temporally resolved T_2* measurements should be done to further evaluate BOLD MRI and to help determine all the confounding factors in BOLD MRI. Better BOLD MRI data that have fewer susceptibility artifacts need to be obtained, which may be obtained with closer RF coils and with oxygen probes that induce fewer susceptibility artifacts.

Renal fat content did not correlate with eGFR, BMI, serum cystatin C, or urine protein. This study does not invalidate a previous study on fat in rodent kidneys, but suggests that there may be more complicated environmental factors in human kidneys. Lipotoxicity is a confirmed effect in kidneys, and so some effect may be measured using more sensitive techniques, such as IDEAL or 3-point Dixon fat imaging. A rodent population can be more controlled than a human population. The high number (~ 100) of subjects suggests that any effects in humans would be slight, if they exist at all. Similar to the BOLD T_2* measurements, there may be more confounding factors than just fat content, and it may be that fat imaging could correlate with eGFR with the addition of other variables, such as T_2* or diffusion coefficients.

The simultaneous imaging system has a huge potential for usefulness, due to its relatively inexpensive cost and lack of other universities' research into such systems. The system is capable of usage for nuclei besides sodium and proton. The system could

be expanded to simultaneously image more than just two nuclei. The vast majority of MRI research has been on single nuclear specie, particularly on protons. SMI will require the clever reimplementation of many proton sequences to obtain optimum images from the separate specie. SMI reduces the flexibility of any single nuclei's scan parameter choice, at the advantage of obtaining more data. SMI has no theoretical limit to how many nuclei can be imaged. SMI may prove useful in obtaining more information that simply improves the proton data – for example, a sodium phase map could be used to obtain B_1, B_0, or temperature map while the proton data could be doing diffusion weighted imaging. There is a vast amount of potential in SMI research, as there are opportunities for implementing unique coils and sequences, and the techniques developed for SMI could prove useful for proton imaging in unexpected ways. At the minimum, the system can be improved with better graphical interfaces and more robust hardware to become easier for researchers to use.

And, the final paper presented a dual-tuned array for obtaining excellent sodium images and good proton images. The most important future work is studying sodium concentration and relaxation parameters of cancers at higher resolutions than has previously been done. Sodium imaging has not been proven to be useful, and it may be many years before sodium imaging becomes part of a clinical routine, if ever. Currently, there is a study on sodium breast cancer patients to evaluate the sodium content of the cancer and observe if there is any correlation between sodium content and the type of cancer.

Further improvements may be possible to the composite sodium / proton coil, as the coil was developed as a proof of concept and not the end goal. Additionally, the hydrogen portion of the coil was added on as a secondary goal and not a primary goal.

Nonpublished studies seem to indicate that sodium coils made of copper tape may obtain higher SNR than those of copper wire, which could give an increased 10% boost to the coil's SNR. The coil may also perform better with shorter connections between the preamplifiers and the coils, which may result in higher preamplifier decoupling, reduced resonance changes to the proton coils, and reduced signal loss from the long cable length. The use of lower impedance preamplifiers could reduce the coupling between sodium coils, improving SNR further.

APPENDIX

PHASE RELATIONSHIP DURING MIXING

The mixer acts as a frequency multiplier between the ^{1}H MR signal $S(t) = S_0 e^{-t/T_2^*} \cos(\omega t + \theta(t))$ with a time-varying phase error $\theta(t)$ and the synthesizer signal $S_s(t) = S_s^o \cos(\omega_s t + \theta_s^o)$ with an initial phase θ_s^o:

$$\begin{aligned} S(t) \cdot S_s(t) &= S_o S_s^o e^{-t/T_2^*} \cos(\omega t + \theta(t)) \cos(\omega_s t + \theta_s^o) \\ &= \frac{1}{2} S_o S_s^o e^{-t/T_2^*} (\cos((\omega + \omega_s)t + \theta(t) + \theta_s^o) + \cos((\omega - \omega_s)t + \theta(t) - \theta_s^o)) \end{aligned} \tag{1.77}$$

After low-pass filtering, the converted signal becomes,

$$S'(t) = \frac{1}{2} S_o S_s^o e^{-t/T_2^*} \cos((\omega - \omega_s)t + \theta(t) - \theta_s^o) . \tag{1.78}$$

Equation (1.78) indicates that the converted ^{1}H signal retains the same phase error $\theta(t)$ as in the original ^{1}H signal and also amplified by the amplitude of the reference signal.

REFERENCES

1. Lubovsky O, Liebergall M, Mattan Y, Weil Y, Mosheiff R. Early diagnosis of occult hip fractures: MRI versus CT scan. Injury 2005;36(6):788-792.

2. Aisen AM, Martel W, Braunstein EM, McMillin KI, Phillips WA, Kling T. MRI and CT evaluation of primary bone and soft-tissue tumors. Am J Roentgenology 1986;146(4):749-756.

3. Kalita J, Misra U. Comparison of CT scan and MRI findings in the diagnosis of Japanese encephalitis. J Neurological Sci 2000;174(1):3-8.

4. Iyer VR, Lee SI. MRI, CT, and PET/CT for ovarian cancer detection and adnexal lesion characterization. Am J Roentgenology 2010;194(2):311-321.

5. Duyn JH. The future of ultra-high field MRI and fMRI for study of the human brain. Neuroimage 2012;62(2):1241-1248.

6. Klein A, Andersson J, Ardekani BA, Ashburner J, Avants B, Chiang M-C, Christensen GE, Collins DL, Gee J, Hellier P. Evaluation of 14 nonlinear deformation algorithms applied to human brain MRI registration. Neuroimage 2009;46(3):786-802.

7. Frangi AF, Niessen WJ, Viergever MA. Three-dimensional modeling for functional analysis of cardiac images, a review. IEEE Trans Medl Imag 2001;20(1):2-5.

8. Kuhl C. MRI of breast tumors. Eur Radiol 2000;10(1):46-58.

9. Rode A, Bancel B, Douek P, Chevallier M, Vilgrain V, Picaud G, Henry L, Berger F, Bizollon T, Gaudin J-L. Small nodule detection in cirrhotic livers: evaluation with US, spiral CT, and MRI and correlation with pathologic examination of explanted liver. J Comput Assist Tomogr 2001;25(3):327-336.

10. Röntgen WC. On a new kind of rays. Science 1896;3(59):227-231.

11. Rabi II. Space quantization in a gyrating magnetic field. Phys Rev 1937;51(8):652-654.

12. Carr HY. Field gradients in early MRI. Physics Today 2004;57(7):83-83.

13. Damadian R. Tumor detection by nuclear magnetic resonance. Science 1971;171(3976):1151-1153.

14. Lauterbur PC. Image formation by induced local interactions: examples employing nuclear magnetic resonance. Nature 1973;242(5394):190-191.

15. Mansfield P, Maudsley A. Medical imaging by NMR. Br J Radiol 1977;50(591):188-194.

16. Damadian R, Goldsmith M, Minkoff L. NMR in cancer: XVI. FONAR image of the live human body. Physiol Chem Phys 1977;9(1):97.

17. Steckner M. Advances in MRI equipment design, software, and imaging procedures. Med Phys 2006;33(6):2156-2157.

18. Roemer PB, Edelstein WA, Hayes CE, Souza SP, Mueller OM. The NMR phased array. Magn Reson Med 1990;16(2):192-225.

19. Gold GE, Thedens DR, Pauly JM, Fechner K, Bergman G, Beaulieu CF, Macovski A. MR imaging of articular cartilage of the knee: new methods using ultrashort TEs. Am J Roentgenology 1998;170(5):1223-1226.

20. Kaggie, J. D., Hadley, J. R., Badal, J., Campbell, J. R., Park, D. J., Parker, D. L., Morrell, G., Newbould, R. D., Wood, A. F. and Bangerter, N. K., A 3 T sodium and proton composite array breast coil. Magn Reson Med 2014;71: 2231–2242.

21. Lee SW, Hilal SK, Cho ZH. A multinuclear magnetic resonance imaging technique--simultaneous proton and sodium imaging. Magn Reson Imaging 1986;4(4):343-350.

22. Keupp J, Rahmer J, Grässlin I, Mazurkewitz PC, Schaeffter T, Lanza GM, Wickline SA, Caruthers SD. Simultaneous dual-nuclei imaging for motion corrected detection and quantification of 19F imaging agents. Magn Reson Med 2011;66(4):1116-1122.

23. Cooley JW, Tukey JW. An algorithm for the machine calculation of complex Fourier series. Math Comp 1965;19(90):297-301.

24. Weinstein S, Ebert P. Data transmission by frequency-division multiplexing using the discrete Fourier transform. IEEE Trans Commun Technol 1971;19(5):628-634.

25. Atkinson DJ, Edelman R. Cineangiography of the heart in a single breath hold with a segmented turboFLASH sequence. Radiology 1991;178(2):357-360.

26. Pelc NJ, Herfkens RJ, Shimakawa A, Enzmann DR. Phase contrast cine magnetic resonance imaging. Magn Reson Q 1991;7(4):229-254.

27. Dutt A, Rokhlin V. Fast Fourier transforms for nonequispaced data. SIAM J Sci Comput 1993;14(6):1368-1393.

28. Duijndam A, Schonewille M. Nonuniform fast Fourier transform. Geophysics 1999;64(2):539-551.

29. Hoult DI, Richards RE. The signal-to-noise ratio of the nuclear magnetic resonance experiment. J Magn Reson 1976;24(1):71-85.

30. Hoult D, Lauterbur PC. The sensitivity of the zeugmatographic experiment involving human samples. J Magn Reson 1979;34(2):425-433.

31. Edelstein W, Bottomley P, Hart H, Smith L. Signal, noise, and contrast in nuclear magnetic resonance (NMR) imaging. J Comput Assist Tomo 1983;7(3):391-401.

32. Hart Jr H, Bottomley P, Edelstein W, Karr S, Leue W, Mueller O, Redington R, Schenck J, Smith L, Vatis D. Nuclear magnetic resonance imaging: contrast-to-noise ratio as a function of strength of magnetic field. Am J Roentgenology 1983;141(6):1195-1201.

33. Parker DL, Gullberg GT. Signal-to-noise efficiency in magnetic resonance imaging. Med Phys 1990;17(2):250-257.

34. Bradley Jr W, Kortman K, Crues J. Central nervous system high-resolution magnetic resonance imaging: effect of increasing spatial resolution on resolving power. Radiology 1985;156(1):93-98.

35. Pedersen M, Dissing TH, Mørkenborg J, Stødkilde-Jørgensen H, Hansen LH, Pedersen LB, Grenier N, Frøkiaer J. Validation of quantitative BOLD MRI measurements in kidney: application to unilateral ureteral obstruction. Kidney Int 2005;67(6):2305-2312.

36. Warner L, Glockner JF, Woollard J, Textor SC, Romero JC, Lerman LO. Determinations of renal cortical and medullary oxygenation using blood oxygen level-dependent magnetic resonance imaging and selective diuretics. Invest Radiol 2011;46(1):41-47.

37. Ries M, Basseau F, Tyndal B, Jones R, Deminière C, Catargi B, Combe C, Moonen CW, Grenier N. Renal diffusion and BOLD MRI in experimental diabetic nephropathy. Blood oxygen level-dependent. J Magn Reson Imaging 2003;17(1):104-113.

38. Textor SC, Glockner JF, Lerman LO, Misra S, McKusick MA, Riederer SJ, Grande JP, Gomez SI, Romero JC. The use of magnetic resonance to evaluate tissue oxygenation in renal artery stenosis. J Am Soc Nephrol 2008;19(4):780-788.

39. Juillard L, Lerman LO, Kruger DG, Haas JA, Rucker BC, Polzin JA, Riederer SJ, Romero JC. Blood oxygen level-dependent measurement of acute intra-renal ischemia. Kidney Int 2004;65(3):944-950.

40. Gloviczki ML, Glockner JF, Lerman LO, McKusick MA, Misra S, Grande JP, Textor SC. Preserved oxygenation despite reduced blood flow in poststenotic kidneys in human atherosclerotic renal artery stenosis. Hypertension 2010;55(4):961-966.

41. Epstein FH, Veves A, Prasad PV. Effect of diabetes on renal medullary oxygenation during water diuresis. Diabetes Care 2002;25(3):575-578.

42. Priatna A, Epstein FH, Spokes K, Prasad PV. Evaluation of changes in intrarenal oxygenation in rats using multiple gradient-recalled echo (mGRE) sequence. J Magn Reson Imaging 1999;9(6):842-846.

43. Prasad PV, Edelman RR, Epstein FH. Noninvasive evaluation of intrarenal oxygenation with BOLD MRI. Circulation 1996;94(12):3271-3275.

44. Chang JS, Taouli B, Salibi N, Hecht EM, Chin DG, Lee VS. Opposed-phase MRI for fat quantification in fat-water phantoms with 1H MR spectroscopy to resolve ambiguity of fat or water dominance. AJR Am J Roentgenol 2006;187(1):W103-106.

45. Bobulescu IA. Renal lipid metabolism and lipotoxicity. Curr Opin Nephrol Hypertens 2010;19(4):393-402.

46. Peng XG, Bai YY, Fang F, Wang XY, Mao H, Teng GJ, Ju S. Renal lipids and oxygenation in diabetic mice: Noninvasive quantification with MR imaging. Radiology 2013;269(3):748-757.

47. Boada FE, Gillen JS, Shen GX, Chang SY, Thulborn KR. Fast three dimensional sodium imaging. Magn Reson Med 1997;37(5):706-715.

48. Leenov D. The silicon PIN diode as a microwave radar protector at megawatt levels. IEEE Trans Electron Devices 1964;11(2):53-61.

49. Li L, Sotak CH. An efficient technique for decoupling NMR transmit coils from surface-coil receivers. J Magn Reson 1964;93(1):207-213.

50. Doherty WE, Joos RD. The Pin diode circuit designers' handbook. Watertown: Microsemi; 1999.

51. Liang Z-P, Lauterbur PC. Principles of magnetic resonance imaging: a signal processing perspective. Bellingham, Wash: SPIE Optical Engineering Press; 2000.

52. Hipps K, Vij D. Handbook of applied solid state spectroscopy. Scanning Tunneling Spectroscopy 2006:1-33.

53. Haacke EM, Brown RW, Thompson MR, Venkatesan R. Magnetic resonance imaging. Physical Principles and Sequence Design; 1999.

54. Sharma B. Spectroscopy. Meerut, India: Krishna Prakashan Media; 1981.

55. Oldfield E, Chapman D, Derbyshire W. Deuteron resonance: a novel approach to the study of hydrocarbon chain mobility in membrane systems. Febs Letters 1971;16(2):102-104.

56. Keller CE, Piersma BJ, Mains GJ, Carper WR. Determination of nuclear quadrupole coupling constants in 1: 2 LiCl-Ethylaluminum dichloride solutions. Inorg Chem 1994;33(24):5601-5603.

57. Bertini I, Luchinat C. NMR of paramagnetic molecules in biological systems. Menlo Park: Benjamin/Cummings Publishing Company; 1986.

58. Holzmann R, Loiselet M, Van Hove MA, Vervier J. High-spin states in 157, 158Er and 158, 159Tm. Phys Rev C 1985;31(2):421-442.

59. Slichter CP. Principles of magnetic resonance. New York: Springer Series in Solid-State Sciences; 1990.

60. Siegel HP. Inadequacy of the gyromagnetic theorem. Am J Phys 1976;44(4):344-347.

61. Pollack GL, Stump DR. Electromagnetism. Boston: Addison-Wesley; 2002.

62. Landau L, Lifshitz E. Statistical physics, Part 1. Vol 5. Waltham: Butterworth-Heinemann;1980.

63. Bloembergen N, Purcell EM, Pound RV. Relaxation effects in nuclear magnetic resonance absorption. Phys Rev 1948;73(7):679.

64. Pervushin K, Riek R, Wider G, Wüthrich K. Attenuated T2 relaxation by mutual cancellation of dipole–dipole coupling and chemical shift anisotropy indicates an avenue to NMR structures of very large biological macromolecules in solution. Proceedings of the National Academy of Sciences 1997;94(23):12366-12371.

65. Hubbard PS. Nonexponential nuclear magnetic relaxation by quadrupole interactions. J Chem Phys 1970;53(3):985-987.

66. Brüschweiler R, Ernst RR. Molecular dynamics monitored by cross-correlated cross relaxation of spins quantized along orthogonal axes. J Chem Phys 1992;96(3):1758-1766.

67. Yablonskiy DA, Haacke EM. Theory of NMR signal behavior in magnetically inhomogeneous tissues: the static dephasing regime. Magn Reson Med 1994;32(6):749-763.

68. Hernando D, Liang ZP, Kellman P. Chemical shift-based water/fat separation: a comparison of signal models. Magn Reson Med 2010;64(3):811-822.

69. Bloch F. Nuclear induction. Phys Rev 1946;70(7-8):460.

70. Schenck JF. The role of magnetic susceptibility in magnetic resonance imaging: MRI magnetic compatibility of the first and second kinds. Med Phys 1996;23(6):815-850.

71. Sacolick LI, Wiesinger F, Hancu I, Vogel MW. B1 mapping by Bloch-Siegert shift. Magn Reson Med 2010;63(5):1315-1322.

72. Pruessmann KP, Weiger M, Scheidegger MB, Boesiger P. SENSE: sensitivity encoding for fast MRI. Magn Reson Med 1999;42(5):952-962.

73. Elster AD. Gradient-echo MR imaging: techniques and acronyms. Radiology 1993;186(1):1-8.

74. Ernst RR, Bodenhausen G, Wokaun A. Principles of nuclear magnetic resonance in one and two dimensions. Vol. 14. Oxford: Clarendon Press; 1987.

75. Bydder G, Pennock J, Steiner R, Khenia S, Payne J, Young I. The short TI inversion recovery sequence—an approach to MR imaging of the abdomen. Magn Reson Imag 1985;3(3):251-254.

76. Edelman RR, Wielopolski P, Schmitt F. Echo-planar MR imaging. Radiology 1994;192(3):600-612.

77. Deichmann R, Josephs O, Hutton C, Corfield D, Turner R. Compensation of susceptibility-induced BOLD sensitivity losses in echo-planar fMRI imaging. Neuroimage 2002;15(1):120-135.

78. Rahmer J, Börnert P, Schröder C, Stehning C. 3D Radial FID-sampling for ultrashort TE imaging at 3 T. Proceedings of the 12th Annual Meeting of the ISMRM, Kyoto, Japan. 2004.

79. Gurney PT, Hargreaves BA, Nishimura DG. Design and analysis of a practical 3D cones trajectory. Magn Reson Med 2006;55(3):575-582.

80. O'Sullivan J. A fast sinc function gridding algorithm for Fourier inversion in computer tomography. IEEE Trans Med Imag 1985;4(4):200-207.

81. Jackson JI, Meyer CH, Nishimura DG, Macovski A. Selection of a convolution function for Fourier inversion using gridding [computerised tomography application]. IEEE Trans Med Imag 1991;10(3):473-478.

82. Kunis S, Potts D. Time and memory requirements of the nonequispaced FFT. Techn. Univ., Fak. für Mathematik; 2006.

83. Sarty GE, Bennett R, Cox RW. Direct reconstruction of non-Cartesian k-space data using a nonuniform fast Fourier transform. Magn Reson Med 2001;45(5):908-915.

84. Gertner I. A new efficient algorithm to compute the two-dimensional discrete Fourier transform. Trans Acoust, Speech, Signal Processing 1988;36(7):1036-1050.

85. Ware AF. Fast approximate Fourier transforms for irregularly spaced data. SIAM Review 1998;40(4):838-856.

86. Samsonov A, Block WF, Field AS. Reconstruction of MRI data using sparse matrix inverses. Signals, Systems and Computers. ACSSC 2007. Conference Record of the Forty-First Asilomar Conference on. IEEE, 2007; 1884-1887.

87. Cannon B, Nedergaard J. Developmental biology: neither fat nor flesh. Nature 2008;454(7207):947-948.

88. Hu HH, Kim HW, Nayak KS, Goran MI. Comparison of fat–water MRI and single-voxel MRS in the assessment of hepatic and pancreatic fat fractions in humans. Obesity 2010;18(4):841-847.

89. Brix G, Heiland S, Bellemann ME, Koch T, Lorenz WJ. MR imaging of fat-containing tissues: valuation of two quantitative imaging techniques in comparison with localized proton spectroscopy. Magnetic Resonance Imaging 1993;11(7):977-991.

90. Dixon WT. Simple proton spectroscopic imaging. Radiology 1984;153(1):189-194.

91. Semelka RC, Chew W, Hricak H, Tomei E, Higgins CB. Fat-saturation MR imaging of the upper abdomen. Am J Roentgenology 1990;155(5):1111-1116.

92. Reeder SB, McKenzie CA, Pineda AR, Yu H, Shimakawa A, Brau AC, Hargreaves BA, Gold GE, Brittain JH. Water-fat separation with IDEAL gradient-echo imaging. J Magn Reson Imaging 2007;25(3):644-652.

93. Glover G, Schneider E. Three-point dixon technique for true water/fat decomposition with B0 inhomogeneity correction. Magn Reson Med 1991;18(2):371-383.

94. Ogawa S, Lee TM, Nayak AS, Glynn P. Oxygenation-sensitive contrast in magnetic resonance image of rodent brain at high magnetic fields. Magn Reson Med 1990;14(1):68-78.

95. Sahu SC, Simplaceanu V, Gong Q, Ho NT, Tian F, Prestegard JH, Ho C. Insights into the solution structure of human deoxyhemoglobin in the absence and presence of an allosteric effector. Biochem 2007;46(35):9973-9980.

96. Thulborn KR, Waterton JC, Matthews PM, Radda GK. Oxygenation dependence of the transverse relaxation time of water protons in whole blood at high field. Biochim Biophys Acta 1982;714(2):265-270.

97. Kwong KK, Belliveau JW, Chesler DA, Goldberg IE, Weisskoff RM, Poncelet BP, Kennedy DN, Hoppel BE, Cohen MS, Turner R. Dynamic magnetic resonance imaging of human brain activity during primary sensory stimulation. Proceedings of the National Academy of Sciences 1992;89(12):5675-5679.

98. Ogawa S, Tank DW, Menon R, Ellermann JM, Kim SG, Merkle H, Ugurbil K. Intrinsic signal changes accompanying sensory stimulation: functional brain mapping with magnetic resonance imaging. Proceedings of the National Academy of Sciences 1992;89(13):5951-5955.

99. Feig E, Greenleaf F, Perlin M. Magnetic resonance imaging with non-uniform fields. Phys Med Biol 1986;31(10):1091.

100. Prammer MG, Haselgrove JC, Shinnar M, Leigh JS. A new approach to automatic shimming. J Magn Reson 1988;77(1):40-52.

101. Herráez MA, Burton DR, Lalor MJ, Gdeisat MA. Fast two-dimensional phase-unwrapping algorithm based on sorting by reliability following a noncontinuous path. Applied Optics 2002;41(35):7437-7444.

102. Abdul-Rahman H, Gdeisat M, Burton D, Lalor M. Fast three-dimensional phase-unwrapping algorithm based on sorting by reliability following a non-continuous path. International Society for Optics and Photonics, 2005; 32-40.

103. Adriany G. Transmit arrays and circuitry. Proceedings of the 22nd Annual Meeting of the ISMRM, Milan, Italy, 2014.

104. Morrell GR. A phase-sensitive method of flip angle mapping. Magn Reson Med 2008;60(4):889-894.

105. Simmons A, Tofts PS, Barker GJ, Arridge SR. Sources of intensity nonuniformity in spin echo images at 1.5 T. Magn Reson Med 1994;32(1):121-128.

106. Kanal E, Shellock FG, Talagala L. Safety considerations in MR imaging. Radiology 1990;176(3):593-606.

107. Insko EK, Bolinger L. Mapping of the radiofrequency field. J Magn Reson A 1993;103(1):82-85.

108. Allen SP, Morrell GR, Peterson B, Park D, Gold GE, Kaggie JD, Bangerter NK. Phase-sensitive sodium B1 mapping. Magn Reson Med 2011;65(4):1125-1130.

109. Park DJ, Bangerter NK, Javed A, Kaggie J, Khalighi MM, Morrell GR. A statistical analysis of the Bloch-Siegert B1 mapping technique. Phys Med Biol 2013;58(16):5673-5691.

110. Cosmus TC, Parizh M. Advances in whole-body MRI magnets. IEEE Trans Appl Supercond 2011;21(3):2104-2109.

111. Hennig J, Speck O. High-field MR imaging. Berlin Heidelberg: Springer; 2011.

112. Lvovsky Y, Stautner EW, Zhang T. Novel technologies and configurations of superconducting magnets for MRI. Supercond Science Technol 2013;26(9):093001.

113. Lvovsky Y, Jarvis P. Superconducting systems for MRI-present solutions and new trends. IEEE Trans Appl Supercond 2005;15(2):1317-1325.

114. Barth C. High temperature superconductor cable concepts for fusion magnets. Karlsruhe: KIT Scientific Publishing; 2013.

115. Hornak JP. The basics of MRI. JP Hornak. http://www.cis.rit.edu/htbooks/mri/: Interactive Learning Software; 2008.

116. Morich MA, Lampman D, Dannels W, Goldie F. Exact temporal eddy current compensation in magnetic resonance imaging systems. IEEE Trans Med Imag 1988;7(3):247-254.

117. Reilly J. Peripheral nerve stimulation by induced electric currents: exposure to time-varying magnetic fields. Med Biol Eng Comput 1989;27(2):101-110.

118. Vogt FM, Ladd ME, Hunold P, Mateiescu S, Hebrank FX, Zhang A, Debatin JrF, Göhde SC. Increased time rate of change of gradient fields: effect on peripheral nerve stimulation at clinical MR imaging 1. Radiology 2004;233(2):548-554.

119. Irnich W, Schmitt F. Magnetostimulation in MRI. Magn Reson Med 1995;33(5):619-623.

120. Goodrich KC, Hadley JR, Moon SM, Chronik BA, Scholl TJ, Debever JT, Parker DL. Design, fabrication and testing of an insertable double-imaging-region gradient coil. Concepts Magn Reson Part B Magn Reson Eng 2009;35B(2):98-105.

121. Parker DL, Goodrich KC, Hadley JR, Kim SE, Moon SM, Chronik BA, Fontius U, Schmitt F. Magnetic resonance imaging with composite (dual) gradients. Concepts Magn Reson Part B Magn Reson Eng 2009;35(2):89-97.

122. Kao Y-H, MacFall JR. Correction of MR k-space data corrupted by spike noise. IEEE Trans Med Imag 2000;19(7):671-680.

123. Bernstein MA, Grgic M, Brosnan TJ, Pelc NJ. Reconstructions of phase contrast, phased array multicoil data. Magn Reson Med 1994;32(3):330-334.

124. Mispelter J, Lupu M, Briguet A. NMR probeheads for biophysical and biomedical experiments: theoretical principles & practical guidelines. London: Imperial College Press; 2006.

125. Bowick C. RF circuit design. Newton: Newnes; 1982.

126. Smith P. Electronic applications of the Smith chart. Stevenage: The Institution of Engineering and Technology; 1995.

127. Hoult D. The principle of reciprocity in signal strength calculations—a mathematical guide. Concepts in Magnetic Resonance 2000;12(4):173-187.

128. Jackson J. Classical electrodynamics. New York: John Wiley & Sons, Inc; 1999.

129. Ballantine S. The Lorentz reciprocity theorem for electric waves. Proc IRE 1928;16:513-518.

130. Hayes CE, Edelstein WA, Schenck JF, Mueller OM, Eash M. An efficient, highly homogeneous radiofrequency coil for whole-body NMR imaging at 1.5 T. Journal of Magnetic Resonance (1969) 1985;63(3):622-628.

131. Giovannetti G, Pingitore A, Positano V, De Marchi D, Valvano G, Gibiino F, Aquaro GD, Lombardi M, Landini L, Santarelli MF. Improving sodium magnetic resonance in humans by design of a dedicated 23Na surface coil. Measurement 2014;50:285-292.

132. Montgomery DB, Terrell J. Some useful information for the design of air-core solenoids. Cambridge, Mass: National Magnet Laboratory, Massachusetts Institute of Technology; 1961.

133. Smythe WR. Static and dynamic electricity. New York: McGraw-Hill Book Company; 1950.

134. Avdievich NI, Hetherington HP. 4 T actively detunable transmit/receive transverse electromagnetic coil and 4-channel receive-only phased array for 1H human brain studies. Magn Reson Med 2004;52(6):1459-1464.

135. Hayes CE, Hattes N, Roemer PB. Volume imaging with MR phased arrays. Magn Reson Med 1991;18(2):309-319.

136. Hayes CE, Mathis CM, Yuan C. Surface coil phased arrays for high-resolution imaging of the carotid arteries. J Magn Reson Imaging 1996;6(1):109-112.

137. Wiggins GC, Polimeni JR, Potthast A, Schmitt M, Alagappan V, Wald LL. 96-Channel receive-only head coil for 3 Tesla: design optimization and evaluation. Magn Reson Med 2009;62(3):754-762.

138. Wiggins GC, Triantafyllou C, Potthast A, Reykowski A, Nittka M, Wald LL. 32-channel 3 Tesla receive-only phased-array head coil with soccer-ball element geometry. Magn Reson Med 2006;56(1):216-223.

139. de Zwart JA, Ledden PJ, van Gelderen P, Bodurka J, Chu R, Duyn JH. Signal-to-noise ratio and parallel imaging performance of a 16-channel receive-only brain coil array at 3.0 Tesla. Magn Reson Med 2004;51(1):22-26.

140. Haase A, Odoj F, Von Kienlin M, Warnking J, Fidler F, Weisser A, Nittka M, Rommel E, Lanz T, Kalusche B. NMR probeheads for in vivo applications. Concepts in Magnetic Resonance 2000;12(6):361-388.

141. Ohliger MA, Sodickson DK. An introduction to coil array design for parallel MRI. NMR Biomed 2006;19(3):300-315.

142. Hayes CE, Axel L. Noise performance of surface coils for magnetic resonance imaging at 1.5 T. Med Phys 1985;12(5):604-607.

143. Barberi EA, Gati JS, Rutt BK, Menon RS. A transmit-only/receive-only (TORO) RF system for high-field MRI/MRS applications. Magn Reson Med 2000;43(2):284-289.

144. Friis HT. Noise figures of radio receivers. Proceedings of the IRE 1944;32(7):419-422.

145. Blalock T. A low-noise charge-sensitive preamplifier with a field-effect transistor in the input stage. IEEE Trans Nucl Sci 1964;11(3):365-372.

146. Gonord P, Kan S. Pulsed NMR preamplifier protection at ultrahigh frequency: an improved scheme. Rev Sci Instrum 1986;57(9):2280-2282.

147. Doty FD, Entzminger G, Kulkarni J, Pamarthy K, Staab JP. Radio frequency coil technology for small-animal MRI. NMR Biomed 2007;20(3):304-325.

148. Plana R, Escotte L, Llopis O, Amine H, Parra T, Gayral M, Graffeuil J. Noise in AlGaAs/InGaAs/GaAs pseudomorphic HEMTs from 10 Hz to 18 GHz. IEEE Trans Electron Devices 1993;40(5):852-858.

149. Nelson C, Walls F, Sicarrdi M, De Marchi A. A new 5 and 10 MHz high isolation distribution amplifier. Proceedings of the 1994 IEEE International, 1994;567-571.

150. Spiegel RJ. A review of numerical models for predicting the energy deposition and resultant thermal response of humans exposed to electromagnetic fields. IEEE Trans Microw Theory Techn 1984;32(8):730-746.

151. Avdievich NI, Hetherington HP. 4 T Actively detuneable double-tuned 1H/31P head volume coil and four-channel 31P phased array for human brain spectroscopy. J Magn Reson 2007;186(2):341-346.

152. Vaughan JT, Garwood M, Collins CM, Liu W, DelaBarre L, Adriany G, Andersen P, Merkle H, Goebel R, Smith MB, Ugurbil K. 7T vs. 4T: RF power, homogeneity, and signal-to-noise comparison in head images. Magn Reson Med 2001;46(1):24-30.

153. Vaughan JT, Snyder CJ, DelaBarre LJ, Bolan PJ, Tian J, Bolinger L, Adriany G, Andersen P, Strupp J, Ugurbil K. Whole-body imaging at 7T: preliminary results. Magn Reson Med 2009;61(1):244-248.

154. Avdievich NI, Bradshaw K, Kuznetsov AM, Hetherington HP. High-field actively detuneable transverse electromagnetic (TEM) coil with low-bias voltage for high-power RF transmission. Magn Reson Med 2007;57(6):1190-1195.

155. Tropp J. The theory of the bird-cage resonator. J Magn Reson 1989;82(1):51-62.

156. Chen C-N, Hoult D, Sank V. Quadrature detection coils—a further $\sqrt{2}$ improvement in sensitivity. J Magn Reson 1983;54(2):324-327.

157. Leifer MC. Resonant modes of the birdcage coil. J Magn Reson 1997;124(1):51-60.

158. Vullo T, Zipagan RT, Pascone R, Whalen JP, Cahill PT. Experimental design and fabrication of birdcage resonators for magnetic resonance imaging. Magn Reson Med 1992;24(2):243-252.

159. Boissoles P, Caloz G. Accurate calculation of mutual inductance and magnetic fields in a birdcage coil. Preprint IRMAR 2006:06-07.

160. Alecci M, Collins CM, Wilson J, Liu W, Smith MB, Jezzard P. Theoretical and experimental evaluation of detached endcaps for 3 T birdcage coils. Magn Reson Med 2003;49(2):363-370.

161. Doherty Jr W, Joos R. The Pin diode circuit designers' handbook. Watertown: Microsemi; 1999.

162. Li L, Sotak CH. An efficient technique for decoupling NMR transmit coils from surface-coil receivers. J Magn Reson 1964;93(1):207-213.

163. Li L, Sotak CH. An efficient technique for decoupling NMR transmit coils from surface-coil receivers. J Magn Reson 1991;93(1):207-213.

164. Li L, Zhang H, Ji T, Wyrwicz AM. A simple and effective decoupling circuit for three-RF-coil ASL MRI experiments. Proceedings of the 12th Annual Meeting of the ISMRM, Kyoto, Japan, 2004;1361.

165. Alagappan V, Adalsteinsson E, Setsompop K, Fontius U, Zelinski A, Wiggins G, Hebrank F, Schmitt F, Wald L. Comparison of three transmit arrays for parallel transmit. 2007. Proceedings of the 15th Annual Meeting of the ISMRM, Berlin, Germany, 2007;165.

166. Meise FM, Rivoire J, Terekhov M, Wiggins GC, Keil B, Karpuk S, Salhi Z, Wald LL, Schreiber LM. Design and evaluation of a 32-channel phased-array coil for lung imaging with hyperpolarized 3-helium. Magn Reson Med 2010;63(2):456-464.

167. Meise FM, Groebner J, Nagel AM, Umathum R, Stark H, Hoffman SH, Semmler W, Bock M. A 30-channel phased array for oxygen-17 (17O) brain MRI at 7 tesla. Proc Intl Soc Mag Reson Med 2011;19:472.

168. Horowitz P, Hill W, Hayes TC. The art of electronics. Cambridge, UK: Cambridge University Press; 1989.

169. Zennaro M, Fonda C. Radio laboratory handbook. Trieste, Italy: International Centre for Theoretical Physics; 2004.

170. Bleakney W, Gould AJ. The relative abundance of hydrogen isotopes. Phys Rev 1933;44(4):265.

171. Koller H, Engelhardt G, Kentgens AP, Sauer J. 23Na NMR spectroscopy of solids: Interpretation of quadrupole interaction parameters and chemical shifts. J Phys Chem 1994;98(6):1544-1551.

172. Ouwerkerk R. Sodium magnetic resonance imaging: from research to clinical use. J Am Coll Radiol 2007;4(10):739-741.

173. Karaghiosoff K. Phosphorus-31 NMR: Wiley Online Library; 1996.

174. Ruiz-Cabello J, Barnett BP, Bottomley PA, Bulte JW. Fluorine (19F) MRS and MRI in biomedicine. NMR Biomed 2011;24(2):114-129.

175. Kirsch S, Augath M, Seiffge D, Schilling L, Schad LR. In vivo chlorine-35, sodium-23 and proton magnetic resonance imaging of the rat brain. NMR Biomed 2010;23(6):592-600.

176. Frieden E. The chemical elements of life. Scientific American 1972;227(1):52-60.

177. Parrish TB, Fieno DS, Fitzgerald SW, Judd RM. Theoretical basis for sodium and potassium MRI of the human heart at 1.5 T. Magn Reson Med 1997;38(4):653-661.

178. Ouwerkerk R, Bleich KB, Gillen JS, Pomper MG, Bottomley PA. Tissue sodium concentration in human brain tumors as measured with 23Na MR imaging. Radiology 2003;227(2):529-537.

179. Ouwerkerk R, Jacobs MA, Macura KJ, Wolff AC, Stearns V, Mezban SD, Khouri NF, Bluemke DA, Bottomley PA. Elevated tissue sodium concentration in malignant breast lesions detected with non-invasive 23Na MRI. Breast Cancer Res Treat 2007;106(2):151-160.

180. Borthakur A, Shapiro EM, Beers J, Kudchodkar S, Kneeland JB, Reddy R. Sensitivity of MRI to proteoglycan depletion in cartilage: comparison of sodium and proton MRI. Osteoarthr Cartil 2000;8(4):288-293.

181. Reddy R, Insko EK, Noyszewski EA, Dandora R, Kneeland JB, Leigh JS. Sodium MRI of human articular cartilage in vivo. Magn Reson Med 1998;39(5):697-701.

182. Borthakur A, Shapiro EM, Akella SV, Gougoutas A, Kneeland JB, Reddy R. Quantifying sodium in the human wrist in vivo by using MR imaging. Radiology 2002;224(2):598-602.

183. Wheaton AJ, Borthakur A, Shapiro EM, Regatte RR, Akella SV, Kneeland JB, Reddy R. Proteoglycan loss in human knee cartilage: quantitation with sodium MR imaging--feasibility study. Radiology 2004;231(3):900-905.

184. Maril N, Rosen Y, Reynolds GH, Ivanishev A, Ngo L, Lenkinski RE. Sodium MRI of the human kidney at 3 Tesla. Magn Reson Med 2006;56(6):1229-1234.

185. Rosen Y, Lenkinski RE. Sodium MRI of a human transplanted kidney. Acad Radiol 2009;16(7):886-889.

186. Thulborn KR, Davis D, Snyder J, Yonas H, Kassam A. Sodium MR imaging of acute and subacute stroke for assessment of tissue viability. Neuroimaging Clin N Am 2005;15(3):639-653, xi-xii.

187. Inglese M, Madelin G, Oesingmann N, Babb JS, Wu W, Stoeckel B, Herbert J, Johnson G. Brain tissue sodium concentration in multiple sclerosis: a sodium imaging study at 3 Tesla. Brain 2010;133(Pt 3):847-857.

188. Boada FE, Christensen JD, Huang-Hellinger FR, Reese TG, Thulborn KR. Quantitative in vivo tissue sodium concentration maps: the effects of biexponential relaxation. Magn Reson Med 1994;32(2):219-223.

189. Ra J, Hilal S, Cho Z. A method for in vivo MR imaging of the short T2 component of sodium-23. Magn Reson Med 1986;3(2):296-302.

190. Greenwood N, Terence C. Mössbauer spectroscopy. London: CRC Press; 1971.

191. Adriany G, Gruetter R. A half-volume coil for efficient proton decoupling in humans at 4 Tesla. J Magn Reson 1997;125(1):178-183.

192. Murphyboesch J, Srinivasan R, Carvajal L, Brown TR. Two configurations of the four-ring birdcage coil for ^{1}H imaging and ^{1} H-decoupled ^{31}P spectroscopy of the human head. J Magn Reson B 1994;103(2):103-114.

193. Lanz T, Ruff J, Weisser A, Haase A. Double tuned 23Na 1H nuclear magnetic resonance birdcage for application on mice in vivo. Rev Sci Instrum 2001;72(5):2508-2510.

194. Doty FD, Entzminger Jr G, Hauck CD. Error-tolerant RF litz coils for NMR/MRI. J Magn Reson 1999;140(1):17-31.

195. Bottomley PA, Hardy CJ, Roemer PB, Mueller OM. Proton-decoupled, Overhauser-enhanced, spatially localized carbon-13 spectroscopy in humans. Magn Reson Med 1989;12(3):348-363.

196. Adriany G, Gruetter R. A half-volume coil for efficient proton decoupling in humans at 4 tesla. J Magn Reson 1997;125(1):178-183.

197. Alecci M, Romanzetti S, Kaffanke J, Celik A, Wegener H, Shah N. Practical design of a 4 Tesla double-tuned RF surface coil for interleaved 1H and 23Na MRI of rat brain. J Magn Reson 2006;181(2):203-211.

198. Dabirzadeh A, McDougall MP. Trap design for insertable second-nuclei radiofrequency coils for magnetic resonance imaging and spectroscopy. Concepts Magn Reson Part B Magn Reson Eng 2009;35(3):121-132.

199. Schnall M, Harihara Subramanian V, Leigh Jr J, Chance B. A new double-tuned probed for concurrent 1H and 31P NMR. J Magn Reson 1985;65(1):122-129.

200. Dürr W, Rauch S. A dual-frequency circularly polarizing whole-body MR antenna for 69/170 MHz. Magn Reson Med 1991;19(2):446-455.

201. Tomanek B, Volotovskyy V, Gruwel ML, Mckenzie E, King SB. Double-frequency birdcage volume coils for 4.7 T and 7T. Concepts Magn Reson Part B Magn Reson Eng 2005;26(1):16-22.

202. Fitzsimmons JR, Beck BL, Ralph Brooker H. Double resonant quadrature birdcage. Magn Reson Med 1993;30(1):107-114.

203. Rath AR. Design and performance of a double-tuned bird-cage coil. J Magn Reson 1990;86(3):488-495.

204. Amari S, Müfit Uluğ A, Bornemann J, Van Zijl P, Barker PB. Multiple tuning of birdcage resonators. Magn Reson Med 1997;37(2):243-251.

205. Joseph PM, Lu D. A technique for double resonant operation of birdcage imaging coils. IEEE Trans Med Imaging 1989;8(3):286-294.

206. Lu D, Joseph PM. A technique of double-resonant operation of 19F and 1H quadrature birdcage coils. Magn Reson Med 1991;19(1):180-185.

207. Ha S, Hamamura MJ, Nalcioglu O, Muftuler LT. A PIN diode controlled dual-tuned MRI RF coil and phased array for multi nuclear imaging. Phys Med Biol 2010;55:2589.

208. Nakashima T, Naganawa S, Sugiura M, Teranishi M, Sone M, Hayashi H, Nakata S, Katayama N, Ishida IM. Visualization of endolymphatic hydrops in patients with Meniere's disease. Laryngoscope 2007;117(3):415-420.

209. Nakashima T, Naganawa S, Teranishi M, Tagaya M, Nakata S, Sone M, Otake H, Kato K, Iwata T, Nishio N. Endolymphatic hydrops revealed by intravenous gadolinium injection in patients with Ménière's disease. Acta Otolaryngol 2010;130(3):338-343.

210. Silver RD, Djalilian HR, Levine SC, Rimell FL. High-resolution magnetic resonance imaging of human cochlea. Laryngoscope 2002;112(10):1737-1741.

211. Underhill HR, Yuan C, Hayes CE. A combined solenoid-surface RF coil for high-resolution whole-brain rat imaging on a 3.0 Tesla clinical MR scanner. Magn Reson Med 2010;64(3):883-892.

212. Counter SA, Bjelke B, Klason T, Chen Z, Borg E. Magnetic resonance imaging of the cochlea, spiral ganglia and eighth nerve of the guinea pig. Neuroreport 1999;10(3):473-479.

213. Lane JI, Witte RJ, Bolster B, Bernstein MA, Johnson K, Morris J. State of the art: 3T imaging of the membranous labyrinth. AJNR Am J Neuroradiol 2008;29(8):1436-1440.

214. Zou J, Pyykkö I, Bretlau P, Klason T, Bjelke B. In vivo visualization of endolymphatic hydrops in guinea pigs: magnetic resonance imaging evaluation at 4.7 tesla. Ann Otol Rhinol Laryngol 2003;112(12):1059-1065.

215. Zou J, Zhang W, Poe D, Zhang Y, Ramadan UA, Pyykko I. Differential passage of gadolinium through the mouse inner ear barriers evaluated with 4.7T MRI. Hear Res 2010;259(1-2):36-43.

216. Koizuka I, Seo Y, Murakami M, Seo R, Kato I. Micro-magnetic resonance imaging of the inner ear in the guinea pig. NMR Biomed 1997;10(1):31-34.

217. Fiorino F, Pizzini FB, Beltramello A, Barbieri F. MRI performed after intratympanic gadolinium administration in patients with Ménière's disease: correlation with symptoms and signs. Eur Arch Otorhinolaryngol 2011;268(2):181-187.

218. Herrmann KH, Schmidt S, Kretz A, Haenold R, Krumbein I, Metzler M, Gaser C, Witte OW, Reichenbach JR. Possibilities and limitations for high resolution small animal MRI on a clinical whole-body 3T scanner. MAGMA 2012;25(3):233-244.

219. Guidance for industry and staff. FDA Guidelines. Volume 2013;2003.

220. Particular requirements for the safety of magnetic resonance equipment for medical diagnosis. Diagnostic imaging equipment. Geneva, Switzerland: International Electrochemical Commission; 2000.

221. Zhang B, Yen YF, Chronik BA, McKinnon GC, Schaefer DJ, Rutt BK. Peripheral nerve stimulation properties of head and body gradient coils of various sizes. Magn Reson Med 2003;50(1):50-58.

222. Brockmann MA, Kemmling A, Groden C. Current issues and perspectives in small rodent magnetic resonance imaging using clinical MRI scanners. Methods 2007;43(1):79-87.

223. Beuf O, Jaillon F, Saint-Jalmes H. Small-animal MRI: signal-to-noise ratio comparison at 7 and 1.5 T with multiple-animal acquisition strategies. MAGMA 2006;19(4):202-208.

224. Keil B, Wiggins GC, Triantafyllou C, Wald LL, Meise FM, Schreiber LM, Klose KJ, Heverhagen JT. A 20-channel receive-only mouse array coil for a 3 T clinical MRI system. Magn Reson Med 2011;66(2):584-595.

225. Insko EK, Bolinger L. Mapping of the radiofrequency field. J Magn Reson 1993;103(1):82-85.

226. Yamazaki M, Naganawa S, Tagaya M, Kawai H, Ikeda M, Sone M, Teranishi M, Suzuki H, Nakashima T. Comparison of contrast effect on the cochlear perilymph after intratympanic and intravenous gadolinium injection. AJNR Am J Neuroradiol 2012;33(4):773-778.

227. Eckardt KU, Coresh J, Devuyst O, Johnson RJ, Kottgen A, Levey AS, Levin A. Evolving importance of kidney disease: from subspecialty to global health burden. Lancet 2013;382(9887):158-169.

228. 2014 National Chronic Kidney Disease Fact Sheet. http://www.cdc.gov/DIABETES/pubs/factsheets/kidney.htm: Centers for Disease Control and Prevention; 2014.

229. Heyman SN, Khamaisi M, Rosen S, Rosenberger C. Renal parenchymal hypoxia, hypoxia response and the progression of chronic kidney disease. AJNR Am J Nephrol 2008;28(6):998-1006.

230. Brezis M, Rosen S. Hypoxia of the renal medulla--its implications for disease. N Engl J Med 1995;332(10):647-655.

231. Palm F, Cederberg J, Hansell P, Liss P, Carlsson PO. Reactive oxygen species cause diabetes-induced decrease in renal oxygen tension. Diabetologia 2003;46(8):1153-1160.

232. Johannes T, Mik EG, Nohé B, Unertl KE, Ince C. Acute decrease in renal microvascular PO2 during acute normovolemic hemodilution. Am J Physiol Renal Physiol 2007;292(2):F796-803.

233. Sadowski EA, Fain SB, Alford SK, Korosec FR, Fine J, Muehrer R, Djamali A, Hofmann M, Becker B, Grist TM. Assessment of acute renal transplant rejection with blood oxygen level-dependent MR imaging: initial experience. Radiology 2005;236:911–919.

234. Michaely HJ, Metzger L, Haneder S, Hansmann J, Schoenberg SO, Attenberger UI. Renal BOLD-MRI does not reflect renal function in chronic kidney disease. Kidney Int 2012;81(7):684-689.

235. Zhang JL, Morrell G, Rusinek H, Warner L, Vivier PH, Cheung AK, Lerman LO, Lee VS. Measurement of renal tissue oxygenation with blood oxygen level-dependent MRI and oxygen transit modeling. Am J Physiol Renal Physiol 2014;306(6):F579-587.

236. Clark LC, Lyons C. Electrode systems for continuous monitoring in cardiovascular surgery. Ann N Y Acad Sci 1962;102(1):29-45.

237. Pohlmann A, Cantow K, Hentschel J, Arakelyan K, Ladwig M, Flemming B, Hoff U, Persson PB, Seeliger E, Niendorf T. Linking non-invasive parametric MRI with invasive physiological measurements (MR-PHYSIOL): towards a hybrid and integrated approach for investigation of acute kidney injury in rats. Acta Physiol (Oxf) 2013;207(4):673-689.

238. Pohlmann A, Arakelyan K, Hentschel J, Cantow K, Flemming B, Ladwig M, Waiczies S, Seeliger E, Niendorf T. Detailing the relation between renal T2* and renal tissue pO2 using an integrated approach of parametric magnetic resonance imaging and invasive physiological measurements. Invest Radiol 2014.

239. Jones CA, Krolewski AS, Rogus J, Xue JL, Collins A, Warram JH. Epidemic of end-stage renal disease in people with diabetes in the United States population: do we know the cause? Kidney Int 2005;67(5):1684-1691.

240. Wang Z, Jiang T, Li J, Proctor G, McManaman JL, Lucia S, Chua S, Levi M. Regulation of renal lipid metabolism, lipid accumulation, and glomerulosclerosis in FVBdb/db mice with type 2 diabetes. Diabetes 2005;54(8):2328-2335.

241. Weinberg JM. Lipotoxicity. Kidney Int 2006;70(9):1560-1566.

242. Schaffer JE. Lipotoxicity: when tissues overeat. Curr Opin Lipidol 2003;14(3):281-287.

243. Kim HJ, Moradi H, Yuan J, Norris K, Vaziri ND. Renal mass reduction results in accumulation of lipids and dysregulation of lipid regulatory proteins in the remnant kidney. Am J Physiol Renal Physiol 2009;296(6):F1297-1306.

244. Coombs BD, Szumowski J, Coshow W. Two-point Dixon technique for water-fat signal decomposition with B0 inhomogeneity correction. Magn Reson Med 1997;38(6):884-889.

245. Lee VS, Kaur M, Bokacheva L, Chen Q, Rusinek H, Thakur R, Moses D, Nazzaro C, Kramer EL. What causes diminished corticomedullary differentiation in renal insufficiency? J Magn Reson Imaging 2007;25(4):790-795.

246. Yu H, Shimakawa A, McKenzie CA, Brodsky E, Brittain JH, Reeder SB. Multiecho water-fat separation and simultaneous R2* estimation with multifrequency fat spectrum modeling. Magn Reson Med 2008;60(5):1122-1134.

247. Ouwerkerk R, Jacobs MA, Macura KJ, Wolff AC, Stearns V, Mezban SD, Khouri NF, Bluemke DA, Bottomley PA. Elevated tissue sodium concentration in malignant breast lesions detected with non-invasive 23Na MRI. Breast Cancer Res Treat 2007;106(2):151-160.

248. Borthakur A, Shapiro EM, Beers J, Kudchodkar S, Kneeland JB, Reddy R. Sensitivity of MRI to proteoglycan depletion in cartilage: comparison of sodium and proton MRI. Osteoarthr Cartilage 2000;8(4):288-293.

249. Reddy R, Insko EK, Noyszewski EA, Dandora R, Kneeland JB, Leigh JS. Sodium MRI of human articular cartilage in vivo. Magn Reson Med 1998;39(5):697-701.

250. Maril N, Rosen Y, Reynolds GH, Ivanishev A, Ngo L, Lenkinski RE. Sodium MRI of the human kidney at 3 Tesla. Magn Reson Med 2006;56(6):1229-1234.

251. Stehning C, Keupp J, Rahmer J. Simultaneous 23Na/1H imaging with dual excitation and double tuned birdcage coil. Proceedings of the 19th Annual Meeting of the ISMRM, Montreal, Canada. 2011;1501.

252. Glunde K, Ackerstaff E, Mori N, Jacobs MA, Bhujwalla ZM. Choline phospholipid metabolism in cancer: consequences for molecular pharmaceutical interventions. Mol Pharm 2006;3(5):496-506.

253. Brown TR, Stoyanova R, Greenberg T, Srinivasan R, Murphy-Boesch J. NOE enhancements and T1 relaxation times of phosphorylated metabolites in human calf muscle at 1.5 Tesla. Magn Reson Med 1995;33(3):417-421.

254. Luyten PR, Bruntink G, Sloff FM, Vermeulen JW, van der Heijden JI, den Hollander JA, Heerschap A. Broadband proton decoupling in human 31P NMR spectroscopy. NMR Biomed 1989;1(4):177-183.

255. Mancini L, Payne GS, Leach MO. Implementation and evaluation of CSI-localized J cross-polarization for detection of 31P magnetic resonance spectra in vivo. Magn Reson Med 2005;54(5):1065-1071.

256. Klomp DW, Kentgens AP, Heerschap A. Polarization transfer for sensitivity-enhanced MRS using a single radio frequency transmit channel. NMR Biomed 2008;21(5):444-452.

257. Klomp DW, Wijnen JP, Scheenen TW, Heerschap A. Efficient 1H to 31P polarization transfer on a clinical 3T MR system. Magn Reson Med 2008;60(6):1298-1305.

258. Jeong EK, Sapkota N, Shi X, Kaggie J. Simultaneous dual-Nuclear 31P/1H MRS at a clinical MRI system with time-sharing second RF channel. Salt Lake City, Utah, USA, 2013;2781.

259. James J, Lin C, Stark H, Dale B, Bansal N. Optimization and Characterization of Sodium MRI Using 8-channel 23 Na and 2-channel 1 H RX/TX Coil. 13th International Conference on Biomedical Engineering, 2009;23:138-141.

260. Kim J-H, Kim K-N, Moon C, Hong S-M, Park B-W, Park HJ, Bae KT. 1H/23Na dual-tuned RF unicoil for human body MR imaging at 3T. In Proceedings of the 18th Annual Meeting of ISMRM. Stockholm, Sweden, 2010;3837.

261. Kim JH, Moon CH, Park BW, Furlan A, Zhao T, Bae KT. Multichannel transceiver dual-tuned RF coil for proton/sodium MR imaging of knee cartilage at 3 T. Magn Reson Imaging 2012;30:562–571.

262. Ha S, Hamamura MJ, Nalcioglu O, Muftuler LT. A PIN diode controlled dual-tuned MRI RF coil and phased array for multi nuclear imaging. Phys Med Biol 2010;55:2589.

263. Brown R, Madelin G, Lattanzi R, Chang G, Regatte RR, Sodickson DK, Wiggins GC. Design of a nested eight-channel sodium and four-channel proton coil for 7T knee imaging. Magn Reson Med 2013;70(1):259-268.

264. Kaggie JD, Hadley JR, Badal J, Campbell JR, Park DJ, Parker DL, Morrell G, Newbould RD, Wood AF, Bangerter NK. A 3 T sodium and proton composite array breast coil. Magn Reson Med 2014;71: 2231–2242.

265. Keupp J, Rahmer J, Grasslin I, Mazurkewitz PC, Schaeffter T, Lanza GM, Wickline SA, Caruthers SD. Simultaneous dual-nuclei imaging for motion corrected detection and quantification of 19F imaging agents. Magn Reson Med 2011;66(4):1116-1122.

266. Payne A, Merrill R, Minalga E, Vyas U, de Bever J, Todd N, Hadley R, Dumont E, Neumayer L, Christensen D, Roemer R, Parker D. Design and characterization of a laterally mounted phased-array transducer breast-specific MRgHIFU device with integrated 11-channel receiver array. Med Phys 2012;39(3):1552-1560.

267. Klose U. In vivo proton spectroscopy in presence of eddy currents. Magn Reson Med 1990;14(1):26-30.

268. Helms G, Piringer A. Restoration of motion-related signal loss and line-shape deterioration of proton MR spectra using the residual water as intrinsic reference. Magn Reson Med 2001;46(2):395-400.

269. Boada FE, Shen GX, Chang SY, Thulborn KR. Spectrally weighted twisted projection imaging: reducing T2 signal attenuation effects in fast three-dimensional sodium imaging. Magn Reson Med 1997;38(6):1022-1028.

270. Shi X, Kim SE, Kholmovski E, Parker D, Jeong EK. Improvement of accuracy of diffusion MRI using real-Time 2D self-gated data acquisition. NMR Biomed 2009;22(5):545-550.

271. Li Y, Thapa B, Zhang H, Li X, Yu F, Jeong E-K, Yang Z, Jiang Z-X. Synthesis of gemini surfactants with twelve symmetric fluorine atoms and one singlet 19F MR signal as novel 19F MRI agents. Tetrahedron 2013;69(46): 9586–9590.

272. Jiang ZX, Liu X, Jeong EK, Yu YB. Symmetry-guided design and fluorous synthesis of a stable and rapidly excreted imaging tracer for 19F MRI. Angewandte Chemie 2009;121(26):4849-4852.

273. Siegel R, Naishadham D, Jemal A. Cancer statistics, 2012. CA Cancer J Clin 2012;62(1):10-29.

274. Jemal A, Bray F, Center MM, Ferlay J, Ward E, Forman D. Global cancer statistics. CA Cancer J Clin 2011;61(2):69-90.

275. Saslow D, Boetes C, Burke W, Harms S, Leach MO, Lehman CD, Morris E, Pisano E, Schnall M, Sener S, Smith RA, Warner E, Yaffe M, Andrews KS, Russell CA, Group ACSBCA. American Cancer Society guidelines for breast screening with MRI as an adjunct to mammography. CA Cancer J Clin 2007;57(2):75-89.

276. Jacobs MA, Stearns V, Wolff AC, Macura K, Argani P, Khouri N, Tsangaris T, Barker PB, Davidson NE, Bhujwalla ZM, Bluemke DA, Ouwerkerk R. Multiparametric magnetic resonance imaging, spectroscopy and multinuclear (^{23}Na) imaging monitoring of preoperative chemotherapy for locally advanced breast cancer. Acad Radiol 2010;17(12):1477-1485.

277. Glunde K, Jacobs MA, Pathak AP, Artemov D, Bhujwalla ZM. Molecular and functional imaging of breast cancer. NMR Biomed 2009;22(1):92-103.

278. Staroswiecki E, Bangerter NK, Gurney PT, Grafendorfer T, Gold GE, Hargreaves BA. In vivo sodium imaging of human patellar cartilage with a 3D cones sequence at 3 T and 7 T. J Magn Reson Imaging 2010;32(2):446-451.

279. Sodickson DK, Manning WJ. Simultaneous acquisition of spatial harmonics (SMASH): fast imaging with radiofrequency coil arrays. Magn Reson Med 1997;38(4):591-603.

280. Griswold MA, Jakob PM, Heidemann RM, Nittka M, Jellus V, Wang J, Kiefer B, Haase A. Generalized autocalibrating partially parallel acquisitions (GRAPPA). Magn Reson Med 2002;47(6):1202-1210.

281. Hardy CJ, Bottomley PA, Rohling KW, Roemer PB. An NMR phased array for human cardiac 31P spectroscopy. Magn Reson Med 1992;28(1):54-64.

282. Lee RF, Giaquinto R, Constantinides C, Souza S, Weiss RG, Bottomley PA. A broadband phased-array system for direct phosphorus and sodium metabolic MRI on a clinical scanner. Magn Reson Med 2000;43(2):269-277.

283. Zaaraoui W, Konstandin S, Nagel AM, Wichmann T, Berthel D, Confort-Gouny S, Cozzone PJ, Audoin B, Pelletier J, Schad LR, Ranjeva J-P. Total sodium brain concentrations in compartments of patient with Multiple Sclerosis. A preliminary in vivo 23Na MRI study. In Proceedings of the 19th Annual Meeting of ISMRM. Montreal, Quebec, Canada, 2011;1496.

284. Lanz T, Mayer M, Robson MD, Neubauer S, Ruff J, Weisser A. An 8 Channel 23Na Heart Array for Application at 3 T. In Proceedings of the 15th Annual Meeting of ISMRM. Berlin, Germany, 2007;241.

285. Finnerty M, Yang X, Zheng T, Heilman J, Castrilla N, Herczak J, Fujita H, Wiggins G, Brown R, Madelin G. A 7-Tesla transmit with 15-channel receive-only array knee coil for sodium imaging. In Proceedings of the 19th Annual Meeting of ISMRM. Montreal, Quebec, Canada, 2011;1900.

286. Qian Y, Zhao TZ, Wiggins GC, Wald LL, Zheng H, Weimer J, Boada F. Sodium imaging of human brain at 7 T with 15-channel array coil. Magn Reson Med 2012;68:1808-1814.

287. Staroswiecki E, Nnewihe A, Bangerter NK, Daniel BL, Hargreaves BA. In vivo sodium imaging and relaxometry of the breast at 3T. In Proceedings of the 17th Annual Meeting of ISMRM. Honolulu, Hawaii, USA, 2009;2129.

288. Kaggie J, Park D, Newbould RD, Morrell GR, Hargreaves B, Staroswiecki E, Gold GE, Bangerter NK. In vivo breast sodium T1 measurements using inversion recovery 3D Cones. In Proceedings of the 19th Annual Meeting of ISMRM. Montreal, Quebec, Canada, 2011;3506.

289. Alecci M, Romanzetti S, Kaffanke J, Celik A, Wegener H, Shah N. Practical design of a 4 Tesla double-tuned RF surface coil for interleaved 1H and 23Na MRI of rat brain. J Magn Reson 2006;181(2):203-211.

290. Dabirzadeh A, McDougall MP. Trap design for insertable second-nuclei radiofrequency coils for magnetic resonance imaging and spectroscopy. Concepts Magn Reson B 2009;35(3):121-132.

291. Leach MO, Hind A, Sauter R, Requardt H, Weber H. The design and use of a dual-frequency surface coil providing proton images for improved localization in 31P spectroscopy of small lesions. Med Phys 1986;13(4):510-513.

292. Jevtic J; IGC-Medical Advances, Inc., assignee. Phased array local coil for MRI imaging having non-overlapping regions of sensitivity. U.S. Patent No. 7,091,721. 15 Aug. 2006.

293. Hayes CE, Edelstein WA, Schenck JF. Radio frequency resonators. In: Partain CL, Price RR, Patton JA, Kulkarni MV, James AE, editors. Magn Reson Imaging. Volume II: W. B. Saunders Company 1988;1183-1200.

294. Qian Y, Zhang Z, Stenger VA, Wang Y. Self-calibrated spiral SENSE. Magn Reson Med 2004;52(3):688-692.

295. Pruessmann KP, Weiger M, Börnert P, Boesiger P. Advances in sensitivity encoding with arbitrary k-space trajectories. Magn Reson Med 2001;46(4):638-651.